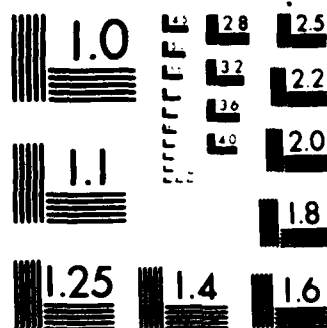


UNCL



MICROCOPY RESOLUTION TEST CHART
 NATIONAL BUREAU OF STANDARDS-1963-A

SC595.32SA

①
SC595.32SA

2

INTERDISCIPLINARY PROGRAM FOR QUANTITATIVE FLAW DEFINITION

SEMI-ANNUAL REPORT

Covering Period 07/01/77 through 01/01/78

Contract Number F33615-74-C-5180

Project Number 7351

Approved FOR PUBLIC RELEASE
DISTRIBUTION UNLIMITED

Prepared for:

Advanced Research Projects Agency
Arlington, VA

and

Air Force Materials Laboratory
Air Force Systems Command
Wright-Patterson AFB, OH 45433

DTIC

SEP 06 1983

E



Rockwell International
Science Center

DTIC FILE COPY

ADA 132082

83 09 01 065

SC595.32SA

INTERDISCIPLINARY PROGRAM
FOR
QUANTITATIVE FLAW DEFINITION

SEMI-ANNUAL REPORT

Covering Period 7/01/77 Through 01/01/78

Contract Number F33615-74-C-5180


Project No. 7351

Prepared for

Advanced Research Projects Agency
Arlington, Virginia

and

Air Force Materials Laboratory
Air Force Systems Command
Wright Patterson AFB, Ohio 45433


D. O. Thompson
Program Manager
Center for Advanced NDE

Accession For	
NTIS	<input checked="" type="checkbox"/>
DTIC	<input type="checkbox"/>
US	<input type="checkbox"/>
Dist	<input type="checkbox"/>
A	



Rockwell International
Science Center



TABLE OF CONTENTS

	<u>Page</u>
OVERVIEW	
PROJECT I - QUANTITATIVE ULTRASONIC CHARACTERIZATION.....	iv
PROJECT II - QUANTITATIVE NDE FOR SURFACE FLAWS.....	x
PROJECT III - NDE FOR ADVANCED MATERIALS.....	xiii
INDIVIDUAL REPORTS	
PROJECT I	
UNIT A, TASK 1 - Application of Geometrical Diffraction Theory to QNDE Analysis.....	1
UNIT A, TASK 2 - Theoretical Studies of Ultrasonic Flaw Characterization.....	23
UNIT A, TASK 3 - Theory of Ultrasonic Scattering.....	25
UNIT A, TASK 4 - Ultrasonic Scattering and the Inverse Problem.....	33
APPENDIX A - Quasistatic Approximation to the Scattering of an Arbitrarily Incident Elastic Plane Wave by an Elliptical Crack.....	37
APPENDIX B - Inference of Flaw Characteristics from Ultrasonic Scattering Amplitudes.....	44
UNIT B, TASK 1 - Recovery of Scattering Information in Real Geometries.....	63
UNIT B, TASK 2 - Ultrasonic Samples.....	71
UNIT B, TASK 3 - Signal-Processing Research in Con- nection with Ultrasonics in Non-Destructive Testing.....	74
UNIT C, TASK 1 - New Techniques for Acoustic Non- Destructive Testing.....	82
UNIT C, TASK 2 - Ultrasonic Imaging Techniques.....	95

TABLE OF CONTENTS (CONT'D)

	<u>Page</u>
UNIT C, TASK 3 - Non-Destructive Evaluation.....	99
UNIT C, TASK 4 - Application of Adaptive Learning to Establish Relationships Between Analytical and Empirical NDE Methods.....	102
UNIT C, TASK 5 - Determination of Fracture Mechanics Parameters from Elastic Wave Scattering Measurements at Low Frequencies.....	104
 PROJECT II	
UNIT A, TASK 1 - Experimental Definition of Interaction of Surface Waves from Surface Cracks.....	142
APPENDIX - Measurements of the Angular and Frequency Dependence of Acoustic Surface Wave Scattering from Surface Cracks.....	163
UNIT A, TASK 2 - Optimization of EMATs for Surface Flaw Detection.....	172
UNIT B, TASK 1 - Quantitative Measurement of Crack Parameters using Microwave Eddy-Current Techniques.....	176
UNIT B, TASK 2 - Ferromagnetic Resonance for the Detection of Surface Flaws in Metals.....	185
 PROJECT III	
UNIT A, TASK 1 - Ultrasonic Measurement of Adhesive Bond Strength.....	195
UNIT A, TASK 2 - Ultrasonic Ellipsometer Applied to Adhesive Bond Inspection.....	212
UNIT A, TASK 3 - Cohesive Bond Strength Prediction.....	220
UNIT B, TASK 1 - Moisture Distribution Analyses in Composites.....	242
UNIT B, TASK 2 - Acoustic Emission Signature Analysis in Composites.....	249



TABLE OF CONTENTS (CONT'D)

	<u>Page</u>
UNIT C, TASK 1 - Defect Fracture Probabilities.....	261
UNIT C, TASK 2 - Failure Prediction Analyses.....	279
UNIT C, TASK 3 - High Frequency Ultrasonic Defect Characterization in Ceramics.....	284
UNIT C, TASK 4 - Microfocus X-Ray and Image Enhance- ment of Radiographic Data.....	292
UNIT C, TASK 5 - Conventional Ultrasonic Inspection Methods Applied to Ceramics.....	294

OVERVIEW

PROJECT I - QUANTITATIVE ULTRASONIC CHARACTERIZATION

This project is a continuation of the previous effort that led to the establishment of a quantitative capability for measuring the size, shape and orientation of ellipsoidal flaws. The basic methodology used is illustrated in Fig. 1. The early effort focussed on developing approximate theories, checked against controlled experiments, to describe the ultrasound-flaw interaction. This effort answered the question, "How does ultrasound scatter from a known flaw?". The inverse question, "How does one identify an unknown flaw from measured scattering data?", is the problem of ultimate interest in NDE. This was addressed during the last year of the previous program. Predictive relationships were developed based on the theory and then tested using experimental data as input parameters. Comparison of the results to the known flaw parameters showed that quite satisfactory agreement had been obtained. For example, in eight determinations of the dimensions of ellipsoidal flaws oriented at various angles to the measurement aperture, using a predictor developed by adaptive learning techniques, the average absolute error was only 15% for the height and 37% for the diameter. Furthermore, much of this error could be attributed to known systematic errors in the approximate theory used. Other procedures yielded equally promising results. These were the first demonstrations of a quantitative NDE capability based solely on first principles.

The present program is dedicated to the refinement and improvement of these results. It is anticipated that a separate Test Bed program will be initiated in the near future whereby a hardware embodiment of the results in a single operational system can be implemented. Consequently, the tasks have been time sequenced and coordinated so that their outputs can be directly transferred to such a program. The tasks are divided into three units, Theory, Experiment, and Inversion, corresponding to the blocks in the methodology illustrated in Figure 1.

Further theoretical development plays an important role in the program. As noted above, much of the error in the previous estimates of flaw



HOW DOES ONE IDENTIFY
DEFECT FROM SCATTERED FIELDS?

HOW DOES SOUND
INTERACT WITH FLAWS?

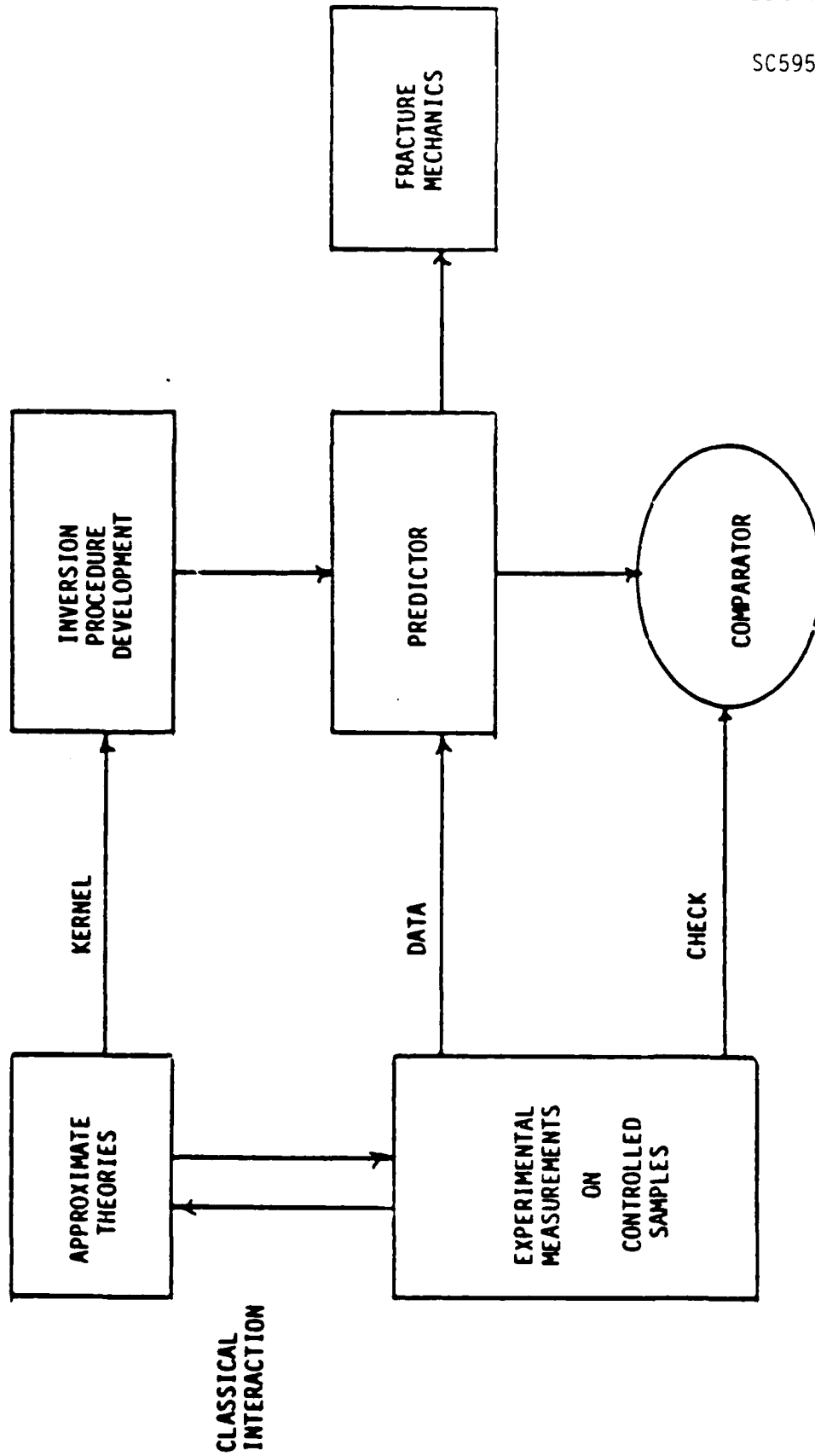


Figure 1

size could be attributed to systematic errors. For example, in the previously cited 37% average error in diameter determination, all of the predicted values were higher than the actual values. Correction of this systematic effect through the development of more accurate theories would greatly improve the result. Furthermore, many important parameters, such as phase and frequency dependencies, were totally neglected in the inversion procedure because of known deficiencies in the theory. However, these parameters contain much information concerning the flaw geometry, and incorporation of them in future predictions when better theories are available should greatly improve their performance.

Four tasks are included in Unit A which is dedicated to the improvement of theoretical models. Achenbach reports on the application of an elastic wave version of geometrical diffraction theory to the case of cracks. This model is particularly applicable to the short wavelength limit, and includes such effects as surface wave rays propagating on the crack surface which have not been previously treated. The results presented include formulae and numerical data for off-axis illumination of a penny-shaped crack and general comments on specific features that should be useful in the inversion of data. These results provide the foundation for understanding the interaction of ultrasound with two-dimensional, crack-like defects at high frequencies. On the other end of the spectrum, at long wavelengths, Teitel and Krumhansl present a report on the scattering from elliptical cracks. Previous results for longitudinal wave scattering have been generalized to all polarizations and angles of incidence. Probably the most difficult theoretical regime is the one in which the wavelength is comparable to the defect size. Here, the approximations that simplify the long and short wavelength limits are not valid, and more difficult schemes must be considered. During previous years, the Born approximation was developed which is, rigorously speaking, correct only for weakly scattering flaws. Domany describes a similar approximation, the distorted wave Born approximation which uses as a first iteration the solution to the scattering of an incident wave from a nearly equivalent spherical object (for which the exact solutions can be obtained) rather than the undisturbed incident wave as in the Born approximation. This holds promise for being particularly accurate for



strongly scattering flaws whose shape approaches a sphere. Also included in his report are some general conclusions regarding the differences in the character of the fields scattered from two-dimensional, crack-like flaws and three-dimensional, inclusions. Negotiations for the fourth task, to be carried out by Gubernatis, has just been completed. However, in the brief working time available, his previously developed codes for the extended quasi-static approximations have been generalized in terms of off-axis incidence and modified in format for use by Mucciardi in developing improved predictions using his adaptive learning techniques.

Unit B is primarily concerned with the experimental verification and guidance of the theoretical developments and the gathering of test data for the inversion techniques. Paton describes new samples that will be made during the year, including spheroidal inclusions, penny-shaped cracks inclined at angles to the part surface and one-dimensional flaws. Adler's work includes substantial improvements of his experimental apparatus, the transmittal of L→L and L→T, data to Mucciardi for testing his scattering predictor, and a comparison of new data for both amplitude and phase of signals scattered from crack-like flaws to geometrical diffraction theory. As a means for improving data, White discusses a new, monolithic transducer which holds promise for many possible applications, including acoustic emission detection, array construction, and signal processing device fabrication.

The primary emphasis of the present program is in the development of inversion techniques, since this is the end product needed to determine flaw parameters from ultrasonic data. Progress on six approaches is included in Unit C (the work of Rose is part of the Cornell report in Unit A). Even at very long wavelengths, it has recently been shown that considerable information can be obtained from scattered fields regarding flaw size, shape, and orientation. In particular, under certain conditions the stress intensity factor can be directly obtained from the data. In a comprehensive report, Elsley and Richardson report the philosophy of this approach and present discussions of the theory, experiment, and inversion of data. Using experimental data as input to the computational procedures developed, they find that the dimensions and orientations of ellipsoidal flaws can be determined with a high degree of accuracy. Included is a discussion of a

number of experimental problems that arise in long wavelength measurements and solutions that have been developed to overcome them. In a brief report reflecting a planned low level of effort, Mucciardi also discussed the development of techniques to treat low frequency information in scattered signals. Techniques to invert scattering data based on specific solutions to scattering problems are presented separately by Rose and Bleistein. Rose and Krumhansl present an inversion procedure based on the Born approximations. Despite the fact that this model is only rigorous for weakly scattering objects, the derived inversion procedure has given excellent results for the reconstruction of a spherical void, even in the presence of substantial noise. A detailed discussion of this result is given as well as an outline of future plans for more general tests of the procedure. Bleistein and Cohen consider a different algorithm based on an assumed strongly scattering object. In this work, as in that of Rose, reconstruction of the object is accomplished by appropriate spatial Fourier transformation of measured data. A discussion is given of various possible approaches to this, including some of the relative merits of dense versus sparsely spaced transducer positions as it effects the data processing requirements. New imaging approaches are presented by Kino and Lakin. Kino describes a new system presently under construction which makes extensive use of digital signal processing for the formation of the image. Its essential feature is that the pulse echo waveform from each transducer is individually recorded in memory and then recombined with appropriate delays for each point in the image. It is thus essentially a synthetic aperture system. Discussion is given of many novel features of the system including the use of compression techniques for side lobe reduction and the ensuing possibility of thinned array operation, the use of look-up-tables to increase system speed, and the use of an inverse filter to improve resolution. Lakin's system is based on pulsed cw operation, and is in many ways equivalent to a holographic system. By recording the amplitude and phase at each point in a 64 by 64 element grid, and performing appropriate convolution integrals, the fields at a flaw can be reconstructed. One of the key features of the system is the use of a recently developed hardware multiplier (with accumulator) to rapidly evaluate the convolutions.



**Rockwell International
Science Center**

SC595.32SA

Projections include the formation of an image in the near real time of 200 msec in a water tank or 14 sec if full compensation is made for the influence of the solid-liquid interface.

It is believed that all of these results, theoretical advances, experimental improvements, and advancement of several types of version procedures, constitute major progress towards the goal of full quantitative NDE.

OVERVIEW

PROJECT II - QUANTITATIVE NDE FOR SURFACE FLAWS

Project II is a newly initiated effort with the objective of quantitatively measuring the fracture related properties of surface flaws. Two forms of interrogating energy are being utilized. Ultrasonic surface wave and angle beam approaches are being developed through an extension of the techniques recently developed for the interior defect case. Eddy current techniques, which are suitable for interior defects but which are extensively used in the detection of surface flaws, are also being investigated in a series of tasks designed to increase their quantitative capabilities.

The ultrasonic surface wave characterization of flaws is addressed in three closely related reports in Unit A as noted in Figure 1 of the overview for Project I. A first step in the establishment of a defect characterization capability is the development of quantitative theoretical and experimental techniques. Auld discusses the former in a report written jointly with Buck and Tittmann. In this first phase of his theoretical efforts, he considers the analytically simple, but practically important, case of the long wavelength limit. In this regime, he develops formulae for the back-scattering, as a function of angle for a semicircular crack, a part circle crack, and a part ellipse crack. The theoretical efforts make use of recently developed reciprocity relations to place the results in a form that can be directly compared to the electrical signals measured using either piezoelectric or electromagnetic transducers. Also included is a discussion



be a part of this program, they are included for completeness. Important highlights include the demonstration of three distinct techniques for precise measurements of the frequency and angular dependence of surface wave scattering at frequencies ranging from 2 to 100 MHz, and the measurement of scattered signals in regimes when the wavelength is comparable to and much less than the scattering object. In the latter case, the results indicate considerable promise for a simple approach to the problem of estimating the surface length of the cracks.

In his joint report with Auld, Buck discussed the transducers and samples that will be used during the later phases of this program. Particular attention in the selection of samples has been paid to establishing a direct link between the idealized flaws having stress free, smooth surfaces which are being studied theoretically and experimentally approximated by EDM notched, and fatigue cracks that will be encountered in practice. As a part of this, a sequence of experiments is proposed to ascertain the effects of most radius of the crack, closure, and surface roughness. Included are the fracture mechanics relationships necessary for interpretation of the results.

A key step in transferring these research results into field use is addressing specific problems with an engineering optimization point-of-view. Such an effort is being undertaken by Thompson, Vasile, and Fortunko for the case of electromagnetic transducers. In their report they present some preliminary results of design calculations that will be used to define transducer configurations optimized for defect characterization.

Unit B is concerned with improvements in eddy current techniques. There is much that can be done to improve the interpretation of signals obtainable in presently used frequency ranges so that flaw parameters can be more quantitatively defined. Work initiated in this unit to date focusses upon a newer, less familiar, approach to eddy current testing which makes use of microwave frequencies to increase the sensitivity to small flaws by decreasing the electromagnetic skin depth (penetration of the eddy currents into the material). For example, in aluminum, the skin depth is 3.50 mils (89 μm) at 1 MHz as is commonly used in eddy current testing, 0.11 mils (2.8 μm) at 1 GHz as is being studied by Auld and Fortunko, and 0.011 mils (0.28 μm) at 100 GHz as is being studied by Bahr. In addition to decreasing

the skin depth, these higher frequencies place one in a new regime in which the interaction of the electromagnetic energy with the flaw has a substantially different character. It is believed that data obtained by microwave frequencies will yield additional information, which would complement conventional eddy current techniques and result in better quantification of flaws. For example, Bahr analyzes the interaction of electromagnetic energy with a rectangular flaw. By describing the fields inside the flaw in terms of cut-off waveguide modes, he finds that the change in scattered energy varies linearly with flaw depth over a substantial range of parameters as long as the depth is less than the surface length (a condition realized by most naturally occurring flaws). A specific example is given for the case of a 0.040 mil (1 mm) long crack, interrogated by 100 GHz radiation. It is interesting to note that this depth dependence is predicted despite the fact that the skin depth is less than $0.1 \mu\text{m}$. His future work will be directed at utilizing this, and other related results to be derived from the model, to develop procedures to quantitatively measure crack parameters.

The work of Auld and Fortunko is also concerned with the use of microwave frequencies to interrogate flaws. However, their experimental approach is significantly different since a ferromagnetic resonator is used to excite a very localized eddy current distribution at the surface of the metal. This approach promises to combine high sensitivity with high spatial resolution. In their report they discuss the principles of this device, describe a compact breadboard model and present some recently obtained experimental data including the detections of fatigue crack. Future plans include refinements in the probe design and the study of its use in measuring quantitative flaw parameters. A new probe design inquiry on self-containing transistor oscillators is also being studied. It is believed that the transistor oscillator approach may result in considerable reduction in instrumentation over the presently used passive probe approach.

A new effort has been just started with Kincaid and General Electric. This effort will focus its attention upon the utilization of finite element analysis to enhance quantification capability in the conventional eddy current frequency regime.



OVERVIEW

PROJECT III - NDE FOR ADVANCED MATERIALS

Unit A addresses the long standing problem of predicting the strength of a completed adhesive bond from nondestructive measurements on the joint. The approach being used here is to apply new and powerful techniques in ultrasonic signal processing as well as studies of the failure mechanisms that govern the strength of bonds which appear homogeneous and acceptable to currently used radiographic or ultrasonic C-scan methods. In this way, advanced concepts in quantitative ultrasonic NDE can be applied to the problem and NDE techniques specifically designed to measure the key failure related conditions can be developed. At General Dynamics, computer controlled scanning and ultrasonic spectroscopy are being used to deduce the physical properties of the layer of adhesive in completed bonds and then to use these data to predict the mechanical capabilities of the joint. At the Rockwell Science Center, the emphasis is being placed on determination of the microscopic mechanisms of failure so that alternate means of interrogating the bond line can be predicted. During the current reporting period, the General Dynamics research has been aimed at decreasing the scatter observed previously in the data that demonstrated the correlation between the cohesive strength of an adhesive joint made with a commercial adhesive and the values of the velocity and attenuation of sound in the bulk of that adhesive. Data on the acoustic properties of the adhesive alone have now been collected in order to define the effects of moisture and cure temperature as well as to determine the uncertainties caused by the inhomogeneities introduced into commercial adhesives by the scrim cloth and the metallic fillers. Now that this basic information is available on three commercial adhesives, carefully controlled measurements on typical aircraft adhesive bonds will be made using not only a newly developed computer signal processing method but also the Fokker Bondtester. It is anticipated that more reliable predictions of the strength of these bonds can be deduced from the acoustic measurements by introducing the data on the adhesives into the interpretation of the measurements. For the problem of establishing the failure mechanisms in weak joints that would

would pass current NDE inspection practices, the Rockwell Science Center has chosen to study a model adhesive system that does not have a source of error due to fillers, porosity or scrim cloth. Both peel and shear type specimens have been prepared with moderately degraded adherend to adhesive interfaces and detailed comparisons between their strength values and features in the Fourier transform representation of the ultrasonic signals reflected from the joints are now being carried out. The fracture surfaces of the broken specimens are also being examined with electron and optical microscopy in order to determine the nature of the weak interfaces. It is anticipated that the results of these studies will suggest better ways of interpreting the ultrasonic spectroscopy data as well as alternate techniques for performing nondestructive tests. One new NDE method already being studied is based on using electromagnetic, noncontact transducers (EMATS) to excite particular shear wave modes that propagate parallel to the adhesive bond line. Special transducers to excite and detect those unique plate wave modes which have different polarizations but identical propagation velocities are being constructed and will be used in a configuration analogous to the optical ellipsometer to see if the characteristics of the thin layers at the adherend to adhesive interface can be measured. Another potentially useful interrogation technique is to study the low frequency mechanical response of the adhesive joint in order to use measurements of the viscoelastic relaxation parameters to detect weak interfacial joints.

Unit B has concentrated on the development of advanced NDE techniques applicable to the graphite epoxy class of fiber reinforced composite materials.

Two particular problem areas are being investigated: the establishment of the acoustic emission signal characteristics for the individual processes that contribute to the failure of a composite and the development of instrumentation for measuring the magnitude and spatial distribution of moisture in composites. During the past six months, specimen geometries and test procedures that can be expected to be dominated by only one failure mechanism have been designed and fabricated so that many acoustic emission signals characteristic of a particular failure mechanism can be generated at will. These signals will be presented to a new signal analysis



system built on Science Center research funds which will record sixteen descriptive parameters of each individual acoustic emission burst. A computer program to sort these parameters and perform signature analysis on them is almost completed and will be put into operation within the month. Using the by-products that accompanied the development of these signal analysis capabilities, a special acoustic emission monitoring system was designed and put into operation on composite coupon fatigue tests at the Illinois Institute of Technology Research Institute (IITRI) in Chicago as part of the AFML sponsored Composites Serviceability program. Also, a procedure for calibrating acoustic emission transducers and their associated frequency spectrum analysis systems was established in cooperation with the joint U.S.-Britain Technical Cooperation Program (TTCP) organization.

The task directed at developing instrumentation for measuring the moisture content of graphite-epoxy composites has advanced through the fabrication of special chambers for fully enclosing small composite samples and for testing a small section of long bar or rod shaped section. Chambers for making moisture measurements on the surface of large plates on inside of holes have been designed and are being assembled. All of these devices will be capable of providing data on the effusion rate of moisture from the surface of composites and these data will be processed by a new mathematical procedure designed to yield the initial distribution of moisture as a function of depth within the composite. For these cases in which the diffusion rates obey the classical diffusion laws, the predicted profiles have been verified and the computer programs that accomplished the data analysis are being prepared for installation in the class of small minicomputers that are available for field applicable instruments. For the cases where the effusion rate deviates from classical behavior, a new model of diffusion is being developed which considers the composite as a two-phase mixture of microcracks and a continuum each of which obeys the Fickian diffusion laws but with different parameters.

Unit C was initiated in October of 1977 following encouraging nondestructive defect detectability studies in structural ceramics, using high frequency ultrasonics and microfocus X-rays (as well as promising results obtained using microwave methods and acoustic microscopy). The primary intent of the unit is to quantify the ability of nondestructive methods to predict

failure - in structural ceramic materials of technological interest - both on an individual basis and in optimum combinations. This ability will be compared with the predictability that can be achieved using overload proof test procedures.

The unit, as conceived, has three primary components: (i) defect characterization using each of the techniques that have exhibited promising preliminary results (ii) the characterization of fracture from typical defects in structural ceramics (iii) the development of quantitative reliability relations based on the defect characterization and fracture analyses. Initially, the approach will be applied to disc samples, of two or three of the prime structural ceramics, containing individual defects of the type and size that typically cause premature failure. Subsequent tests will be performed on actual components. For analysis of bulk defects (inclusions, voids), disc samples have been fabricated with the principal defect located near the center. These samples are firstly being inspected using those techniques that are amenable to the detection of defects remote from the surface, viz. ultrasonics and X-rays. The studies are being conducted by J. Schuldies (microfocus X-ray), G. S. Kino (high frequency ultrasonics) and G. A. Alers (conventional, ≈ 45 MHz, ultrasonics). When these initial inspections have been completed, the samples will be surface ground such that the defect of interest is located $\sim 100 \mu\text{m}$ below the surface. The samples will then be inspected by techniques that are most sensitive to the presence of subsurface defects, i.e., microwaves (A. Bahr, S. Sahrian), Rayleigh waves (G. S. Kino), acoustic microscopy (L. Kessler, C. Quate). In each case, the most sophisticated mode of signal analysis, as it emerges from Project I or other research activities, will be used to obtain the pertinent defect parameters (type, dimension, orientation). Subsequently, the samples will be fractured (using ramp-loading conditions) in order to obtain relations between the defect fracture stress and the defect size and type. The ancillary fracture mechanics theory needed for this purpose is being concurrently developed in this unit. A biaxial flexure test will be used for the fracture studies; because this test method averts undesirable edge failures and concentrates the tension in a narrow zone of the sample, chosen to coincide



with the defect location. Finally, the fracture origin on each sample will be characterized by scanning electron microscopy, to obtain an unambiguous measure of the defect dimensions.

For surface defects, disc samples of the same materials containing surface cracks will be prepared using the indentation method. Various grinding treatments will then be superimposed to produce backgrounds of typical machining damage. The samples will be inspected using the same surface sensitive methods applied to the volume defects. Inspection will again be followed by fracture tests.

The correlation between the defect characterization and the defect fracture results, needed to obtain quantitative false-accept, false-reject curves, will utilize recent reliability theory (developed, in general terms, using Rockwell IR&D funding) that is being extended to the specific requirements of this unit.

The first material selected for study is hot-pressed Si_3N_4 manufactured by the Norton Co. (NC 132) because this is the standard material being used in most of the current DoD ceramics programs. Fracture studies on this material have indicated two primary sources of fracture; volume defects (inclusions and voids) introduced during fabrication, and surface cracks introduced during machining. The ability to predict failure from both types of fracture origin is being investigated. Disc samples, nominally containing single inclusions (in the size range 25-200 μm) of the types that typically cause fracture in this material (Si, SiC, WC), have been prepared and recently (December) delivered by the Norton Co. These samples have been circulated for the first set of X-ray and ultrasonic inspections. The results are very preliminary and hence, the reports by the respective investigators primarily contain their inspection plans, rather than detailed results. However, detailed initial results are imminent. Samples containing voids (made by diffusion bonding) and defect free samples suitable for surface crack studies have been ordered, and will arrive in a few weeks.

The second material selected will be contingent on decisions made in other programs funded by ARPA and AFML; but will almost certainly be either sintered SiC or reaction bonded Si_3N_4 . these studies will not commence until substantial progress has been achieved on the NC 132 material.

While awaiting the first defect characterization results, the fracture mechanics and reliability theories are being developed and correlated with available defect fracture and characterization data. Substantial progress has been achieved, as reported in tasks 1 and 2. In particular, the probabilities of fracture from spherical voids have been derived, as function, of the strength level and void radius. The probability functions that have been derived will form the basis for interpreting the strength data and obtaining the distribution parameters for the void surface cracks pertinent to the test material (e.g., NC 132 Si₃N₄). These parameters will constitute the input into the reliability analysis.



PROJECT I, UNIT A, TASK 1
APPLICATION OF GEOMETRICAL DIFFRACTION THEORY
TO QNDE ANALYSIS

J.D. Achenbach, A.K. Gautesen and H. McMaken

Department of Civil Engineering
Northwestern University
Evanston, Illinois

Introduction

/

An analysis is presented of the diffraction by a penny-shaped crack of time-harmonic signals emitted by a point-source. The analysis is based on elastodynamic ray theory, which yields relatively simple approximations to the diffracted fields of $\omega a/c_L$ is sufficiently larger than unity, where ω is the circular frequency of the incident waves, a is the radius of the crack and c_L is the velocity of longitudinal waves. The diffracted fields include direct diffractions from the crack edges as well as diffractions of signals which travel via the crack faces. For three positions of the point of observation, numerical results for the three displacement components have been display in graphs.

The solution of the direct scattering problem, that is, the computation of the field generated when an ultrasonic wave is diffracted by a given flaw, is a necessary preliminary to the solution of the inverse problem, which is the problem of inferring the geometrical characteristics of a flaw from either the angular dependence of the far-field scattering amplitude at fixed frequency, or from the frequency dependence of the far-field scattering amplitude at fixed angle.

In this report the direct problem is considered. The diffraction of time-harmonic signals by a penny-shaped crack is analyzed on the basis of linearized elasticity theory for a homogeneous, isotropic solid. A considerable literature exists on diffraction of plane waves by penny-shaped cracks. Much of this work was recently summarized in a review article by Kraut (1976). The exact mathematical formulation of these problems is very difficult to work with, since they are mixed-boundary-value problems.

In this report an approximate method is developed, which is based on geometrical diffraction theory. This theory has recently been discussed in some detail by Achenbach and Gautesen (1977) and Gautesen, Achenbach and McMaken (1978). Geometrical diffraction theory provides relatively simple results, and it can be applied to cracks of complicated shape. The theory is applicable if $\omega a/c_L \gg 1$, where ω is the circular frequency, a is a characteristic dimension of the crack, and c_L is the velocity of longitudinal waves.

Formulation

We consider a penny-shaped crack of radius a in an elastic solid. As shown in Fig. 1, a cartesian coordinate system (x', y', z) is introduced such that the crack is in the $(x'y')$ -plane, and the origin is at the center of the crack. The direction of the y' -axis would generally be suggested by the overall geometry; for example, the y' -axis could be normal to the free surface if the crack were located in a half-space. At point $P(x', y', z_0)$ a time-harmonic longitudinal wave of spherical symmetry is generated. For the purposes of analysis it is convenient to define another coordinate system (x, y, z) , such that P is located in the (yz) -plane. The (x', y', z) and (x, y, z) systems are related by a rotation over an angle α_0 around the z -axis, as shown in Fig. 1. We also define a cylindrical coordinate system (R, α, z) relative to the (x, y, z) -system. Point $Q(x, y, z)$ is a point of observation.

The incident wave is a spherical longitudinal wave of the form

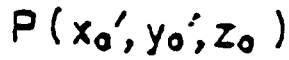
$$u_{inc} = \frac{iAc_L}{\omega} \nabla \left(\frac{1}{S} e^{i\omega(S/c_L - t)} \right) \quad (1)$$

where

$$S^2 = x^2 + (y - y_0)^2 + (z - z_0)^2, \quad (2)$$

and

$$c_L = [(\lambda + 2\mu)/\rho]^{1/2} \quad (3)$$



3

is the velocity of longitudinal waves. Equation (2) corresponds to the wave motion generated by a center of dilatation. Sufficiently far from the source, the spherical wave motion generated at P may be assumed in the simple form

$$u_{inc} = (A/S) e^{i\omega(S/c_L - t)} \nabla S + O(\omega^{-1}) \quad (4)$$

The faces of the crack are assumed free of surface tractions, i.e.,

$$z = 0, R < a: \tau_z = \tau_{zR} = \tau_{z\chi} \equiv 0 \quad (5)$$

These are the usual conditions considered in the elastodynamic diffraction literature.

Canonical Solutions

The diffraction problems formulated in the preceding section will be treated by geometrical diffraction theory. Geometrical diffraction theory is based on the use of canonical solutions, which are asymptotic results for diffraction of a plane wave by a semi-infinite crack. For an incident longitudinal wave, the pertinent canonical solutions have been obtained by Achenbach and Gautesen (1977). Here we briefly review these canonical solutions. For consistency we use the coordinate system and the indicial notation of Achenbach and Gautesen (1977). In this coordinate system the x_3 -axis coincides with the crack edge, and x_2 -axis is normal to the plane of the crack. The geometry is shown in Fig. 2.

The displacement components of the incident longitudinal wave are

$$(u_i)_{inc} = A_0 p_i \exp[i\omega(x_j p_j / c_L - t)] \quad (6)$$

where p_i are the components of a unit vector which defines both the directions of propagation and of displacement. In terms of angles shown in Fig. 2 we have

$$(p_1, p_2, p_3) = (\sin\phi_L \cos\theta_L, \sin\phi_L \sin\theta_L, \cos\phi_L) \quad (7)$$



Rockwell International
Science Center
SC595.32SA

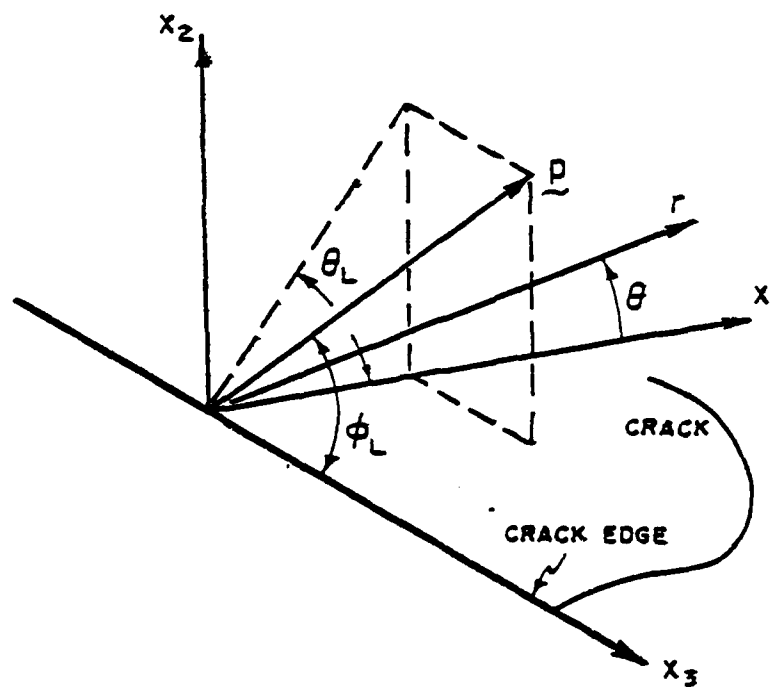


Fig. 2 Canonical problem: plane longitudinal wave with

characterization capability is the development of quantitative theoretical and experimental techniques. Auld discusses the former in a report written jointly with Buck and Tittmann. In this first phase of his theoretical efforts, he considers the analytically simple, but practically important, case of the long wavelength limit. In this regime, he develops formulae for the back-scattering, as a function of angle for a semicircular crack, a part circle crack, and a part ellipse crack. The theoretical efforts make use of recently developed reciprocity relations to place the results in a form that can be directly compared to the electrical signals measured using either piezoelectric or electromagnetic transducers. Also included is a discussion of the surface wave analog of the relationship reported between long wave scattering and the stress intensity factor of interior defects, although further effort is required before this result can be fully defined.

The development of surface wave measurement techniques is presented in a paper by Tittmann, DeBilley, Cohen - Tenoudji, Jungman, and Quantin included as an Appendix to the Auld, Buck, Tittmann report. These results were not obtained under the support of this program. However, since they were obtained by one of the key investigators while on leave at the University of Paris, and since the results will be incorporated in later efforts that will

x

SC595.32SA

In the plane $x_2 = 0$, the stress components corresponding to Eq.(6) are

$$\tau_{2i} = i\mu A_0 D_i E(x_1, x_3, t) \quad (8)$$

where

$$D_i = \omega c_L^{-1} [(c_L^2/c_T^2 - 2) \delta_{2i} + 2p_2 p_i] \quad (9a)$$

$$E(x_1, x_3, t) = \exp[i\omega[(x_1 p_1 + x_3 p_3)/c_L - t]] \quad (9b)$$

For the canonical solution we now analyze the elastodynamic response of an unbounded solid containing a semi-infinite crack whose surfaces are subjected to surface tractions equal and opposite to the ones stated in Eq.(8). Superposition of this solution on the incident field renders the surfaces of the crack free of tractions, and provides the solution to the canonical diffraction problem. Considering the half-plane $x_2 \geq 0$ the boundary conditions on $x_2 = 0$ for the symmetric problem are

$$x_1 > 0, \tau_{22} = -i\mu A_0 D_2 E(x_1, x_3, t) \quad (10)$$

$$x_1 \leq 0, u_2 = 0 \quad (11)$$

$$-\infty < x_1 < \infty, \tau_{21} = \tau_{23} = 0 \quad (12)$$



where r and θ are defined in Fig. 2, and

$$u_{\beta}^L = \exp(i\omega S_{\beta}/c_{\beta}) S_{\beta}^{-1/2} D_{\beta}^L(\theta; \phi_L, \theta_L) \hat{i}_{\beta}^L A_0 E(0, x_3, t) \quad (17)$$

Here $\beta = L$ and $\beta = T$ refer to the diffracted longitudinal and transverse wave, respectively. The angle ϕ_T is determined from $c_L \cos \phi_T = c_T \cos \phi_L$, and $S_{\beta} = r/\sin \phi_{\beta}$ is the distance from the point of diffraction to the point of observation. The unit vectors \hat{i}_{β}^L relate the displacement directions of the diffracted fields to those of the incident fields and explicit expressions for these vectors are given in Achenbach and Gautesen (1977). The functions $D_{\beta}^L(\theta; \phi_L, \theta_L)$ are the diffraction coefficients, which each consist of two components: one from the symmetric and one from the antisymmetric problem, i.e.,

$$D_{\beta}^L(\theta; \phi_L, \theta_L) = (D_{\beta}^L)_S + (D_{\beta}^L)_A \quad (18)$$

Expression for the diffraction coefficients have been derived by Achenbach and Gautesen (1977). Let us define the absolute value of a dimensionless diffraction coefficient as

$$\bar{D}_{\beta}^L = |(\omega/c_L)^{1/2} (c_L/c_{\beta}) \sin \phi_{\beta} (\cos \phi_{\beta} - \cos \theta) D_{\beta}^L(\theta; \phi_{\beta}, \theta_{\beta})|, \quad (19)$$

In Figs. 3 and 4 these dimensionless diffraction coefficients have been plotted versus the angle θ . The coefficients \bar{D}_L^L and \bar{D}_T^L have been computed for the range $0 \leq \theta \leq 2\pi$. It is noted that at $\theta = 0$ and $\theta = 2\pi$ we find that \bar{D}_L^L vanishes, i.e. there are, in first approximation, no longitudinal diffracted waves on the crack faces. It is, however, also noted that \bar{D}_T^L does not vanish on the crack faces. Thus, there are diffracted transverse waves propagating over the faces of the crack. The particle motions of these waves are polarized in the plane of the crack, i.e., relative to the crack faces they are horizontally polarized.

Application of Geometrical Diffraction Theory

Geometrical diffraction theory is based on ray theory. In a homogeneous isotropic, linearly elastic solid the rays are straight lines,

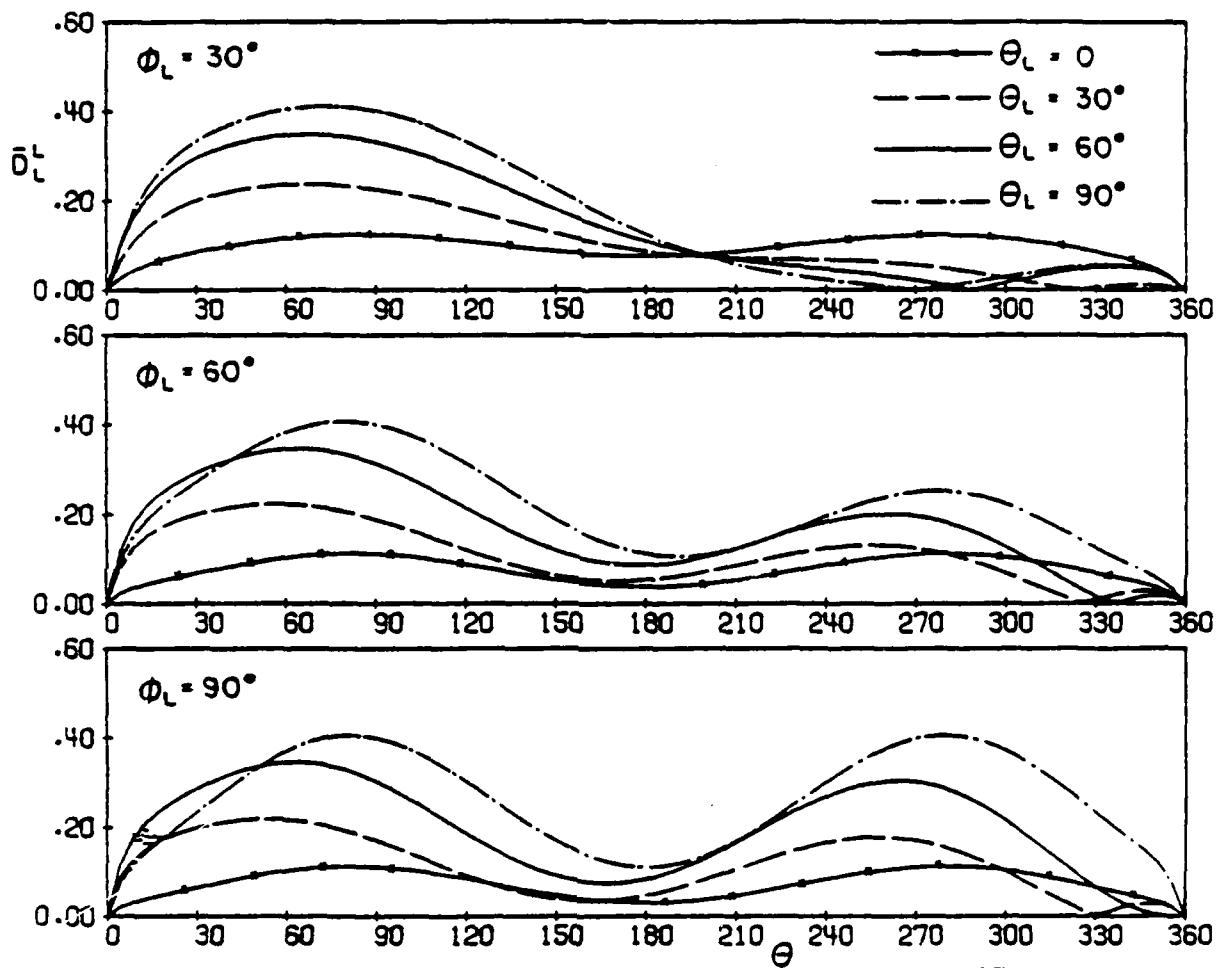


Fig. 3 Dimensionless diffraction coefficients for a crack.

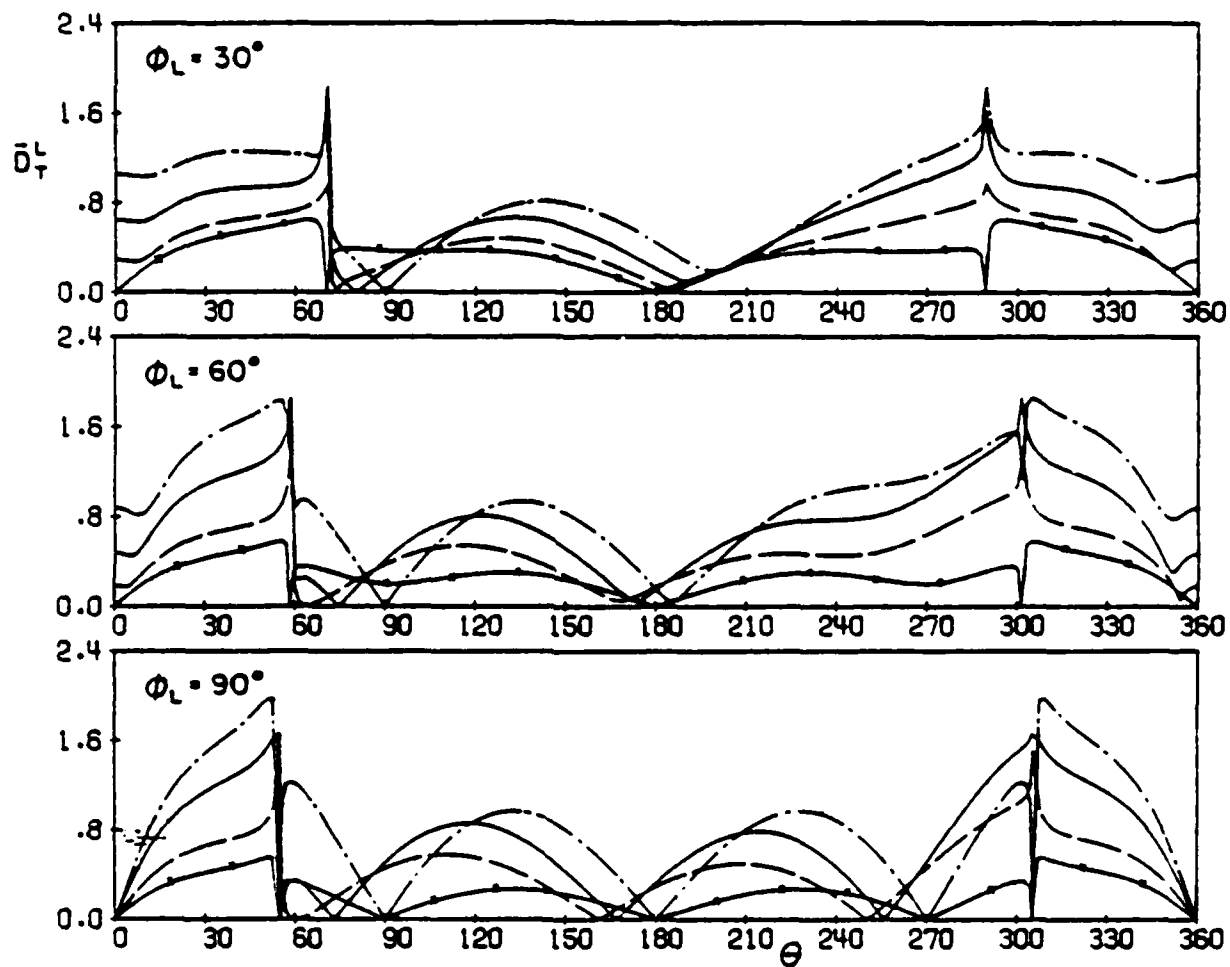


Fig. 4 Dimensionless diffraction coefficients for a crack.

which are normal to the wavefronts. For time-harmonic wave motion, ray theory provides a method to trace the amplitude of a high frequency mechanical disturbance as it propagates along a ray. Elastodynamic ray theory has been presented in some detail by Karal and Keller (1959).

Generally the application of a time-harmonic disturbance to the surface of a body, generates rays of longitudinal as well as rays of transverse motion, which are denoted as L-rays and T-rays, respectively. Upon striking an interface, rays produce reflected and refracted rays. Such reflection and refraction problems are well in hand. Diffraction by smooth obstacles has also been investigated in some detail, e.g. Resende (1963). The latter reference also appears to be the first one to deal with diffraction by an edge in a solid, at least for the two-dimensional case. A more general groundwork for a three-dimensional geometrical diffraction theory for cracks in an elastic solid was given by Achenbach and Gautesen (1977). Basic to the theory is the result that two cones of diffracted rays are generated when a ray carrying a high-frequency body-wave strikes the edge of a crack. The surfaces of the inner and outer cones consist of L-rays and T-rays, respectively. The half-angles of the cones are related by Snell's law.

For plane longitudinal and transverse waves, which are under arbitrary angles of incidence with a traction-free semi-infinite crack, the fields on the diffracted rays can be obtained by asymptotic considerations for $\omega r/c_L \gg 1$. Geometrical diffraction theory provides modifications to the semi-infinite crack results, to account for curvature of incident wavefronts and curvature of crack edges, and finite dimensions of the crack. In the usual terminology the results for diffraction of plane waves by a semi-infinite crack are the canonical solutions. For the problem at hand the canonical solutions have been reviewed in the previous section.

The total fields at a point of observation Q are not just comprised of the fields on the "primary diffracted body wave rays". At the edge of the crack there are also rays of crack-face motion generated. These rays intersect the crack edges again and generate additional diffracted body wave rays. Some of these "secondary diffracted rays" will pass through point Q . On the faces of the crack, important contributions to the diffracted fields are coming from rays of surface waves. These rays are important, because in the first approximation the diffraction coefficients for the body wave motions



vanish on the crack faces, except for diffracted horizontally polarized transverse wave motions. In addition, surface wave motions suffer less geometrical decay than body wave motions. In a recent paper, Gautesen, Achenbach and McMaken (1978) have presented a theory for surface wave rays (SW-rays) which are generated by the diffraction of body wave rays.

When a SW-ray intersects the edge of a crack, a ray of reflected surface wave motion is generated, as well as cones of diffracted rays of longitudinal and transverse motions. The reflection coefficients can be computed. The cones of diffracted L- and T-rays can also be analyzed, and the associated diffraction coefficients can be obtained. With the aid of these results the contributions to the diffracted fields of waves which travel via the crack faces can be computed. Thus, the total diffracted field consists of primary diffractions and a system of secondary diffractions.

The results of geometrical diffraction theory are not valid at shadow-boundaries. Moreover, for curved wavefronts and for curved diffracting edges, the cones of diffracted rays have envelopes, at which the rays coalesce and the fields become singular. The envelopes are called caustics. The results of the geometrical theory of diffraction are also not valid near caustics. It is, however possible to extend the theory to shadow boundaries and caustics.

Before returning to the diffraction of a point source field by a penny-shaped crack, we summarize some pertinent expressions. The details can be found in the paper by Gautesen, Achenbach and McMaken (1978).

Primary diffracted body-wave rays. For an incident ray of longitudinal motion, indicated in Fig. 1 by PP_β , the displacement fields on the diffracted body-wave rays are

$$u_\beta^L = e^{i\omega S} / c_\beta \left[S_\beta (1 + S_\beta / \rho_\beta^L) \right]^{-1/2} D_\beta^L(\theta; \phi_L, \theta_L) \hat{i}_\beta^L u^L \quad (20)$$

Here u^L defines the incident wave at the point of diffraction. In Eq.(20) the superscript β defines the nature of the wave motion on the diffracted rays. Thus we have $\beta = L$ or $\beta = T$. the distances S_β are along the diffracted rays from the point of diffraction P_β , to the point of observation. The unit vectors \hat{i}_β^L relate the displacement directions of the diffracted fields to those of the incident fields. The symbols ρ_β^L define the distances from P_β

along the rays to the caustics, and D_β^L are the diffraction coefficients which have been plotted in Fig. 3. For an incident longitudinal wave we have

$$D_\beta^L = -a \sin^2 \phi_\beta \left[a \left(\frac{d\phi_\beta}{ds} \right) \sin \phi_\beta + \cos \phi_\beta \right]^{-1} \quad (21)$$

where a is the radius of curvature of the edge at the point of diffraction, s is the distance measured along the edge, and δ_β are the angles between the relevant diffracted rays and the normal to the crack edge, see Fig. 5. The angles ϕ_L , and ϕ_T are related by

$$c_T \cos \phi_L = c_L \cos \phi_T \quad (22)$$

Diffracted surface wave rays. Both symmetric and antisymmetric surface wave motions are generated on the faces of the crack. The displacements on the diffracted surface wave rays are

$$u_\beta^L = e^{i\omega S_R/c_R} (1 + S_R/\rho_R)^{-1/2} D_\beta^L(\phi_L, \theta_L) i_\beta^L u^L \quad (23)$$

where we have $\beta = RS$ and $\beta = RA$ for symmetric and antisymmetric surface waves, respectively. The symbols S_R and ρ_R are used in Eq.(23), because there is no difference for the two cases $\beta = RS$ and $\beta = RA$. The principal difference between Eqs.(20) and (23) is the additional term $S_\beta^{-1/2}$ in Eq.(20). This term reflects three-dimensional (spherical) growth and decay in Eq.(20) versus two dimensional (cylindrical) growth and decay in Eq.(23).

In Eq.(23) we have

$$\phi_R = -a \sin \phi_\beta \left(a \frac{d\phi_\beta}{ds} + 1 \right)^{-1} \quad (24)$$

where ϕ_R is related to ϕ_L by

$$c_L \cos \phi_R = c_R \cos \phi_L \quad (25)$$

Reflection of surface wave rays. A surface wave ray which intersects the edge of a crack, gives rise to a ray of reflected surface waves, and to two cones of diffracted body rays. for a surface wave incident on the edge of

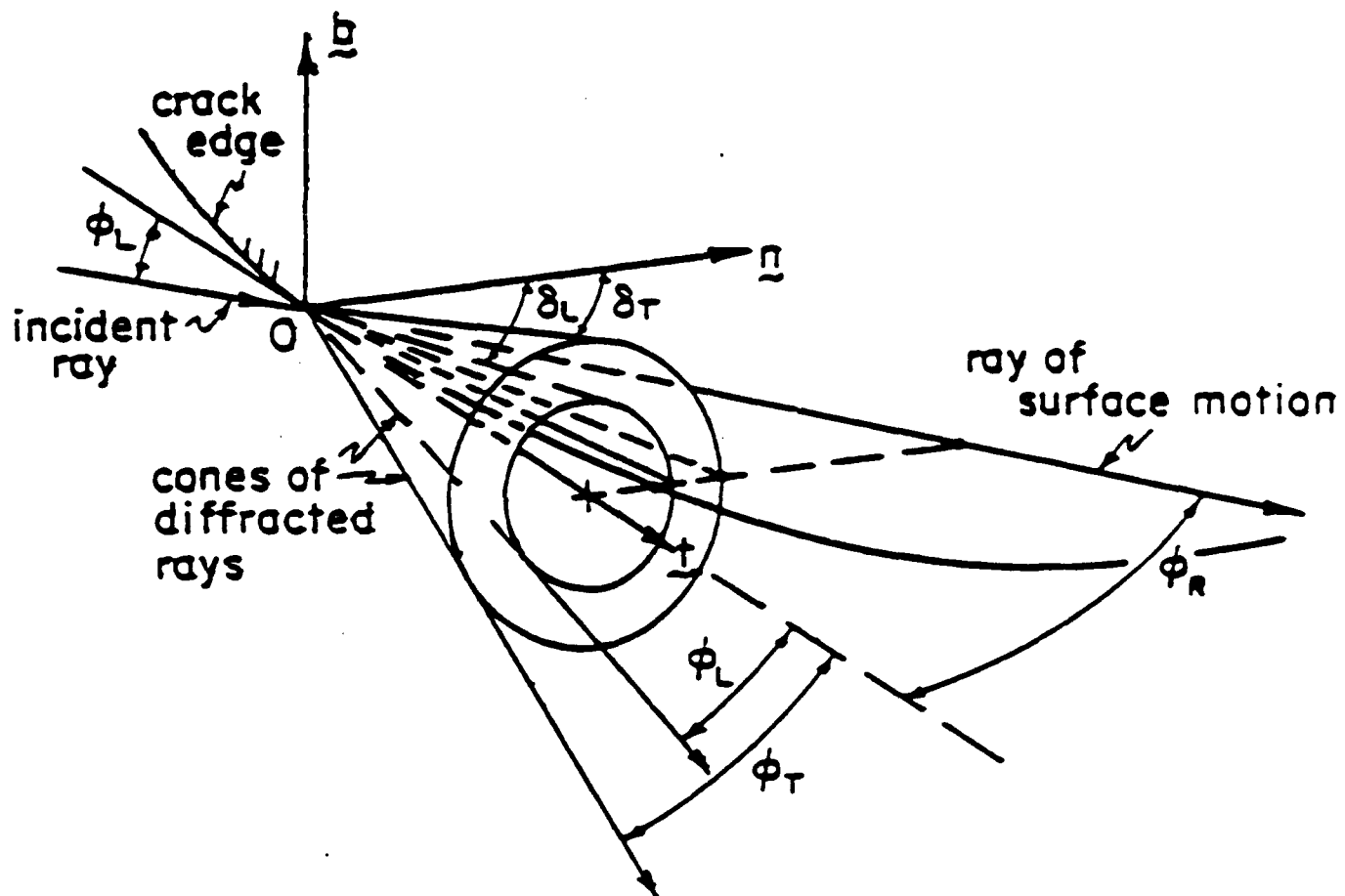


Fig. 5 Diffracted surface-wave ray and cones of diffracted body-wave rays

a semi-infinite crack these reflection and diffraction processes have been studied by Freund (1972). In the spirit of geometrical diffraction theory, we can immediately introduce the appropriate corrections for curvature of the incident wavefront and for curvature of the edge of the crack.

A surface wave ray is reflected such that the angle between the reflected ray and the tangent to the edge is just the same as the angle of incidence, ϕ_R , between the incident ray and the tangent to the edge. Moreover, rays of symmetric (antisymmetric) surface waves are reflected as rays of symmetric (antisymmetric) surface waves.

The incident field is defined by Eq.(23). Quantitatively the fields on the reflected surface rays are given by

$$u_\alpha^\alpha = e^{i\omega S_R/CR} (1 + S_R/\phi_R)^{-1/2} R_\alpha^\alpha \underline{u}^\alpha \quad (26)$$

Here α defines the nature of the motions on the incident surface rays as well as on the reflected surface rays. In Eq.(26), S_R is the distance from the point of reflection to the point of observation, R_α^α is the reflection coefficient and ϕ_R is the distance to the caustic, where

$$\phi_R = -a \sin \phi_R (a \phi_R/ds + 1)^{-1} \quad (27)$$

This is the same formula as given by Eq.(24), but here $\phi_R(s)$ is the given angle of incidence, while in Eq.(24) ϕ_R was computed from Eq.(25).

Expressions for R_{RA} and R_{RS} are given by Gautesen, Achenbach and McMaxen (1978).

Body wave rays generated by diffraction of surface-wave rays. For a surface wave ray incident at an angle ϕ_R with respect to the edge, the direction of a diffracted ray is

$$e_\beta = \cos \phi_\beta \underline{t} + \sin \phi_\beta (\cos \theta \underline{n} + \sin \theta \underline{b}) \quad (28)$$

where $\beta = L$ and T correspond respectively to a diffracted longitudinal and transverse ray, ϕ_β is the half angle of the diffracted cone of rays which is related to the incident angle ϕ_R by



$$c_R \cos \phi_\beta = c_\beta \cos \phi_R, \quad (29)$$

In Eq.(28), $\theta \in [0, 2\pi]$ is a parameter which defines the individual rays on the diffracted cone; it represents the angle with vector \underline{n} of the projection of the diffracted ray onto the plane normal to \underline{z} . We remark that if the angle ϕ_β is imaginary, then the corresponding cone of diffracted rays is absent.

The displacement fields are of the general form

$$\underline{u}_\beta^\alpha = e^{i\omega S_\beta/c_\beta} \left[S_\beta (1 - S_\beta/p_\beta^\alpha) \right]^{-1/2} D_\beta^\alpha(\theta; \phi_\alpha) \underline{u}_\beta^\alpha \quad (30)$$

where α defines the incident surface wave, i.e.,

$$\alpha = RS \text{ or } \alpha = RA, \quad (31)$$

and β defines the diffracted body-wave, i.e.,

$$\beta = L \text{ or } \beta = T \quad (32)$$

Also D_β^α are the pertinent diffraction coefficients which have been computed by Gautesen, et al. (1978). The distance to the caustics are given by

$$D_\beta^{RA} = D_\beta^{RS} = -a \sin^2 \phi_\beta (a \sin \phi_\beta d\phi_\beta/ds + \cos \delta_\beta)^{-1} \quad (33)$$

where ϕ_β is related to the incident angle ϕ_R by Eq.(29), and δ_L and δ_T are the angles between the relevant diffracted rays and the normal to the edge.

Ray Analysis

We now return to the problem formulated earlier, and observe that the field at the point of observation Q is determined by the summation of the contributions from each of the rays passing through this point. The nature of the rays passing through Q depends on the location of Q relative to the crack and relative of the source point P . There can be direct L-rays, reflected L- and T-rays and diffracted L- and T-rays. If Q is in the shadow zone, only diffracted rays can pass through Q . The magnitudes of the signals carried by

diffracted rays is $O[(\omega a/c_L)^{-1/2}]$ as compared to the signals of the direct ray and of the reflected rays. Among the diffracted rays we will include primary diffracted rays which are generated by the incident rays, and diffracted rays generated by rays travelling via the crack faces. For the latter we will, however, only include the L- and T-rays that are generated at first reflections and diffractions at the crack-edge of the SW-rays and T-rays. This is justifiable because the reflection coefficients are small. With this simplification there are still at least 16 diffracted rays passing through a point of observation.

The diffracted field u_d at Q can be represented by

$$u_d = \sum u_{\beta}^L + \sum u_{\beta\gamma}^L \quad (34)$$

where u_{β}^L and $u_{\beta\gamma}^L$ represent the primary and secondary diffractions, respectively. In $u_{\beta\gamma}^L$ the symbol β denotes the crack-face ray, i.e., $\beta = RS$, $\beta = RA$ or $\beta = T$. The symbol γ defines the body-wave rays generated by diffraction of a crack-face ray; thus, $\gamma = L$ or $\gamma = T$. The summations in Eq.(34) are carried out over all rays of a particular type passing through Q.

Let us first consider the primary diffractions. The position of point of diffraction on the crack edge, P_{β} , is defined by χ_{β} as shown in Fig. 1. For a fixed field point Q, those values of χ_{β} which satisfy a simple equation, determine the incident rays PP_{β} which generate cones of diffracted rays which contain a ray passing through Q. This simple equation is Eq.(40) of a recent paper by Achenbach, Gautesen and McMaken (1978). For each value of β , this equation always has at least two solutions and it may have as many as four. To visualize the latter case, we observe that a ray from each of the cones of rays of type β diffracted at the symmetric points $(\pm a \cos \chi_{\beta}, a \sin \chi_{\beta}, 0)$, $\chi_{\beta} \neq \pi/2, 3\pi/2$ on the edge will strike some common point Q in the v-z plane. Each of the cones of rays of type β diffracted at the points defined by $\chi_{\beta} = \pi/2, 3\pi/2$, actually circles in this case, maps out the entire y-z plane, and therefore yields two more rays which pass through Q.

Other diffracted rays that will be taken into account at Q, are the ones generated by the diffraction of rays that have travelled once over the faces of the crack. On the crack faces we have surface-wave rays (SW-rays), and rays of transverse motion in the plane of the crack (T-rays). These are



indicated by u_{β}^L . The fields generated by diffraction of these crack-face rays are denoted by $u_{\beta\gamma}^L$, where $\beta = RS, RA$ or T now defines the incident upon rays, and $\gamma = L$ or T defines the diffracted rays. When a ray of type β is incident upon the crack edge at P_{γ} under an angle $\phi_{\beta\gamma}$ with the tangent, it diffracts cones of L - and T -rays. Two equations must be solved simultaneously to yield the point P_{β} from which a diffracted crack-face ray emanates, and the corresponding point P_{γ} at which it diffracts a ray of type γ passing through the observation point Q . These two equations are stated as Eq.(47) in Achenbach et al. (1978). There are always at least two sets of solutions, and there may be more.

Diffracted Fields

In the $(x'y'z)$ -coordinate system shown in Fig. 1, the source point was placed at $P(2a, -2a, 3a)$. Numerical results for the diffracted displacement field were obtained for three points of observation relative to the (x', y', z) -systems. These were $Q(2a, 0, 3a)$, $Q(2a, 2a, 3a)$ and $Q(2a, 5a, 3a)$. No direct reflected signals of the incident wave from the crack surface pass through these points. The displacement components in the (x', y', z) -system were computed from Eq.(34). The calculations were carried out for a value of Poisson's ratio $\nu = 0.25$. The absolute values of the displacement components have been plotted in Figs. 6-8.

We will comment briefly on the inverse problem, i.e., the problem of determining the location of the crack edge, on the basis of measurements at a number of points of the amplitudes have been measured as function of the frequency, so that the data are available in the general form shown in Figs. 6-8. We also assume that the crack is planar, and that the plane of the crack has been detected from measurements of reflections of short duration pulses by the crack surfaces. Directly usable information to determine the location of the crack edge can then be obtained from the diffracted fields by filtering out the dominant harmonics from the amplitude versus frequency data. The harmonics with the lowest frequencies generally correspond to the primary diffractions. The primary diffractions show an amplitude decay of order $O(\omega^{-1/2})$. The higher-frequency harmonics correspond to the secondary diffraction of signals which have travelled via the crack faces. These may be separated into three distinct classes, decaying as $O(\omega^{-1/2})$, $O(\omega^{-1})$ and

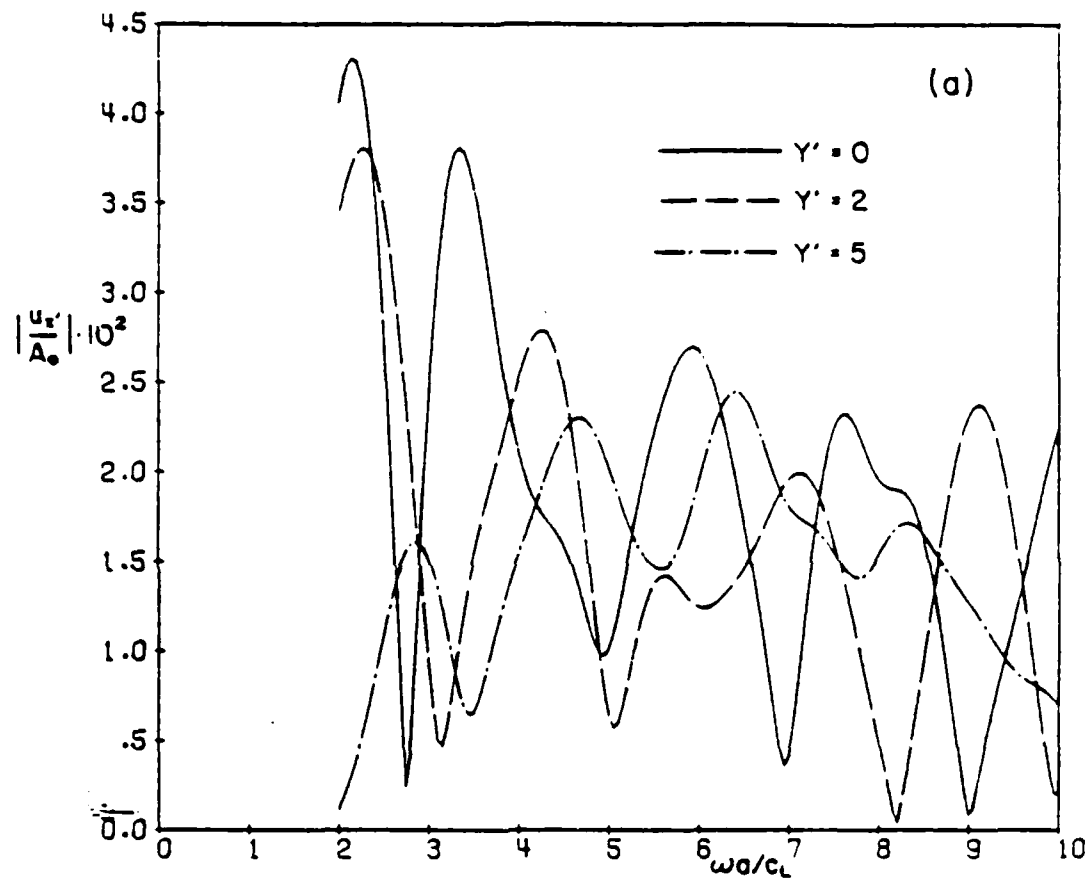


Fig. 6 Absolute value of the diffracted displacement in the x' direction versus the dimensionless frequency for three positions of the point of observation.



Rockwell International
Science Center
SC595.32SA

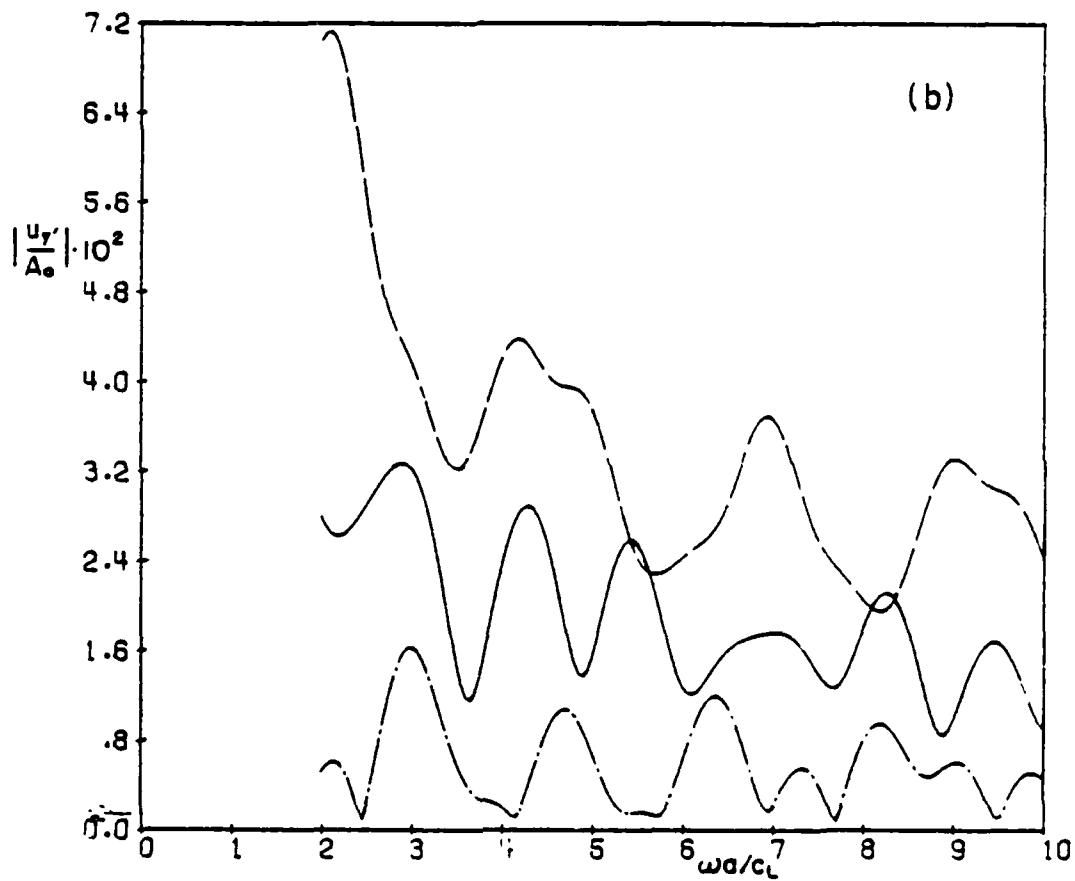


Fig. 7 Absolute value of the diffracted displacement in the y' direction versus the dimensionless frequency for three positions of the point of observation.

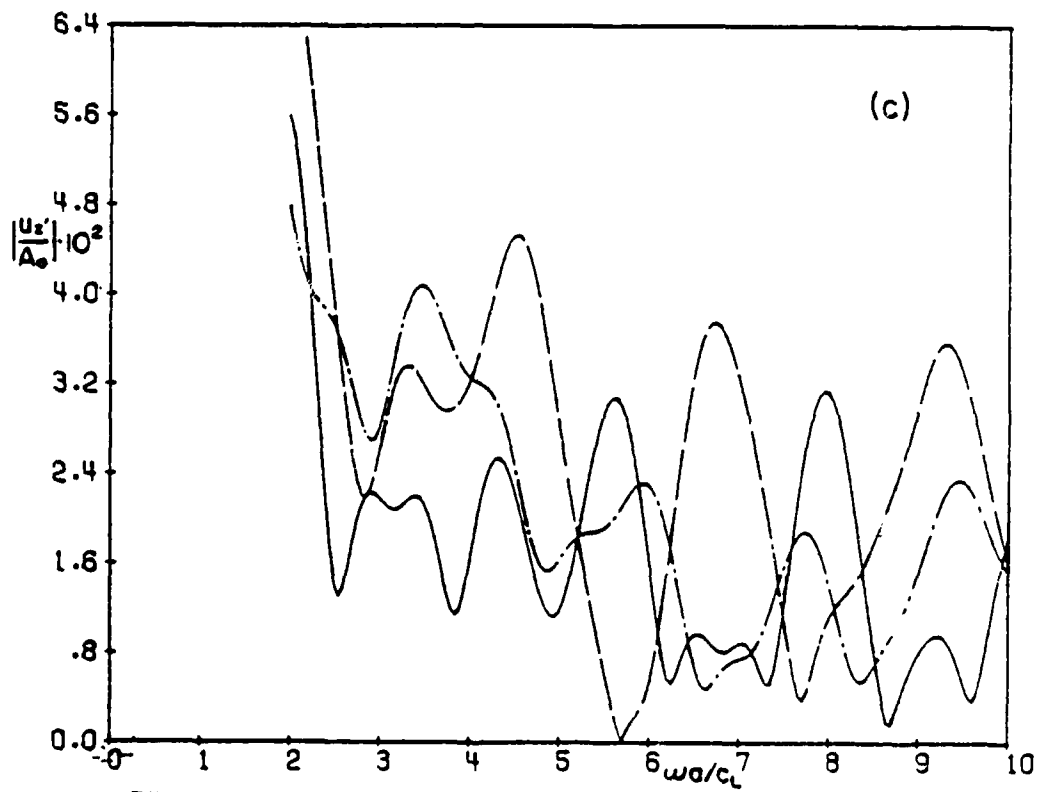


Fig. 8 Absolute value of the diffracted displacement in the z-direction versus the dimensionless frequency for three positions of the point of observation.



faster than $O(\omega^{-1})$, respectively. Harmonics of the last type have not been considered in this paper, and it may be assumed that they can be ignored. The higher-frequency harmonics decaying as $O(\omega^{-\frac{1}{2}})$ are generated by Rayleigh surface waves travelling over the crack faces, while the ones decaying as $O(\omega^{-1})$ represent the secondary diffractions generated by horizontally polarized transverse motions on the crack faces. Once the identification of the component harmonics has been accomplished, their frequencies must be related to interference of wave motions due to the differences in travel paths via the various ray patterns. The so obtained differences in travel paths provide information on the location of the crack edge and on the size and shape of the crack.

Future Work

For appropriate choices of the parameters, computations based on the theory presented in this Progress Report will next be compared with experimental results for scattering by a penny-shaped crack, which have been obtained by Professor L. Adler of the University of Tennessee. Next the theory discussed in this report will be extended to elliptical cracks for which experimental results have also been obtained by Adler.

References

- Achenbach, J.D. and A.K. Gautesen (1977). Geometrical theory of diffraction for 3-D elastodynamics, J. Acoust. Soc. Amer. 61, 413.
- Achenbach, J.D., A.K. Gautesen and H. McMaken (1978). Diffraction of point-source signals by a circular crack, B. Seism. Soc. Amer., forthcoming.
- Freund, L.B. (1972). Surface waves guided by a slit in an elastic solid, J. Appl. Mech., 39, 1027.
- Gautesen, A.K., J.D. Achenbach, and H. McMaken (1978). Surface wave rays in elastodynamic diffraction by cracks, J. Acoust. Soc. Amer., forthcoming.
- Karal, F.C. and J.B. Keller (1959). Elastic wave propagation in homogeneous and inhomogeneous media, J. Acoust. Soc. Amer. 31, 694.
- Kraut, E.A. (1976). Review of theories of scattering of elastic waves by cracks, IEEE Trans. SU23, 162.
- Resende, E. (1963). Propagation, reflection and diffraction of elastic waves, Ph.D. dissertation, New York University (unpublished).



PROJECT I, UNIT A, TASK 2

THEORETICAL STUDIES OF ULTRASONIC FLAW CHARACTERIZATION

J. E. Gubernatis
Theoretical Division
Los Alamos Scientific Laboratory

Introduction

Since official agreement on the proposed research was just reached, the main research effort will come in the second half of the fiscal year. However, important steps have been both accomplished and new ones initiated and are herein described.

Code Transfer

Modification and transfer of an existing computer code to be used in the work of A. Mucciardi at Adaptronics, Inc. has been completed. This code computes the scattering of a plane elastic wave from spheroidal flaws using the extended quasi-static approximation, an approximation that mitigates several limitations found in the currently used Born approximation. The modifications consisted of the removal of system dependent features to allow the code's use on Mucciardi's computer system, the incorporation of a requested form of output and the generalization of the analysis for arbitrary angle of incidence.

More specifically, as originally written, the code was intended for use in an interactive (time sharing) mode with various supporting graphics facilities proper to Los Alamos. The use intended by Mucciardi is in a batch mode without the availability of these supporting facilities. As a result, considerable modification of input/output procedures was necessary. An additional and significant modification was the generalization of the code for a plane wave incident at an arbitrary angle to allow the code's use in a larger variety of experimental situations. Originally, the plane wave was incident only along the principal axes of the spheroid.

Items sent to Mucciardi include:

1. A source deck of the code
2. A listing of this deck
3. Results of three test runs
4. A data deck for these runs
5. A description of input/output procedures

New Research

The research effort to come in the second half of the fiscal year will focus on an inverse scattering problem. One will try to answer the question, "To what extent can large classes of flaws be effectively modeled by spheroidally-shaped flaws?" We will start by defining a specific model for a flaw: a spheroidally-shaped void or inclusion whose scattering is described by the extended quasi-static approximation. The model thus depends on several variables (scattering angles, frequency, etc.) and parameters (changes in material properties, size, orientation, etc.) In an experimental situation measurements give data corresponding to a given set of variables. With this data one will attempt to determine in a least-squares sense the parameters in the model. This determination, however, corresponds to a complete characterization of the flaw. One is basically attempting to go from the data, through a model, to characterization of the flaw without any a priori information about the flaw other than the assumption of a spheroidal shape. The program to be undertaken will attempt to build upon itself in several steps by gradually increasing the number of parameters to be determined. One will first see if the radius of a spherical void can be determined, then see if a spherical void can be distinguished from an inclusion, then ask related questions about spheroidal flaws. Increasing the number of parameters significantly increases the difficulty of their determination. Attention will be paid to the stability of the analysis to experimental errors in data acquisition.



PROJECT I, UNIT A, TASK 3

THEORY OF ULTRASONIC SCATTERING

E. Domany, K. Newman, C. Lam
Department of Physics
University of Washington
Seattle, WA 98195

Introduction

Research concerning two different tasks is summarized. (1) A new approximation scheme for scattering of elastic waves, the Distorted Wave Born Approximation (DWBA), is being developed. (2) The Quasi Static Approximation (QSA) is used to characterize the signal scattered by cracks and volume defects.

The library of existing approximate solutions of the scattering problem for volume defects includes, among others, the Born Approximation¹ and the Quasi Static Approximation². These approximations have the deficiency of (1) not containing phase information and (2) providing unreliable frequency dependence in the intermediate to high frequency range ($ka > 1$). We hope that the DWBA will be a first step in providing such information for non-ellipsoidal defects³.

The DWBA is based on a perturbative solution of the scattering equation, much in the same way as the Born Approximation. However, while in the BA the unperturbed problem (or zeroth order solution) is the incident wave (propagating in a homogeneous medium with no defect), the DWBA uses the solutions of the scattering problem for a spherical defect as the unperturbed zeroth order approximation. Thus while the BA is exact only in the limit of vanishing difference between the properties of medium and defect, the DWBA has an additional "small parameter," i.e., a measure of the deviation of the defect from spherical. As shown below, in order to calculate the scattered wave within the DWBA, one needs the Green's function, g^S , of an infinite medium with a spherical defect. When g^S is approximated by the infinite medium Green's function g^0 , we obtain an approximation expected to be of intermediate quality between BA and DWBA. Our research effort was planned along two parallel lines. The first is evaluation of g^S , while the second concentrates on setting up the necessary numerical integrations and evaluating

the integrals with g^S replaced by g^0 . When g^S is obtained, we hope to use it in the integration routines that were developed, thus obtaining the DWBA.

The second part of our research deals with identification of features to be used to characterize cracks versus volume defects. This is based on the QSA. In December, a computer code⁴ that utilizes the QSA for elliptical cracks and general angle of incidence was transferred to us from Cornell. Changes needed to run this program at the UW are currently being made. Meanwhile, an investigation based on the QSA for cracks is carried out in collaboration with J. E. Gubernatis using the code (that handles special angles of incidence) at Los Alamos.

The Distorted Wave Born Approximation.

The differential equation for the propagation of elastic waves in a medium characterized by the (position dependent) elastic constants C_{ijkl} and density ρ is given by

$$C_{ijkl} u_{k,jl} + \rho \omega^2 u_i = 0 \quad (1)$$

where u_i is the displaced field and ω the frequency. Consider the geometry depicted in Figure 1, i.e.,

$$\begin{aligned} C(\underline{r}) &= C^0 + \theta_R(\underline{r}) \delta C \\ \rho(\underline{r}) &= \rho^0 + \theta_R(\underline{r}) \delta \rho \end{aligned} \quad (2)$$

where $\theta(\underline{r}) = 1$ if $\underline{r} \in R$, and zero otherwise. The defect R is separated into two regions: a spherical one (S) and a remainder \bar{R} , such that $R = S + \bar{R}$. Then one can define $\theta_S(\underline{r})$ and $\theta_{\bar{R}}(\underline{r})$ in a similar way, so that (see Fig. 1)

$$\theta_R(\underline{r}) = \theta_S(\underline{r}) + \theta_{\bar{R}}(\underline{r}) . \quad (3)$$

We can now consider as our unperturbed problem the case where only the spherical defect S is present. To do this, define



$$\begin{aligned} C^S(\underline{r}) &= C^0 + \theta_S(\underline{r}) \delta C \\ \rho^S(\underline{r}) &= \rho^0 + \theta_S(\underline{r}) \delta \rho \end{aligned} \quad (4)$$

and we can obviously write

$$\begin{aligned} C(\underline{r}) &= C^S(\underline{r}) + \theta_R(\underline{r}) \delta C \\ \rho(\underline{r}) &= \rho^S(\underline{r}) + \theta_R(\underline{r}) \delta \rho \end{aligned} \quad (5)$$

Using now (5) and (1), the scattering equation takes the form

$$C_{ijkl}^S u_{k,jl} + \rho \omega^2 u_i = -\theta_R \left[\delta C_{ijkl} u_{k,jl} + \omega^2 \delta \rho u_i \right] \quad (6)$$

If the right hand side vanishes, the solutions of this equation are the scattered waves by a spherical defect, obtained by Ying and Truell⁵. These solutions have been programmed and are readily evaluated numerically. Proceeding in a similar fashion as Gubernatis et al⁶, we obtain the integral equation

$$\begin{aligned} u_i(\underline{r}) &= u_i^S(\underline{r}) + \delta \rho \omega^2 \int_{\bar{R}} d\underline{r}' g_{im}^S(\underline{r}, \underline{r}') u_i(\underline{r}') \\ &\quad - \delta C_{ijkl} \int_{\bar{R}} d\underline{r}' g_{im,jl}^S(\underline{r}, \underline{r}') u_{k,jl}(\underline{r}') \end{aligned} \quad (7)$$

where $u_i^S(\underline{r})$ is the solution of the scattering problem with a spherical defect only

$$C_{ijkl}^S u_{k,jl} + \rho^S \omega^2 u_i = 0 \quad (8)$$

and $g_{im}^S(\underline{r}, \underline{r}')$ is the Green's function in the presence of a spherical defect, i.e.,

$$C_{ijkl}^S g_{im,jl}^S(\underline{r}, \underline{r}') + \rho^S \omega^2 g_{im}^S(\underline{r}, \underline{r}') = -\delta_{im} \delta(\underline{r} - \underline{r}') \quad (9)$$

Note that in Eq. (7)

$$g_{im,j}^S(\underline{r}, \underline{r}') = \frac{\partial}{\partial r_j} g_{im}^S(\underline{r}, \underline{r}') \quad (10)$$

and that since C_{ijk}^S and ρ_{ijk}^S are not translationally invariant, $g_{ij}^S(\underline{r}, \underline{r}')$ is not a function of $\underline{r} - \underline{r}'$ only. The DWBA consists of replacing $u_i(\underline{r}')$ in the integrands on the right hand side of Eq. (7) by $u_i^S(\underline{r}')$:

$$\begin{aligned} u_i^{DWB}(\underline{r}) = & u_i^S(\underline{r}) + \delta\rho\omega^2 \int_{\bar{R}} d\underline{r}' g_{im}^S(\underline{r}, \underline{r}') u_i^S(\underline{r}') \\ & - \delta C_{ijk} \int_{\bar{R}} d\underline{r}' g_{im,j}^S(\underline{r}, \underline{r}') u_{k,l}^S(\underline{r}') \end{aligned} \quad (11)$$

To evaluate u_i^{DWB} , we need the functions u^S and g^S , and perform the integration over the region \bar{R} numerically. The relative corrections to the Born approximation are of order $R\delta C$; to the DWBA of order $\delta C\bar{R}/S$. This means that we introduced a geometrical "small parameter," namely the deviation of the defect from spherical. We also hope to determine the "optimal sphere" to be used for treatment of various defects. Since the function g^S has not been calculated previously, we start by setting up an intermediate approximation, replacing g^S in Eq. (11) by the infinite medium Green's function g^0 . Since g^S satisfies an equation of the form (schematic)

$$g^S = g^0 + \int_S \delta C g^0 g^S$$

the error caused by replacing g^S by g^0 in (11) is of order $R\delta C \cdot S\delta C$. This intermediate approximation is given by

$$\begin{aligned} u_i^I = & u_i^S + \delta\rho\omega^2 \int_{\bar{R}} d\underline{r}' g_{im}^0(\underline{r} - \underline{r}') u_i^S(\underline{r}') \\ & + \delta C_{ijk} \int_{\bar{R}} d\underline{r}' g_{im,j}^0(\underline{r} - \underline{r}') u_{k,l}^S(\underline{r}') \end{aligned} \quad (12)$$



(where we used $g_{im,j}^0 = -g_{im,j}^0$). A computer code that will evaluate (12) is in an advanced state of development.

The Green's Function g^S . This function, defined by (9), describes the displacement field at point \underline{r} , given a point source stress at point \underline{r}' , in an infinite medium in which a spherical defect is embedded. We first treat the case where \underline{r}' is outside the defect. Choosing the line that passes through \underline{r}' and the center of the sphere as our z axis, we have calculated the component $g_{i3}^S(\underline{r} - \underline{r}')$. The calculation is closely related to the solution for scattering of longitudinal waves by spherical defects. We denote $g_{i3}^{S(in)}(\underline{r}, \underline{r}')$ the solution with \underline{r} inside and by $g_{i3}^{S(out)}(\underline{r}, \underline{r}')$ with \underline{r} outside the defect. These fields solve the equations

$$C_{ijkl} g_{k3,jl}^{S(in)} + \rho \omega^2 g_{i3}^{S(in)} = 0 \quad (13.1)$$

$$C_{ijkl} g_{k3,jl}^{S(out)} + \rho \omega^2 g_{i3}^{S(out)} = -\delta_{i3} \delta(\underline{r} - \underline{r}') \quad (13.2)$$

Substitute now

$$g_{i3}^{S(out)} = g_{i3}^0 + g_{i3}^1$$

into (13.2), with g_{i3}^0 the infinite medium Green's function; g_{i3}^1 satisfies

$$C_{ijkl} g_{k3,jl}^1 + \rho \omega^2 g_{i3}^1 = 0 \quad (14)$$

Equations (13.1) and (14) are similar to those treated by Ying and Truell⁵; we use the same functions as there to expand $g^{(in)}$ and g^1 . Expanding g^0 in the same set of functions, we can match boundary conditions (continuity of displacement and normal stress). Then, by numerically inverting the same matrix as Ying and Truell, the Green's function $g_{i3}^S(\underline{r}, \underline{r}')$ is obtained. Details of this section will be presented elsewhere⁷. At present we work on extension of our solution to $g_{ij}^S(\underline{r} - \underline{r}')$ with the direction $\hat{x}_j \perp \underline{r}'$. To do this, we have to utilize the (more complicated) solution for the scattering of shear waves.

Scattering by Elliptical Cracks - Quasi Static Approximation⁸.

We consider an elliptical crack with major axis $a > b$, and choose our axes with $x \parallel a$, $y \parallel b$, and z perpendicular to the face of the crack. The scattered wave has longitudinal and shear components, denoted by A_i and B_i , respectively given by

$$A_i = \hat{r}_i \hat{r}_j f_j(\underline{\alpha}) \quad (15.1)$$

$$B_i = (\delta_{ij} - \hat{r}_i \hat{r}_j) f_j(\underline{\beta}) \quad (15.2)$$

where

$$f_i(\underline{k}) = \frac{-ik^3}{4\pi\rho\omega^2} C_{ijkl} \hat{r}_j \gamma_{klmn} e_{mn}^0 S(q) \quad (16)$$

with $S(q)$ the "shape factor" for a crack⁹, e_{mn}^0 is the incident stress field, which, in the long wave length limit, is given by

$$e_{mn}^0 \approx \frac{i}{2} (u_m^0 k_n^0 + u_n^0 k_m^0)$$

where u_i^0 is the incident displacement field and k_i^0 the incident wave vector, we first consider the leading order in k , i.e., put $S(q) \approx 1$. The tensor γ_{klmn} that appears in (16) can be calculated by taking appropriate limits (that reduce finite volume ellipsoids to cracks) in Eshelby's expressions¹⁰. Investigation of (16) for various incident waves yields a set of interesting results⁹. Here we only summarize a few.

1. Incident longitudinal wave:

(a) When \underline{k}^0 is either perpendicular or parallel to the plane of the crack, one obtains the same angular distribution of scattered power (in the crack frame). This fact may turn out to be important in differentiating between cracks and volume defects.

(b) By analytic evaluation of the backscattered longitudinal power, we found the optimal position of the transducer (operating in the pulse-echo mode) to obtain information about the eccentricity of the ellipsoidal crack. With the transducer located at (θ, ϕ) the backscattered longitudinal power is proportional to $A(\theta, \phi)^2$ with



$$A(\theta, \phi) \propto \left(1 + \frac{1-2\sigma}{\sigma} \cos^2 \theta\right) \left(1 + \frac{2(1-\sigma)}{\sigma} \cos^2 \theta\right) + \frac{\sin^2 2\theta}{4} (C_1 + C_2 \cos 2\phi)$$

The constant C_2 measures the deviation of the crack from circular; thus, by fixing θ at 45° and varying ϕ , the variation of the backscattered signal is maximized and can be used to estimate the eccentricity.

2. Incident shear wave

When the incident wave vector and polarization are in the plane of the crack, no power is scattered (in the long wavelength limit). This feature may also serve to differentiate cracks and volume defects.

Because of the additional freedom to vary the polarization, it may well turn out that incident shear waves are a more effective tool for defect characterization than incident longitudinal. A detailed investigation of this type of scattering is now under way.

References

1. J. E. Gubernatis, E. Domany, J. A. Krumhansl, and M. Huberman, J. Appl. Phys. 48, 2812 (1977).
2. J. E. Gubernatis, to be published.
3. Scattering by ellipsoidal defects has been treated with success by Y. H. Pao and V. Varadan (unpublished).
4. Development of this code started in 1976 by S. Teitel and E. Domany.
5. C. F. Ying and R. Truell, J. Appl. Phys. 27, 1086 (1956).
6. J. E. Gubernatis, E. Domany, and J. A. Krumhansl, J. Appl. Phys. 4, 2804 (1977).
7. C. Lam, K. Newman, and E. Domany, to be published.
8. Research summarized in this section was carried out in collaboration with J. E. Gubernatis.
9. E. Domany and J. E. Gubernatis, to be published.
10. J. D. Eshelby, Proc. Roy. Soc. A241, 376 (1957).

$$R = S + \bar{R}$$

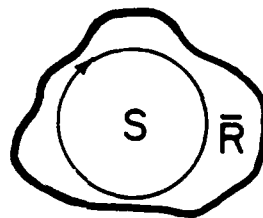


Fig. 1 The defect R is represented as a sphere S and a "remainder" volume \bar{R} .



PROJECT I, UNIT A, TASK 4
ULTRASONIC SCATTERING AND THE INVERSE PROBLEM

J.A. Krumhansl
Cornell University, Ithaca, New York

with

P. Mansfield, J. Rose, and S. Teitel

Introduction

During the last semi-annual period three projects have been pursued. First we have obtained new results for the scattering of long wavelength elastic waves from flat cracks. Second, a new inversion procedure is being tested and calibrated. Finally, an attempt was made to derive numerically exact results for the scattering of elastic waves from the prolate and oblate spheroids.

Scattering From a Crack

New results have been obtained for the long wavelength scattering of elastic plane waves from a flat crack using the quasi-static approximation. Previously, we have given results for a longitudinally polarized ultrasonic wave incident along the axis of symmetry of a circular stress free crack.¹ These results have been extended to the following more general case: 1) the polarization of the incident wave is not arbitrary, 2) the incident beam is now allowed to strike the crack at an arbitrary angle of incidence and, 3) the shape of the crack has been generalized to an ellipse. These changes should greatly extend the usefulness of our results for interpreting experimental results. First we can now consider the case of an incident shear wave scattering from the crack. Secondly, the generalization of the results to an arbitrary angle of incidence should give much useful information when analyzed. For example, an a priori interesting question would be the amount of directly backscattered power from a circular crack as we rotate the crack from a face on configuration to an edge on configuration. Finally, by extending the shape of the scatterer to an ellipse, we consider a much broader class of scatterers than previously. In particular, by taking the ellipticity of the crack to be small, we can approximate a long thin flat crack. The

orientation dependence of the scattering from such a scatterer is of great interest.

The results for the scattering from the crack discussed in the last paragraph are given in detail in Appendix A. As indicated there, we have obtained the final computable results. The programs to evaluate these cross-sections have been written and we are currently in the process of evaluating these results for general qualitative features which may be of interest in interpreting experimental results. An example of a case where these results should be applicable is as follows. Recently, Budiansky and Rice² have proposed an inversion scheme for the crack which allows them to estimate: i) the stress intensity factor for a crack, and ii) the orientation of a crack, assuming that the position of the crack is known. Their technique is based on the same formalism which was used to generate the result discussed above. Hence, by using our far-field amplitudes, one can calculate the stress intensity factor and the orientation of the crack. These results, may then be compared with the chosen orientation of the crack and the assumed stress intensity factor. Such a comparison would show whether the results of Budiansky and Rice are in fact consistent, and give some idea of the range of validity of their results.

Inversion Procedure

One of the major problems in ultrasonic applications to NDT is the determination of the flaw size, shape, and orientation from the scattering intensities. We have addressed this problem using a simplified approach based on the Born approximation. A complete description of our formal treatment and some initial results are given in Appendix B. Salient features of the Born inversion technique are as follows. First, the approximation is easily implemented, involving only a Fourier transform of the scattering amplitudes. Secondly, the technique is rigorously valid in the weak scattering limit, where the material properties of the flaw are only weakly different from those of the host material. Finally, the technique is quite insensitive to random noise in the scattering intensities.

Most NDT problems occur in the strongly scattering limit, where the material parameters of the flaw are quite different from those of the host (for example a void). Since our inversion procedure is rigorously valid in



the weak scattering limit, it was not a priori clear whether it would be useful for these strong scattering cases. Our approach is to simply test the inversion procedure for a wide range of strong scattering cases and see how well it works.

In order to test the inversion procedure, we need to know a subset of the scattering amplitudes for a given flaw. The exact subset of the scattering amplitudes needed is discussed in detail in Appendix B. Generally, such scattering intensities are not yet available from experiment. However, there are currently available theoretical scattering amplitudes (both exact and approximate) for several simple shapes. These shapes include the sphere, the prolate spheroid and the oblate spheroid. In all these cases, the problem has been solved for both the case of the elastic inclusion and the cavity. Our program is, given these theoretically generated scattering amplitudes, to test the ability of the inversion procedure to determine the size, shape and orientations of these flaws.

In Appendix B, we report the result of inverting the scattering amplitudes for a spherical flaw (using the exact solutions for an elastic inclusion and a void). The results were surprisingly good, indicating that one could determine the radius of the defect to within about 5%. This indicates that the procedure will probably be quite good for determining the size of the flaws. On the other hand, these results give no indication, one way or the other, as to whether the techniques can be used to determine the shape and orientation of the flaw since we restricted ourselves to spherical defects.

Hence, the major part of our current effort and our effort for the last several months has been to test the inversion procedure for spheroidal defects. These tests should indicate to what degree the approximation can determine the shape and orientation of a flaw. To test the procedure, it is necessary to have good scattering amplitudes for spheroidally shaped defects. There are both approximate and, recently, essentially exact results for $ka \ll 3$ (here ka is the product of the wave vector and a characteristic dimension of the object). We have attempted to obtain these results in a form suitable for evaluating the inversion algorithm.

First, there was an attempt here to calculate numerically exact results for the scattering amplitudes of the spheroids. This work has not yet

been successful. Since Varadan and Pao³ have obtained solutions for this problem, we do not expect to continue our efforts along these lines. Contact has been made with Varadan in order to obtain their results in a form suitable for our needs. These results should be available within the next several months.

As a temporary measure, we will first use approximate results for the scattering amplitudes. The particular approximation we have chosen to implement is the extended quasi-static approximation of Gubernatis.⁴ A computer program has been written to generate these approximate scattering amplitudes. We are currently engaged in evaluating the inversion procedure in terms of these approximate computations. Preliminary results should be available towards the end of March, 1978.

References

1. E. Domany, J.A. Krumhansl and S. Teitel, submitted to J. Appl. Phys.
2. B. Budiansky and J.R. Rice, preprint.
3. V. Varatharajula (Varadan) and Pao, J. Acoust. Soc. Am. 60, 556 (1976). Numerical results for elliptic cylinders are contained in a preprint by V. Varadan (submitted J. Acoust. Soc. Am.).
4. Private Communication, J.E. Gubernatis.



Rockwell International

Science Center
SC595.32SA

APPENDIX A

QUASISTATIC APPROXIMATION TO THE SCATTERING OF AN ARBITRARILY INCIDENT ELASTIC PLANE WAVE BY AN ELLIPTICAL CRACK

S. Teitel

Laboratory of Atomic and Solid State Physics
Cornell University, Ithaca, NY 14853

ABSTRACT

We extend the work of a previous paper to give a long wavelength approximation for elastic wave scattering by an elliptical flat crack. Explicit formulas for the far-field scattered amplitudes in this approximation are given for various experimental configurations.

In a previous paper¹ we reviewed the problem of scattering of a normally incident longitudinal wave by a circular crack and presented a new quasi-static approximation found to be good in the long wavelength region. In this paper we extend this approximation to the case of longitudinal and transverse waves at an arbitrary angle of incidence scattered by an elliptical crack.

Modeling the crack as a stress free surface of fixed shape, one can express the far-field scattered amplitudes in terms of the vector²

$$f_i(\vec{k}) = \frac{ik^3}{4\pi\rho\omega^2} C_{ijkl} \hat{r}_j \int_{S^+} ds' n_k^+ [u_l] e^{-i\vec{k} \cdot \vec{r}'} \quad (1)$$

where n_k^+ is the outward normal of the side S^+ of the crack, ω is the frequency of the incident wave, and C_{ijkl} and ρ are the elastic tensor and density of the medium. $[u_l]$ is the jump in the l th component of the displacement field across the surface

$$[u_l] = u_l(r' \in S^+) - u_l(r' \in S^-) \quad (2)$$

In terms of the vector f the far-field amplitude for the longitudinal scattered wave is

$$A_i(\vec{r}) = \hat{r}_i \hat{r}_j f_j(\vec{\alpha}) \quad (3)$$

and for the transverse scattered wave is

$$B_i(\vec{r}) = (\delta_{ij} - \hat{r}_i \hat{r}_j) f_j(\vec{\beta}) \quad (4)$$

where $\vec{\alpha}$ and $\vec{\beta}$ are the longitudinal and transverse wave vectors corresponding to ω and point from the center of the crack to the point of observation.

For the case of an elliptical crack lying in the xy plane with major axis along x in a homogeneous isotropic medium,

$$C_{ijkl} = \lambda \delta_{ij} \delta_{kl} + \mu (\delta_{il} \delta_{jk} + \delta_{ik} \delta_{jl}) \quad (5)$$

$$n_k^+ = \delta_{3k}$$



In the static limit $[u_i]$ is proportional to T_{i3} where T_{ij} is the stress tensor on the surface of the crack in the coordinate system specified above. The exact solution for $[u_i]$ in the static case can be obtained from the work of Eshelby³

$$\begin{aligned} [u_1] &= c_1 T_{13} \left(1 - \frac{x^2}{a^2} - \frac{y^2}{b^2}\right)^{\frac{1}{2}} \\ [u_2] &= c_2 T_{23} \left(1 - \frac{x^2}{a^2} - \frac{y^2}{b^2}\right)^{\frac{1}{2}} \\ [u_3] &= c_3 T_{33} \left(1 - \frac{x^2}{a^2} - \frac{y^2}{b^2}\right)^{\frac{1}{2}} \end{aligned} \quad (6)$$

where for the ellipse bonded by $\frac{x^2}{a^2} + \frac{y^2}{b^2} = 1$ and $a > b$ we have,

$$c_3 = \frac{4b}{E(k)} \frac{1 - \sigma^2}{Y}, \quad c_2 = \frac{2a}{\mu \eta_2}, \quad c_1 = \frac{2b}{\mu \eta_1} \quad (7)$$

where

$$\eta_1 = E(k) + \frac{\sigma}{1 - \sigma} \frac{k'^2}{k^2} (K(k) - E(k))$$

$$\eta_2 = \frac{E(k)}{k'} + \frac{\sigma}{1 - \sigma} \frac{1}{k'} \frac{E(k) - k'^2 K(k)}{k^2}$$

$$k = (1 - b^2/a^2)^{\frac{1}{2}}, \quad k' = b/a$$

$$\text{For } a = b, \quad \eta_1 = \eta_2 = \frac{\pi(2 - \sigma)}{4(1 - \sigma)}$$

Here σ is Poisson's ratio, μ is the shear modulus, Y is Young's modulus, and $E(k)$ and $K(k)$ are the complete elliptic integrals of 2nd and 1st kind respectively.

For an incident wave vector \vec{k}_i , T_{23} will have the form

$$T_{23} = \tau_{23ik} e^{i\vec{k}_i \cdot \vec{r}} \quad (8)$$

In quasi-static approximation we assume that at low k_i the relations given by (6) are still accurate enough to use in the integral (1). Substituting Eq. (8) into (6) and then (6) and (5) into (1) results in

$$f_i(\vec{k}) = -\frac{k^3 k_i}{4\pi\rho\omega^2} I(\vec{k}_i, -\vec{k}) \left\{ \mu c_{113} (\delta_{i1} \hat{r}_3 + \delta_{13} \hat{r}_1) + \mu c_{223} (\delta_{i2} \hat{r}_3 + \delta_{23} \hat{r}_2) + c_{333} (\lambda \hat{r}_i + 2\mu \delta_{i3} \hat{r}_3) \right\} \quad (9)$$

$$\begin{aligned} \text{where } I(\vec{\gamma}) &= 2\pi ab \int_0^1 dr r(1-r^2)^{\frac{1}{2}} J_0(\gamma r \sin\theta_\gamma \sqrt{a^2 \cos^2 \varphi_\Lambda + b^2 \sin^2 \varphi_\Lambda}) \\ &= 2\pi ab \frac{1}{\Delta^2} \left(\frac{\sin \Delta}{\Delta} - \cos \Delta \right), \quad \Delta = (a^2 \gamma_x^2 + b^2 \gamma_y^2)^{\frac{1}{2}} \end{aligned}$$

We now substitute this f vector into (3) and (4) to get

$$\vec{A} = -\hat{r} \frac{a^3 k \Lambda}{4\pi\rho\omega^2} I(\vec{k}_i, -\vec{a}) \left\{ c_{333} (\lambda + 2\mu \cos^2 \theta) + \mu \sin 2\theta (c_{113} \cos \varphi + c_{223} \sin \varphi) \right\} \quad (10)$$

$$\begin{aligned} \vec{B} = -\frac{b^3 k \Lambda}{4\pi\rho\omega^2} I(\vec{k}_i, -\vec{b}) \mu \left\{ \hat{e}_\theta [c_{333} \sin 2\theta - \cos 2\theta (c_{113} \cos \varphi + c_{223} \sin \varphi)] \right. \\ \left. + \hat{e}_\varphi \cos \theta (c_{223} \cos \varphi - c_{113} \sin \varphi) \right\} \quad (11) \end{aligned}$$

Here the angles specify the point of observation with respect to the coordinate frame of the crack.

In order to put these formulas to use we must now calculate τ_{ij} for various experimental configurations.

For an incident wave coming in at polar angles θ_i, φ_i with respect to the coordinate frame of the crack we consider the three polarizations given by the axis of the primed coordinate system shown in Fig. 1. \hat{z}' is the direction of the incident wave, \hat{x}' lies in the plane of the crack and is orthogonal to \hat{z}' , an \hat{y}' completes the right handed coordinate system.

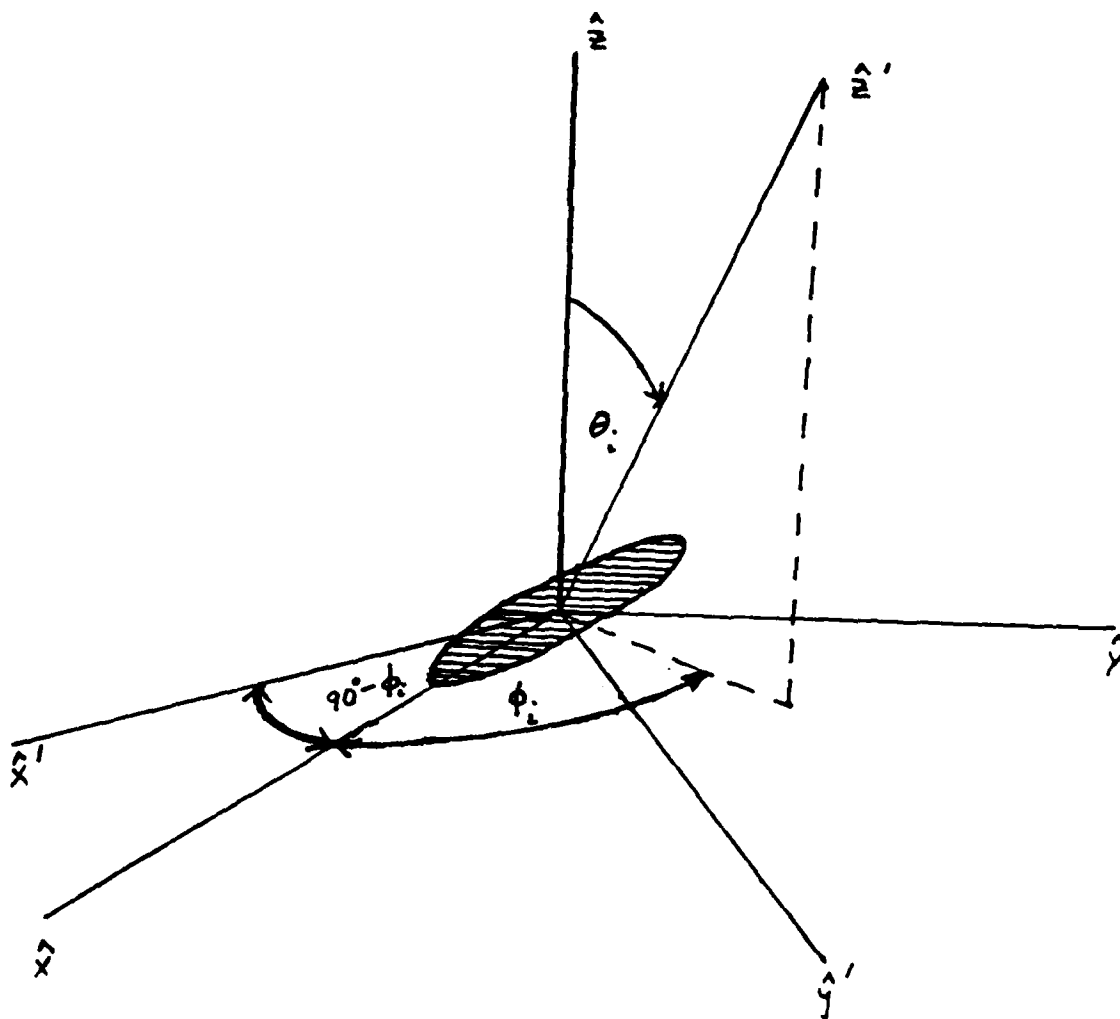


Fig. 1 Geometry of scattering. Incident wave travels along \hat{z}' , and is polarized along \hat{x}' , \hat{y}' or \hat{z}' . The crack lies in xy plane with major axis along \hat{x} . Scattered field is given as a function of spherical angles with respect to the unprimed coordinate system.

We consider the three cases:

- 1) Longitudinal incident wave polarized along \hat{z}' .

For an incident displacement field of unit amplitude,

$$\vec{u}_0 = \hat{z}' e^{ik_j z'}$$

we have

$$\begin{aligned} \tau_{13} &= \mu \sin 2\theta_i \cos \varphi_i \\ \tau_{23} &= \mu \sin 2\theta_i \sin \varphi_i \\ \tau_{33} &= \lambda + 2\mu \cos^2 \theta_i \end{aligned} \quad (12)$$

- 2) Transverse incident wave polarized in plane of crack along \hat{x}' .

For $\vec{u}_0 = \hat{x}' e^{ik_j z'}$ we have

$$\begin{aligned} \tau_{13} &= \mu \cos \theta_i \sin \varphi_i \\ \tau_{23} &= -\mu \cos \theta_i \cos \varphi_i \\ \tau_{33} &= 0 \end{aligned} \quad (13)$$

- 3) Transverse incident wave polarized out of plane of crack along \hat{y}' .

For $\vec{u}_0 = \hat{y}' e^{ik_j z'}$ we have

$$\begin{aligned} \tau_{13} &= \mu \cos 2\theta_i \cos \varphi_i \\ \tau_{23} &= \mu \cos 2\theta_i \sin \varphi_i \\ \tau_{33} &= -\mu \sin 2\theta_i \end{aligned} \quad (14)$$

It is now up to the experimentalist to specify the experimental configuration, choose from Eqs.(12), (13) or (14) the values of τ_{ij} appropriate for it, and substitute them into Eqs.(10) and (11) to completely determine the far-field amplitudes in the quasi-static approximation.

I would like to thank Dr. J.E. Gubernatis, Dr. E. Domany and Dr. J.A. Krumhansl for many useful discussions.



Rockwell International

Science Center
SC595.32SA

Acknowledgements

Work supported by Rockwell International under Contract No. F33615-74-C-5180. We would like to thank the Cornell Materials Science Center for their technical assistance.

References

1. E. Domany, J.A. Krumhansl, S. Teital, (J. Appl. Phys., to be published).
2. The f-vector approach for scattering of flaws of finite volume is developed in J.E. Gubernatis, E. Domany, J.A. Krumhansl, J. Appl. Phys. 48, 2804 (1977). The extension to cracks was done by J.E. Gubernatis, unpublished.
3. J.D. Eshelby, Proc. Roy. Soc. London, Ser. A 271, 376 (1957).

APPENDIX B

INFERENCE OF FLAW CHARACTERISTICS FROM ULTRASONIC
SCATTERING AMPLITUDES*

J.H. Rose and J.A. Krumhansl

Laboratory of Atomic and Solid State Physics
Cornell University, Ithaca, NY 14853

ABSTRACT

We give a procedure for approximately determining the size and shape of a flaw in an elastic medium from ultrasonic scattering amplitudes. The inversion procedure is rigorously valid for the case of weakly scattering flaws. We report preliminary tests of the technique for strongly scattering flaws and include the effects of noise in the scattering data. These preliminary tests indicate that the inversion procedure will be a useful tool for measuring the size and shape of flaws in many different experimental circumstances. In the report we discuss the required experimental measurements needed to determine the flaw's size and shape; and consider the application of the technique to non-destructive testing.



Introduction

The determination of the size and shape of flaws from ultrasonic scattering data is an important part of the current effort to develop non-destructive testing (NDT) techniques. The Born approximation for ultrasonic scattering has recently been extensively developed.^{1,2} In this approximation, the scattering amplitudes are proportional, within a known angular factor, to the Fourier transform of the region occupied by the flaw. It has been generally recognized that this relation could be used as the basis of an inversion technique. This report details the inverse Born procedure for measuring the size and shape of a general flaw. Rigorous results are obtained for weakly scattering flaws. In order to test the inversion procedure for strongly scattering flaws, the exact numerical scattering amplitudes for several realistic spherical flaws^{2,3,4} were used. These spherical flaws included the case of a void in Ti, and an Al inclusion in Ti. Strikingly successful results were obtained, both when we used the exact noise-free scattering amplitudes, and when we simulated noisy scattering data. These numerical experiments indicate that the inverse Born approximation may yield accurate determinations for the size and shape of flaws for a wide variety of circumstances.

The structure of this report is as follows. In Section 2 we formulate the inversion technique in detail for the case of longitudinal to longitudinal scattering ($L \rightarrow L$). In Section 3 we discuss the experimental measurements necessary to carry out the inversion. Section 4 treats as an example the inversion of the scattering amplitudes for strongly scattering spherical flaws. The effect of noisy data on the inversion procedure is discussed in Section 5. Our results are summarized and discussed in Section 6. An appendix contains the relevant formulas for an inversion procedure based on longitudinal to transverse ($L \rightarrow T$), transverse to transverse ($T \rightarrow T$), or transverse to longitudinal ($T \rightarrow L$) scattering.

The Inverse Born Procedure

In an ultrasonic scattering experiment, the scattered waves far from the flaw can be written as:

$$\vec{U}^S(\vec{r}) = \vec{A}(\hat{r}^0, \hat{r}^S, \gamma) \frac{e^{i\alpha r}}{r} + \vec{B}(\hat{r}^0, \hat{r}^S, \gamma) \frac{e^{i\beta r}}{r} \quad (2.1)$$

Here the scattering amplitudes \vec{A} and \vec{B} are vector quantities whose directions denote the polarization of the scattered waves. In particular, \vec{A} is the amplitude of the longitudinal component and points along the scattering direction, \hat{r}^S . \vec{B} denotes the transverse component and points normal to the scattering direction. The magnitude of the wave vectors of the various waves is given as α for the longitudinal scattered component, as β for the transverse component, and as γ for the incident wave. Generally, \vec{A} and \vec{B} are measured as functions of the incident direction, \hat{r}^0 , the scattering direction, \hat{r}^S , and the wave vector magnitudes α , β , and γ . The Born approximation allows us to calculate \vec{A} and \vec{B} in a particularly simple manner for an incident plane wave. The resulting \vec{A} and \vec{B} are simply related to the Fourier transform of the shape of the flaw. The inverse Born procedure then uses an inverse Fourier transform to yield the size and shape of the flaw.

In order to make the inversion procedure explicit we consider the case of an incident longitudinal wave the the cross-section for longitudinal scattering ($L \rightarrow L$). For this case, the Born approximation for the scattering amplitude is

$$\begin{aligned} A(\hat{r}^S, \hat{r}^0, \alpha) &= \vec{A}(\hat{r}^S, \hat{r}^0, \alpha) \cdot \hat{r}_S \\ &= \alpha^2 \left\{ \frac{\delta\rho}{\rho} \cos \theta - \frac{\delta\lambda + 2\delta\mu \cos^2 \theta}{\lambda + 2\mu} \right\} \int d^3\vec{r} \gamma(\vec{r}) e^{i\alpha(\hat{r}^0 - \hat{r}^S) \cdot \vec{r}} \end{aligned} \quad (2.2)$$

The mass and Lamé parameters of the host material are denoted by ρ , λ and μ , respectively. The quantities $\delta\rho = \rho_f - \rho$, $\delta\lambda = \lambda_f - \lambda$, and $\delta\mu = \mu_f - \mu$ denote the differences between the material parameters of the flaw (these are denoted by subscript f) and the host material. The angle between the incident beam direction and the scattering direction is given by θ ; also, α is the wave vector magnitude of a longitudinal wave in the host material. Finally, $\gamma(\vec{r})$ is the characteristic function of the flaw. That is, $\gamma(\vec{r}) = 1$ for \vec{r} inside the flaw, and $\gamma(\vec{r}) = 0$ for \vec{r} outside the flaw. The expression for the scattering amplitude A separates into a product of three terms within the Born approximation. The first term is α^2 . The second term is given by



$$G(\theta) = \frac{\delta\rho}{\rho} \cos \theta - \frac{\delta\lambda + 2\delta\mu \cos^2 \theta}{\lambda + 2\mu} \quad (2.3)$$

and depends only on θ for a given set of material parameters. The third term is the shape factor of the flaw, and is given by

$$S(\vec{\kappa}) = \int d^3\vec{r}' e^{i\vec{\kappa} \cdot \vec{r}'} \gamma(\vec{r}') \quad (2.4)$$

Here the change in wave vector between the incoming and outgoing wave is denoted by $\vec{\kappa} = \alpha(\hat{r}_0 - \hat{r}_s)$. Equation (2.2) can now be rewritten as:

$$S(\vec{\kappa}) = \frac{A(\hat{r}_s, \hat{r}_0, \alpha)}{\alpha^2 \left[\frac{\delta\rho}{\rho} \cos \theta - \frac{\delta\lambda + 2\delta\mu \cos^2 \theta}{\lambda + 2\mu} \right]} \quad (2.5)$$

Using Eq.(2.5), the shape factor, $S(\vec{\kappa})$ can be inferred from a measurement of the scattering amplitude A^{ex} (here the superscript ex is used to indicate that A^{ex} is an experimentally measured quantity). Equation (2.5) as written appears to require the measurement of $A^{\text{ex}}(\hat{r}_0, \hat{r}_s, \alpha)$ for all incident directions, all scattering directions and all wave vectors α . Fortunately, only a much smaller subset of the scattering amplitude need be measured in order to determine $S(\vec{\kappa})$; this results since many different scattering events have the same wave vector transfer $\vec{\kappa}$. In the next section we will discuss what set of measurements are needed to determine $S(\vec{\kappa})$. It turns out that S can be determined from several different experimental measurements. Assuming for the moment that we have determined $S(\vec{\kappa})$ from one of the set of measurements to be discussed, then the inverse Fourier transform of $S(\vec{\kappa})$ yields

$$\gamma(\vec{r}) = \left(\frac{1}{2\pi}\right)^3 \int d^3\vec{k} e^{i\vec{k} \cdot \vec{r}} S(\vec{k}) \quad (2.6)$$

The determination of the size and shape of a flaw from Eqs.(2.5) and (2.6) is rigorously valid in the weak scattering limit. For strongly scattering flaws only an approximate determination of the size and shape can be obtained due to

the approximate nature of the Born results (which for example fails to yield the exact scattering amplitude in the static limit for a general flaw). However, this approximate inversion is still expected to yield rather good results for both size and shape; since, the Born approximation yields good results for the part of the scattering spectrum which determine the gross feature of $\gamma(\vec{r})$. The relevant part of the spectrum is the backscattering regime for $ka \approx 1$. In Section 4, we test the inversion procedure for several flaws of various scattering strengths, including a void. There we use the exact numerical solutions for the $L \rightarrow L$ scattering amplitudes of a spherical elastic inclusion and a spherical void, as artificial scattering data. This artificial scattering data is used to determine $S(\vec{\kappa})$ and then $\gamma(\vec{r})$. Surprisingly good results are obtained for strongly scattering flaws, even the void.

Methods for Determining the Shape Factor from the Measured Scattering Amplitudes

The shape factor, $S(\vec{\kappa})$, depends only on the wave vector transfer $\kappa = \alpha(\hat{r}^0 - \hat{r}^s)$. There are many scattering events which have the same $\vec{\kappa}$, and hence can be used to determine $S(\vec{\kappa})$ for that value of $\vec{\kappa}$. The experimentalist need only measure some subset of the scattering amplitude $A_{ex}(\hat{r}^0, \hat{r}^s, \alpha)$, such that $S(\vec{\kappa})$ is uniquely defined for all $\vec{\kappa}$ by that subset. Two different criteria suggest themselves in choosing the set of measurements to be made. First, we would like to determine the subset which would yield the best determination of the flaw's size and shape. On the other hand, it may be that some other determination of $S(\vec{\kappa})$ may be of greater experimental ease. Below we will first deal with the question of the optimum set of data for the purposes of inversion. Then we will comment on some of the features of the problem which may have implications for the experimental collection of data. We note here that Bleistein and Bajorski⁵ have treated the inverse problem for scalar waves using a Kirchoff-like, high frequency, approximation. They find a proportionality between the shape factor and the scattering amplitudes as in the inverse Born procedure. In their work they discussed many of the geometrical ideas which are used below to choose the various subsets of A which determines $S(\vec{\kappa})$.



For long wavelength backscattering ($\theta = 180^\circ$), the Born approximation generally yields relatively good values for the scattering amplitude; for forward scattering ($\theta = 0^\circ$), the Born approximation fails badly. In order to optimize the data inversion, a reasonable choice of $A_{\text{ex}}(\hat{r}^0, \hat{r}^S, \alpha)$ would be that subset which is best predicted in the Born approximation. We choose direct backscatter. If the backscattered amplitude is measured for all different incident directions, and all frequencies, then the shape factor is completely determined, in principle. To see this, we note that for backscattering $\vec{k} = \alpha(\hat{r}^0 - \hat{r}^S) = 2\alpha\hat{r}^S$ since $\hat{r}^S = -\hat{r}^0$. If we then allow α to vary from zero to infinity and allow \hat{r}^0 to point in all directions, we completely determine $S(\vec{k})$, which for this case is given by

$$S(\vec{k}) = \text{const} \frac{A(\hat{r}^0, -\hat{r}^0, \alpha)}{\alpha^2} \quad (3.1)$$

Once $S(\vec{k})$ is determined, we obtain the size and shape of the flaw by an inverse Fourier transform (Eq.(2.6)).

There are other possible ways of determining $S(\vec{k})$. Some of these techniques may be of greater experimental ease than the backscattering method suggested above. First, we consider what data may be collected from a single transmitting transducer, when the scattering amplitude is measured at all angles. For a single value of the incident wave vector amplitude, α , these measurements determine a spherical shell of values for $S(\vec{k})$ in \vec{k} space. The relevant geometric considerations are shown in Fig. 3.1. By varying α from zero to infinity we sweep out the entire right half-space of \vec{k} space as shown in the figure. If the flaw has a known symmetry we may be able to infer a set of values for $S(\vec{k})$ in the left half-space. If there is no such symmetry, we must also measure A_{ex} for this region in the \vec{k} space. The most straightforward choice would be to put a second transmitter at $\theta = 180^\circ$ (i.e. irradiate the flaw from the opposite direction). This suffices to determine $S(\vec{k})$ for all \vec{k} .

Perhaps the most interesting case from the point of view of NDT is the situation where there is only a limited aperture in \vec{r} -space. As when, for example, one only has access to one surface of a wing section. The limitation in \vec{r} -space measurements, reflects itself by limiting the region in \vec{k} -space

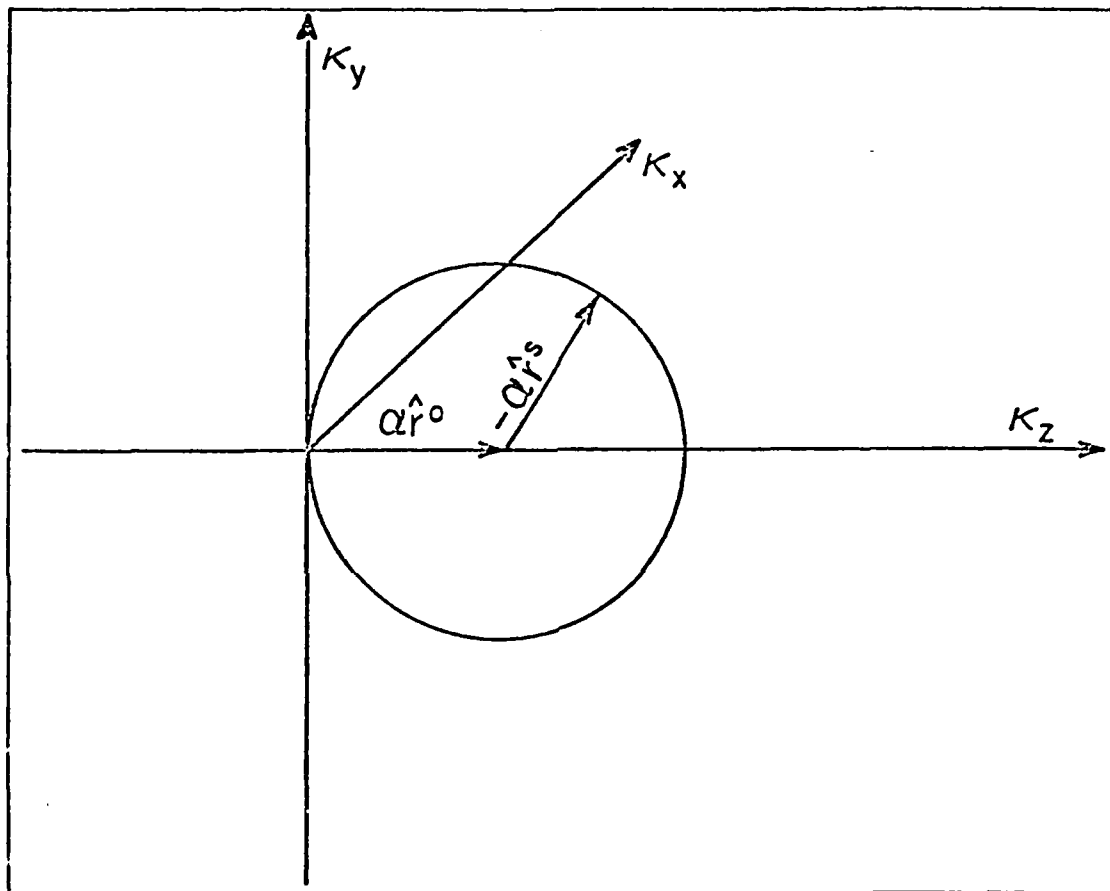


Figure 3.1 In this figure a longitudinal ultrasonic wave is incident from the left along the z -axis. The spherical shell shows those values in \vec{k} -space for which $S(\vec{k})$ may be measured for a given value of α , the incident wavevector magnitude.



which can be measured. We will not comment substantially on this problem in this report. We note that it requires further study.

To summarize this section, we have discussed a method involving only the backscattered amplitudes to determine the size and shape of the flaw. We expect this procedure to be the optimum one for our technique. We further indicated briefly what data could be determined from a single transmitting transducer, when the scattering amplitudes are measured at all angles. Finally, we showed that irradiating the flaw from opposite directions and measuring the scattering amplitudes at all angles and all frequencies sufficed to determine the shape factor.

Applications of the Inverse Born Procedure

In this section we test the utility of the inverse Born procedure. There are several realistic ultrasonic scattering problems for which accurate numerical calculations are available. Among these solved problems are the scattering of ultrasound from spherical voids and spherical elastic inclusions. To test the inversion procedure, we use these "exact solutions" as a "data base" for the scattering amplitudes $A(\hat{r}^0, \hat{r}^S, \alpha)$ required by the approximate inverse Born procedure. Below we calculate thus the characteristic function $\gamma(\vec{r})$ for the three different cases. These are a spherical void in Ti, an Al inclusion in Ti and finally, the case of a weakly scattering elastic inclusion in Ti (here the material parameters of the inclusion differ by ~1% from those of Ti).

Next we discuss specifically how the inversion was performed. Then the results of the inversion are presented in graphical form. Finally, we discuss the results briefly.

As discussed in Section 3, it is necessary to select from the scattering data $A(\hat{r}^0, \hat{r}^S, \alpha)$, a subset which defines $S(\vec{k})$ for all \vec{k} . We choose to use the first procedure discussion in Section 3, namely to use only direct backscattering data where the incident direction is varied over all possible orientations with respect to the scatterer. For a spherical flaw, the scattering amplitude, A , is independent of the incident direction. Since $S(\vec{k})$ is related by A by means of Eq.(3.1), it follows that $S(\vec{k})$ is independent of the direction of \vec{k} and depends only on the magnitude of the wave vector

transfer, $|\vec{r}|$ which for the case of backscattering is given by $|\vec{r}| = 2\alpha$. Using these results we can rewrite Eq.(3.1) as:

$$\gamma(|\vec{r}|) = (\text{const}) \int_0^\infty \frac{d\alpha A(\hat{r}^0, \hat{r}^s, \alpha) \sin(2\alpha|\vec{r}|)}{2\alpha|\vec{r}|} \quad (4.1)$$

The calculation yields the result that $\gamma(\vec{r})$ is also spherically symmetric and depends only on the radial coordinate r . In order to obtain $\gamma(r)$ from Eq.(4.1) we substitute in our calculated values for A and integrate numerically up to some maximum value of α , α_{max} . Here, we note a couple of technical points. First, the cutoff at α_{max} causes our results to contain characteristic ringing frequencies, but introduces no difficulties in the interpretation of the results.

Secondly, the scattering amplitudes are in general complex. As will be discussed in detail in a later report, this leads to a small imaginary part in $\gamma(r)$. The complex part of $\gamma(r)$ is unphysical, and results from the approximate nature of our inversion procedure. In the graphs, we have plotted $|\gamma(r)|$. Alternatively, we could have used only the real part of A in Eq.(4.1) and thus obtained a real $\gamma(r)$. Both procedures yield essentially the same result for these calculations.

Figure 4.1 shows the calculated $\gamma(r)$ for a spherical void in Ti. For purposes of comparison, we have compared the radial part of $\gamma(r)$ with the characteristic function of a sphere (namely $\theta = 1$ if r is less than the radius while $\theta = 0$ if r is greater than the radius). As can be seen, the calculated characteristic function does a good job of indicating clearly the presence of a flaw for $r < a$, and the absence of scattering $r > a$. We feel these results for the void are very supportive of the possible utility of the inverse Born approximation for determining the size and shapes of flaws. First of all, the void is an extremely strong scattering situation where we would expect the Born procedure to be at its worst. Hence, good success for this case indicates that the procedure may have a very wide range of validity. Further, there is nothing in our general procedure which presupposes or is predicated on the geometry of the sphere. Hence, we feel that the inverse Born procedure will likely work for more complicated shapes. Of course, this point needs

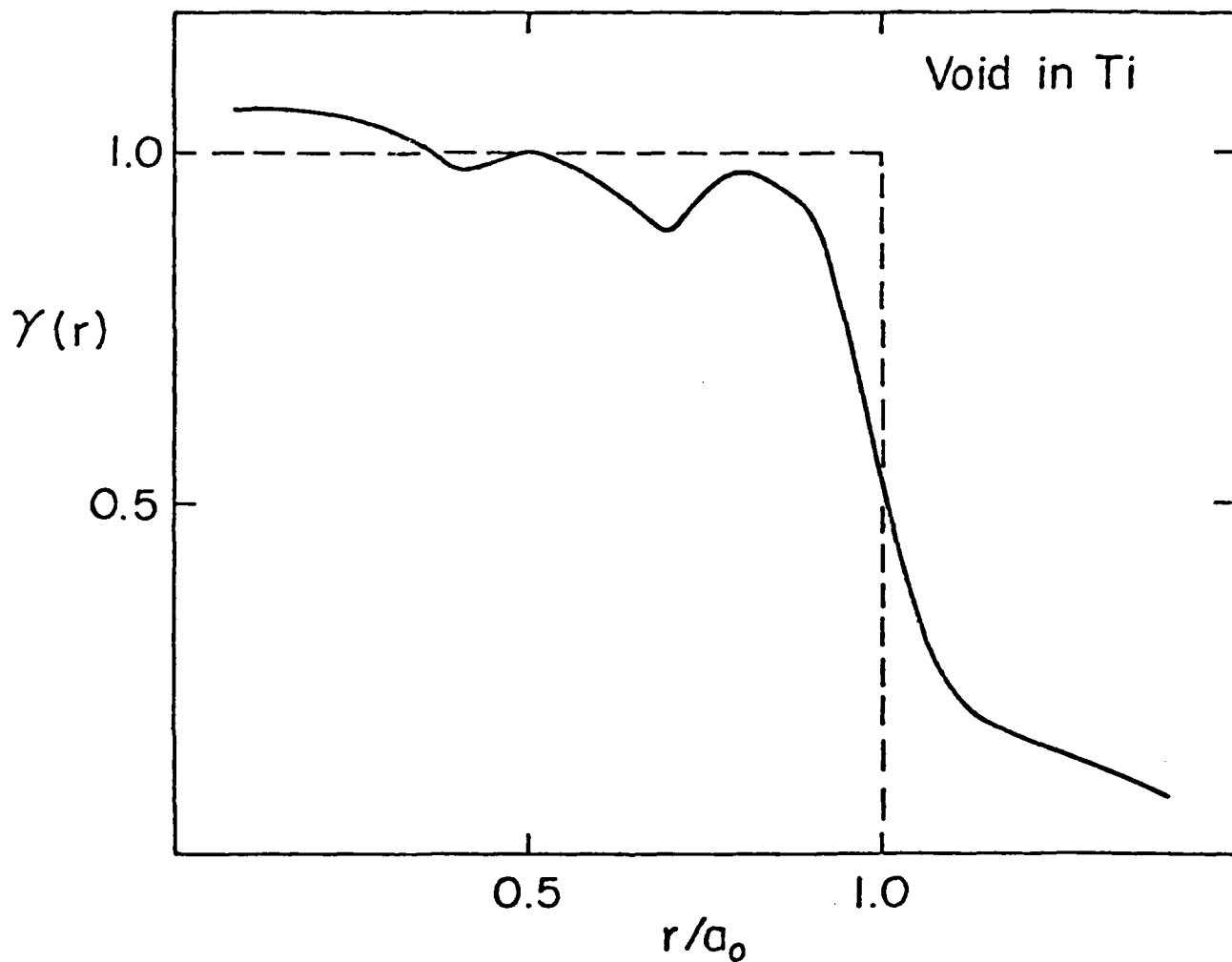


Figure 4.1 The calculated characteristic function, $\gamma(r)$, for a spherical void in Ti is shown and compared with the exact result shown by dotted lines.

verification, either with experimental scattering data from flaws of known size and geometry, or from accurate numerical calculations of the scattering amplitudes for more complicated shapes.

Figures 4.2 and 4.3 show similar results for $\gamma(r)$ in the case of an elastic inclusion. Figure 4.2 presents the results for an Al sphere in Ti and Fig. 4.3 shows the case of a weakly scattering inclusion in Ti. As expected from the results for the void, these cases also yield an extremely well defined scattering center. We define the surface of the flaw as that point where $\gamma(r)$ has one-half of its value in the plateau region interior to the flaw. Table 4.1 then shows the calculated radii as compared to the actual radii.

Table 4.1

Ratio of Calculated Sphere Radii to actual Values

<u>Flaw</u>	<u>Ratio</u>
Void in Ti	1.01
Al in Ti	0.90
Weak Scatterer in Ti	0.96

The wiggles in the plateau region are the result of the extremely sharp fall off in $\gamma(r)$ and the truncation of our integration at α_{\max} as mentioned above.

The Effects of Noise on the Inversion Procedure

In Section 4 we reported several numerical tests of the inverse Born procedure using the "exact solutions" for various spherical voids and inclusions. These tests were unrealistic in that our data base was essentially noise free. This is a considerable idealization of the current state of the art for many ultrasonic scattering experiments. In this section we discuss the effects of noise in degrading the inversion procedure. The ideal way to test the procedure would be to use real experimental data. Dr. B. Tittmann has agreed to provide us with backscattering data from a spherical void (and a tungsten carbide sphere) in Ti. These data were not at hand before this report was written, so we present the results of a preliminary study in which our "exact data base" was mixed with a random

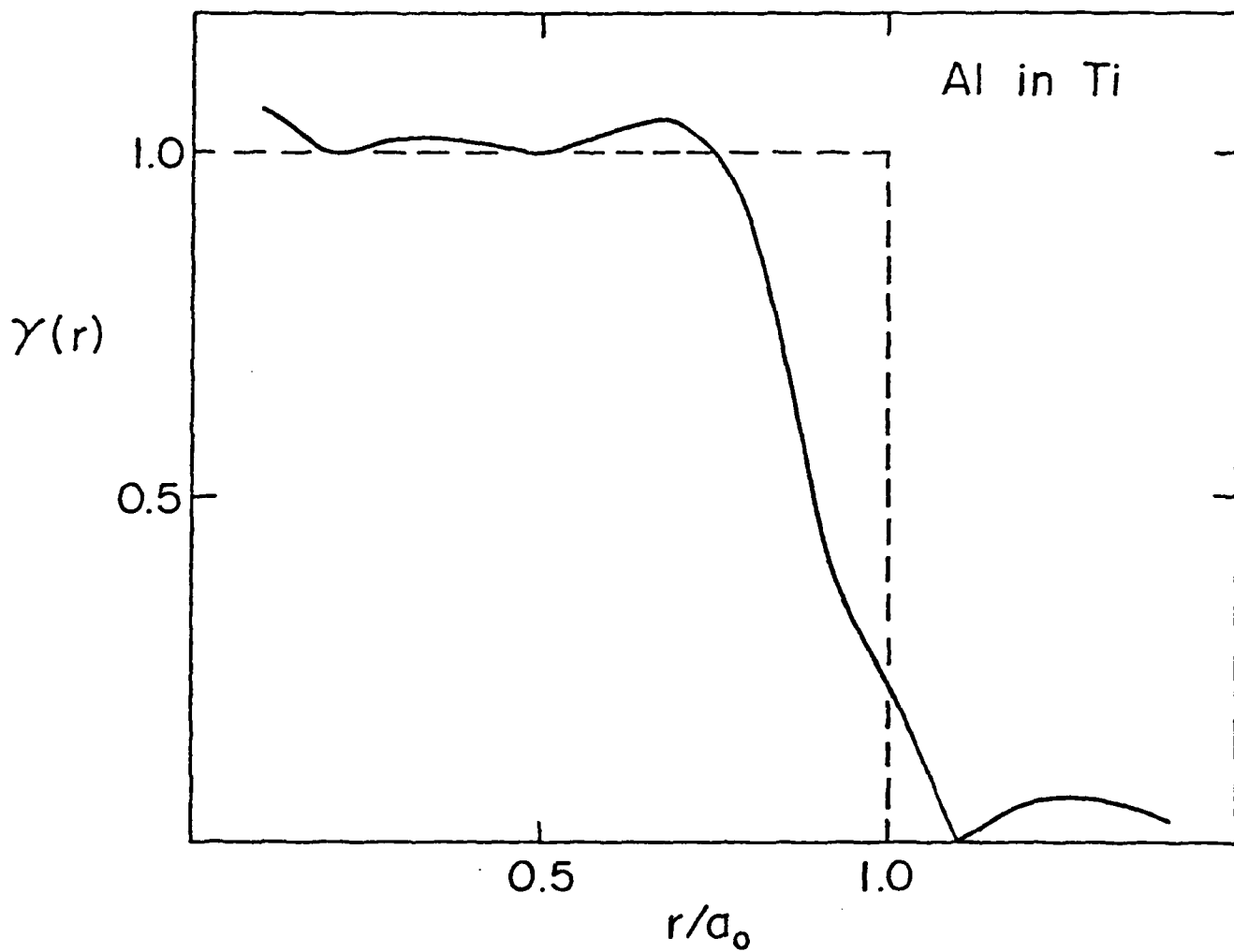


Figure 4.2 The calculated $\gamma(r)$ for a spherical Al inclusion Ti is shown.

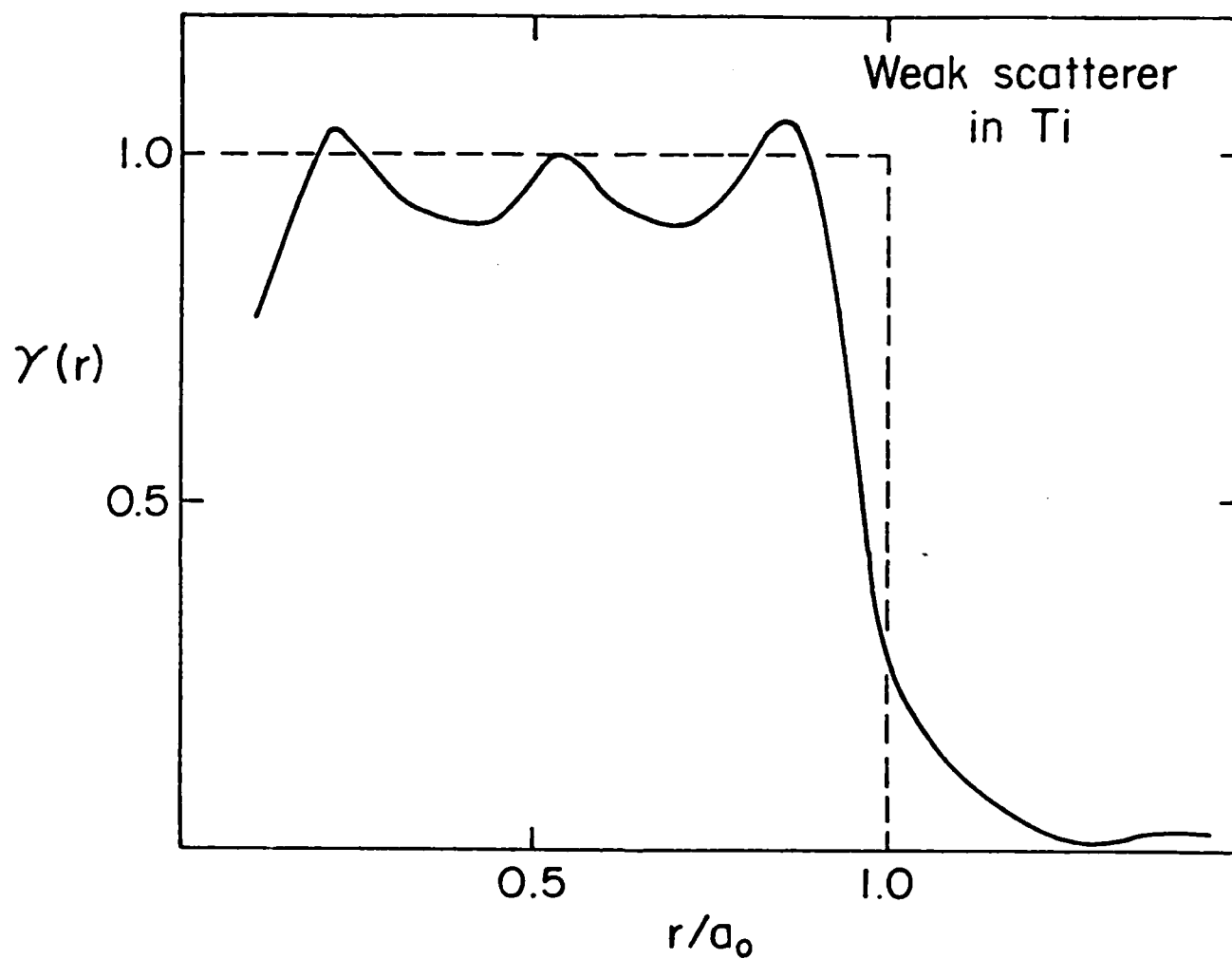


Figure 4.3 The calculated $\gamma(r)$ is shown for a weakly scattering spherical elastic inclusion in Ti. The material parameter of this inclusion are 99% those of Ti.



signal component in order to mimic random noise. These preliminary studies indicate that the inversion procedure is surprisingly insensitive to random errors in the data as we will be discussed below. In the future we intend to present a more complete report in which the results for the inversion of experimental data are presented, and in which a detailed explanation will be given for the insensitivity of the procedure to random noise.

In order to simulate noise in our data base, we used a random number generator to introduce a noise component in the signal using the following formula

$$A_{\text{noisy}}(\hat{r}_0, -\hat{r}_0, \alpha) = 1 + \delta\beta A_{\text{exact}}(\hat{r}_0, -\hat{r}_0, \alpha) \quad (5.1)$$

Here β is a Gaussian random number with a standard deviation on one. A different random value is introduced for each value of A in our data set. A is calculated on a discrete mesh whose spacing $\Delta\alpha = 0.1/a_0$, and a_0 is the radius of the sphere. Finally, δ is a parameter which controls the ratio of the initial exact values of A , and the randomly introduced signal.

The results obtained are illustrated in the case of the void in Ti. In Fig. 5.1, we show the results for $\gamma(r)$ of the void when a quite large noise component (here δ is 0.5) is included. The effect of the noise was to cause some increased scatter in the results. However, the presence of the edge for $r \approx a_0$ is still quite distinct. In a set of five runs using different random numbers (to simulate different experimental runs), we found that the calculated radius was constant to within a few percent. We emphasize that these results were obtained from a quite noisy signal. The condition, $\delta = 0.5$, means that for a given value of A , the random error is on the order of 50%.

In concluding, the sections on numerical tests of the inverse Born procedure, we would like to say that results for the spherical problems have provided an extremely promising initial test of the technique. We feel that such successful agreement for these preliminary trials fully justifies an attempt to invert data for more complicated flaws and more realistic NDT situations.

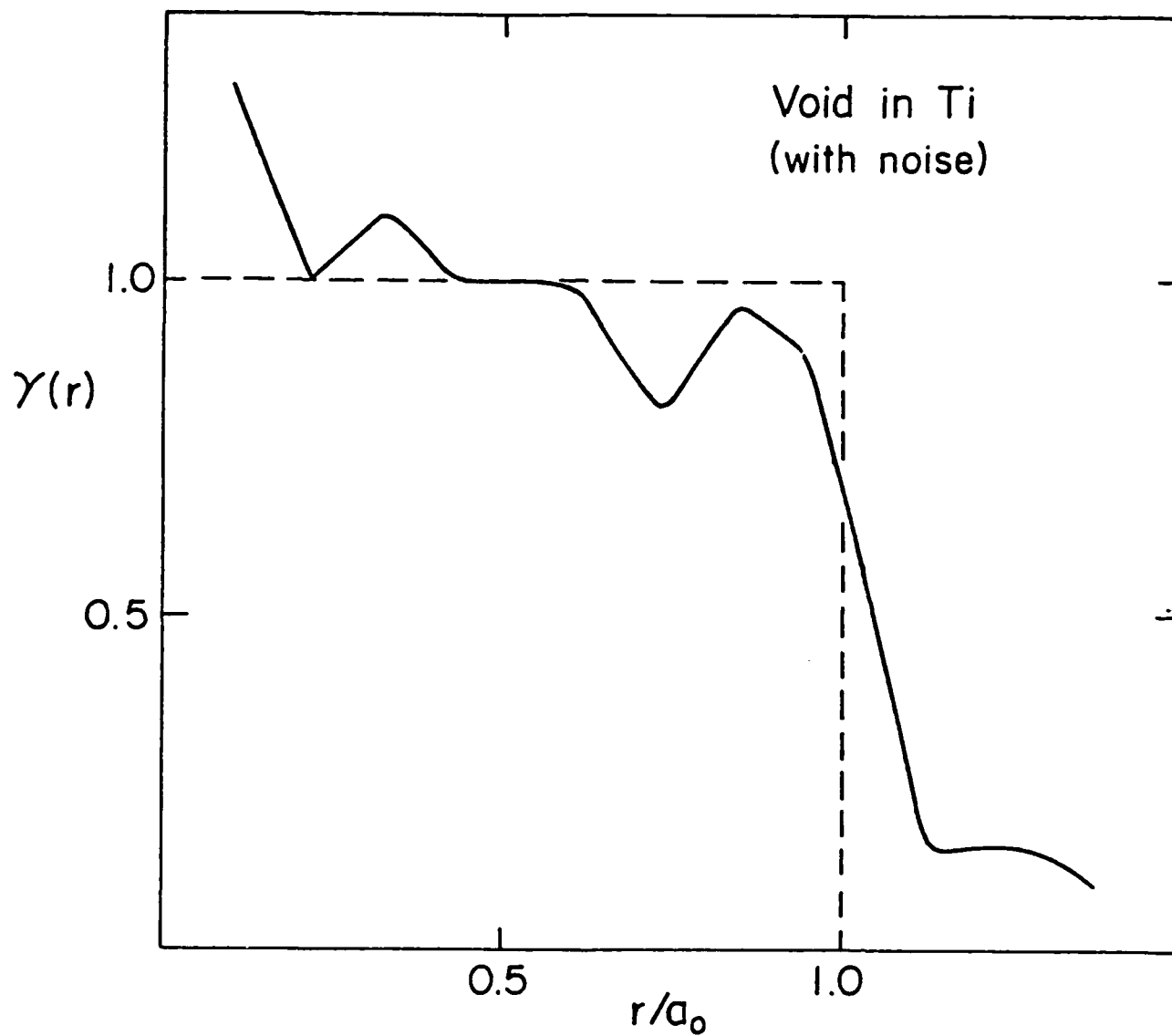


Figure 5.1 The relatively weak effects of noise are shown for the determination of the characteristic function, $\gamma(r)$, of a spherical void in Ti. Here we have included a random signal component in our scattering amplitude data base. The random component is on the average 50% of the exact signal.



Discussion and Summary

The determination of the size and shape of a flaw via the inverse Born approximation has been discussed for the case of $L \rightarrow L$ scattering. The procedure is rigorously valid for the case of weakly scattering flaws. The solutions for scattering from a spherical void in Ti (and an Al inclusion in Ti) were used to calibrate the inversion procedure. These tests indicate that the size of these spherical flaws can easily be determined to within 10%. These preliminary studies for strongly scattering flaws are considered to be highly encouraging. However, there are still several questions which must be answered before the inverse Born procedure can be considered to be an established tool.

The first question concerns irregular flaws. The inversion procedure works well for strongly scattering spherical flaws. Can it be used to establish the shape of non-spherical flaws which are strongly scattering? We feel that this question should be addressed either by experimental measurement, or the theoretical calculation of the backscattered amplitudes for more complicated shapes than the sphere. As regards theoretical approaches to backscattering data, we feel that it would be desirable to test the technique against essentially exact data. If approximate calculations were used for data, one would not know whether to attribute the failure or success of the inversion procedure to the inversion process per se, or to the particular approximation used to generate the approximate scattering data. For example, the inversion procedure will work remarkably well if the scattering amplitudes are generated using the Born approximation. The detailed calculation of Varadan and Pao⁶ may be of interest as calibration tools.

A second and perhaps more difficult class of questions is as follows. What is the effect of a limited viewing aperture on the inversion procedure? To what degree can the shape of an object be determined from data collected over a limited aperture? If for a given aperture, the shape of a flaw cannot be determined, what can be said about the average size of the flaw, or the presence of regions of high stress? These questions are quite complex, and we feel that answers to them will require sizable amounts of effort by many different groups. In this context, the reports of Lewis,⁷ Bojarski,⁵ Perry,⁸ and Bleistein^{5,9} may be of interest.

We conclude this report with a summary. The Born approximation was used as the basis for an inversion procedure for ultrasonic scattering data. Rigorous results for the size and shape of weakly scattering flaws were obtained. Very encouraging results were obtained for the size and shape of strongly scattering spherical flaws. Work is currently in progress concerning the problems of: (1) The effect of noisy data on the determination of flaw size and shape; (2) The evaluation of the inversion procedure for strongly scattering flaws whose shape is other than spherical; and (3) The effects of limited aperture on the inversion technique.



APPENDIX 1

In the main body of this report, we used the result that the shape factor, $S(\vec{\kappa})$, can be determined from the $L \rightarrow L$ scattering amplitudes within the Born approximation. Similar results hold for $T \rightarrow T$, $L \rightarrow T$, and $T \rightarrow L$ scattering. These formulas are listed below. We note that $L \rightarrow T$, and $T \rightarrow L$ scattering amplitudes are identically zero on the backscattering directions for reasons of symmetry. Since this is the direction for which the Born approximation is expected to yield its best results, it appears likely that best results for the inversion procedure will be obtained from $L \rightarrow L$ and $T \rightarrow T$ scattering.

We first consider $T \rightarrow T$ scattering using an incident right hand circularly polarized incident wave. There are two values for the shape factor corresponding to the two different polarization direction of the scattered wave.

$$S(\vec{\kappa}) = \frac{4\pi \vec{B} \cdot \hat{x}^+ e^{-i\varphi}}{\beta^2} \left\{ \frac{\delta\rho}{\rho} \frac{(1 + \cos\theta)}{2} - \frac{\delta\mu}{\mu} \frac{(\cos\theta + \cos^2\theta)}{2} \right\} \quad (A.1)$$

and

$$S(\vec{\kappa}) = \frac{4\pi \vec{B} \cdot \hat{x}^- e^{-i\varphi}}{\beta^2} \left\{ \frac{\delta\rho}{\rho} \frac{(\cos\theta - 1)}{2} + \frac{\delta\mu}{\mu} \frac{(\cos\theta - \cos^2\theta)}{2} \right\} \quad (A.2)$$

Here $\hat{x}^+ = \frac{1}{\sqrt{2}} (\hat{\theta} + i\hat{\varphi})$ and $\hat{x}^- = \frac{1}{\sqrt{2}} (\hat{\theta} - i\hat{\varphi})$ where $\hat{\theta}$ and $\hat{\varphi}$ are unit vectors in the θ and φ directions. The wave vector transfer is given by $\vec{\kappa} = \beta(\hat{r}^0 - \hat{r}^s)$. The vector $\vec{B} = \vec{B}(\hat{r}^0, \hat{r}^s, \beta)$ gives the scattering amplitude. Finally β is the magnitude of the wave vector for transverse waves, as α is for longitudinal waves.

For $L \rightarrow T$ scattering we obtain

$$S(\vec{\kappa}) = \frac{4\pi \vec{B} \cdot \hat{r}^s}{\beta^2} \left\{ \frac{1}{\frac{\alpha\delta\mu}{\beta\mu} \sin 2\theta - \frac{\delta\rho}{\rho} \sin\theta} \right\} \quad (A.3)$$

Here $\vec{\kappa} = (\alpha \hat{r}_0 = \beta \hat{r}^S)$ and \hat{r}^P is an arbitrary unit vector such as $\hat{\phi}$ in the plane perpendicular to the scattering director.

For $T \rightarrow L$ scattering assuming a right-hand polarized incoming wave, the formula for $S(\vec{\kappa})$ is given by

$$S(\vec{\kappa}) = 4\pi(\vec{A} \cdot \hat{r}^S) e^{-i\varphi} \left\{ \frac{1}{\frac{\delta\rho}{\rho} \sin\theta - \frac{\beta}{\alpha} \frac{\delta\mu}{\gamma+2\mu} \sin 2\theta} \right\} \quad (\text{A.4})$$

Here $\vec{\kappa} = (\beta \hat{r}^0 - \alpha \hat{r}^S)$.

References

1. J.E. Gubernatis, E. Domany and J.A. Krumhansl, J. Appl. Phys., June, 1977 (in press).
2. J.E. Gubernatis, E. Domany, J.A. Krumhansl and M. Huberman, J. Appl. Phys., June 1977 (in press).
3. C.F. Ying and R. Truell, J. Appl. Phys. 27, 1086 (1956).
4. G. Johnson and R. Truell, J. Appl. Phys. 36, 3466 (1965).
5. N. Bleistein and N.N. Bojarski, Report #MS-5-7501 prepared under ONR Contract No. N00014-67-A-0467-0027.
6. V. Varatharajulu and Y.-H. Pao, J. Acoust. Soc. Am. 60, 556, 1976. Numerical results for elliptic cylinders are contained in a preprint by V. Varadan (submitted to J. Acoust. Soc. Am.).
7. R.M. Lewis, IEEE Trans. Antennas and Propagation, AP-17, 308 (1969).
8. W.L. Perry, IEEE Trans. Antennas and Propagation, AP-22, 826 (1974).
9. N. Bleistein, J. Acoust. Soc. Am. 59, 1259 (1976).

* Supported by Rockwell International under Contract No. F33615-74-C-5180 and the Materials Science Center, Cornell University, under MSC Report No. 2846.



PROJECT I, UNIT B, TASK 1

RECOVERY OF SCATTERING INFORMATION IN REAL GEOMETRIES

Laszlo Adler
Department of Physics
The University of Tennessee
Knoxville, Tennessee 3 916

Introduction

During the past six months a number of items of interest have been pursued. These include the improvement of our experimental system, data acquisition and transfer to Adaptronics, an application of Keller's geometrical theory, and an analysis of phase data obtained from spherical cavities. These are discussed below.

Improved Experimental System.

The new system uses a minicomputer with a plotter to collect data from a crystal controlled sampling unit and perform on-line Fast Fourier Transform analysis, obtaining both amplitude and phase spectra from a given scattering center. The system also has the capability for permanent data storage and transfer of the data to other systems (Adaptronics). We have also begun to use a new wide band Panametric transducer. The amplitude transfer function is shown on Fig. 1 obtained by the new system.

Providing L-L and L-S Data to Adaptronics.

In order to provide Adaptronics with test data to determine size and orientation of oblate spheroidal cavities--based on Born approximation--we have precalculated the various polar and azimuthal angles one needs in the laboratory coordinate system which correspond to a complete cone about the defect. For the 200 x 800 oblate spheroidal cavity we have completed the data for four different orientations using incident L waves and recorded both scattered L and S waves. The data are on magnetic tape and were sent to Adaptronics for evaluation.

Application of Keller's Geometrical Theory of Diffraction to L-Waves.

Previously we introduced the use of the acoustical Keller's theory to study L-L scattering from planar defects. By way of getting hold of the

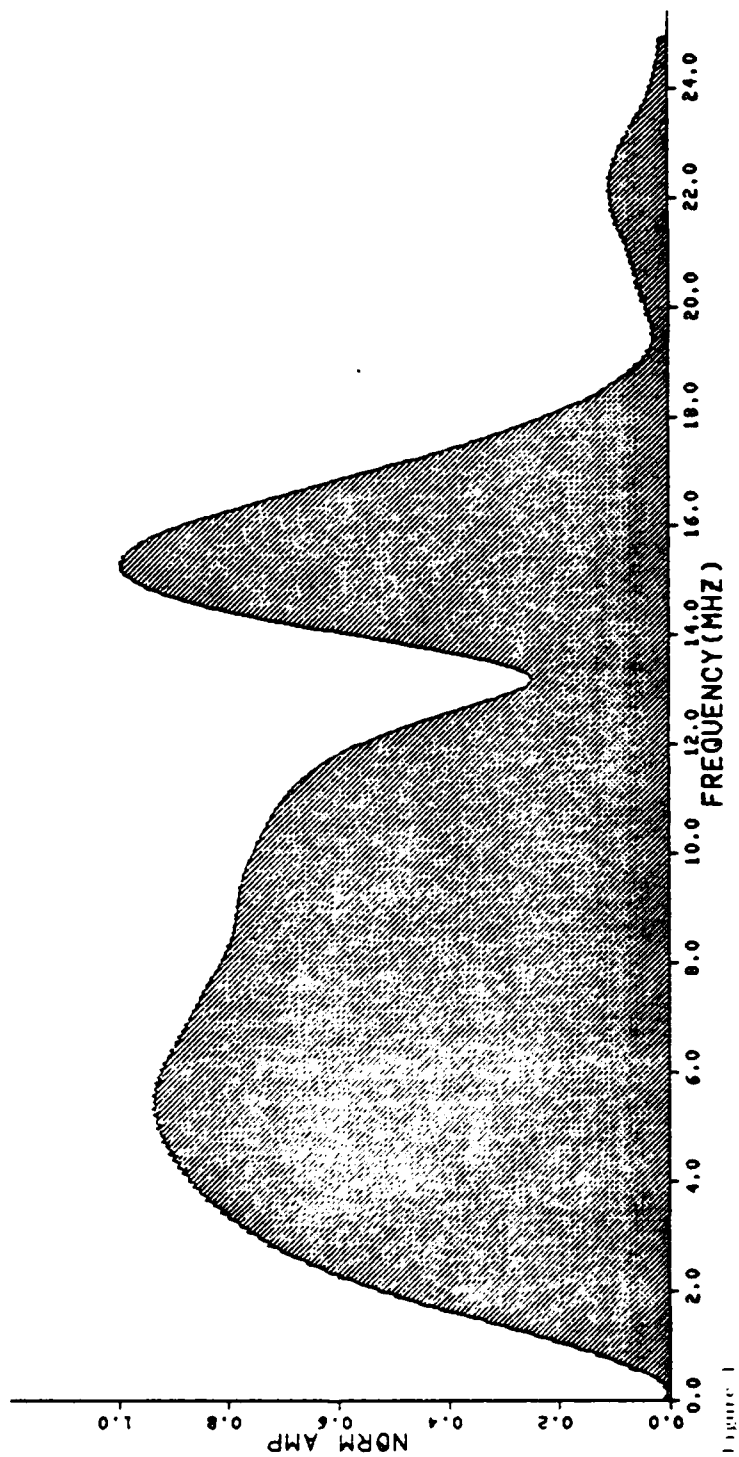


Figure 1



"Seismic Project" we have found Maue's result to the semi-infinite plane for elastic waves. Assuming that an incident L ray will produce cones of diffracted L and diffracted S rays (see Fig. 2), we have derived expressions for the far field diffracted field. For a circular planar flaw in solid the diffracted L field is given by:

$$u_k = \frac{k^2}{\sqrt{k}} \frac{\cos \phi}{(\frac{\sin \phi}{a})^{1/2}} \{ [\cos(k \sin \phi) [P(-k \sin \phi)] + P(k \sin \phi) \sin(k \sin \phi)] - i [P(-k \sin \phi) \sin(k \sin \phi) + P(k \sin \phi) \cos(k \sin \phi)] \} \quad (1)$$

$$u_K = \frac{K^2}{\sqrt{K}} \frac{\cos \phi}{(\frac{\sin \phi}{a})^{1/2}} \{ [Q(K \sin \phi) \sin(K \sin \phi) - Q(-K \sin \phi) \cos(K \sin \phi)] + i [Q(-K \sin \phi) \sin(K \sin \phi) - Q(K \sin \phi) \cos(K \sin \phi)] \} \quad (2)$$

where k and K are the L and S wave numbers, a is the radius of the flaw, ϕ is the diffracted angle, P and Q are known functions. Equation 1 was programmed and compared to the experimental data in Fig. 3.

It should be mentioned that future experimental data will be compared to geometrical theory developed by Achenbach which, in addition to diffracted L and S rays, considers surface rays also.

Phase Analysis from Spherical Cavities.

Because of our new system we are capable of obtaining phase information. The FFT calculates the phase spectra from a given rf waveform scattered from a cavity. In order to gain insight into the phase problem we have adopted a Fortran program (sent to us by Jim Rose from Cornell) which calculates the scattering cross section for spheres based on Ying and Truell's theory to calculate the phase as a function of frequency and angle. Figure 4

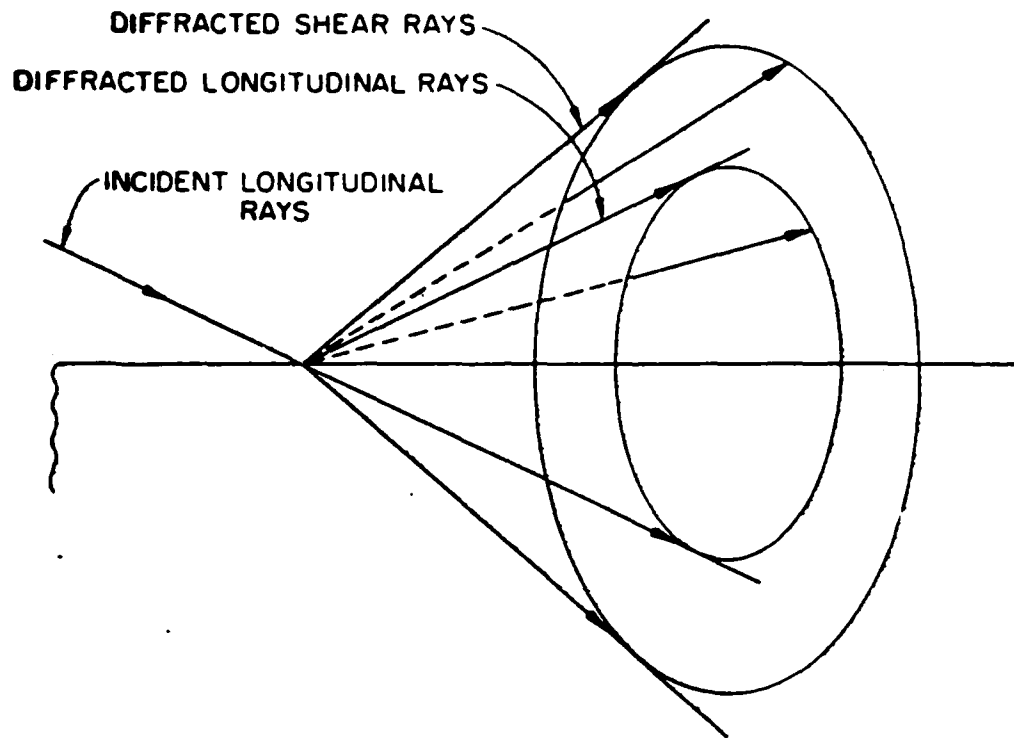


Fig. 2 Schematic diagram for diffracted ray formation at an edge.



SC595.32SA

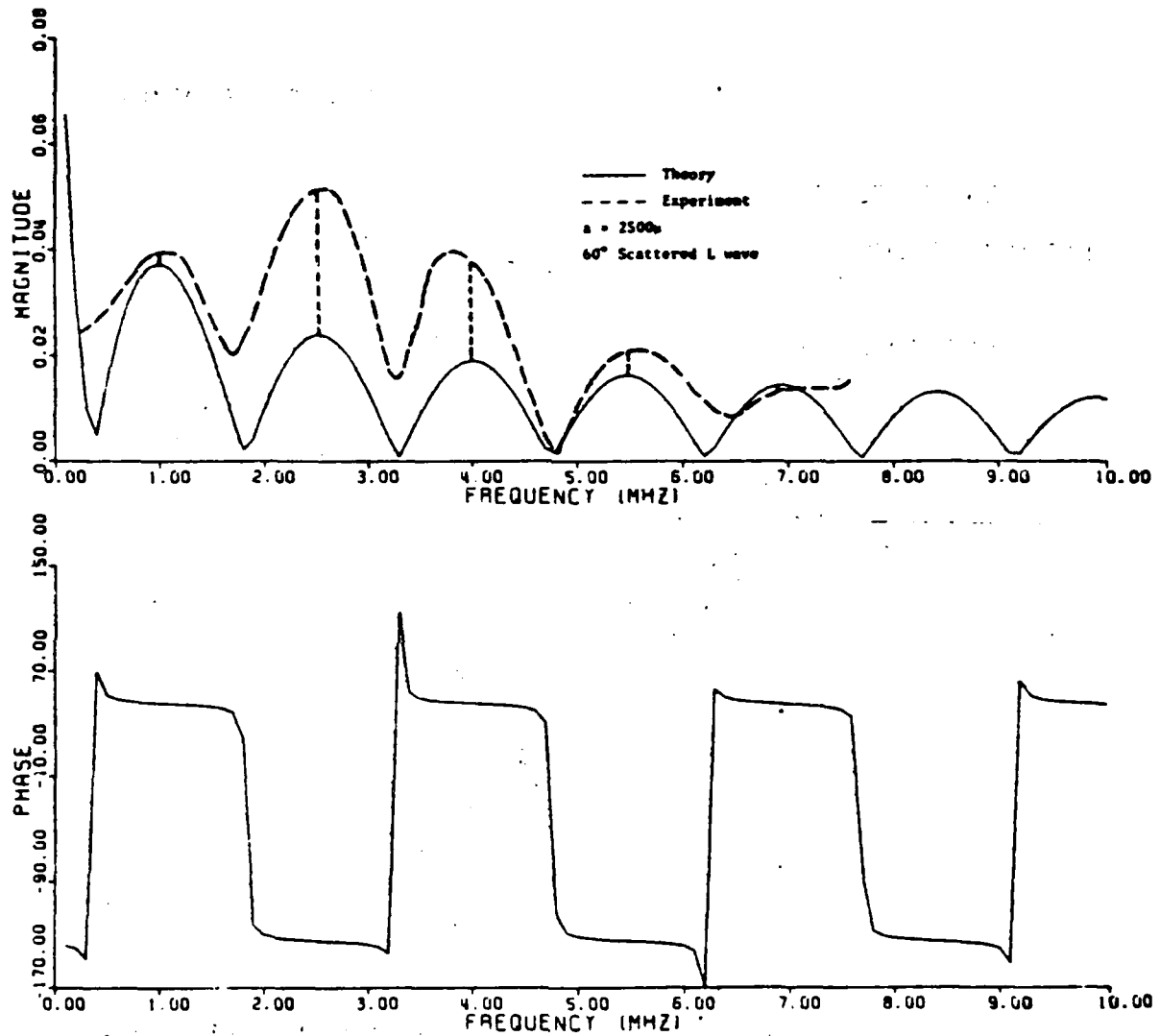


Fig. 3 Plot of the scattered L amplitude and phase spectrum for a 2500μ circular flaw.

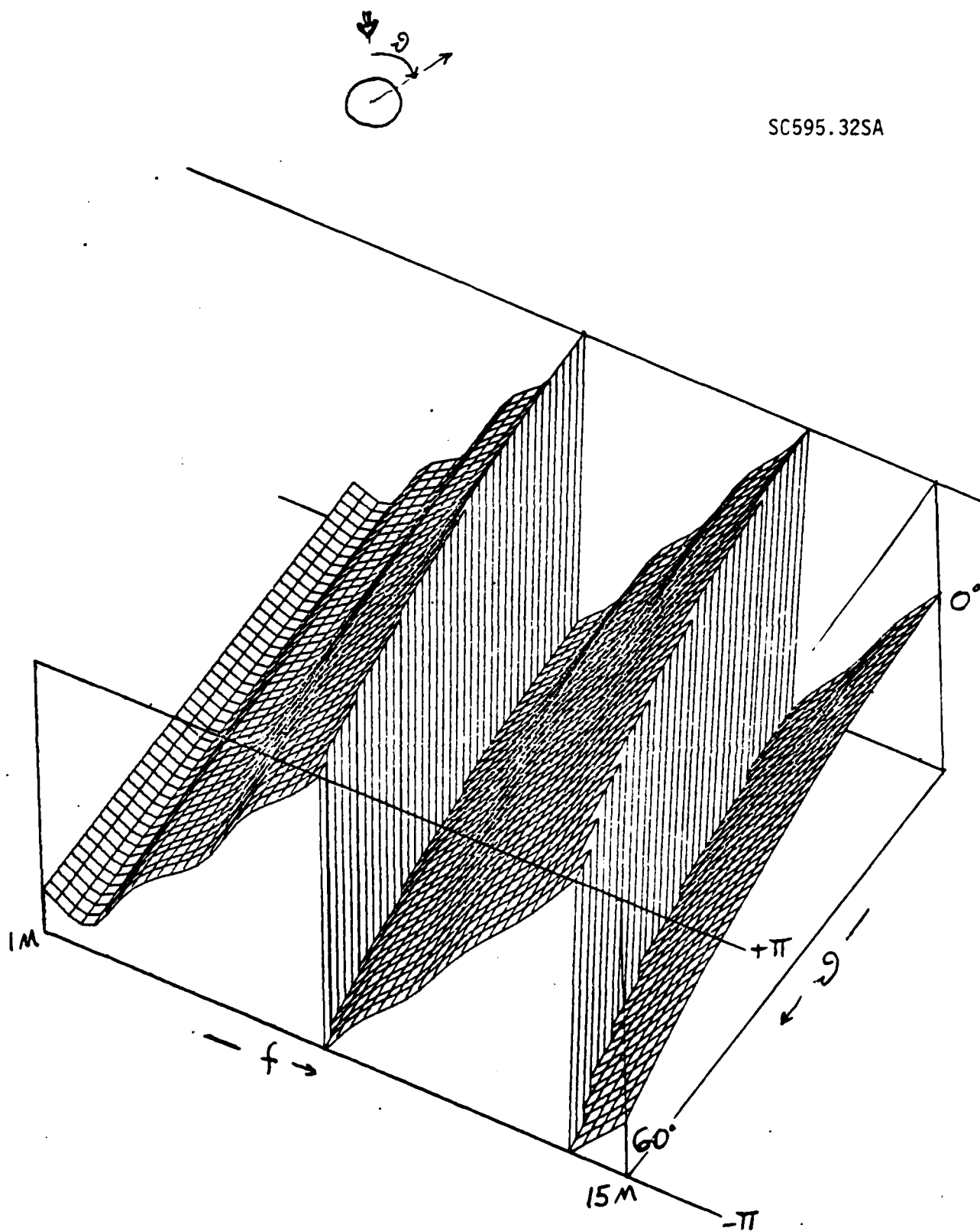


Fig. 4 Phase for 1200μm sphere.



is a 3D plot for a 1200μ diameter spherical cavity. The phase is plotted from $-\pi$ to π . The frequency ranges from 1 MHz to 15 MHz and the scattered angle (backward scattering) from 0 to 60° . Initial experimental data taken from and 800μ diameter spherical cavity along θ^0 (pulse-echo) compares reasonably well with the theory.

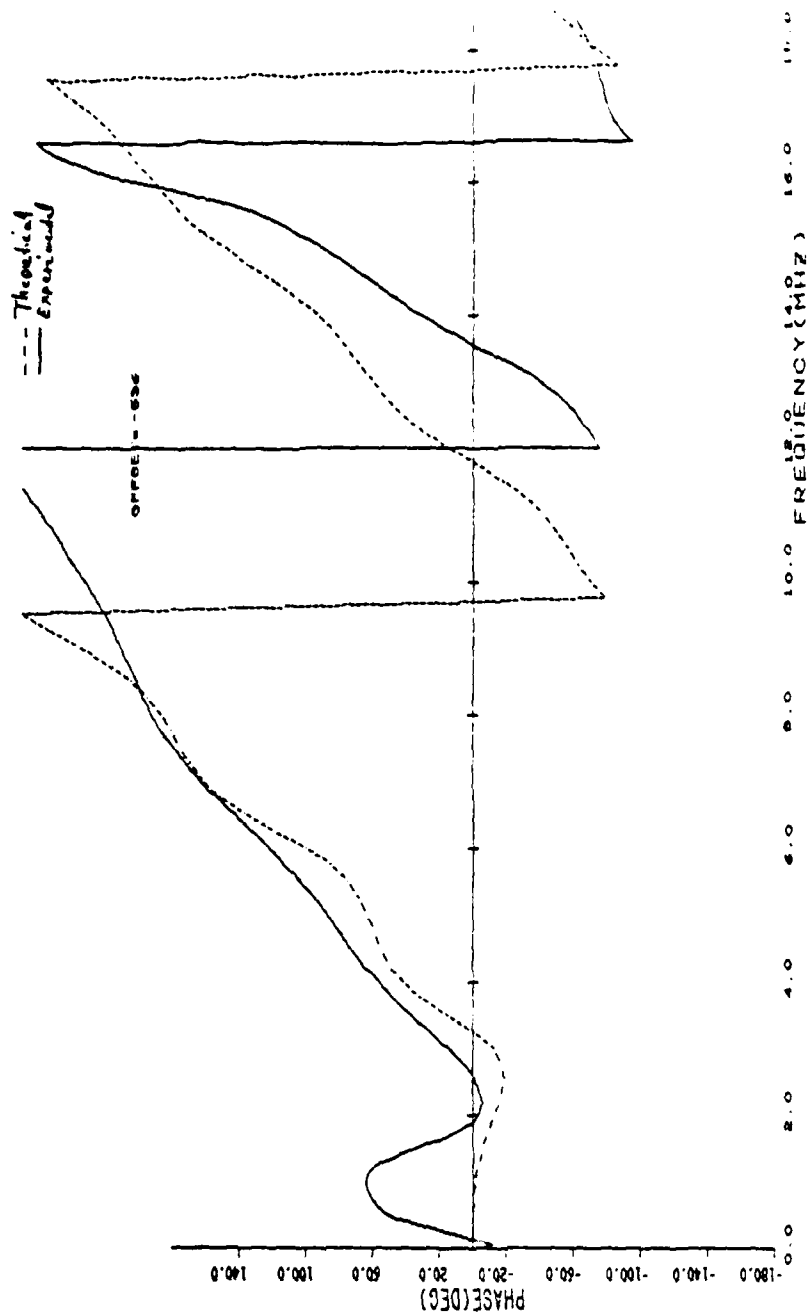


Figure 5



PROJECT I, UNIT B, TASK 2

ULTRASONIC SAMPLES

N.E. Paton
Rockwell International Science Center
Thousand Oaks, California 91360

Introduction

The objective of this task is to provide specific types of internal defects to be used as ultrasonic reference standards. In the program to date, numerous types of internal defects have been produced in titanium alloys with the defects being known geometric shapes such as spheres, prolate and oblate spheroids, disks and so forth.

The production of internal defects in titanium and titanium alloys has been fairly well understood for some time now based on the work of various investigations, and in the program so far, a total of 67 ultrasonic reference standards have been produced, with over half of them being fabricated by a diffusion bonding method described in an earlier report.⁽¹⁾

In the current program it is planned to continue to use these established methods to fabricate some additional defects with somewhat more unusual defect geometries to further test the validity of new developments in ultrasonic characterization. In addition, it is planned to make a small number of ceramic samples containing internal voids, to test the methods that have been proposed for diffusion bonding of ceramic materials based on earlier work at the Science Center on metals.⁽²⁾

Program Plans

Titanium Samples. Spherical samples containing various sizes and shapes of internal voids have been produced previously to characterize scattering from voids. Plans for this year call for producing a series of samples containing a similar range of sizes and shapes of defect, but instead of the defect being a void, samples will contain inclusions having an acoustic impedance both higher and lower than the host material. The material of the inclusion will be either aluminum (for an acoustic impedance less than titanium) or tungsten, (for an acoustic impedance greater than titanium). In

addition to these samples containing inclusions, a few samples will be produced containing crack-like defects. These defects will simulate a crack, acoustically, and will be formed by placing a thin layer of yttria powder over a controlled area of the bond interface before diffusion bonding. Explicit details of the samples to be produced are contained in Table I.

In addition to the spherical samples, some four inch diameter by one inch high ultrasonic samples will be made with defect geometries different from those produced to date. Specifically, there will be 1200 μ m diameter disk-shaped (penny-shaped) defects, with the defect plane lying at an angle of 30 $^{\circ}$, 60 $^{\circ}$ and 20 $^{\circ}$ to the plane of the diffusion bond. One such defect would have an elliptical rather than circular shaped cavity.

Scattering from essentially one-dimensional defects is also of interest, and consequently several samples will be produced having a linear defect in the bond plane. A typical cross section of the defect would be 1200 μ m x 100 μ m or a 600 μ m radius semicircle with the defect being ~3 inches long.

Ceramic Samples

Initial studies of the elevated temperature plasticity of silicon nitride at 1500-2000 $^{\circ}$ C indicates that this material might be diffusion bonded in this temperature range. Consequently, it is planned to test diffusion bonding as a means to make ceramic samples containing voids of controlled size and shape.

Present methods employ powder hot pressing of ceramics to produce ceramic samples containing inclusions, and it is contemplated that diffusion bonding would enable ultrasonic reference standards of ceramics to be produced with internal voids of controlled size, shape and location.

References

1. N. Paton, "Sample Preparation," Interdisciplinary Program for Quantitative Flaw Definition, Contract No. F33615-74-C-5180, covering period July 1, 1975 - June 30, 1975, D.O. Thompson, Program Manager.
2. G. Garmong, N.E. Paton and A.S. Argon, "Attainment of Full Interfacial Contact During Diffusion Bonding," Met. Trans. 6A, 1269 (1975).

TABLE I

External Sample Geometry		Defect Geometry	Type
Sphere	2.125 inch diameter	Sphere	Aluminum
Sphere	2.125 inch diameter	Oblate Spheroid	Aluminum
Sphere	2.125 inch diameter	Prolate Spheroid	Aluminum
Sphere	2.125 inch diameter	Sphere	Tungsten
Sphere	2.125 inch diameter	Oblate Spheroid	Tungsten
Sphere	2.125 inch diameter	Prolate Spheroid	Tungsten
Sphere	2.125 inch diameter	Simulated Crack	Yttria
<hr/>			
Disk	4 inch diameter	Penny-shaped ⁽¹⁾ 0 angle	Void
Disk	4 inch diameter	Penny-shaped ⁽¹⁾ 30 angle	Void
Disk	4 inch diameter	Penny-shaped ⁽¹⁾ 60 angle	Void
Disk	4 inch diameter	Penny-shaped ⁽¹⁾ 90 angle	Void
Disk	4 inch diameter	Elliptical-shaped 60 angle	Void
Disk	4 inch diameter	Linear Defect ⁽¹⁾	Void
Disk	4 inch diameter	Linear Defect ⁽²⁾	

(1) Rectangular cross-section 1200 μ m x 100 μ m

(2) Semicircular cross-section 600 μ m radius

PROJECT I, UNIT B, TASK 3

SIGNAL-PROCESSING RESEARCH IN CONNECTION WITH
ULTRASONICS IN NONDESTRUCTIVE TESTING

Richard M. White
University of California, Berkeley
Berkeley, California 94720

Introduction

During the report period work has continued on both a CCD-based burst processor and an integrated ultrasonic transducer having application to NDE both as a receiving transducer and as a SAW signal processor. Tests have been made of the transducer using four different modes of excitation, showing the device functions well in all four. Analysis and experiment have shown that the use of the zinc oxide transducing element with a dual-gate field-effect transistor provides a highly linear dependence of transistor gain upon gate control voltage, thus making the unit attractive for use as an element in a SAW transversal filter signal processor.

CCD and Integrated Transducer

Past reports have included mention of work on a charge-coupled device (CCD) inverse filter for use in processing ultrasonic nondestructive testing waveforms. This work proceeded to the point of a demonstration of a burst processor system employing a commercial CCD video delay line (Fairchild 321CCD with its associated driving module) to capture a receiving waveform from a commercial (Panametrics) NDT transducer. The waveform was captured (sampled and stored) using a fast clock, and then read out at a slow rate into an inverse filter based on a commercial CCD shift register having its tapping electrodes available externally (Reticon TAD-32). Limitations resulting from the operating constraints of the commercial CCDs were identified. Some of the problems experienced were found to be related to the internal designs of the CCDs used -- "corner-turning" spikes and effects of a current sensing capacitor were evident. Other limitations in speed of the systems built here were related to the speed of components used other than the CCDs. The CCDs are being redesigned by their manufacturers, and we are changing some



components in our circuits, in preparation for additional tests of their performance.

The work on the integrated transducer has proceeded during the report period both in terms of experimental work and analysis of the devices. This work will be summarized in some detail here.

Integrated Ultrasonic Transducer

The device consists of one or more thin films of a piezoelectric (zinc oxide) deposited by RF sputtering upon a wafer of silicon in which field-effect transistors (FETs) have been fabricated. The structure is primarily a receiving transducer which is capable of a number of different modes of excitation. If it is used with a dual-gate FET then the signal from the piezoelectric can be applied to one gate while a control voltage is applied to the other gate. One use for the control voltage is gain control of the FET amplifier. In order to provide a wide range of amplification signal frequencies, a double-diffused metal-oxide-semiconductor (D-MOS) transistor has been used.

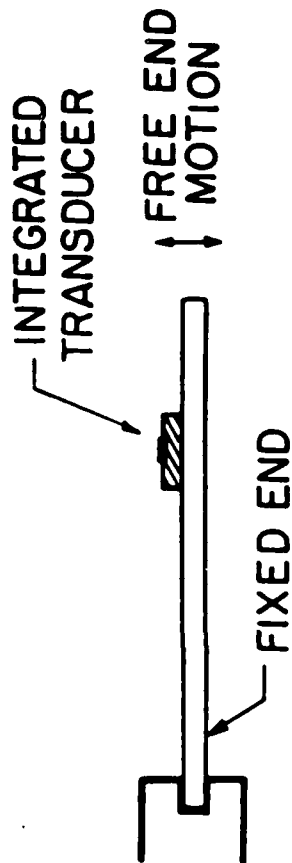
Four different modes of excitation of the integrated transducer are shown in Fig. 1. In each part of the figure, the cross-hatched rectangle represents a silicon wafer, while the solid rectangles represent the piezoelectric films with their electrodes. The modes are as follows:

A. Flexural Mode. If one end of the wafer is clamped in support, deflection of the free end flexes the film producing a piezoelectrically induced voltage which alters the drain current in the transistor. Such flexural response extends to very low frequencies. Measurements at 600 Mz yielded an effective gauge factor (defined as fractional change in source-drain current per unit strain) of 160,000 which is much larger than the gauge factors of most other low-frequency strain sensors. Similar gauge factors were observed in these devices at frequencies well below 1 Hz.

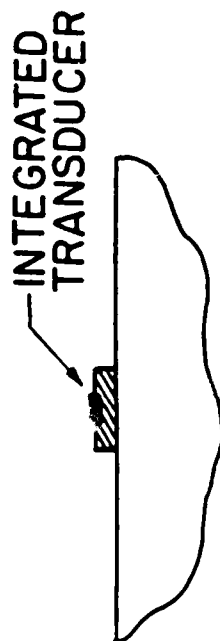
B. Thickness Mode. The transducer may be enclosed in a housing which provides mechanical protection and electrical shielding for use in a conventional immersion system or as a contact transducer on the surface of a solid. In this application, the transducer could be used to detect bulk waves resulting from acoustic emission or scattering from defects in a

MODES OF EXCITATION

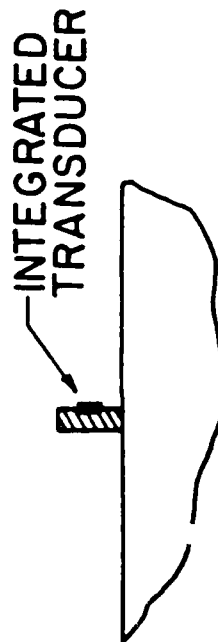
A. FLEXURAL MODE



B. THICKNESS MODE



C. END EXCITATION



D. SURFACE WAVE EXCITATION

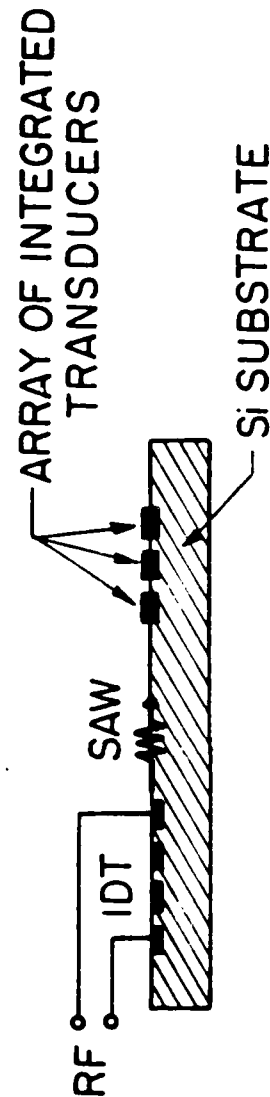


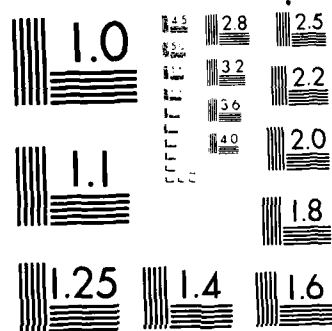
Fig. 1 Four modes of excitation of the transducer, all of which have been observed experimentally at frequencies ranging from less than one Hz for flexural mode to about 90MHz in SAW mode.

INTERDISCIPLINARY PROGRAM FOR QUANTITATIVE FLAW
DEFINITION(U) ROCKWELL INTERNATIONAL THOUSAND OAKS CA
SCIENCE CENTER 1978 SC595.325A F33615-74-C-5180

NL

F/G 14/2

[illegible]



MICROCOPY RESOLUTION TEST CHART
NATIONAL BUREAU OF STANDARDS-1963-A



nondestructive testing system. The silicon wafer can serve as the wear plate for the transducer, or the wafer can be bonded onto a protective metal plate which is coupled to the system being examined.

C. End Excitation. Here the piezoelectric film is driven by a source located at one end of the silicon wafer so that waves propagate along the wafer, past the film, and on toward the other end where they may be absorbed with attenuating material.

The computed response to a compressional bulk wave can be expressed as a conversion efficiency, defined as power delivered to the electrical load divided by power in the acoustic wave. The conversion efficiency in decibels can be positive, owing to the presence of the active transistor. The conversion efficiency is proportional to

$$\frac{\sin^2(k_B L/2)}{(k_B L/2)^2} ,$$

where $k_B L = \omega L/v_B$, with ω = angular frequency, L = film dimension in direction of propagation, and v_B = phase velocity of bulk wave.

D. Surface Wave Excitation. Figure 2 shows the computed conversion efficiency vs. frequency for a transducer employing a D-MOS transistor and a single electroded zinc oxide film either 10 or 20 microns long. These are results of a simplified analysis based upon the use of only a single decaying exponential surface-wave component. As expected, the response vanishes where the film length is an integral number of wavelengths ($k_S L/2 = n\pi$, $n = 0, 1, 2, \dots$). Significant conversion gain results at some frequencies for the device parameters assumed in this calculation.

Applications

This transducer can be applied to NDE (or possible acoustic emission) applications as a receiving transducer having its own impedance transforming amplifier built in and situated close to the transducing piezoelectric film so as to reduce the magnitude of the parasitic circuit elements such as cabling and the like. The active transducing area (area of piezoelectric) can be shaped and dimensioned to provide control of its

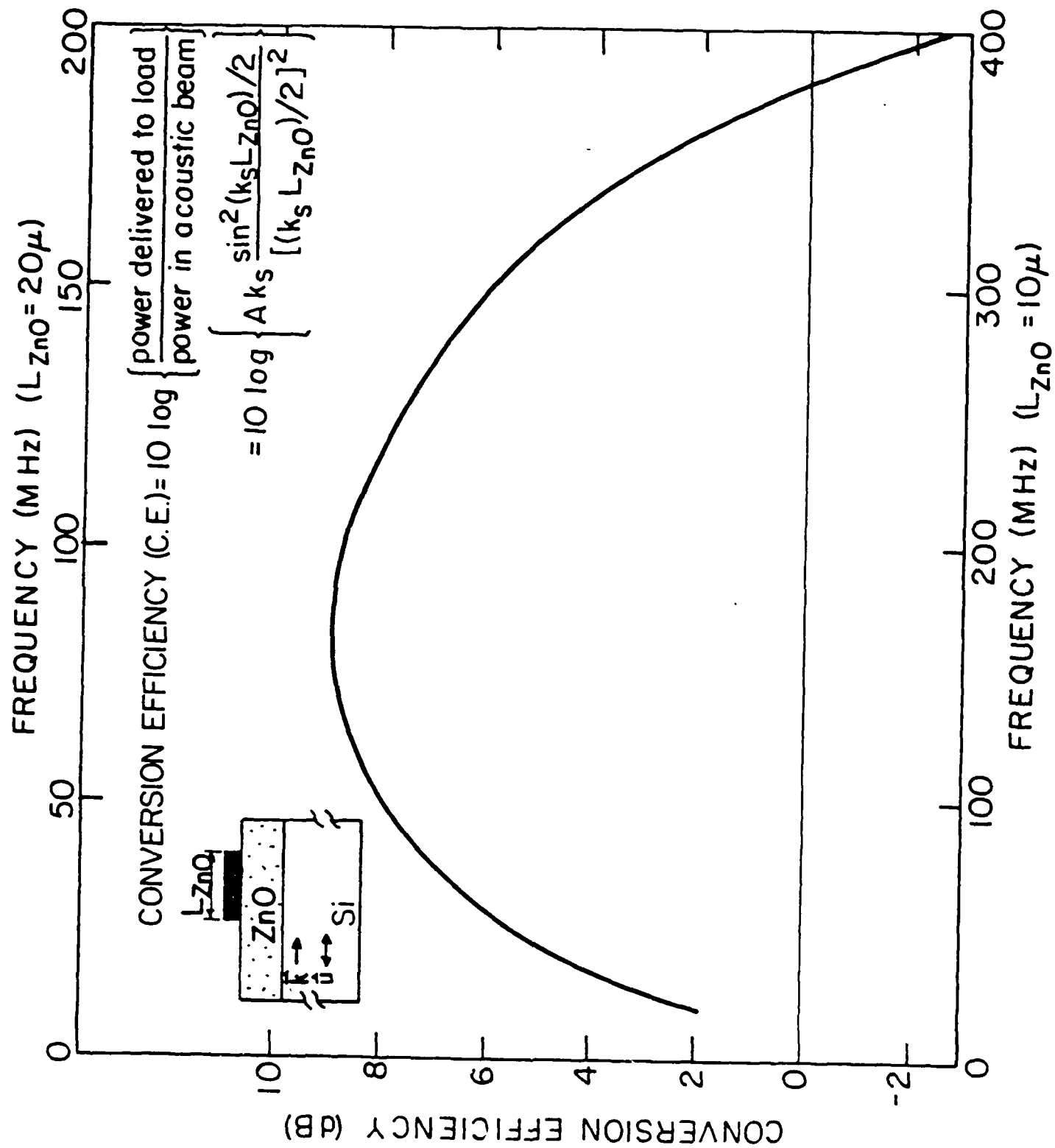


Fig. 2 Computed conversion efficiency for SAW excitation.



acoustic directivity; the area is defined by photolithography and so can be precisely controlled. For example, transducing regions which are relatively nondirective in one direction and highly directive in the other can easily be made. The electronic control of the transducer provided by the accessibility of the second FET gate is another advantage to be explored in future work.

Finally, connecting the transducers into arrays for purposes of signal processing is possible. In particular we have found that, when pairs of D-MOS transistors are connected in a differencing circuit as illustrated schematically in Fig. 3, a very linear dependence of gain for the signal input upon control gate voltage V_{G1} results as shown in Fig. 4. This result -- initially surprising because of the quite nonlinear dependence of gain upon the control gate voltage -- has been explained recently by an analysis (carried out here by Kent Chuang).

Staff Supported During this Period:

C.-T. K. Chung, M. S. Candidate

Professor R. M. White

Publications

"Integrated Ultrasonic Transducer," S. H. Kwan, R. M. White and R. S. Muller, presented at the Ultrasonics Symposium, Nov. 1977.

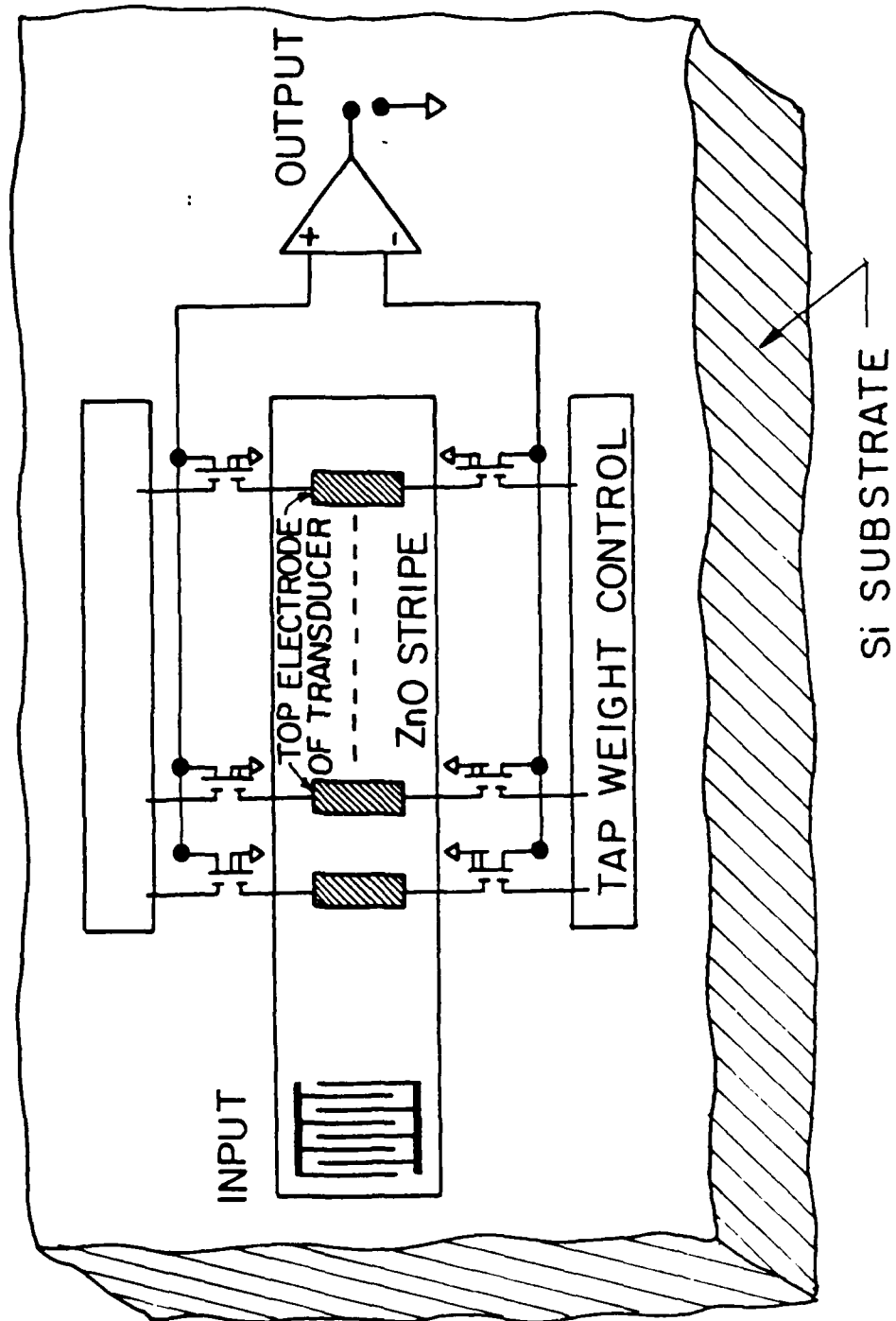


Fig. 3 Schematic arrangement of SAW transversal filter signal processor employing array of integrated transducers with dual-gate transistors and differential output.

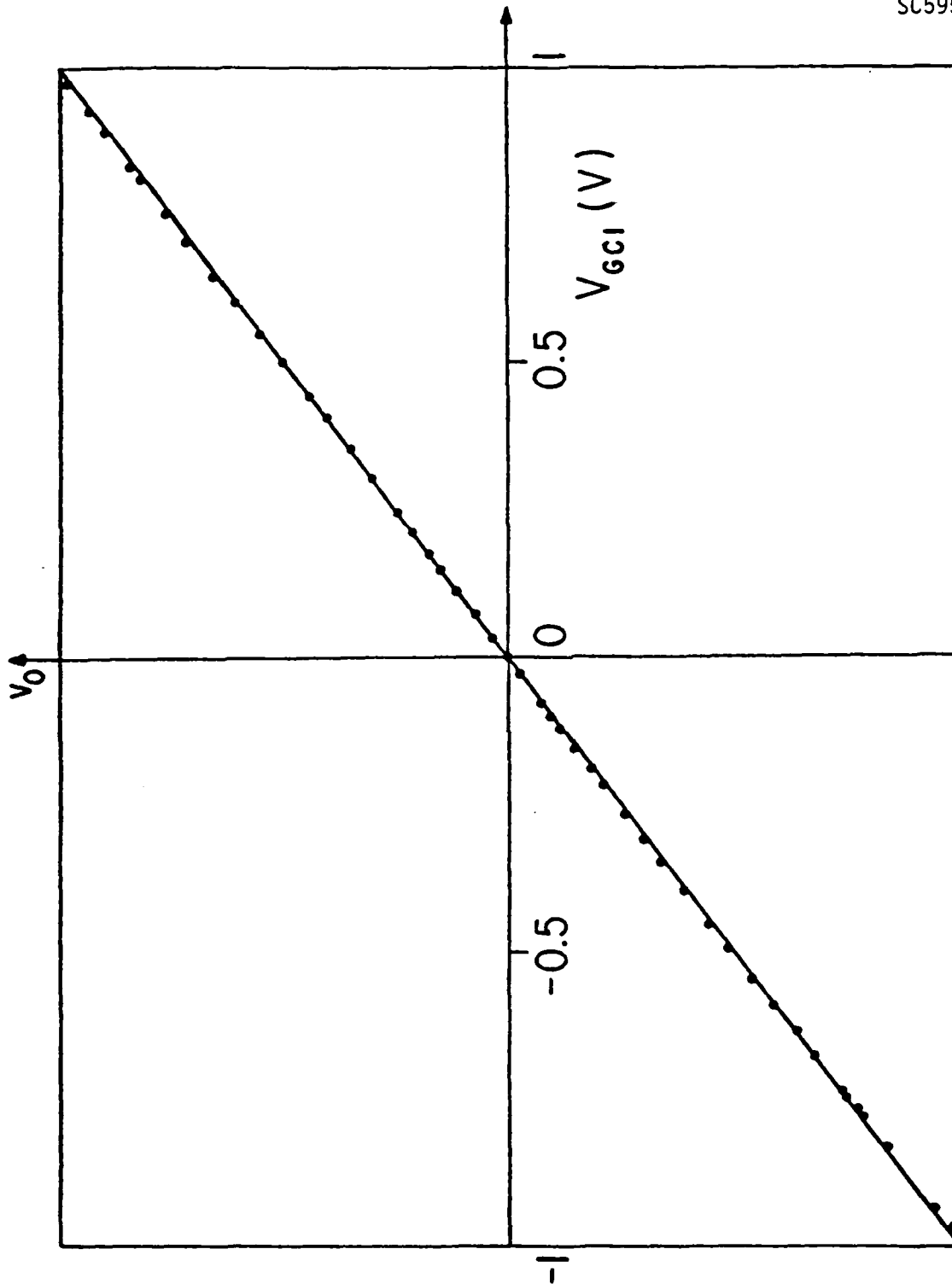


Fig. 4 Plot of amplification factor versus control gate voltage V_{GCl} .

PROJECT I, UNIT C, TASK 1

NEW TECHNIQUES FOR ACOUSTIC NONDESTRUCTIVE TESTING

G.S. Kino,
Edward L. Ginzton Laboratory
W.W. Hansen Laboratories of Physics
Stanford University
Stanford, California

Introduction

After three years of operating prototype versions of our present electronically focused and scanned acoustic imaging system in NDT applications, we have gained considerable insight into its advantages and disadvantages. Our present system operates by actively generating a chirp waveform, which is used with a SAW tapped delay line and a transducer array, to focus and scan transmitted and received acoustic waves in a B-scan reflection mode imaging system. As our primary application is NDT, experiments have been performed imaging targets in a water bath and defects located in metal samples.

The relative merits of this system are briefly reviewed in the context of other significant acoustic imaging systems reported in the literature. This is followed by an explanation of the principles and design of a new improved system which is currently under construction in our laboratory.

Current Systems

The advantages of our present system are the basic ones to be expected: high speed, a large field of view in the direction normal to the array; and good definition parallel and normal to the array. The disadvantages are: complexity, a relatively limited field of view in the direction parallel to the array, because of the limited number of array elements used in our research system, higher side lobe levels than we would like (at least in the high speed mode), small aperture, which restricts the range of viewing angles and results in poor images of specular reflectors, and operation at a lower frequency (2.5 MHz) than optimum.

Another system employed by Thurston¹ used lumped delay lines on each element of the receiver array. Time delay through the delay lines can be



switched by means of a minicomputer to compensate for the time differences between the different rays reflected from a given point in space. The lumped delay lines are switched in steps so as to give a continuous focused scan along a radial line. The receiver focusing is changed dynamically as the transmitter pulse travels out from the array. The problem with this technique is excessive complexity, the large space taken up by the lumped delay lines and the high minicomputer operating speed required to provide dynamic focusing. This has limited the number of elements used in the receive-mode to 16.

A further system which is presently being worked on in the Integrated Circuit Laboratory at Stanford employs analog CCD delay lines in place of the lumped delay lines to implement the dynamic focus control.² The problem with the systems that have been suggested so far is, that if one wants to increase the field of view or the aperture of the system, a large number of elements is required. In this case, the electronic component requirement becomes extremely costly, making the lumped circuit devices impractical for a large number of elements. The CCD devices tend to run into problems with digital noise and need complicated control circuits. They also have had difficulties increasing the working frequency above that presently employed (1.8 MHz) although improvements are expected in this respect.

New System

We have been experimenting with the components of a new real-time synthetic aperture imaging system which we believe will eliminate many of the deficiencies encountered in the previously mentioned systems. The system we intend to build is functionally equivalent to a tomographic imaging system with filtered back-projection, operating in real-time. The basic principles of a very closely related system have already been demonstrated by Johnson, et al.,³ using relatively slow computer reconstruction techniques. In this system, we transmit from one element at a time, and receive the return signal on the same element. The received signal passes through an analog multiplexer, an amplifier, and an A to D converter before storage in the signal memory. This operation is repeated for successive array elements with the analog multiplexer selecting the desired element, and the appropriate memory location. Once we have stored the signals from a sufficient number of

elements, typically 32, we can reconstruct an entire two-dimensional image by adding the information from the appropriate locations in the signal memory, corresponding to equal time delays to the point of interest, in order to reconstruct this given point in the image plane.

There are a number of important factors relating to the design of a practical imaging system using the approach described here which must be considered. When a signal is transmitted and received by only one element at a time, very efficient transducers are required in order to obtain adequate signal-to-noise ratio (SNR). We have designed and constructed a high efficiency array utilizing $\lambda/4$ matching layers which we believe will be adequate for our application. Another possible approach to obtaining a good SNR is to transmit a coded pulse train or FM chirp and employ a matched filter or an inverse filter in the receiver. This technique could improve the SNR by 20 dB without great difficulty. We have tested both acoustic surface wave matched filters and a microprocessor controlled CCD inverse filter for this purpose. We also have intentions of using acoustic surface wave storage correlators for such an inverse filter. The advantages of using an inverse filter rather than a matched filter are the possibility of optimizing the resolution in all directions and the side lobe level. Because the system is linear, a filter such as this could be placed at front-end of the system, ahead of the A to D converter, or at the system output, after the signals from the individual memory locations have been added together and converted back to an analog signal.

One important advantage of the synthetic aperture approach is that it requires only a single front-end amplifier, regardless of how many elements of the transducer array are to be used. This means that a great deal of effort can be put into the design of the front-end amplifier with little regard for its complexity, number of adjustments, expense, etc., all of which are important considerations in a system where an amplifier is required for each element of the array.

In the system employed by Thurston,¹ the received signals are compressed before being added. This gives the equivalent of lower side lobe levels. Because our synthetic aperture system requires only a single front-end amplifier, it would be ideally suited to the implementation of such a compression technique, since we would not need to worry about matching the



characteristics of a large number of compression circuits, and other complications. As an example of the type of improvement obtainable using a compression technique, consider the case where we take the square root of the amplitude of the signal, but leave the sign or phase of the signal unchanged. We take the signal received by a single element from a reflector at the focus to be of amplitude a , and that from an interfering point away from the focus to be of amplitude, b . The side lobe level is given by $S = b/Na$, where N is the number of transducer elements. Now, suppose we use the square root compression technique. In this case, the side lobe level after the compressed signals have been added is $S = (b/a)^{1/2}/N$. If the signal is then expanded by squaring to restore the original linear relation between input and output, the new side lobe level would be $S = b/N^2a$.

Thus, in our initial experiments we are intending to work with an 8-element system with and without compression to determine whether we can obtain this radical improvement in side lobe level. On the basis of the theory given here, it should be possible to improve the dynamic range of the system by using the compression techniques ahead of the A to D converter. However, these improvements would be obtained at the expense of a degraded SNR.

To implement this synthetic aperture imaging system we must be able to store a complete set of signals, one from each transducer element. In order to do this, we propose to use an ultra-high speed A to D converter and random access memories. To provide adequate sampling of amplitude and phase we must operate the A to D converter at a sampling rate greater than twice the upper cutoff frequency of the transducer elements. Thus, if the upper cutoff frequency of the transducer elements is 5 MHz, the system clock rate must be greater than 10 MHz. The A to D converter and digital memories we intend to use are capable of operating at clock frequencies up to 20 MHz.

The optimum reconstruction of a two-dimensional image from the set of signals stored in the digital memories is a formidable computational task. Since we desire to obtain a real-time image, we must find a simplified algorithm to perform this reconstruction. The method we have chosen to implement is back-projection. The back-projection method of reconstruction requires that a set of geometric calculations be performed to control the addressing of signal memories; however, once the required addressing information has been computed, it can be stored in table form in a high speed

memory which we refer to as the focus memory. In a typical 32-element system, the focus memory will be about 1/4 the size of the signal memory. However, the focus memory can be implemented using a PROM (Programmable Read Only Memory) which is much denser than the RAM (Random Access Memory) which we intend to use in our experimental systems. With this technique we can generate scan lines perpendicular to the array, perform a radial sector scan, or any other desired scan format. We can also vary the spacing between scan lines either by reprogramming the focus memory from the microprocessor or by interpolation techniques.

Another important advantage of the synthetic aperture approach over the previously mentioned imaging systems is that the transverse resolution is twice as good as that of an equivalent imaging system in which a parallel beam is transmitted and the system is focused on receive. This is due to the fact that the time and phase difference to a point, R , from a transducer element is doubled, because the signal travels to the image point and back. Thus, our system is equivalent to a conventional imaging system operating at twice the frequency. The range resolution is the same using either the synthetic aperture technique or any of the other techniques previously described. The system therefore provides the same improvement in transverse resolution capability which has already been demonstrated in scanned holographic imaging.⁴ But, in addition, as we are using time delay rather than phase delay techniques to reconstruct the image, we should also obtain excellent range resolution.

We have used analytic methods to predict the side lobe levels of an N element imaging system, and we have performed a computer simulation to verify these results. Ideally, one would prefer a short pulse approximately one RF cycle long which can be obtained by the use of a previously designed transducer array. Alternatively, the appropriate inverse filter can be used if the transducer array does not perform adequately. In this case, the near-in side lobes are much like those of any conventional imaging system, but the far-out side lobes are down from the main lobe by a factor of $1/N$. With such short pulses, the grating lobes do not exist. On this basis, we predict that for a 32-element system, without compression, the side lobe level would be on the order of -30 dB, with the possibility of some slightly higher side lobes close to the main lobe.



Prototype System

A. The Imaging System

In our initial experiments, we intend to work with an 8-element system, to test the basic principles of operation, and to gain experience with the hardware design. This initial system will also enable us to verify the side lobe levels and to test the advantages and drawbacks of gain compression. This system will have a field of view, using shear waves in metal, which is 5 cm wide and 14 cm deep, beginning about 2 cm from the array, however, this can be varied under software control by changing the information in the focus memory. The display will consist of 96 lines, with about 150 points on each line. This initial system will be designed to operate with transducer arrays having upper cutoff frequencies up to 5 MHz.

At the present time we are nearing completion of the digital portion of the imaging system and we have tested a number of receiver and transmitter circuits as well as an analog multiplexer which we believe might be adapted to suit this application. We have also developed a high efficiency transducer array with good impulse response. We do not foresee any major difficulty in using these components to build a new, electronically scanned and focused ultrasonic imaging system with reasonably low side lobe levels and an operating frequency up to 5 MHz. Furthermore, this initial system will enable us to investigate possible directions for future developments.

One problem with most electronically scanned acoustic imaging systems is that the display line and frame times are not usually compatible with a TV monitor. This is a disadvantage because the grey scale image quality of the magnetically deflected cathode tubes in TV systems is far better than is available with the alternative electrostatic deflection tubes typically used in oscilloscopes.

Our present design should, in fact, be compatible with the line time of a TV display but the number of lines employed, ~100, is far less than in a TV display (525). So the image will not look continuous. One technique to eliminate this difficulty is to use only part of the screen. Another is to use interpolation routines for filling in. But in all cases, a more arbitrary choice of line and frame rates would be helpful, as would some facility for storing the picture for times comparable to one frame. This is discussed further in the section on Future Development.

The most obvious method to fill this need is to use a scan converter. In analog form this device consists of a semiconductor mosaic irradiated by a scanning electron beam, as in a TV display. Readout is by a second beam at an arbitrary rate compatible with a TV display. Digital scan converters are also beginning to come on the market.

In order to obtain some feel for the capabilities of such scan converters, we have been experimenting with a commercial PEP analog device, using our present electronically scanned and gated system, described in the last progress report. A display which is much more convenient to use is obtained with the scan converter. Furthermore, far more detail on the nature of any problems in the display is easy to observe. For instance, we found and eliminated ripple in the line scan, a problem which had not been apparent to us before.

We have also experimented with a digital scan converter, using a Unirad system donated to us. This system is similar to our own imaging device. Again the digital format provided a vastly better display capability, but is more limited in its flexibility.

B. The Inverse Filter

The principles of our microprocessor-controlled tapped delay line CTD (charge transfer device) inverse filter were described in the last progress report. Further progress was made during the summer with this device which was controlled by a minicomputer available in our own laboratory.

In order to test the device, an LC resonator was constructed to simulate the response of a distorting medium. The sequence of photographs in Fig. 1 shows the inverse filter output with the CTD being clocked at a 50 kHz sampling rate. The processor operates by initiating the test pulse to the distorting medium, Fig. 2(a), and clocking it into the CTD. The sign of the filter output during the 32 appropriate clock periods is then loaded, as two 16-bit words, into the computer. The updated tap weights are subsequently computed and loaded, as thirty-two 8-bit words, into the storage latches associated with the digital-to-analog converters. This sequence of steps is performed repeatedly and the filter output is shown with the tap weights at some arbitrary initial value, Fig. 1(b), and after 50, 100, 150, and 300 iterations, Fig. 1(c)-(f). The complete sequence of 300 iterations takes

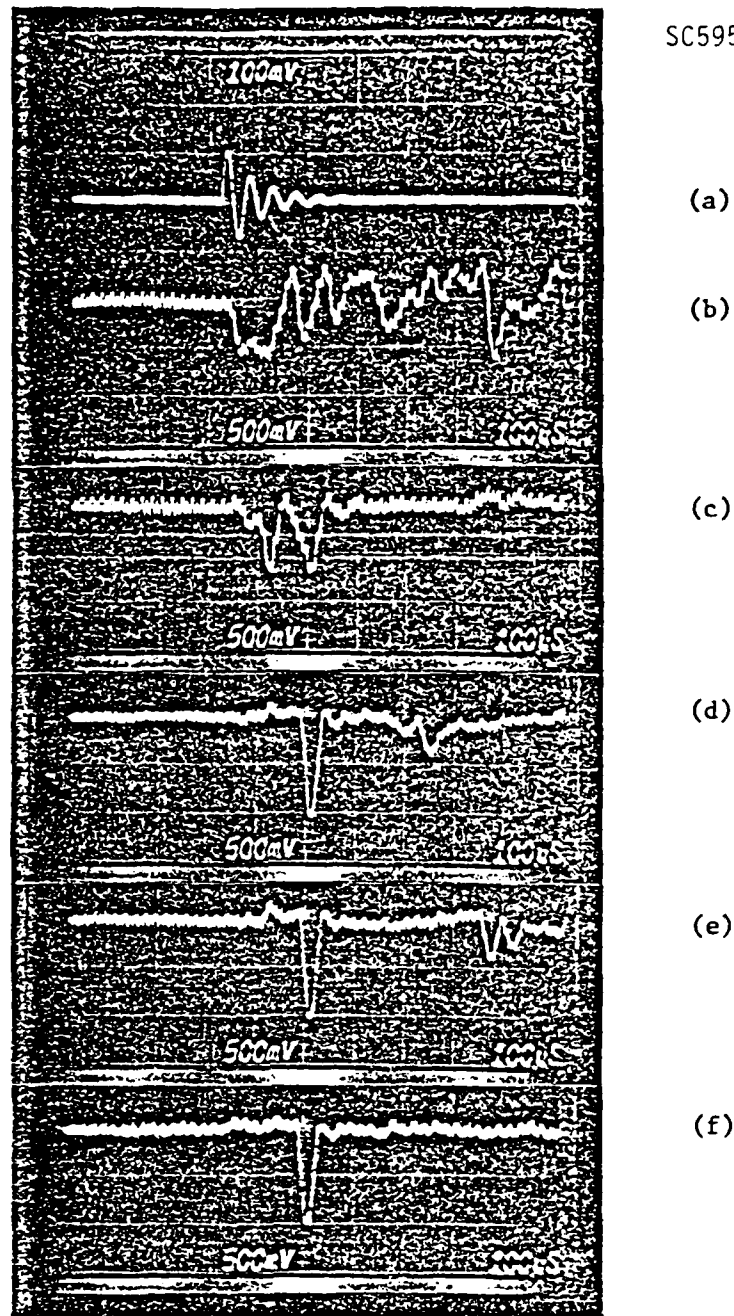
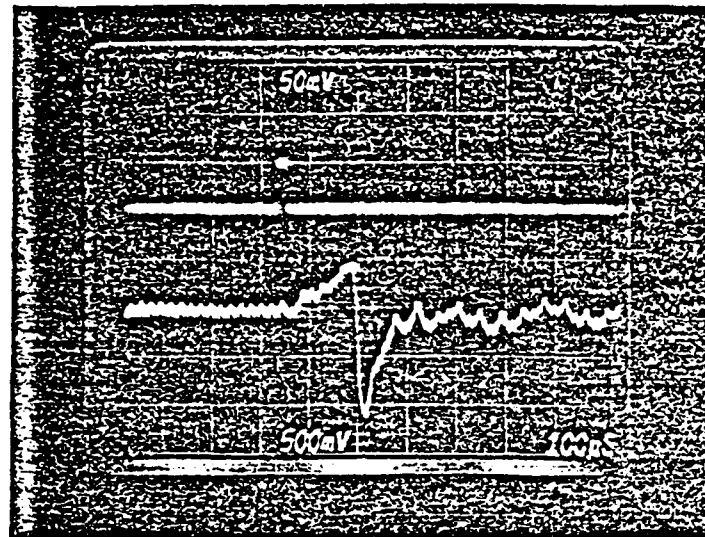


FIG. 1--Convergence of the filter:

- | | |
|---------------------------------|---------------------|
| (a) Reference input; | (d) 100 iterations; |
| (b) Initial filter output; | (e) 150 iterations; |
| (c) Output after 50 iterations; | (f) 300 iterations. |



(a)

(b)

FIG. 2—Inverse filter impulse response.

- (a) Input pulse;
- (b) Filter output.



approximately 3 seconds to complete, and after the filter has converged, Fig. 1(f), we can send a pulse into the CTD input in order to examine the impulse response, Fig. 2.

In order to demonstrate the ability of the inverse filter to deconvolve partially overlapping distorted pulses, a series of closely spaced pulses were sent through the LC resonator and then through the inverse filter. In each of the individual photographs of Fig. 3, the top trace shows how the distorted pulses overlap one another, while the bottom trace shows the filter output, with the separate pulses clearly discriminated.

Our demonstration processor is limited to operating at sample rates below 300 kHz and it suffers from a dynamic range limitation, both of these problems being related to the tap weighting circuitry. The use of improved tap weighting circuitry, employing transconductance multipliers or multiplying digital-to-analog converters, should provide a dynamic range better than 40 dB and allow the CTD to operate close to its maximum clock rate of several MHz. Alternatively, by using the acoustic surface wave storage correlation being developed in our own laboratory on another program as the appropriate delay line, we plan to make a device with the bandwidth required in our acoustic imaging applications as well as with a dynamic range of at least 40 dB. At the present time we have demonstrated feasibility, but we do not yet have a real time inverse filter of the quality required for imaging applications.

Future Developments

Some of the possible directions which we believe this new approach will allow us to pursue include three-dimensional imaging, ultra-high frequency operation, very long array scanning, and improved B-scan imaging of the type used in medical systems.

The implications of the hoped for reduction in side lobe levels by using gain compression are of major importance. For instance, if compression is as effective as we hope, then the side lobe levels will be low enough with a modest number of transducer elements (eight for example). It then becomes practical to consider the use of a two-dimensional array of perhaps 32 elements to obtain good definition in all three-dimensions. The optimum configuration of such a two-dimensional array is something which still needs

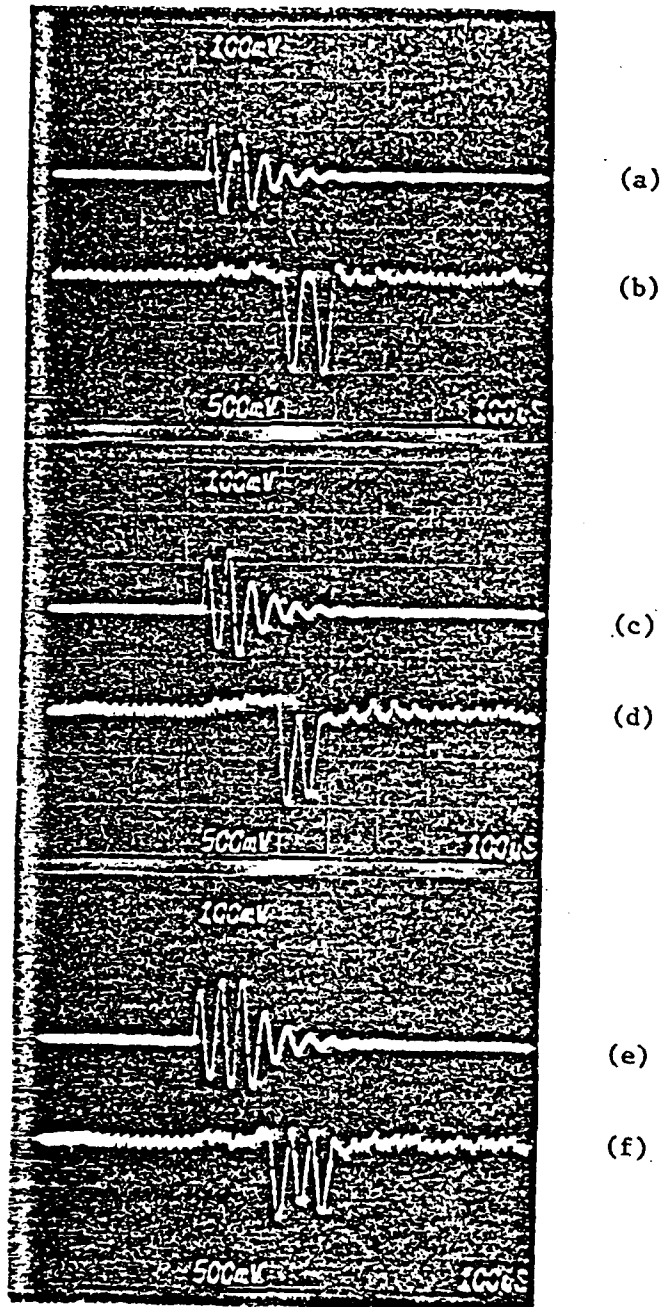


FIG. 3--Deconvolution of overlapping distorted pulses using the inverse filter of Fig. 1(f).

- (a) Two overlapping distorted pulses;
- (b) Inverse filter output;
- (c) Two overlapping distorted pulses
- (d) Inverse filter output;
- (e) Three overlapping distorted pulses;
- (f) Inverse filter output.



to be considered; however, three-dimensional imaging does appear to be practical using this approach.

A second interesting possibility is the use of ultra-high frequency ZnO on sapphire transducer arrays operating at 200 MHz, such as have already been developed in our laboratory, to construct an imaging system for examining such materials as ceramics and integrated circuits. Sampling circuits, such as are employed in sampling oscilloscopes, can be used to count down the received frequency to a range below 10 MHz, prior to being digitized at the front-end of our imaging system.

A third possibility is the use of this approach to scan a very long transducer array, of perhaps several hundred elements, to obtain a very wide field of view. With this approach, we would process the information from a modest number of elements, 32 for example, then use the multiplexer to select the next group of 32 elements in the array. The total picture field obtained would be stored in a scan converter and information from overlapping points added in the scan converter. This would yield a high quality image from a relatively large effective synthetic aperture, with a large field of view. The additional electronics required for this approach is the additional multiplexer channels and the scan converter. Another possibility is to use this synthetic aperture technique to produce a dynamically focused beam for use with a system much like a conventional medical B-scan imaging system to provide greatly improved resolution and beam tilting capability. In this case, the transducer array could consist of an array of say 32 elements which would provide dynamic focusing and beam tilting in a radial sector. By mounting the array on a mechanical arm and keeping track of its location, the system could be used in the same way as a mechanically scanned medical B-scan system but with better definition. Furthermore, as the beam could be tilted electronically, a hand held array could be used to scan rigid objects like a piece of metal, without requiring the flexibility of the body or of a water bath for beam tilting. Alternatively, a number of concentric rings could provide three-dimensional dynamic focusing along their common axis, and the system could be used in the same way as a standard medical B-scan system. In both cases a scan converter would be required for display of the complete image.

A final possibility is to attempt post processing on the complete image. Schemes such as two-dimensional inverse filtering might be attempted to improve the resolution and reduce the side lobe responses.

As can be seen, there are several different ways of employing this system, many of which we hope to demonstrate. We believe the basic advantage of such a synthetic aperture system is the great flexibility offered by the externally programmed focus memory which permits the scan format to be altered at will while still retaining real time operation.

References

1. F.L. Thurstone and O.T. Von Ramin, "A New Imaging Technique Employing Two-Dimensional Beam Steering," *Acoustical Holography*, Vol. 5, Plenum Press (1973).
2. J.D. Meindl, "Integrated Electronics for Acoustic Imaging Arrays," in g. Wade (ed.) *Acoustic Imaging*, Plenum Press (1975), pp. 127-188.
3. S.A. Johson, J.F. Greenleaf, F.A. Duck, A. Chu, W.R. Samayou and B.K. Gilbert, "Digital Computer Simulation Study of a Real-Time Collecton, Post Processing Synthetic Focursing Ultrasound Cardiac Camera," *Acoustical Holography*, Vol. 6, Plenum Press (1975), p. 193.
4. H. Dale Collins, "Acoustical Interferometry Using Electronically Simulated Variable Reference and Multiple Path Techniques," *Acoustical Holography*, Vol. 6, Plenum Press (1975), p. 597.



PROJECT I, UNIT C, TASK 2

ULTRASONIC IMAGING TECHNIQUES

K. M. Lakin
Department of Electrical Engineering
University of Southern California
Los Angeles, California

Introduction

The objective of this task is to study acoustic image processing and to implement a pulsed CW holographic imaging system as an extension of the work done previously on the amplitude and phase contrast imaging of transducer near and far field radiation patterns. In that work the precision of the holographic process using VW excitation suggested that the method might well be applied to the problem of defect imaging if the same degree of accuracy could be achieved when the system was used in the pulsed mode. In the CW system the overall accuracy was obtained because of the large dynamic range of the network analyzer and its narrow band high resolution phase detection capability. In addition, by using a synthetic array approach, i.e., scanning a 64 x 64 grid using a single transducer, all elements of the array were assured to be identical in response. However, the system was not convenient in terms of data through-put and image processing speed. In addition, the CW mode of operation allows multiple reflections to obscure the desired data, a severe problem in defect imaging where the scattering from front surfaces (such as water-solid) is much stronger than scattered signals coming from the defect located within the solid.

In order to efficiently implement this study, we have defined a number of sub-tasks which are ordered in the approximate flow of image data. The description of the various sub-tasks and their implementation are described below.

Implementation

Pulsed CW Measuring System. The pulsed measuring system consists of an analog region and A/D converters to provide 2's complement data for

reduction and display. The analog portion of the system is a super-heterodyne receiver consisting of a front end mixer followed by a high gain 30 MHz IF amplifier having 4 MHz bandwidth, over 100 dB gain and -120 dBm sensitivity. The first mixer takes the nominally 5 MHz signal from the transducer (or array element) and mixes with a 25 MHz carrier to give the 30 MHz IF signal. The output of the IF amplifier is either a 30 MHz pulse or an envelope of the pulse. In our system the 30 MHz pulse is sent to two double balanced mixers with proper phase shift and mixed with quadrature shifted 30 MHz reference signals. The output of the detectors is then the real and imaginary components of the pulse signals. These base band pulses are then sent to gated sample and hold modules and then to fast 12 bit A/D converters and then to memory via the IEEE 488 interface bus. Because the analog portion of the system uses the super-heterodyne principle, the input signals may be pulses as well as tone bursts. The generation of the transmit signal also uses the heterodyne principle in order to maintain phase coherence between pulses.

Array Design

An array to be used for a holographic imaging system has somewhat different requirements than those used for focused imaging. The holographic transducer array may be constructed with elements more widely spaced than those used for focused beams, the elements are sampled in sequence rather than simultaneously, and the requirements for cross talk in the array are probably somewhat more severe than in focused beam arrays. The more widely spaced array elements makes the array construction somewhat more tractable and the sequential access should make the electronics less costly since $2N$ electronic elements are required for an array of size $N \times N$ rather than N squared similar circuits. Several array designs have been considered with an emphasis placed upon the compatibility of acoustical design and electronic scanning. In general, the array of interest is of size 64×64 with an element spacing of 20 wavelengths, and an operating frequency of 5 MHz. Since the holographic system uses coherent tone burst for measurement, the transducer elements need not be as heavily damped as those used for focused beam A scan. It is hoped that the easing of the damping requirement alone will make the array construction more practical and the elements more uniform and reliable.



Acoustic Image Processing

In order to form an image from the acoustic signals the data must be first cast into a format that allows the inversion to be done with Fourier transform methods. Initially, the data must be windowed to prevent image ringing due to the truncation of the transform and then the parabolic phase factor must be subtracted from the total phase. At first thought one would expect that the Fourier transform would be done using a standard FFT algorithm as we did in our work on transducer fields. However, the tradeoffs in computation time between the FFT and straight DFT are less favorable for the FFT when the transform size is as small as ours (64 point transform) and when complex pre- and post-multiplication are required for the parabolic phase factors. In addition, most work in the literature deals with 1024 point transforms or larger, use "in-place computation" which conserves machine memory but destroys the original data set. However, we must preserve the original data set in order to carry out the many transforms required to image through a water-solid interface. Faced with these trade-offs, we decided to recast the formalism into the form of a double convolution as shown in (1), from [1], for the continuum and in (2) for the discrete case.

$$u(x', y') = \int e^{-ik'(x'-u')^2} \left[\int \tilde{u}(u', v') e^{-ik'(y'-v')^2} dv' \right] du' \quad (1)$$

$$u(I, J) = \sum_K e^{-i \frac{N}{M} \pi (I-K)^2} \left[\sum_L e^{-i \frac{N}{M} \pi (J-L)^2} \tilde{u}(K, L) \right] \quad (2)$$

Clearly, with the parabolic phase factored in, the problem is one of convolving the circular functions with the field data. For the case of a 64 x 64 data set, 4096 complex multiplications are required for each of the 64 rows and the process is repeated for each of the 64 columns for a total of over 500,000 complex multiplications. Accordingly, we are planning to use hardware multipliers to do the complex arithmetic and directly cycle the data to the multipliers transparent to the microprocessor. In this manner we can achieve a good compromise between hardware cost and computational time since memory is relatively inexpensive and the hardware multipliers are less than 200 dollars each and multiply in less than 150 ns. Thus by using two

multiplications per memory cycle, we can obtain the product of two 12 bit numbers in 300 ns and the two dimensional convolution in less than 200 ns which should allow for a near real time display of the transform and a feature for zoom focusing of the image by the operator. In the case of imaging through a water-solid interface, as many as 4096 transforms would be required in the worst case to find the interface fields, but this would take less than 14 seconds. Once having the interface fields, the image within the solid would be obtained in the usual manner in less than 200 ms.

Image Display

For our initial work the mode of display will be the 8 bit grey scale using black and white with the operator having the option of zoom focus and level slicing (contour plots). Eventually, it will be useful to present the data in the form of perspective plots, as was done in the transducer studies, although this requires a lot of code and processing time if hidden lines are to be blanked out. In the meantime, perspective plots of the image will be generated on the Tektronix 4051 Graphics System using recently purchased software.

Interface Field Transitions

Because of the difference in propagation properties across an interface, such as water-to-steel, the acoustic fields cannot be directly transformed from the measurement plane to the image. Instead the fields at the interface must first be determined and then transformed into the solid. Such a procedure must take into account both the magnitude and phase of the fields where the phase is sensitive to the location of the interface. Our initial studies of the problem suggest that the contour of the interface must be known quite precisely due to the sensitivity of the change in Snell's law refraction angle in going from water to solid.

Reference

1. K. M. Lakin and A. Fedotowsky, "Characterization of NDE Transducers and Scattering Surfaces Using Phase and Amplitude Measurements of Ultrasonic Field Patterns," IEEE Trans. Sonics and Ultrasonics, Vol. SU-23, No. 5, September 1976.



PROJECT I, UNIT C, TASK 3

NONDESTRUCTIVE EVALUATION

N. Bleistein and J. K. Cohen
Denver Applied Analytics
Denver, Colorado 80222

Introduction

The general objective of this task is to develop inversion methods suitable for determining the size, shape, orientation, and material properties of flaws in solids. The first objective during this period was to construct a computer code which would accept experimental backscatter observations made on the surface of the diffusion bonded samples at the Science Center and from this data to predict the location and description of voids within that sphere.

Approach

In order to attain this objective, it was necessary to extend the theoretical results previously obtained by us in several ways. First, the analysis had to be adapted to the implied three-dimensional spherical geometry and secondly, the analysis had to be adapted to the type of source employed by the experimentalists in the Rockwell N.D.E. project.

We have two basic approaches to the flaw detection problem. The first is treating the flaw as a small inhomogeneity (direct inversion approach) while the second treats the flaw as a perfect reflector (POFFIS approach). Since our first experiments concern voids, the POFFIS formalism has been considered initially.

We have now completed flow-charting the first computer algorithm. Specifically, we are implementing the POFFIS formalism in three space dimensions and time for a plane wave source of the form, $p(\omega) e^{-i \omega/c \hat{x}_0 \cdot x}$, where \hat{x}_0 denotes the direction of the plane wave and $\omega = 2\pi F$, the angular frequency. Although it is possible to "bootstrap" an estimate of speed inside the flow from the POFFIS formalism, we shall not attempt this in our first code since for a void such an estimate is not relevant.

Having selected the POFFIS formalism, we have a choice of two forms of processing the scattering data. The final and major step in the first approach consists of a three dimensional Fast Fourier Transform (FFT) from wave number space back into physical space. When we seriously considered implementing this, we realized that the spacing for the transform in all three dimensions would be tied to the (dense) spacing implied by the original sampling rate in time used to gather the scattering data. This struck us as being unfortunate on two grounds. First, the FFT would be of large size (typically $512 \times 512 \times 512$) and second, this spatial density ignores the fact that the data is collected much less densely in angular spacing than it is in time spacing (the time spacing ultimately dictates the output radial spacing or resolution). We soon realized that the reason for this loss of control over output spacing is that data is naturally collected with respect to a spherical geometry, while the multi-dimensional FFT insists on a rectangular grid. This latter fact also meant that this approach required a data conversion from a spherical grid to a rectangular grid which would add significantly to processing time.

Thus, we have turned to a second approach whose final and major step is an integration over the unit sphere. We had earlier put aside this version of the POFFIS algorithm because it seemed unlikely that such a multi-dimensional numerical integration could possibly compete with the all powerful FFT. However, because the output step is naturally in spherical geometry and thus compatible with the natural method of data collection, we re-examined this approach and found to our surprise that it not only had the virtue of mirroring the physics more intuitively, but was, in fact, much superior with respect to operation counts than the FFT approach because (1) an extra step can be carried out analytically rather than numerically (essentially a data deconvolution step) and (2) the output angular spacing is no longer tied to the time sampling rate (after all we only wish to "view" the interior of the sphere from a relatively few aspects) and (3) spherical to rectangular interpolation is not needed.

The next step is the specification of the particular locations to be used as observational angles (transducer locations) and viewing angles (rotating the defect information to simulate particular viewing aspect). The



specification of the observation latitude and longitudes depends on what numerical integration schedule we use to integrate over the unit sphere. There are three general categories of such schemes: product Gaussian schemes, product Lobatto schemes, and various ad hoc non-product schemes (which may exhibit, however, beautiful symmetry, such as the 20-point scheme based on the vertices of the regular dodecahedron or the 62-point scheme based on the vertices of the icosahedron, the vertices of the reciprocal dodecahedron and the midpoints of the edges of the icosahedron). The literature we have found is conspicuously silent on comparisons among these three types when a roughly equal number of observations is used. Although many theoretical formulae exist for numerical integration over the surface of a sphere, error estimates are simply not available. Only experimentation with the code can determine the particular scheme and density of laboratory observations required to produce satisfactory resolution of the voids. In our first synthetic runs I am going to use the 9th degree product Gaussian formula which uses the 50 points specified by

$$\alpha = 0^\circ, \pm 32.58^\circ, \pm 64.98^\circ$$
$$\beta = \pm 18^\circ, \pm 54^\circ, \pm 90^\circ, \pm 126^\circ, \pm 162^\circ \text{ (36}^\circ \text{ spacing).}$$

We will undoubtedly experiment with other formulae and will be writing to knowledgeable people in the cubature field. The output will be viewed from three orthogonal aspects, "straight-on", "side", and "top".

This theoretical work has now been completed and furthermore, an algorithm suitable for computer implementation has been developed. The coding and key punching is also virtually completed and, within the next few days, we will begin debugging our code using very simple synthetic data.

Future Work

Once this work has been completed, our next objective will be to run the code on experimental data and to adopt the code to limited aperture observations.

PROJECT I, UNIT C, TASK 4

APPLICATION OF ADAPTIVE LEARNING NETWORKS TO ESTABLISH
RELATIONSHIPS BETWEEN ANALYTICAL AND EMPIRICAL NDE METHODS

Anthony N. Mucciardi
Adaptronics, Inc.
McLean, Virginia 22101

Introduction

The main objectives during this reporting period were to: (1) define the work tasks for FY 1978 and 1979, (2) extend the ultrasonic waveform features (i.e., parameters) to include the "long wavelength" features, and (3) begin testing of the "extended quasi-static model" as a means of generating a new synthetic data base for ALN training.

Technical Progress

A meeting was held at the Rockwell Science Center on September 22, 1977, during which new theoretical results were reviewed and statements of work were prepared for each of the principal investigators for the two-year period October 1, 1977, to September 30, 1979.

Work was begun on constructing a computer program to compute automatically long wavelength features. These include the coefficients of the f^2 and f^4 terms as well as other frequency-dependent parameters. The upper limit of ka for which the magnitude spectrum features will be computed will also be determined as part of this same program.

The computer program implementing the extended quasi-static model was received from J. Gubernatis on December 8, 1977. Test runs were made that matched exactly the correct results that were sent by Gubernatis along with the program.

Plans for January-June 1978

The following activity is planned for the next semiannual period:

The long wavelength feature program will be completed and tested. Its properties will be studied as a function of defect size, shape, and



orientation variations. These features will be added to the list that was used previously.

The Gubernatis program will be thoroughly tested and compared to the results given by the Born approximation under identical tests conditions. The extended quasi-static results will also be compared to experimental observation wherever possible. Upon completion of the testing phase, a data base will be generated for spheres and spheriods.

Adaptive Learning Network (ALN) models will be trained to: (a) classify the scattering data into one of three mutually exclusive classes -- sphere, oblate spheriod, or prolate spheriod -- and, (b) predict the defect size, shape, and orientation after the classification step.

Near the end of this period, experimental data from L. Adler will be used in the ALN models to test the system on all three volumetric scatterers.

PROJECT I, UNIT C, TASK 5

DETERMINATION OF FRACTURE MECHANICS
PARAMETERS FROM ELASTIC WAVE SCATTERING
MEASUREMENTS AT LOW FREQUENCIES

R. K. Elsley, J. M. Richardson, R. B. Thompson
Rockwell International Science Center
Thousand Oaks, California 91360

Introduction

A number of techniques have recently emerged for the determination of fracture related parameters of defects from measured ultrasonic fields. One of the newest of these, and perhaps the most unexpected, is the observation that considerable information can be derived from ultrasonic scattering measurements in which the wavelength is large with respect to the flaw size. From the familiar concept of resolution of an image, one would expect to obtain little useful information under such conditions. However, the elastic nature of the ultrasound-flaw interaction leads directly to results that are quite in contrast to this overly simple point of view.

Here, we summarize recent progress on the demonstration of the feasibility and usefulness of low frequency scattering of elastic waves in the context of nondestructive evaluation. The scope of the present program entails the estimation of a certain crucial parameter in fracture mechanics (the stress intensity factor k_I) from longitudinal-to-longitudinal scattering data extrapolated to low frequencies. This estimate is made under the simplifying assumption that the defect is a single spheroidal void. The size, shape, and orientation, as well as a fracture critical parameters of the defect are determined.

Before considering the detailed results, it is important to ask: What advantages would such an approach have relative to other approaches for defect characterization? The following points can be made in its favor:

- (1) The theory of the scattering of elastic waves at low frequencies is well established for the case of ellipsoidal inclusions and voids. Thus, the inverse scattering problem for this class of scatterers is quite tractable. At higher frequencies, this is not the case.



- (2) Low frequency measurements are sensitive only to the overall shape and size of the defect and not to small textural details. This is also the information of importance in fracture.
- (3) Low frequency scattering measurements are particularly sensitive to cracks compared with other scatterers (e.g., inclusions of the same volume or even the same area). In particular, the scattering measurements are significantly more sensitive to a large crack than to a number of small cracks with the same total area.
- (4) The elastic processes involved in low frequency scattering are intimately related to those involved in the early stages of the fracture process (at least in most metals) as has been pointed out by Budiansky and Rice.⁽¹⁾ A further advantage is that the relevant stress intensity factor is proportional to the $1/6$ power of the scattering amplitude, yielding thereby a substantial reduction of variance in the estimation process, a fact emphasized by Kino.⁽²⁾

Of course, there are also disadvantages. Some of these are:

- (1) Relatively complex post-experiment data processing is involved in deducing the low frequency scattering characteristics. However, the main problems appear to be satisfactorily solved as described in this report.
- (2) A significant problem, not yet confronted, is the isolation of each dominant scatterer from competing scatterers in taking the low frequency limit.

This will be discussed at greater length in the last section.

The total procedure is represented by the block diagram presented in Fig. 1. The structure of this diagram is organized to reflect the present discussion, with individual experimental and theoretical procedures represented as "black boxes." Two kinds of data flow are indicated. The solid line represents the data flow that exists in an operational system in which the flaw's properties, and its severity from the point of view of failure, are determined from the experimental data. The dashed branches indicate an alternate path used in the research phase to verify that the

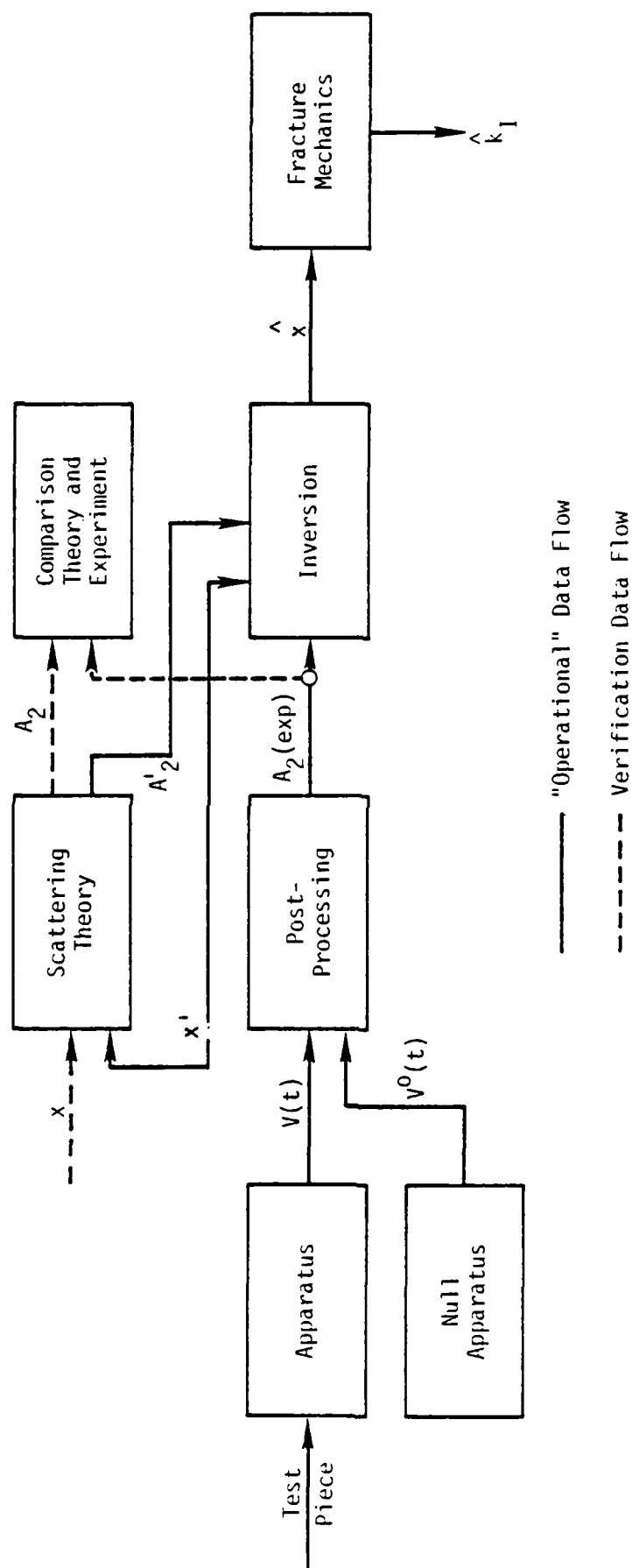


Figure 1. Schematic Representation of NDE Procedure



individual theoretical and experimental components are valid and properly functioning.

The first step is the experimental measurements of scattered waveforms, $V(t)$, from the unknown part. It is also very helpful to obtain a calibration waveform $V^0(t)$ from a similar part, with no flaw. These are then processed to estimate the parameter $A_2(\text{exp})$ which is the coefficient of the ω^2 term in a frequency expansion of the scattering amplitude.

A sufficiently extensive set of these numbers must be calculated for a corresponding set of scattering configurations. This set of values of $A_2(\text{exp})$ constitute the input to the inversion box whose function is to produce a best estimate \hat{x} of the set of parameters (represented by the vector x) characterizing the spheroidal void. The inversion box essentially makes a best least square fit of the set of theoretical values of A_2 to the set of experimental values. In doing so, it must communicate bilaterally with the box labelled scattering theory, sending tentative sets of parameter values x' and receiving corresponding values A_2' . The final box labelled fracture mechanics estimates from x quantities of significance in the prediction of failure. In the present case we have chosen k_I , a normalized stress intensity factor for mode I applied stress (i.e., uniaxial tension along the symmetry axis of the spheroidal void). In the future a more extensive set of fracture mechanics parameters will be considered. The estimates and a posteriori variances of these parameters should provide enough information to enable a future decision algorithm to produce an accept vs reject decision.

The data flows in the last paragraph are of the kind that would occur in an operational system. As stated earlier, we are also interested in data flows (represented by dotted lines) involved in the verification of parts of the overall system. In Fig. 1, we illustrate an example of such data flows in connection with the verification of the scattering experiments. Here the true known value of x (characterizing the spheroidal void) is fed into the box labelled scattering theory. The exact theoretical values of A_2 are then compared with the experimental values of $A_2(\text{exp})$.

Theory of Scattering of Elastic Waves at Low Frequencies

In this section we discuss the basic scattering theory "box," i.e., those principles which relate the flaw parameter vector x to the long wavelength scattering coefficient, A_2 .

The longitudinal-to-longitudinal scattering of elastic waves from an arbitrary scatterer is described by the scalar scattering amplitude $A = A(\vec{e}^s, \vec{e}^i, \omega)$ where \vec{e}^s is the scattered (observer) direction, \vec{e}^i is the incident direction, and ω is the frequency (expressed in radius per unit time). This scattering amplitude can be expanded in a power series in ω in the following form:

$$A = A_2\omega^2 + iA_3\omega^3 + A_4\omega^4 + iA_5\omega^5 + \dots \quad (1)$$

where the A_n are real and are independent of ω , i.e., $A_n = A_n(\vec{e}^s, \vec{e}^i)$. The vanishing of A_0 and A_1 is a general property of localized scatterers. If the scatterer has inversion symmetry about the origin, then A_3 also vanishes,⁽³⁾ but this question need not concern us here. The absolute value of A can also be expanded in powers of ω but here only even powers will enter, namely

$$|A| = a_2\omega^2 + a_4\omega^4 + \dots \quad (2)$$

where, of course, $a_2 = |A_2|$.

In the experiments only the absolute magnitude $|A_2|$ is yielded. Since it is known theoretically that $A_2 > 0$ for spheroidal voids, the absence of the sign of A_2 in the experimental output is of no consequence. However, this may be a serious lack in the case of more general scatterers.

We will not give a detailed discussion here of the theoretical treatment⁽⁴⁻⁶⁾ of the low frequency scattering of elastic waves from general spheroidal inclusions. It will suffice here to present a description of the input and output of the computer program LOWSCATEL. Actually, the input is presently given in a form suitable for general ellipsoidal inclusions of isotropic material even though the internal algorithm has not yet been extended beyond the spheroidal case. In setting up a framework for the description of the input, we use a cartesian coordinate system (x, y, z) with the associated unit vectors \vec{e}_x , \vec{e}_y and \vec{e}_z . The principal axes of the



ellipsoid are defined by the mutually perpendicular vectors \vec{u} , \vec{v} , and \vec{w} and the corresponding semiaxis lengths are directed by a , b , and c . The material properties of the host material are the density and the two Lamé constants denoted by ρ , λ and μ and the corresponding properties of the inclusion are denoted by $\rho + \delta\rho$, $\lambda + \delta\lambda$ and $\mu + \delta\mu$. In the case of a void, we set $\delta\rho = -\rho$, $\delta\lambda = -\lambda$ and $\delta\mu = -\mu$. Finally, we must include the set of incident and scattered wave directions defined by the unit vectors \vec{e}^i and \vec{e}^s , respectively, in order to specify the configurations of interest. The output of the computer program is simply $A_2 = A_2(\vec{e}^s, \vec{e}^i)$ for the case of longitudinal-to-longitudinal scattering of elastic waves.

In the particular cases of interest here, we took

$$\vec{u} = \vec{e}_x, \quad \vec{v} = \vec{e}_y, \quad \vec{w} = \vec{e}_z$$

$$a = b = 0.04 \text{ cm and } c = 0.02 \text{ cm}$$

$$\rho = 4.42 \text{ gm cm}^{-3}, \quad c_e = 0.634 \text{ cm } \mu\text{sec}^{-1}$$

$$c_t = 0.303 \text{ cm } \mu\text{sec}^{-1}$$

The λ and μ for the host material (titanium) were determined from the above values of the host material longitudinal and transverse propagation velocities, c_e and c_t , respectively. The selected sets of incident and scattered directions will be indicated in section IV discussion the comparison of theories and experiment.

Experimental Measurements

A. Apparatus

The long wavelength coefficient, A_2 , was determined experimentally using the "trailer hitch" samples fabricated during previous years of this program. These samples consist of a diffusion bonded piece of titanium whose external surface is machined into the shape of a sphere on a pedestal. At the center is an ellipsoidal cavity of known dimensions. The spherical external surface allows measurements to be made at nearly any angle of incidence and/or scattering. However, these angles can be limited in a particular experiment to simulate the finite aperture that would be available in a real testing situation. For the purpose of calibration, a sample was available with no defect present.

Two sets of measurements have been made. The initial set (made by Tittmann and Morris) used a special purpose fixed bandwidth (1/3 MHz) ultrasonic spectrum analyzer capable of normalizing ("deconvolving") the properties of the transducer out of the data. The pitch-catch (2 transducer) measurements made with this apparatus show relatively good agreement with theory. The latter measurements were performed using a Panametrics 5052PR Pulser Receiver, a Biomation 8100 Transient Recorder, and a minicomputer based Interpretive Signal Processor language. The pulse-echo measurements thus far made in this manner show excellent agreement with theory.

In both cases, commercially available 5 MHz, 1/2 in. diameter broadband transducers were used.

Measurements were made on samples containing a $400\mu\text{m}$ spherical void and a $800\mu\text{m} \times 400\mu\text{m}$ oblate spheroidal void. One requires $ka < 0.5$ to enter the region in which the $A_2\omega^2$ dominates the scattering (see Eq. (1)), and for an $400\mu\text{m}$ diameter void this corresponds to frequencies below 2 MHz. Other than this emphasis of low frequencies, the measurement of the long wavelength scattering properties of a scatterer is, in principle, no different from the intermediate and short wavelength measurements performed previously in this contract. The procedure is: (1) interrogate the scatterer with a sound pulse containing (among others) the frequencies of interest, (2) analyze the scattered sound pulse to determine the response at those frequencies, and (3) estimate the desired property of the scatterer, in this case, the coefficient A_2 of ω^2 . Measurements of A_2 at a variety of angles about the scatterer are taken and then inverted to estimate shape and size of the scatterer.

If the scatterer is isolated from all other scatterers (surfaces of the part, other defects, welds, etc.) by a distance of many times its own size, then interrogation with a short pulse of ultrasound of a suitable frequency will give a measure of A_2 . However, this is rarely the case. There are both temporal limitations due to the nearness of other scatterers and spatial limitations due to the diffraction of low frequency sound. These limitations depend on the geometry of the part being tested. These problems are discussed and solutions to them presented in sections B and C below.



B. Geometrical Effects

In the "trailer hitch" geometry, a primary limitation is that the diffraction of the sound causes there to be some sound energy which passes directly from the transmitting transducer to the receiving transducer along a chord of the sphere. Figure 2(a) shows the path of the defect signal (1) and the path of the longitudinal (2) and shear (3) components of this so-called "direct beam." The properties of these direct beams are discussed below.

1. Longitudinal Direct Beam - The longitudinal component arrives before the defect signal though for large included angles between transmitter and receiver (e.g., 90°), it arrives only very shortly before and, therefore, interferes with the defect signal. (For an included angle of 180° , of course, the receiver is looking directly at the transmitter and the arrivals of direct beam and defect signal are simultaneous.) Figure 3(a) shows the received time domain waveform for a 45° included angle. The longitudinal direct beam pulse occurs between the points marked "X". The beginning of this pulse occurs when sound has traveled from the near edge of the transmitting transducer to the near edge of the receiving transducer ("near-edges" transit time). The end of the pulse occurs at the "far-edges" transit time, plus the duration of the transmitted pulse. Figure 3(b) shows the arrival time of the longitudinal direct beam versus included angle. The dashed line is the arrival time of the defect signal. The shaded area extends from the "near edges" time to the "far edges" time and the arrows indicate the duration of the transmitted pulse. Thus at angles above 90° , there is overlap of the direct beam and the defect signal.

The angular and frequency content of the direct beam are determined by the following factors: (1) the diffraction spreading of the direct beam from the transmitted direction is larger at low frequencies, where the transmitter is more nearly an isotropic source, (2) the amplitude of the transmitted signal is largest at the center frequency of the transducer and drops to zero at zero frequency, and (3) the angle between the normals to the faces of the two transducers causes the longitudinal direct beam to be small at small included angles. These factors combine to give the following dependencies: at a given angle, the direct beam is strongest at some

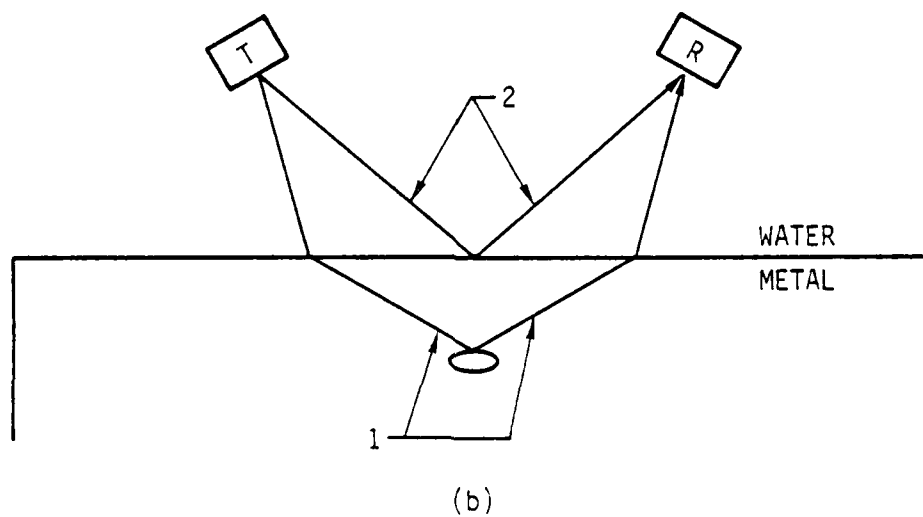
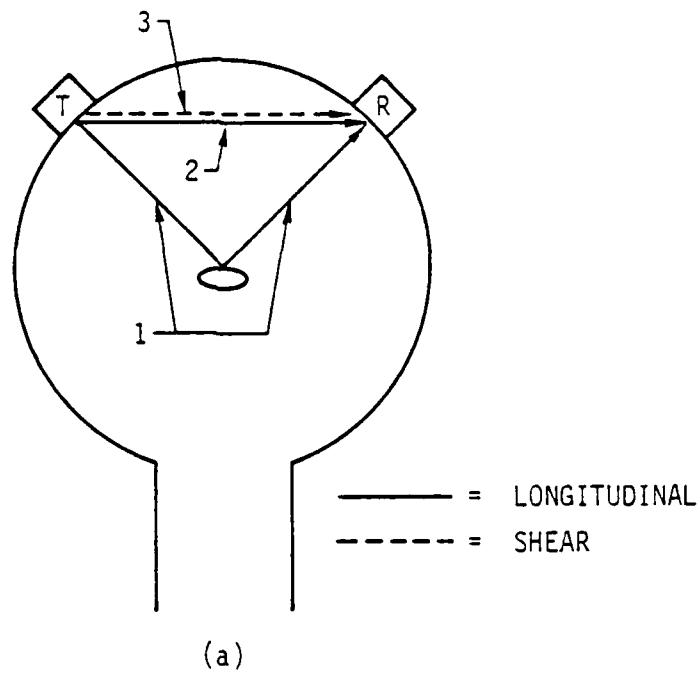


Fig. 2 Sound paths in trailer hitch (a) and flat (b) geometries.

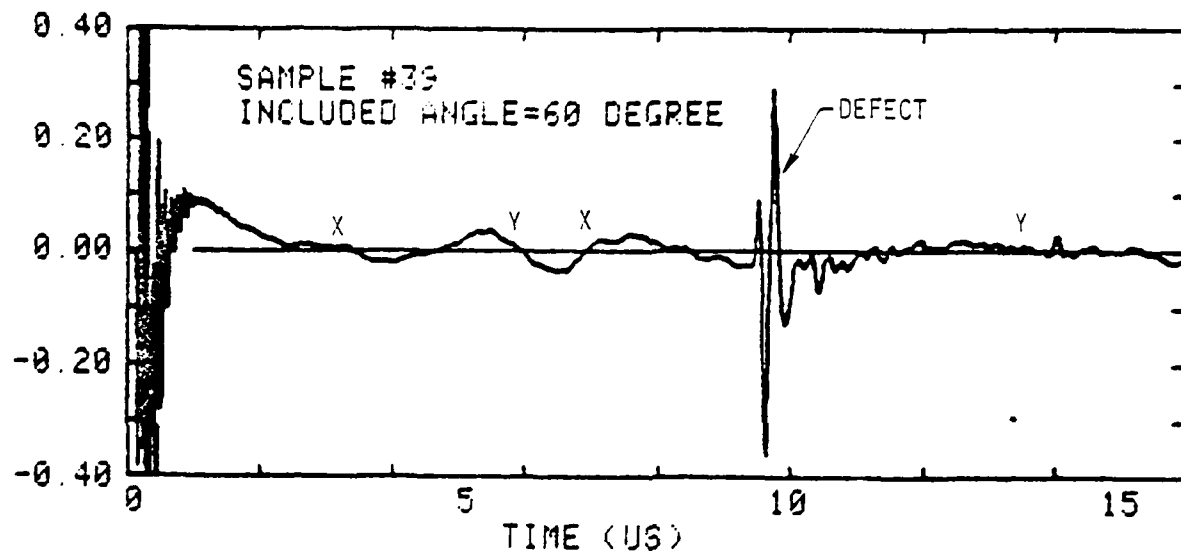


Fig. 3a Waveform from trailer hitch sample.

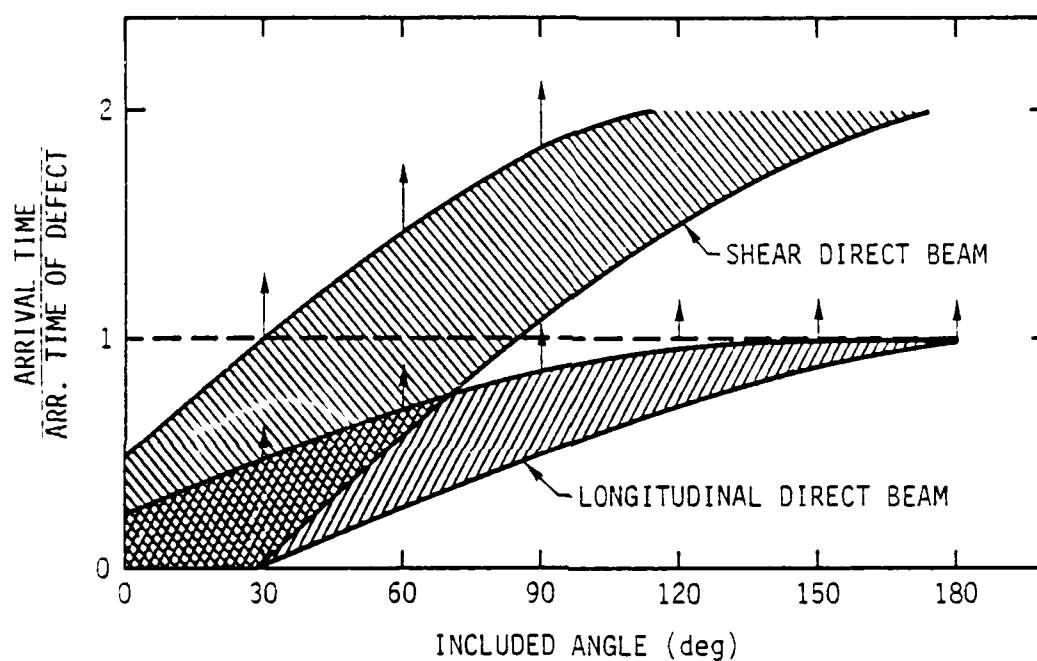


Fig. 3b Arrival times of direct beams.



frequency below the center frequency of the transducer; and at a given frequency, the direct beam is larger at larger included angles.

2. Shear Direct Beam - The shear component of the direct beam travels slower than the longitudinal component and can, therefore, arrive simultaneously with the defect signal. Figure 3(b) shows the shear direct beam arrival time in the same manner as it does the longitudinal. At angles from about 15° to 90° , the shear beam arrives simultaneously with the defect signal. In Fig. 2(a), the direct beam is present between the points marked "Y". The shear beam differs from the longitudinal in that it is smaller at large included angles and vice versa.

Note that there is also a "direct beam" problem in the commonly used geometry of inspecting an immersed part through a flat surface. Figure 2(b) shows a front surface beam (2) which arrives shortly before the defect signal and behaves analogously to the longitudinal direct beam in the "trailer hitch." In either case, the distance of the defect from the surface is the scaling factor for how closely in time the various signals arrive. In the planar geometry (Figure 2(b)), however, there is no analogy to the shear direct beam with its simultaneous arrival at small angles.

C. Time- and Frequency-Domain Processing of the Signals

As indicated above, the defect signal is contaminated by both simultaneously arriving signals (the shear direct beam and the tail of the longitudinal direct beam) and adjacent (in time) but rather large signals (the longitudinal direct beam). There is also, in contact measurements such as these, the possibility of the presence of a tail of the "main bang" (the pulse which excites the transmitter). This is especially true for pulse-echo (i.e., single transducer) measurements where the receiving electronics is overloaded by the main bang and may take a substantial time to recover.

These problems have been overcome by (1) careful selection of the duration and frequency content of the transmitted sound pulse, (2) subtraction from the received waveforms of a reference waveform obtained using the same measurement geometry but applied to a defect-free part, (3) time domain windowing to isolate the desired portion of the waveform, and (4) normalization ("deconvolution") of the frequency spectrum of the waveform

by the use of a reference spectrum of the transmitted pulse. Each of these steps is described below. In the first series of measurements, step 2 was not performed and steps 1 and 3 could only be performed in a crude manner. In the later measurements, all four steps were performed.

1. The Transmitted Pulse - A variety of commercial transducers were examined to determine which provided the best compromise between having sufficient low frequency (1 MHz) energy while not having a pulse length so long that the various signals present in the confined geometry of the trailer hitch cannot be easily separated. It was found that transducers of frequency 2.25 MHz and below produced pulses which were too long. Not only were their pulses longer due to the longer period of low frequency oscillations, but they were also more underdamped (more cycles per pulse) perhaps due to the fact that a constant thickness of backing material is fewer wavelengths thick at low frequencies.

It was, therefore, decided to use higher frequency (5 MHz) transducers because of their short pulse duration ($\sim 1/3 \mu\text{sec}$) and to make the measurements on the low frequency tail of the transducer spectrum. In other words, by the use of spectrum analysis, it is possible to measure the response of the defect to waves whose periods are greater than $1 \mu\text{sec}$ by the use of a pulse whose duration is much less than $1 \mu\text{sec}$.

The choice of the pulsing electronics is also critical. The Panametrics 5052PR pulser which was used has a control for adjusting the electrical damping of the transducer. At one extreme of this control, the pulse has no energy below 3 MHz, while at the other extreme, there is 10% amplitude down to 0.5 MHz. On the other hand, for pulse echo measurements, the overloading of the receiver lasts extremely long ($10 \mu\text{sec}$) when the damping is set for low frequency content. The damping was, therefore, set at an intermediate value which provided a good compromise.

2. Subtraction of the Direct Beam - In order to separate coincident signals, simple time gating will not work. Some prior knowledge of the interfering signals is necessary. Therefore, in order to eliminate the shear direct beam and, at large included angles, the longitudinal direct beam, each



waveform has had subtracted from it a "geometrical reference waveform" obtained from a defect-free sample with the same included angle between transmitter and receiver.

Subtraction processes of this sort are limited by the precision with which the reference geometry reproduces the measurement geometry. Fortunately, small positioning errors affect the low frequencies of interest here less than they do high frequencies.

The subtraction process is found to extend to substantially lower frequencies the region of good data.

Note that in the commonly used geometry of inspecting an immersed part through a flat surface, the reference signal needed for subtraction is simply obtained by translating the transducers to an adjacent, defect-free region of the part.

3. Time Windowing - After subtraction of the geometrical reference waveform, the portion of the waveform containing the defect signal is isolated by multiplication by a shaped window which is zero except at times near the defect signal. Both the width and the shape of the window are important.

The width of the window is dictated by the following considerations: If the window is substantially wider than the duration of the defect signal, then adjacent, unwanted signals will be included. On the other hand, if the window is narrower than the defect signal, the spectrum of the defect will be distorted. In particular, the low frequency (long period) part of the spectrum will be distorted most. The form of this distortion will be as follows: The spectrum of the defect is proportional to f^2 at low frequencies. The effect of a window is to convolve this f^2 spectrum by the spectrum of the window. That is, each point in the spectrum is replaced by an integral over an adjacent region of the true spectrum whose width is of order $1 \div$ the duration of the window. Thus, too short a window causes the higher frequency part of the spectrum to smear into the low frequency part, giving a frequency dependence of less than f^2 .

The duration of the echo signals from a small isolated defect is of order 5 times the transit time of sound across a distance equal to the diameter of the defect, or about $1 \mu s$ for an $800 \mu m$ defect. We have,

therefore, chosen windows which have a full width at half maximum of $1 \mu s$ and a full width at zero of $2 \mu s$.

The window shape chosen must be a smooth one so that signals present at the edge of the window do not cause sidelobe oscillations in the spectrum. A Hanning window was chosen for this purpose.

4. Spectral Normalization - After windowing, the spectrum (Fourier transform) of the signal is obtained and divided by the spectrum of the incident sound pulse in order to remove the properties of the transducers and pulser. The reference spectrum is obtained by placing the transmitter and receiver on opposite sides of a defect-free trailer hitch, aimed directly at one another.

The coefficients of ω^2 were extracted from the slope-of-two, low frequency region of a log-log plot of the spectrum.

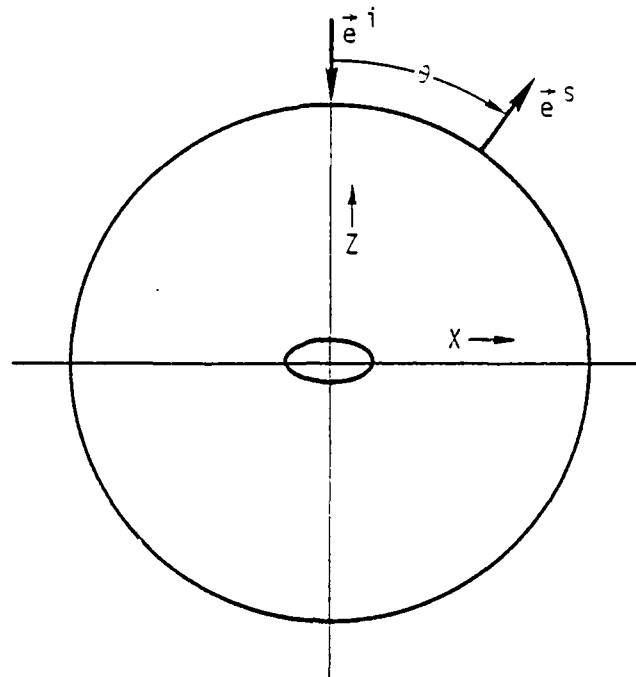
Comparison of Theory and Experiment

We turn now to a comparison of the theoretical and experimental results. As stated earlier, both pitch-catch and pulse-echo types of scattering measurements are considered. In Figs. 4 and 5 the geometries and associated notation pertaining to these types are presented.

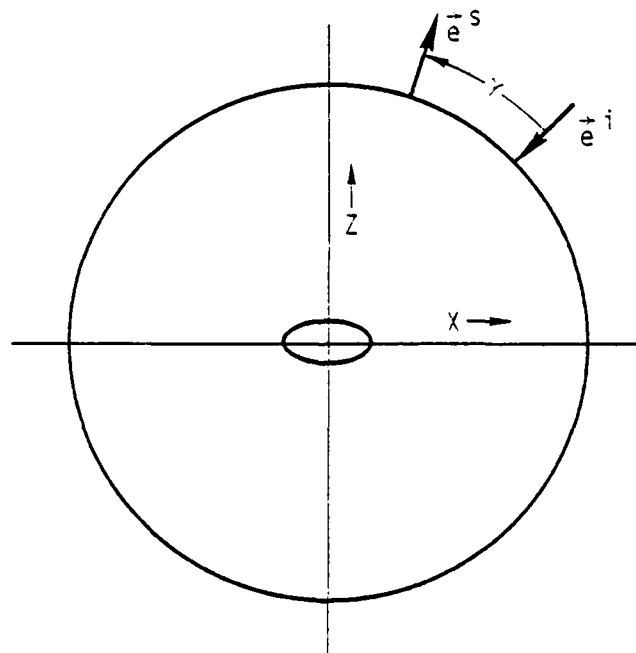
Figure 4(a) shows the geometrical setup in which the incident beam propagates in the negative z-direction (the z-axis is chosen as the axis of symmetry of the spheroid). Figure 4(b) shows the case in which the incident beam propagates in a direction 45° away from the z-axis. In both cases all of the scattering (i.e., observer) directions chosen in the experiments are coplanar with each other and with the incident direction (i.e., there is a single scattering plane common to all experiments). In the first case (Fig. 4(a)), the scattered direction is defined by the polar angle θ as shown. In the second case (Fig. 4(b)), the scattered direction is defined by the angle γ between the incident and scattered directions in the manner illustrated, with positive values of γ correspond to situations in which the scattered direction is oriented counterclockwise (in the plane of the figure) from the incident beam. Clearly, in the case of a spherical void, all



SC595.32SA



(a) Incident Wave Entering at "North Pole"



(b) Incident Wave Entering 45° from "North Pole"

Figure 4. Experimental Geometry for Pitch-Catch Measurements



incident directions are equivalent and thus only the configuration shown in Fig. 4(a) need be considered.

In Fig. 5 the geometry of the pulse-echo type of measurement is shown. Here the common angular position of the "points" of entry and exit of the incident and scattered waves, respectively, is defined by the polar angle θ . As in the previous case the measurements are confined to a single scattering plane.

We first discuss the pitch-catch measurements obtained by Tittmann and Morris several months ago. The absolute value of deconvolved experimental results (appropriately densitized) were extrapolated from a range of frequencies for which they were valid, to low frequencies to obtain a quantity that is proportional to $|A_2|$. The proportionality factor enters because of the calibration experiments used to normalize the data for variation in the transducer efficiency have slightly different diffraction properties than the scattering measurement. Assuming that the proportionality factor is the same for all experiments, we can obtain this factor by comparison of a set of control experiments with theory. For the latter, scattering from a spherical void of $400\text{ }\mu\text{m}$ diameter was chosen. The results are presented in Table I for the configurations of Fig. 4(a) corresponding to $\theta = 35^\circ, 45^\circ, 55^\circ, 65^\circ, \text{ and } 75^\circ$. The results are denoted by $\beta^{-1}A_2$ where β is the experimental proportionality factor. Actually, as stated before, the absolute value $\beta^{-1}|A_2|$ is measured, however, since A_2 is known to be positive, the absolute value symbol $|\cdot|$ will be dropped. The experimental values of $\beta^{-1}A_2$ given in the third column of Table I are divided into the theoretical values of A_2 given in the second column to yield the values of β given in the fourth column. The average value of these last results turned out to be 3.03×10^{-2} , a value used for converting all experimental results into meaningful values of A_2 expressed in the units: $\text{cm } \mu\text{sec}^2$. The comparison of the experimental and theoretical values of A_2 , given in the second and fifth columns of Table I are shown graphically in Fig. 6. The agreement of the sample-average values is, of course, tautological. However, the agreement of trends, which is not tautological, can be seen to be quite satisfactory.

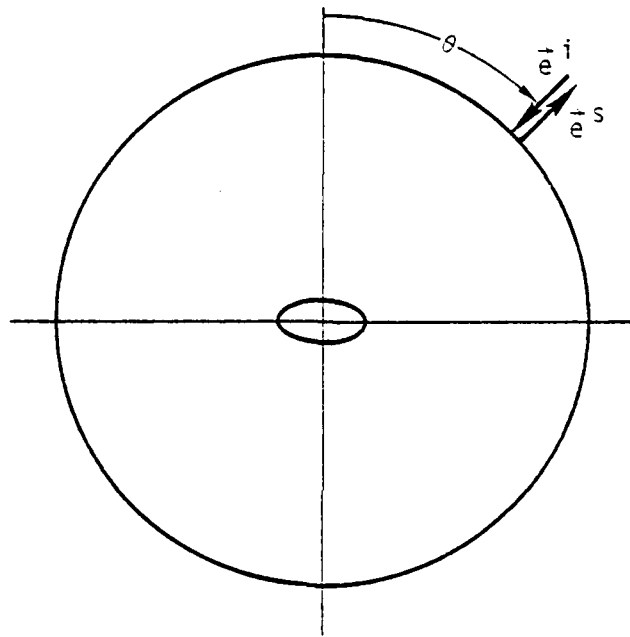


Figure 5. Experimental Geometry for Pulse-Echo Measurements



TABLE I
SCATTERING FROM A SPHERICAL VOID
DETERMINATION OF EXPERIMENTAL FACTOR β

($a = b = c = 0.02$ cm, $\vec{e}^i = -\vec{e}_z$, $\vec{e}^s = \vec{e}_x \sin \theta + \vec{e}_z \cos \theta$)

θ (deg)	Theory		Experiment	
	A_2 (cm μsec^2)	$\beta^{-1} A_2$	β	A_2 (cm μsec^2)
35	0.225×10^{-4}	7.1×10^{-4}	3.17×10^{-2}	0.215×10^{-4}
45	0.208	6.8	3.06	0.206
55	0.189	6.2	3.05	0.188
65	0.171	5.7	3.00	0.172
75	0.154	5.4	2.85	0.163
Av			3.03×10^{-2}	



SC595.32SA

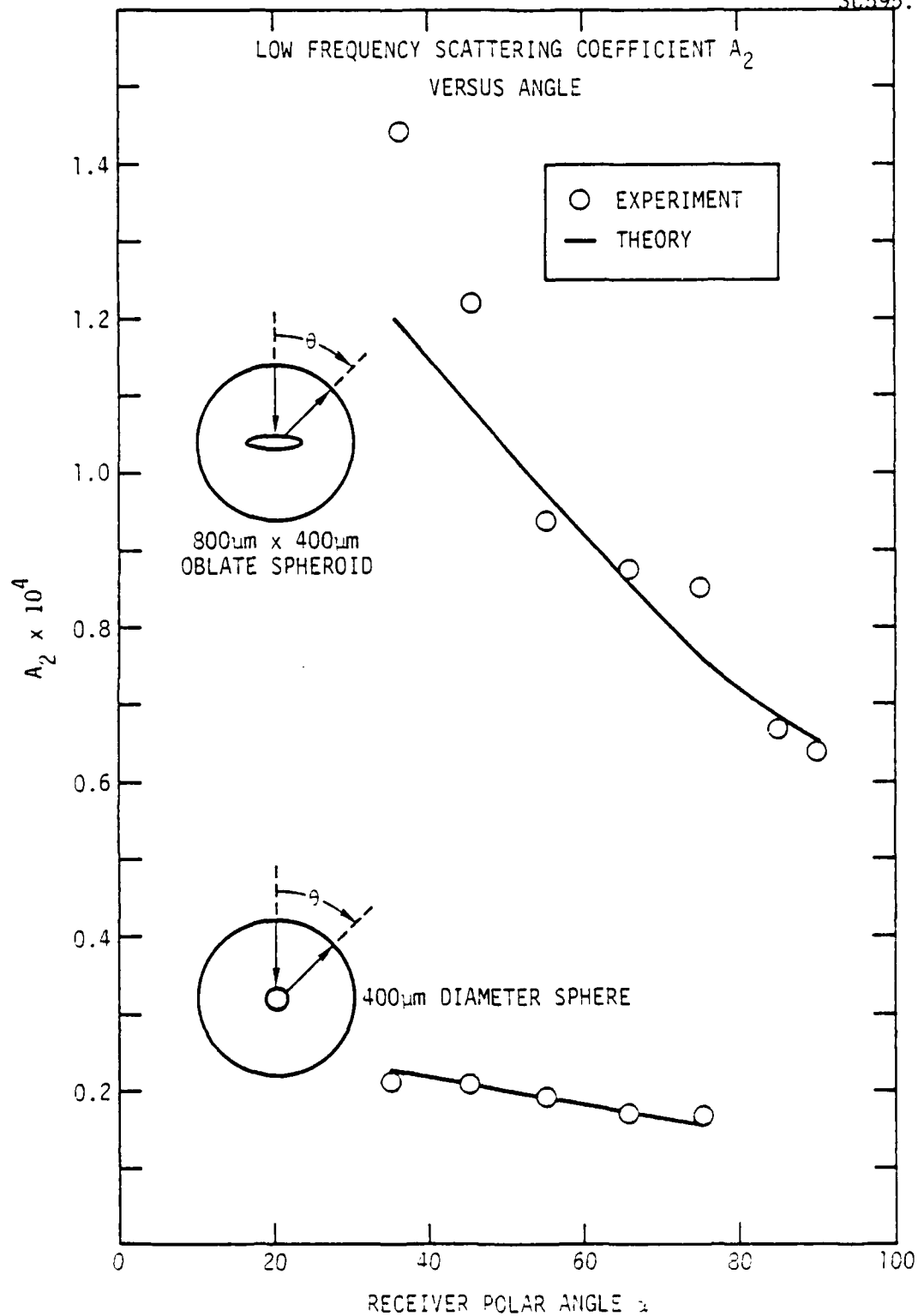


Figure 6. Scattering in configuration of Figure 4a for Spherical void and Spheroidal void.



It is worthy of note that the experimental proportionality factor β can be determined theoretically with the result:

$$\beta = \frac{R}{8\pi^2}$$

in which R is the radius of the sphere in Fig. 1 and where a factor of $(2\pi)^2$ in the denominator comes from the conversion of frequency in cycles per unit time to radians per unit time. Since $R = 1.1 \text{ in} = 2.79 \text{ cm}$, we obtain $\beta = 0.035 \text{ cm}$ which compares surprisingly well with the experimental value 0.0303.

In Table II we give the experimental results $\beta^{-1}A_2$ and the corrected results A_2 for the configurations of Fig. 1(a) with $\theta = 35^\circ$, 45° , 55° , 65° , 75° , 85° , and 90° for an oblate spheroidal void. It is assumed that the same value of β applies. The comparison with the theoretical values of A_2 is very good if the points for $\beta = 35^\circ$ and 45° are omitted. The rather significant deviations at the latter values of θ are believed to involve a substantial systematic component which is presumably due to the spurious propagation effects discussed in section B above. The comparison is also shown graphically in Fig. 6.

In Table III we give the experimental results $\beta^{-1}A_2$ and the corrected results A_2 for the configurations of Fig. 4(b) with $\gamma = -65^\circ$, -55° , -45° , -35° , 35° , 45° , 55° , 65° , 75° , and 85° for the same spheroidal void. The comparison with the theoretical values of A_2 shows even more significant systematic deviations which are clearly evident in Fig. 7. It is evident that the amplitudes of scattered waves emerging near the "north pole" (i.e., γ roughly in the neighborhood of 45°) are too large while the amplitudes of scattered waves emerging near the "equator" are too small.

We turn now to a discussion of the recent pulse-echo measurements obtained by Elsley and Nadler. Their results are compared with theory in Table IV and Fig. 8. The comparison is surprisingly good with a relative error of only 3.9%. It must be emphasized that we have used the old value of the experimental factor β , namely 0.0303. An adjustment of this value would bring down the relative error to 2.8%. It is clear that these measurements



TABLE II
SCATTERING FROM A SPHEROIDAL
VOID (CONFIGURATIONS OF FIGURE 4(a))

($a = b = 0.04$ cm, $c = 0.02$ cm, $\vec{e}^i = -\vec{e}_z$, $\vec{e}^s = \vec{e}_x \sin\theta + \vec{e}_z \cos\theta$)

θ (deg)	Theory	Experiment	
	A_2 (cm μsec^2)	$\beta^{-1}A_2$	A_2 (cm μsec^2)
0	1.402×10^{-4}	---	---
35	1.197	47.8×10^{-4}	1.45×10^{-4}
45	1.085	40.3	1.22
55	0.968	31.0	0.94
65	0.856	28.8	0.87
75	0.759	28.1	0.85
85	0.685	22.0	0.67
90	0.658	21.2	0.64

TABLE III
SCATTERING FROM A SPHEROIDAL
VOID (CONFIGURATIONS OF FIGURE 4(b))

$$(a = b = 0.04 \text{ cm}, c = 0.02 \text{ cm}, \vec{e}^i = -\vec{e}_x, \vec{e}^i = \vec{e}_x \sin 45^\circ - \vec{e}_z \cos 45^\circ \\ \vec{e}^s = \vec{e}_x \sin (45^\circ - \gamma) + \vec{e}_z \cos (45^\circ - \gamma))$$

γ (deg)	Theory	Experiment	
	A_2 (cm μsec^2)	$\beta^{-1}A_2$	A_2 (cm μsec^2)
-65	0.732×10^{-4}	22.5×10^{-4}	0.68×10^{-4}
-55	0.793	20.6	0.62
-45	0.869	22.2	0.67
-35	0.951	26.0	0.79
35	1.154	45.9	1.39
45	1.085	40.3	1.22
55	0.997	30.9	0.94
65	0.898	36.0	1.09
75	0.796	36.0	1.09
85	0.699	25.6	0.76

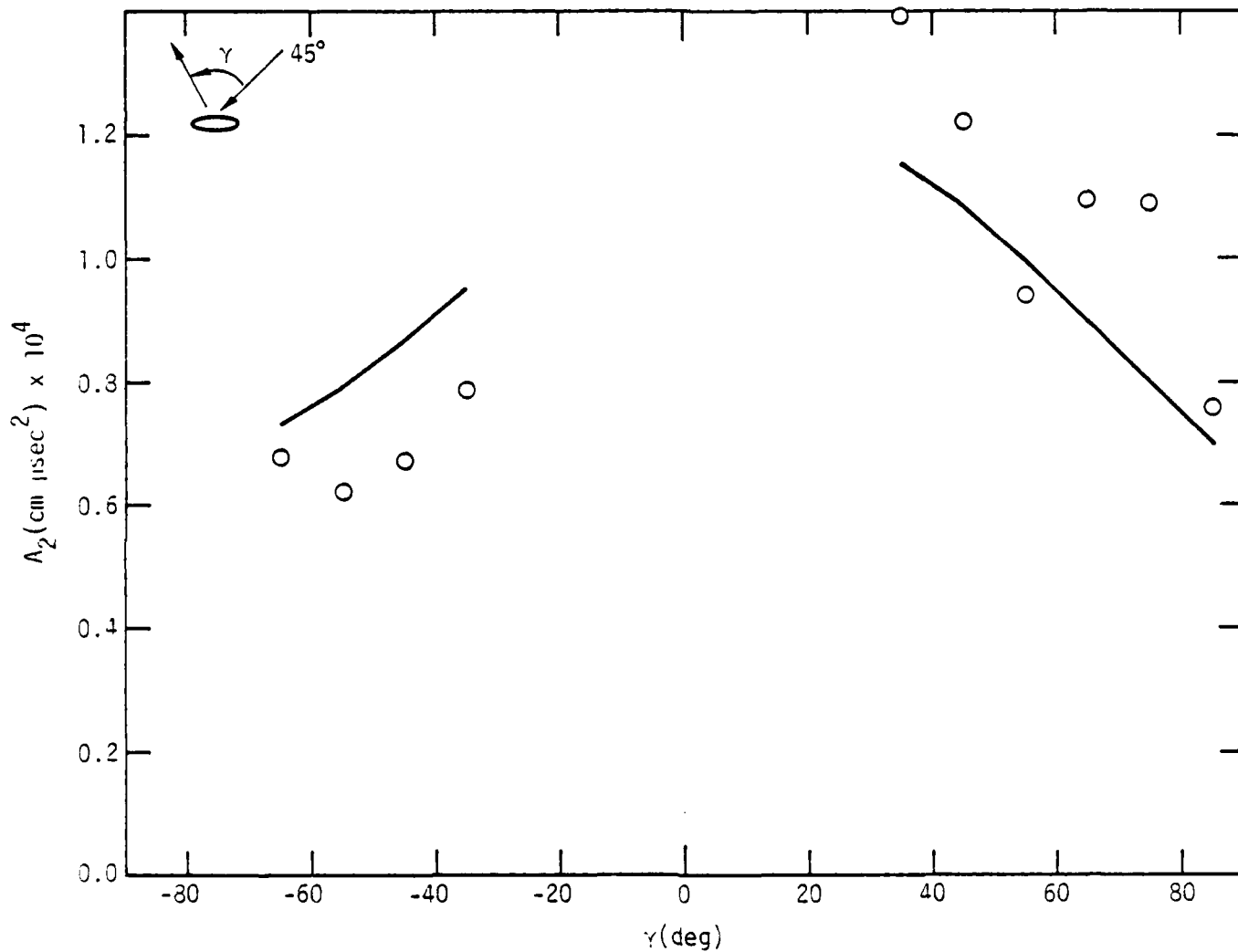


Figure 7. Scattering from Spheroidal Void - Configurations of Fig. 4b.



TABLE IV
SCATTERING FROM A SPHEROIDAL VOID
PULSE-ECHO CASE

$$(a = b = 0.04 \text{ cm}, c = 0.02 \text{ cm}, -\vec{e}_i = \vec{e}_s = \vec{e}_x \sin \theta - \vec{e}_z \cos \theta)$$

$\theta(\text{deg})$	Theory	Experiment	
	$A_2 \text{ (cm } \mu\text{sec}^2)$	$\beta^{-1}A_2 \text{ (dB)}$	$A_2 \text{ (cm } \mu\text{sec}^2)$
0	1.402×10^{-4}	-46.7	1.4×10^{-4}
15	1.374	-47.5	1.3
30	1.296	-47.65	1.25
45	1.189	-48.7	1.11
60	1.080	-49	1.08
75	0.999	-50	0.96
90	0.969	-50	0.96

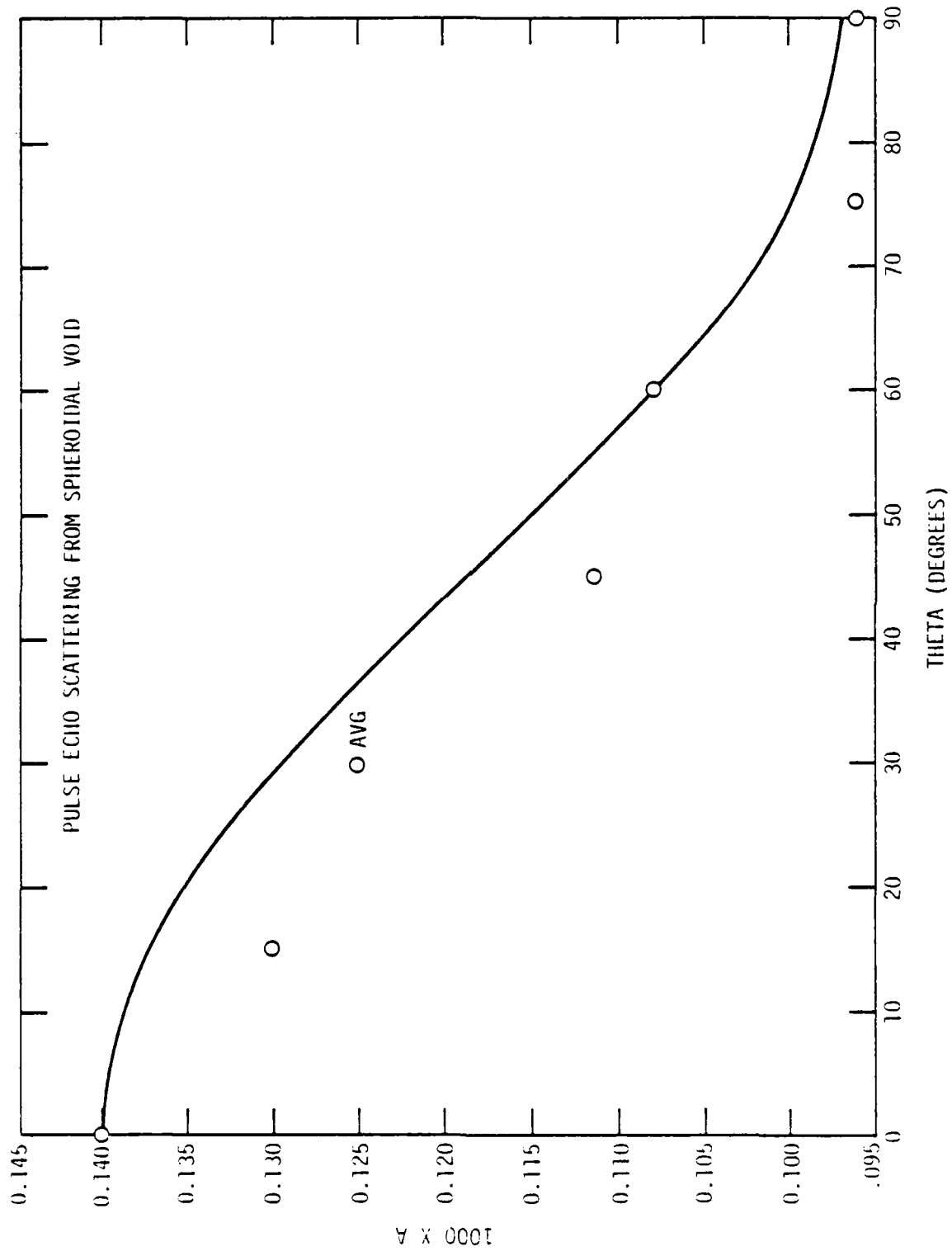


Figure 8. Pulse-echo measurements of scattering from spheroidal void.

are less vulnerable to the kinds of systematic error involved in the earlier pitch-catch measurements.

Inverse Scattering and Fracture Mechanics

In the present section we discuss the inversion procedure employed in deducing the geometrical parameters of the spheroidal void from the scattering data. We also include a short discussion of the calculation of the stress intensity factor k_I . For the purpose of inversion we assume, of course, that we do not know, a priori, the geometrical parameters--only that we know that the scatterer is a spheroidal void of some kind. The material properties of the host material are assumed known and have the values listed in Section II.

We will pursue a probabilistic approach to the problem in which we start with a statistical ensemble of scatterer properties and measurement errors and then remove the members inconsistent with the scattering data obtained from the measurements. The best estimates of the geometrical properties of the spheroidal void are then the average or most probable values of these properties in the resultant reduced ensemble. The a posteriori variances of these properties (i.e., the variances in the reduced ensemble) are used as a measure of significance or, equivalently, the "leverage" exerted by the scattering data on the properties of the scatterer.

Let us model the possible results of the n th scattering measurement (assumed in all cases to be longitudinal-to-longitudinal) by the stochastic expression:

$$y_n = f_n(x) + \nu_n, \quad n = 1, \dots, N \quad (1)$$

where y_n is a possible measured value and ν_n the measurement error. The function $f_n(x)$ is given by

$$f_n(x) = |A_2(\vec{e}_n^s, \vec{e}_n^i; x)| \quad (2)$$

where $A_2(\vec{e}^s, \vec{e}^i; x)$ is the coefficient of ω^2 in the ω -expansion of the longitudinal-to-longitudinal scattering amplitude $A(\vec{e}^s, \vec{e}^i, \omega; x)$ as discussed in Section II. The unit vector \vec{e}^i and \vec{e}^s define the directions of



the incident and scattered longitudinal elastic waves. The subscript n added to these vectors denotes the configuration used in the n th measurement. The vector x represents the geometrical properties of the void. In the spheroidal case we assume that the semi-axis lengths are denoted by a , a and c and that the axis of symmetry is given by

$$\vec{w} = \vec{e}_x \gamma_x + \vec{e}_y \gamma_y + \vec{e}_z \sqrt{1 - \gamma_x^2 - \gamma_y^2} \quad (3)$$

where \vec{e}_x , \vec{e}_y and \vec{e}_z are the unit vectors in the x , y and z directions and where γ_x and γ_y are the direction cosines associated with the x and y directions. Thus the vector x is given by

$$x = \begin{pmatrix} x_1 \\ x_2 \\ x_3 \\ x_4 \end{pmatrix} = \begin{pmatrix} a \\ c \\ \gamma_x \\ \gamma_y \end{pmatrix}, \quad (4)$$

It is to be stressed that the Cartesian coordinates (x,y,z) are defined in the laboratory frame of reference and have no necessary relation to the axis of symmetry of the spheroid.

The definitions of the stochastic model is completed by the specification of the a priori statistical properties of x and the ν_n and is characterized by the probability density (p.d.) $P(x)$. The measurement errors ν_n are assumed to be Gaussian* random variables with the properties

$$E \nu_n = 0 \quad (5)$$

$$E \nu_n \nu_{n'} = \sigma_\nu^2 \delta_{nn'} \quad (6)$$

where E is the averaging (or expectation) operator in the a priori sense.

*The assumption of Gaussianity is inconsistent with the assumption that ν_n and f_n are positive. However, this is unimportant if $f_n/\sigma_\nu \gg 1$.

Whatever is chosen for the criterion of performance of the estimation process, we must calculate the observationally conditioned p.d. of x given by

$$P(x|y) = P(y|x)P(x)/P(y) \quad (7)$$

where

$$y = \begin{pmatrix} y_1 \\ \cdot \\ \cdot \\ \cdot \\ y_N \end{pmatrix} \quad (8)$$

and where

$$P(y) = \int dx P(y|x)P(x) \quad (9)$$

From the previous assumptions we obtain

$$\log P(y|x) = - \frac{1}{2\sigma_v^2} \Psi + \text{const.} \quad , \quad (10)$$

where

$$\Psi = \sum_{n=1}^N \left(y_n - f_n(x) \right)^2 \quad (11)$$

is the sum of squares of the deviations of the y_n from the functions $f_n(x)$.

Let us consider the mean square criterion of optimality

$$\epsilon = E(\hat{x}-x)^T W(\hat{x}-x) \quad (12)$$



where $\hat{x} = \hat{x}(y)$ is the estimator of x and where W is a symmetric positive-definite matrix of weighting factors. The minimum of ϵ with respect to the functional form of $\hat{x}(y)$ is given by a posteriori average

$$\begin{aligned}\hat{x}(y) &= E(x|y) \\ &= \int dx \, x \, P(x|y)\end{aligned}\tag{13}$$

where $P(x|y)$ is given by (7). We will use the a posteriori covariance matrix defined by

$$\text{Cov}(x|y) \equiv E(x \, x^T|y) - E(x|y)E(x^T|y)\tag{14}$$

as the measure of confidence or significance. This tells us how much the a priori p.d. $P(x)$ is "narrowed down" by the experimental factor $P(y|x)$ in (7). In other words, how much "leverage" the experimental data has on the scatterer parameters defined by x .

In the explicit computations we made several approximations. The first was approximating the a posteriori average by a posteriori mode, i.e.,

$$\hat{x} = E(x|y) \simeq x_{\max}\tag{15}$$

where x_{\max} is the value of x for which $P(x|y)$ is a maximum. Alternatively, we could use a different optimality criterion, in terms of which the mode is exact. The second approximation is the computation of the a posteriori covariance by expanding ψ , defined by (11), in a power series about the point x_{\max} and ignoring terms higher than quadratic.

The first set of estimates were made with pitch-catch data as inputs. We considered both noiseless theoretical data and actual experimental data summarized in Table II. From the latter set of data we have selected three different subsets in order to elucidate the effects of the systematic errors occurring at relatively small polar angles. Explicitly, we have used data corresponding to the following sets of angles:

case (a): $\theta = 55^\circ, 65^\circ, 75^\circ, 85^\circ, 90^\circ$,

case (b): $\theta = 45^\circ, 55^\circ, 65^\circ, 75^\circ, 85^\circ, 90^\circ$, and

case (c): $\theta = 35^\circ, 45^\circ, 55^\circ, 65^\circ, 75^\circ, 85^\circ, 90^\circ$

In Table V we present estimates of a , c , γ_x and γ_y based upon the above data subsets. For the sake of verification, we also present estimates based upon theoretical noiseless test data. The estimates based on actual experimental data compare surprisingly well with the exact values, even in spite of the effects of systematic error.

In Table VI are given the a posteriori standard deviations of the scatterer parameters (i.e., the square roots of the diagonal elements of $\text{Cov}(x|y)$ defined by (14)), appropriately normalized. In the case of the semi-axis lengths a and c we divide their respective standard deviations by their best estimates. In the case of the dimensionless direction cosines γ_x and γ_y such normalization seems to be unnecessary. In these computations, the r.m.s. experimental error is assumed to have the value $\sigma_p = 10^{-5}$ (corresponding to an approximate relative r.m.s. relative error of 10%). In the cases where the experimental data, synthetic or actual, is confined to a single scattering plane (assumed to be the xz -plane in our coordinate system), the standard deviations of γ_y (the cosine of the angle between y -axis and the symmetry axis of the spheroid) is omitted because the approximation involved in its computations is not valid. In the last column two orthogonal scattering planes are assumed in the preparation of noiseless theoretical test data. In this case the computed standard direction of γ_y is meaningful and is therefore included.

It may appear inconsistent to present a posteriori standard deviations based on noiseless theoretical test data. It must be pointed out that the standard deviations of x are actually based upon the model (1) with the associated assumptions (5) and (6) giving the statistical nature of the experimental errors. The variance of the experimental errors is determined from an independent comparison of experiment with theory and not from the input data used in the estimation procedure.

We turn next to a consideration of estimates based upon pulse-echo data. Here we use the actual experimental data and noiseless theoretical test data summarized in Table IV of the last section. In Table VII we present estimates of the scatterer parameters a , c , γ_x and γ_y for both kinds of



TABLE V

ESTIMATES BASED ON PITCH-CATCH MEASUREMENTS

Parameter	Exact	Estimates			
		Experimental Data (a)	Experimental Data (b)	Experimental Data (c)	Experimental Test Data
a	.04	.037	.041	.043	.03999
c	.02	.029	.018	.016	.02001
γ_x	0	1.1×10^{-6}	9×10^{-6}	14×10^{-6}	-8×10^{-9}
γ_y		0	0	0	0

TABLE VI

NORMALIZED STANDARD DEVIATIONS (A POSTERIORI)
(A SUMMARY OF ESTIMATES BASED ON PITCH-CATCH
MEASUREMENT ERROR = 1×10^{-5})

Quantity	Experimental Data (a)	Experimental Data (b)	Experimental Data (c)	Theoretical Test Data	
				1 scatt. plane	2 scatt plane
(s.d.a)/a	0.492	0.155	0.071	0.21	0.16
(s.d.c)/c	1.38	1.09	0.62	1.28	0.95
s.d. γ_x	4.01	0.50	0.28	0.54	0.43
s.d. γ_y	-	-	-	-	0.43

TABLE VII
ESTIMATES BASED ON PULSE-ECHO MEASUREMENTS

Parameter	Exact	Estimates	
		Experimental Data	Theoretical
a	0.0400	0.03947	0.04000
c	0.0200	0.01999	0.02000
γ_x	0	-1.24×10^{-5}	2.3×10^{-6}
γ_y	0	0	0

input data. The agreement between the estimates based on actual experimental data and the exact parameter values is unbelievably good and must be regarded as partially accidental. But it is perhaps also due to the fact that it appears, as we will discuss later, that the pulse-echo data has considerably better "leverage" on the scatterer parameters than does the pitch-catch data.

In Table VIII we give the normalized standard directions (a posteriori) of the scatterer parameters in the present case of pulse-echo measurements. In the second and third columns are listed the values of these quantities based on actual experimental and on noiseless theoretical test data, respectively. In these computations, we assume that the r.m.s. experimental error has the value $\sigma_v = 0.46 \times 10^{-5}$, a result based upon the deviations between experimental and theoretical results discussed in the last section. It is to be noted the relative standard deviation of the long semi-axis length a is only about 1.6%. The corresponding quantity for the short semi-axis length c is, as usual, many times larger. The standard deviation of γ_x is about 10% which is still satisfactory for our purposes. The values of the standard deviation of γ_y have been omitted for the same reasons as before.



TABLE VIII

NORMALIZED STANDARD DEVIATIONS(A POSTERIORI)
BASED ON PULSE-ECHO MEASUREMENTS

Quantity	R.M.S. Meas. Error = 0.46×10^{-5}		R.M.S. Meas. Error = 1×10^{-5}	
	Experimental Data	Theoretical Test Data	Experimental Data	Theoretical Test Data
(s.d.a)/a	0.0168	0.0156	0.0364	0.0340
(s.d.c)/c	0.0608	0.0608	0.1320	0.1320
s.d. γ_x	0.1120	0.1057	0.2434	0.2295
s.d. γ_y	-	-	-	-

It is of fundamental interest to reconsider the normalized standard deviations, both in the present pulse-echo case and in the previous pitch-catch case, as measures of experimental "leverage" on the scatterer parameters. For the purpose of comparison, we have recomputed the normalized standard deviations in the pulse-echo with the same value of σ_v as was used in the pitch-catch case, namely $\sigma_v = 1 \times 10^{-5}$. The results are tabulated in the fourth and fifth columns. Comparing the results for noiseless theoretical test data in both cases, the reader will note that the relative standard deviation of a is about 1/6 as large in the pulse-echo case as in the pitch-catch case, the relative standard deviation of c is about 1/9 as large and, finally, the standard deviation of γ_x is about 1/2 as large. Thus the experimental leverage is markedly better in the pulse-echo case than in the pitch-case, particularly for the parameter c. The number of data points is nearly the same in both cases.

It is of critical importance to consider the significance of the present results in the context of failure prediction or, almost equivalently,

the making of an accept-vs-reject decision. Clearly, there ultimately must be developed a relatively complex theoretical structure connecting our present results with the concerns of the final user of an NDE system. In any case, a significant first step in this direction is the estimation of certain quantities of significance in fracture mechanics. One such quantity is the stress intensity factor k_I measuring the tendency of a crack in, for example, a metal to propagate under the application of a mode I stress (i.e., a uniaxial stress oriented perpendicular to the plane of the crack).

To be sure, the spheroidal void considered in the previous discussion, is hardly sufficiently degenerate to be regarded as a crack. However, based upon the discussion of Tetelman and McEvily (7), it appears that the concept can be meaningfully extended to the case of not-so-degenerate spheroidal voids. In a later communication, a detailed discussion will be given to this question. In any case the definition

$$k_I = K_I/\sigma = (\pi a)^{1/2}, \quad (16)$$

where σ is the applied stress, will suffice for our present purposes.

In Table IX we give both the best estimate \hat{k}_I and the relative standard deviation $s.d.k_I/\hat{k}_I$ for both pitch-catch and pulse-echo input data. In our view, the significance of these estimates (as measured by the relative standard deviation) is more than adequate, particularly in the pulse-echo case.

Summary and Discussion

The work reported in the previous sections can be summarized as follows:

- (1) The extraction of A_2 (the coefficient of ω^2 in the ω -expansion of the scattering amplitude) has been successfully carried out. The comparison of theory and experiment, at least in the case of our recent pulse-echo experiments, is highly satisfactory.



TABLE IX

ESTIMATE OF k_I AND RELATIVE ST. DEV.
 $(K_I/\sigma \equiv k_I (\pi a)^{1/2})$

Using Pitch-Catch Data:

Quantity	Experimental Data (a)	Experimental Data (b)	Experimental Data (c)	Theoretical Test Data	
				1 scatt. plane	2 scatt plane
k_I	0.341	0.359	0.368	0.354	0.354
$(s.d.k_I)/k_I$	0.246	0.078	.036	0.105	0.080

Using Pulse-Echo Data:

Quantity	Experimental Data	Experimental Test Data
k_I	0.352	0.354
$(s.d.K_I/k_I)$	0.008	0.008

2. The inverse scattering problem has been adequately solved under the assumption that the scatterer is a spheroidal void of some kind. With theoretical noiseless test data, the inversion procedure yielded nearly exact estimates of the parameters characterizing the spheroid. With experimental input data, the estimates of these parameters were quite satisfactory. The a posteriori standard deviations indicated that the "experimental leverage" on the parameters was generally adequate, but particularly satisfactory in the case of the long dimension a of the spheroid, a quantity of crucial importance in fracture mechanics.

Even though these results have been obtained under simplifying constraints, they strongly suggest that this approach has promise for NDE.

Clearly, there remain a host of problems for future consideration. A few of these are:

- (1) Further improvement of the post-experiment data processing in the pitch-catch case.
- (2) Isolation of a particular scatterer from competing scatterers in taking the low frequency limit.
- (3) Extension of the analysis to include general ellipsoidal inclusions (voids are a special case).
- (4) Extension to the more general case of scatterers not having ellipsoidal geometry.
- (5) Transfer of algorithms to minicomputers suitable for field equipment.
- (6) Formulation of the theoretical structure extending from the outputs of the inverse scattering algorithms to the final accept-vs-reject decision.

References

1. B. Budiansky and J. R. Rice, "On the Estimation of a Crack Fracture Parameter by Long-Wavelength Scattering," informal report, Aug. (1977).
2. G. S. Kino, "Measurement of a Crack Stress Intensity Factor", informal report, Sept. (1977).



3. J. M. Richardson, "Scattering of Elastic Waves at Low Frequencies," to be published.
4. J. E. Gubernatis, J. A. Krumhansl and R. G. Thompson, "Interpretation of Elastic Wave Scattering Theory for Analysis and Design of Flow Characterization Experiments: I. Long Wavelength Limit." Los Alamos Scientific Laboratory Report, LA-UR-76-2546, 1976.
5. W. Kohn and J. R. Rice, "Scattering of Long Wavelength Elastic Waves from localized Defects in Solids," to be published.
6. J. M. Richardson, "Scattering of Elastic Waves in the Rayleigh Limit. I. The Direct Problem," to be published.
7. A. S. Tetelman and A. J. McEively, Jr., "Fracture of Structural Materials," John Wiley, New York (1967) pp. 48-50.

PROJECT II, UNIT A, TASK 1
EXPERIMENTAL DEFINITION OF INTERACTION OF SURFACE WAVES
FROM SURFACE CRACKS

O. Buck, B.R. Tittman and W.L. Morris

Rockwell International Science Center
Thousand Oaks, California 91360

B.A. Auld

Microwave Laboratories
Stanford University, Stanford, California

Introduction

This task is directed towards an understanding of the scattering of elastic surface waves at surface cracks, from both the theoretical and the experimental point of view. During the first six months of the program the model for surface wave scattering at surface cracks in the long wavelength limit has appreciably advanced and is now at a state that allows us to calculate the backscattering coefficient for part circular and part elliptical surface cracks with the elastic wave obliquely incident on the crack. The imposed condition is, however, that $a/\lambda \leq 0.1$ where a is the crack depth and λ the wavelength of the surface wave. Since the existing literature on surface cracks does not give closed solutions for the displacement jump distribution across the crack, new methods to calculate this quantity may have to be developed to be able to calculate k_I , the normalized stress intensity factor K_I/σ , more accurately.

Several samples with semi-circular notches produced by EDM notches have been fabricated which will be used to test the theory. Three of these notches have a crack depth of 1.3mm with different root radii. The fourth and fifth specimens contain notches, having a crack depth of 0.65mm and 0.3mm, respectively. Highly efficient surface wave transducers of 5, 10 and 20 MHz have been developed which show a very high signal-to-noise ratio in the receiver mode. Extensive testing will begin shortly.



Ultrasonic Detection and Characterization of Surface Flaws

Starting from the reciprocity relation and using scattering matrix formulation it can be shown that elastic wave scattering from an arbitrary void in a solid may be characterized by the scattering coefficient

$$S_{ab} = \frac{i\omega}{4} \int_{S_F} u_i' \sigma_{ij} n_j dS, \quad (1)$$

where S_F is the surface of the void and \hat{n}_j is a unit vector along its inward normal. In the angle scattering mode of flaw detection, using two separate transducers a and b, u_i' is the displacement field at the surface at the void due to an input at one transducer and σ_{ij} is the unperturbed stress field at the flaw due to an incident wave launched by the second transducer. For direct backscatter observed at a single transducer the two fields are referred to the same transducer. This scattering relation was first demonstrated, using the elastic reciprocity relation for elastic wave scattering coefficients defined at the emitting surfaces of the transducers.^{1,2,3} It was noted that a significant advantage of the reciprocity relation analysis over the spherical far field analysis of the problem is that the effects of transducer diffraction are included directly in the calculation. Subsequently, it was shown that use of the piezoelectric reciprocity relation allows one to derive in a simpler way scattering coefficients measured at the electric terminals of the transducers.⁴ The scattering coefficient is again given by Eq.(1), but with u_i' and σ_{ij} now referred to unit power at the electrical terminals of the transducers. There is nothing in the derivation that excludes application to a surface crack, in which case the surface S_F in Eq.(1) is closed along the original surface of the unflawed specimen, and the piezoelectric derivation verifies immediately the validity of the scattering formula for any type of piezoelectric surface wave transducer. Recently, the derivation has been extended to electromagnetic and ferromagnetic types of surface wave transducers.

The piezoelectric scattering formula was applied in Reference 4 to the problem of a Rayleigh wave normally incident on a half penny-shaped crack. This calculation used the quasistatic approximation, where n_i' is evaluated on the basis of the static displacement produced by the stresses

associated with the incident wave. For a Rayleigh wave on an isotropic substrate, the incident stress field near the surface is

$$\frac{(\sigma_{zz})_{y=0}}{P_R^{1/2}} = \frac{4\mu}{V_R} \left(1 - \left(\frac{V_S}{V_e} \right)^2 \right) \left(\frac{f_z}{P V_S^2} \right)^{1/2} \omega^{1/2} \quad (2a)$$

$$\frac{(\sigma_{xx})_{y=0}}{(\sigma_{zz})_{y=0}} = \frac{1 - 2 \left(\frac{V_S}{V_e} \right)^2}{2 \left(1 - \left(\frac{V_S}{V_e} \right)^2 \right)} = \text{Poisson's ratio } \nu \quad (2b)$$

$$\frac{(\sigma_{yz})_{y=0}}{(\sigma_{zz})_{y=0}} \cong \frac{\frac{V_S}{V_R} \frac{\alpha_{te}}{\omega/V_S} (\alpha_{ts} - \alpha_{te}) y}{1 - \left(\frac{V_S}{V_e} \right)^2}, \quad (2c)$$

where

P_R = Rayleigh wave power density per unit width

μ = shear modulus

$$\begin{cases} \alpha_{te}^2 = \left(\frac{\omega}{V_r} \right)^2 - \left(\frac{\omega}{V_e} \right)^2 \\ \alpha_{ts}^2 = \left(\frac{\omega}{V_r} \right)^2 - \left(\frac{\omega}{V_s} \right)^2 \end{cases}$$

and V_R , f_z are given in terms of the shear-longitudinal velocity ratio by Fig. 1. According to Eq.(2c) the stress σ_{xy} is negligible compared to σ_{zz} and σ_{xx} at points sufficiently close to the surface. For example, in aluminum ($V_S/V_e = 0.475$). Equation (2c) is less than 0.1 for $\frac{\omega}{V_S} y = k_s y < 0.13$. Over the same range of y the variations on σ_{zz} and σ_{xx} are also less than 10%. One can therefore approximate u_i' in Eq.(1) by the static displacement due to the uniform stress in Eqs.(2a) and (2b) for a surface crack with depth d satisfying the condition $k_s d \geq 0.15$.

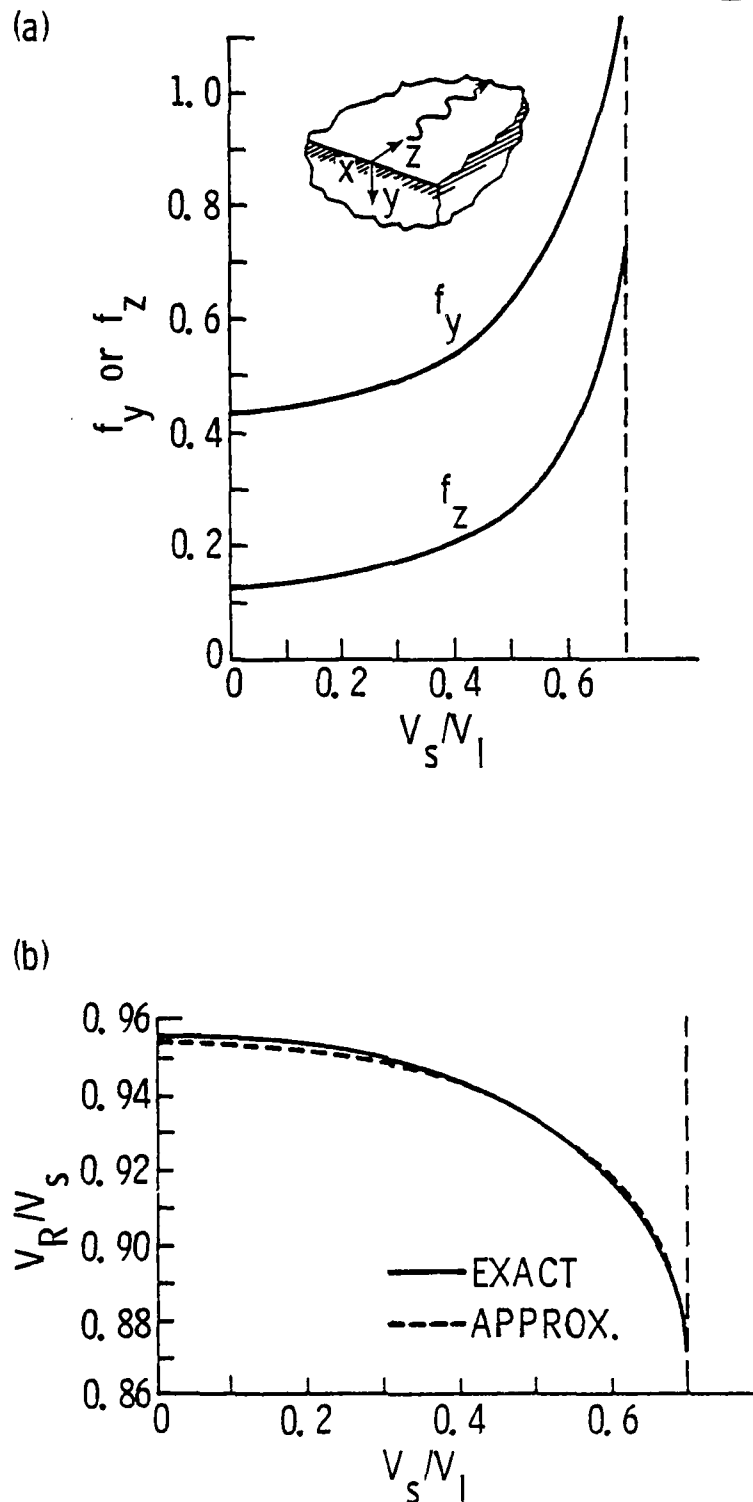


Fig. 1 (a) Field parameters f_y and f_z as a function of the bulk shear wave velocity V_s and the bulk longitudinal wave velocity V_l . (b) Isotropic Rayleigh wave velocity V_R as a function of the bulk shear wave velocity V_s , and the bulk longitudinal wave velocity V_l .



Reference 4 treated backscatter of a normally incident Rayleigh wave from a half-penny-shaped surface crack. In this case, only σ_{zz} enters into the calculation and Eq.(1) reduces to

$$\Gamma = \frac{i\omega}{4} \int_{\text{crack}} \Delta u_z \sigma_{zz} dS \quad (3)$$

$\Delta u_z'$ being the displacement jump across the crack. Many numerical analyses of a half penny-shaped surface crack opened under normal stress have been reported in the literature⁵⁻⁷ but these do not give the distribution of the displacement jump $\Delta u_z'$ required in evaluating Eq.(3). They give, rather, the distribution of stress intensity factor around the periphery of the half crack in terms of the stress intensity factor of a full crack of the same shape within the volume of the body. In the case at a half penny-shaped crack on the surface the stress intensity factor differs from the volume case by less than 10% over much of the crack periphery and has a maximum difference in the neighborhood of 20%. It was therefore judged appropriate to approximate the displacement jump in Eq.(3) by its value for a penny-shaped volume crack

$$\Delta u_z' = k_I \sigma_{zz} \frac{2}{(\pi a)^{1/2}} \frac{1-\nu}{\mu} (a^2 - r^2)^{1/2}, \quad (4a)$$

where

a = crack radius

and

$$k_I = 2 \sqrt{\frac{a}{\pi}} \quad (4b)$$

is the normalized mode I stress intensity factor. The integral of this expression over the area of the actual surface crack is easily evaluated and gives an electrical reflection coefficient at the transducer input

$$\Gamma_{\text{semicircle}} = \frac{i\omega}{3} \frac{1-\nu}{\mu} \sigma_{zz}^2 a^3, \quad (5)$$



where σ_{zz} is the applied stress at the crack due to unit electrical power at the transducer. This result is subject to the approximation discussed in the preceding paragraph and would be expected to develop significant errors for $k_{sa} \geq 0.5$, or $a \geq 0.1\lambda$. For example, in the case of a surface crack with 1mm radius in aluminum the maximum allowed elastic wave frequency would be 300 kHz. For frequencies higher than this the variations of applied stress across the surface of the crack must be considered. This question is now being examined within the framework of the extended quasistatic approximation previously developed for internal flaws. Difficulties to be anticipated in this type of calculation are discussed below.

Within the limitations of the above approximations one can also calculate scattering from part circular and part elliptical surface cracks. That is

$$\Gamma_{\text{part circle}} = \frac{i\omega}{2} \frac{1-\nu}{\mu} \sigma_{zz}^2 a^3 \left[\left(\frac{d}{a}\right)^2 - \frac{1}{3} \left(\frac{d}{a}\right)^3 \right] \quad (6)$$

where a is the crack radius and d is its maximum depth, and

$$\Gamma_{\text{part ellipse}} = \frac{i\omega}{4} \frac{\pi}{E(k)} \frac{1-\nu}{\mu} \sigma_{zz}^2 ab^2 \left[\left(\frac{d}{b}\right)^2 - \frac{1}{3} \left(\frac{d}{b}\right)^3 \right] \quad (7)$$

where b is the minor axis (normal to the surface) and d is the maximum depth, $k^2 = 1 - b^2/a^2$, and $E(k)$ is the complete elliptic integral of the 2nd kind. Another case that can be treated in the same approximation is direct backscatter of a Rayleigh wave obliquely incident on a part circular crack (Fig. 2). In the wave coordinate system the stresses applied to the crack are given by Eqs.(2a) and (2b). These transform in the crack coordinate system to a normal tension

$$\sigma_{z'z'} = \sigma_{xx} \sin^2 \theta + \sigma_{zz} \cos^2 \theta \quad (8)$$

and a parallel shear

$$\sigma_{x'z'} = \frac{\sigma_{xx} - \sigma_{zz}}{2} \sin 2\theta \quad (9)$$

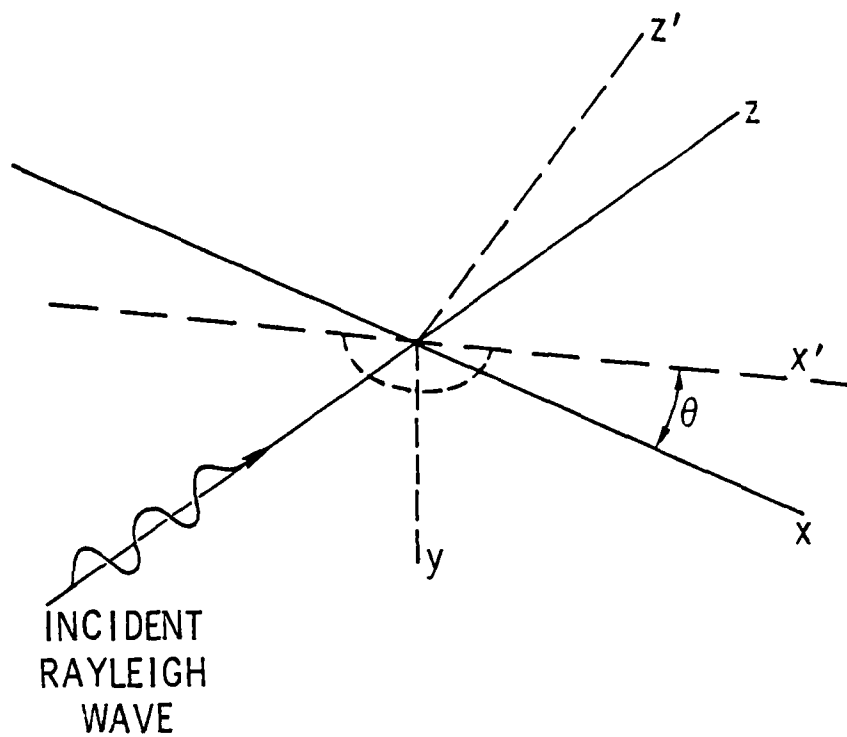


Fig. 2 Rayleigh wave obliquely incident on a part circular surface crack.



Following the same steps as in the previous calculations one obtains, using Ref. 8 for the stress displacement jump across the crack

$$\Gamma_{\text{part circle}} = \frac{i\omega}{2} \frac{1-\nu}{\mu} \left[\sigma'_{zz}{}^2 + \frac{2}{2-\nu} \sigma'_{xz}{}^2 \right] a^3 \left[(d/a)^2 - \frac{1}{3} (d/a)^3 \right] \quad (10)$$

where all of the angle dependence is contained in the curly brackets. For aluminum (Poisson's ratio $\nu = \frac{\sigma_{xx}}{\sigma_{zz}} = 0.355$)

$$\Gamma_{45^\circ} = 0.587 \Gamma_{0^\circ}$$

and

$$\Gamma_{90^\circ} = 0.126 \Gamma_{0^\circ}$$

The problem of 90° angle scattering is also straightforward in the quasistatic approximation.

As noted previously, all of the above calculations used in Eq.(3) the displacement jump corresponding to a full internal crack of the appropriate shape (circle or ellipse). That is, the perturbation of the displacement jump due to the presence of a free surface is not taken into account. The required distribution of Δu_z for a surface crack is not available in the literature, but a number of papers give the variation of normalized stress intensity factor k_I with position along the periphery at the crack. Since σ_{zz} in Eq.(3) has been shown to be constant for a sufficiently small crack and can therefore be removed from the integral, it is natural to look to the Budiansky-Rice relation⁹

$$\int_{\text{crack surfaces}} \Delta u_z dS = \frac{1}{3} \frac{1-\nu}{\mu} \sigma_{zz} \int_{\text{crack periphery } C} \rho_C k_I^2 de \quad (11)$$

as a means of evaluating the required integral in terms of the variation of k_I on the crack periphery. In Eq.(11) ρ_C is the perpendicular distance from an origin within the crack surface to the target line at d . It is easily shown that the contour integral is independent of the origin of ρ_C for cracks bounded by simple closed curves (circle, square, ellipse) and far

removed from any free surface. However, it is apparent when one examines a surface crack that this is no longer true in such cases. A simple example is the rectangular surface crack mentioned in Reference 10 (Fig. 3). For this geometry, ρ_c is a constant on each edge of the crack, and the integral on the right-hand side of Eq.(11) is independent of the choice of origin 0 in Fig. 4 of the distribution of k_I is the same on opposite edges of the rectangle. This will clearly not be true if edge AD is on the surface and has a k_I that is zero or, at least, has a different distribution of k_I than the edge BC. The same problem can be shown to exist for the part circular crack discussed above.

One may conclude, then, that problems exist in applying Eq.(11) to the calculation of scattering from surface cracks. This is an important question because the existing literature on surface cracks, whether uniformly or nonuniformly loaded, gives only distributions of normalized stress intensity factor along the edge of the crack and not the displacement jump distribution on the face of the crack. It is important to solve these problems concerning the applicability of Eq.(11) to surface cracks because the only alternative appears to be either lengthy numerical calculations of the displacement jump or some kind of, as yet undeveloped, variation method. In the case of a nonuniformly loaded crack (ka not small), one has the additional difficulty that σ_{zz} in Eq.(3) is nonuniform and cannot be removed from the integral.

However, first experimental indications are (see Appendix to this task) that half-penny shaped cracks of different crack radii show noticeable differences in the structure of the backscattered signals. The structures show well-defined peaks and nulls, whose spacings scale roughly as the crack radii. These observations are thought to be helpful for further development of the present theory.

Specimen Fabrication and Transducer Design

This part of the task is devoted to the development of techniques for experimental determination of the scattering factors from surface flaws. The first type of flaws produced are EDM notches of three size ranges as shown in Fig. 5. Their geometry has been chosen such that in a series of survey experiments the extent of the ultrasonic responses to the EDM notches can be

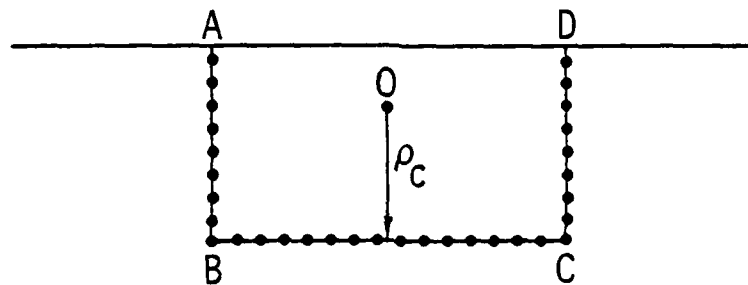


Fig. 3 Rectangular surface crack geometry.

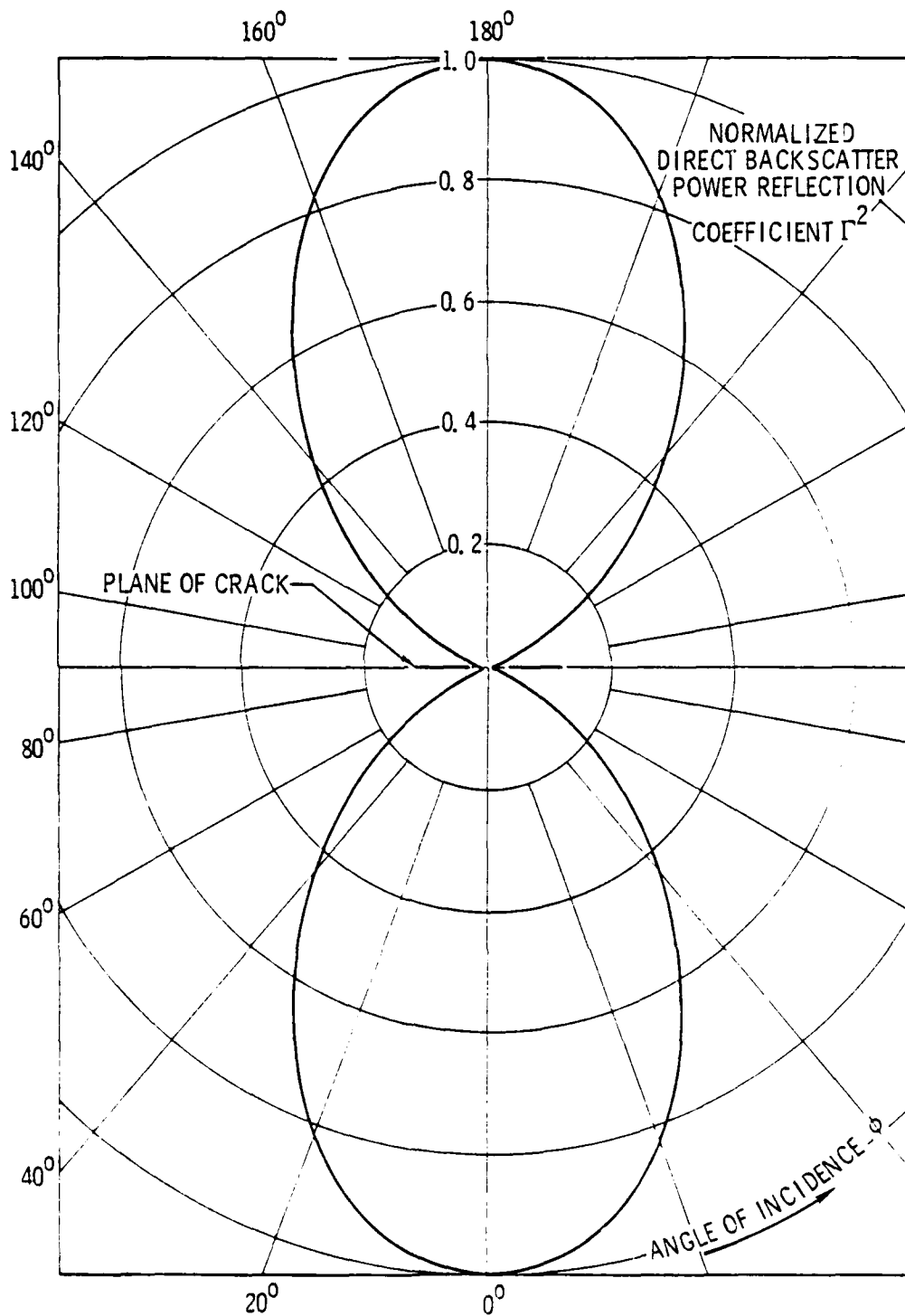
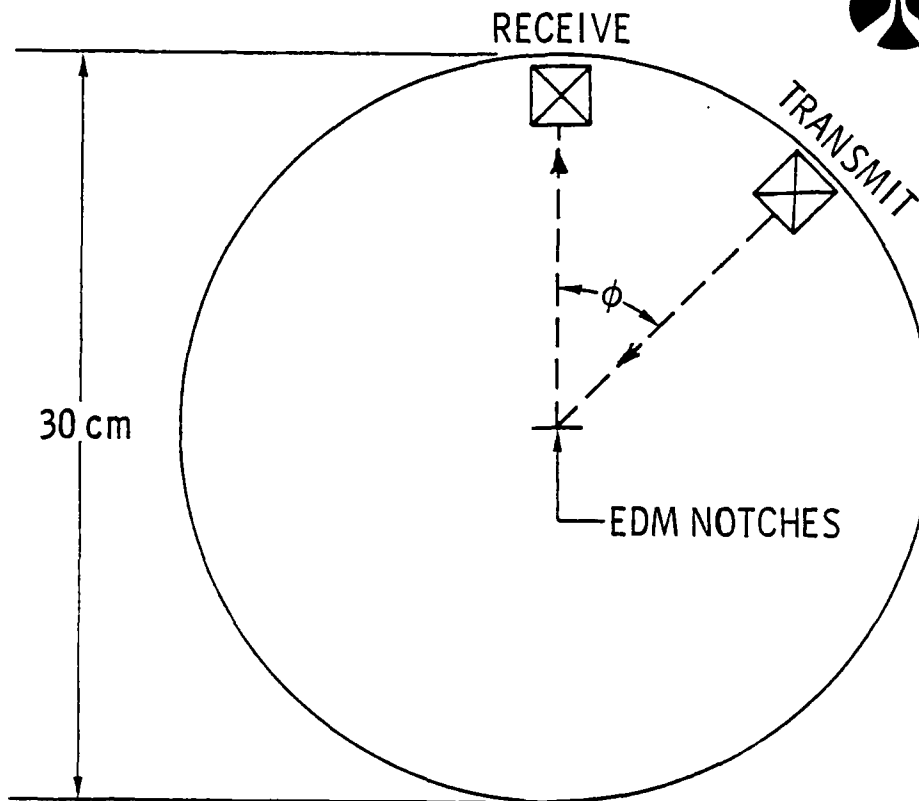


Fig. 4 Rayleigh wave backscattering from a half penny-shaped surface crack in aluminum.



DETAILS ON EDM NOTCHES

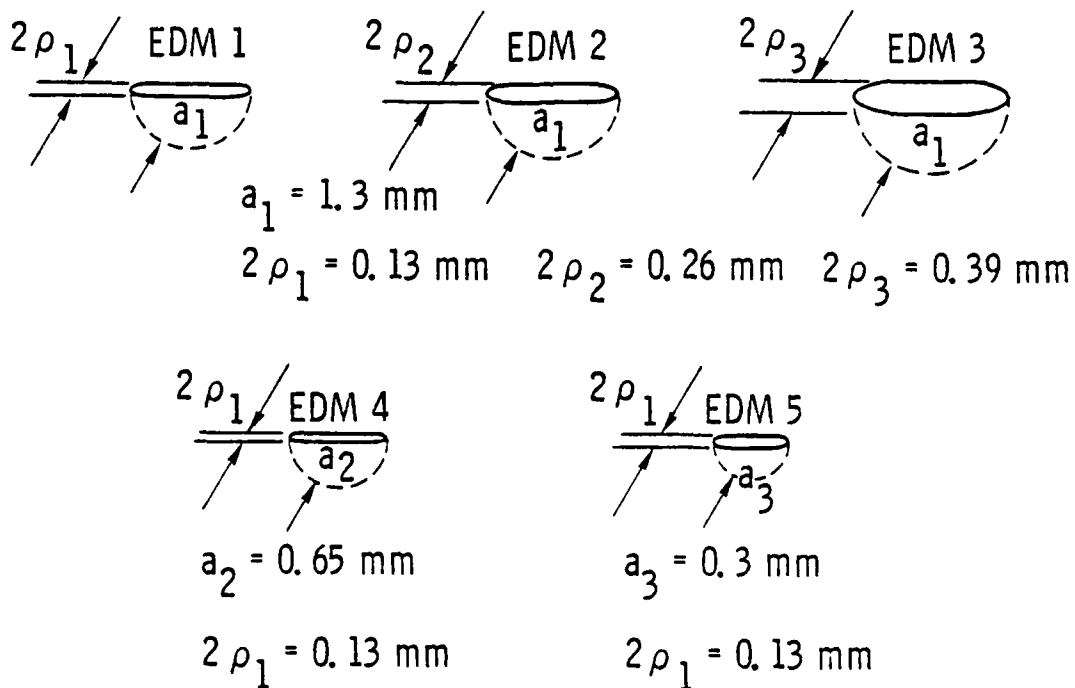


Fig. 5 Geometry of EDM notches and experimental arrangement.

calibrated. The aluminum specimens, containing the notches, are disc shaped and have a diameter of about 30cm. Surface wave transducers, to be described briefly below, will be placed close to the periphery of the discs. The chosen geometry thus guarantees that the notches are in the far field of these transducers. The transducers are basically made out of PZT glued to flint glass wedges. The acoustic coupling of the wedges to the aluminum is achieved by water, as shown in Fig. 6. The wedge can be adjusted to achieve high surface wave generation efficiency. Figure 7(a) shows the received signal (5 MHz) for a wave being directed under 22° towards EDM4 and received perpendicular to the flaw. The signal-to-noise ratio is better than 20 dB, which is considered to be excellent. The surface wave signal disappears completely, as expected, if a damping object (thumb) is placed in its path (see Fig. 7(b)). First experimental data on the relative power backscattered from EDM 4 as a function of incident angle ϕ are shown in Fig. 8 (5 MHz). As can be seen, there are some indications of a fine structure in this curve (similar to that reported in the Appendix). Future experiments will particularly concentrate on this aspect.

After full characterization of the scattering coefficients for all five EDM notches as a function of frequency, and angle of incidence of the acoustic wave over the periphery of the discs, the experimental work will continue with the production of true fatigue cracks. Our first efforts then will concentrate on the comparison of the EDM results with those obtained from the fatigue cracks. Previous work by other investigators indicated that significant differences may exist, which may be caused by a variety of reasons, such as crack closure, e.g. It is our intent to determine and characterize the differences and feed the information into the theoretical models as quickly as possible.

Coupling of Scattering Experiments to Fracture Mechanics

The notches produced in the experimental part of the program have been fully described from a fracture mechanics point of view. Of particular interest to us seemed a comparison of the normalized stress intensity factor

$$k_I = \frac{K_I}{\sigma} \quad (12)$$

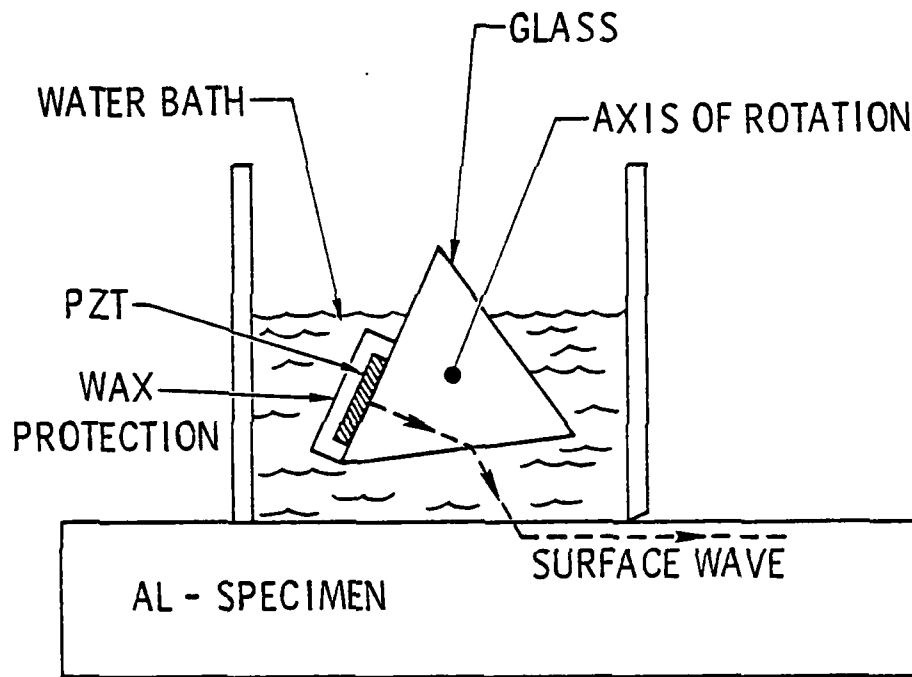
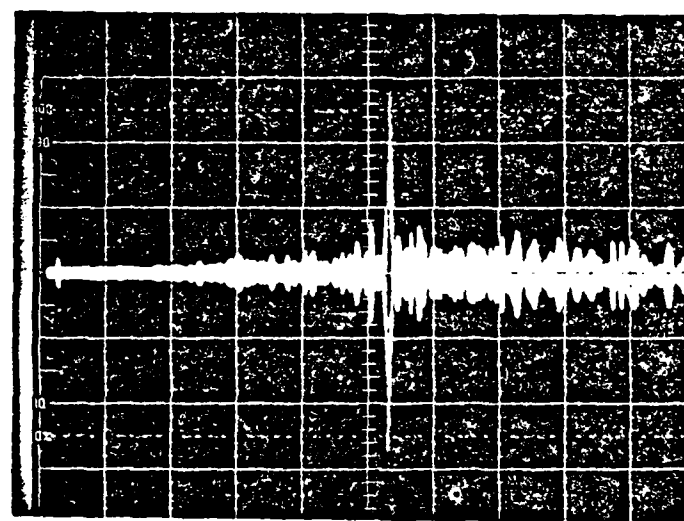


Fig. 6 Surface wave transducers (5, 10, 20 MHz).

(a)



SURFACE WAVE SIGNAL

(b)

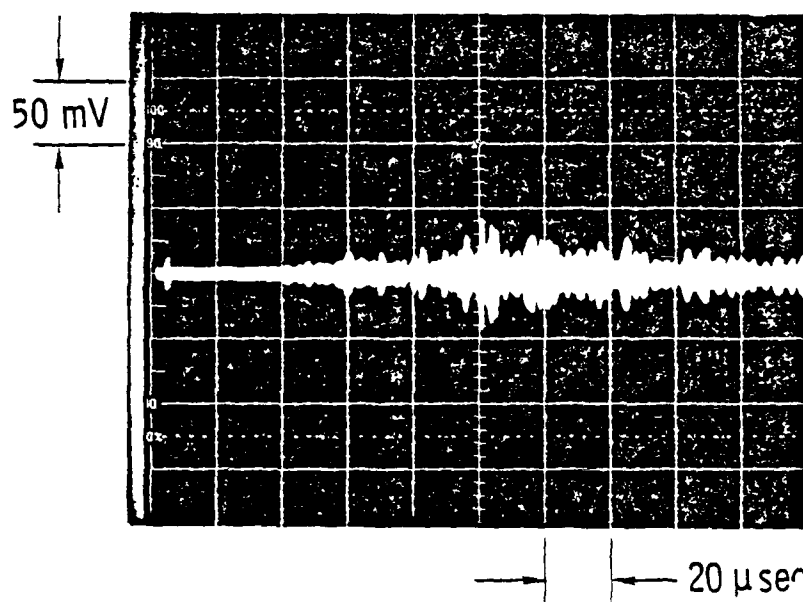


Fig. 7 (a) Surface wave signal received from EDM 4 (Fig. 5) for $\phi = 220^\circ$, $f = 5$ MHz. (b) Same as above, demonstrating disappearance of surface wave signal if damping object in path of the wave.

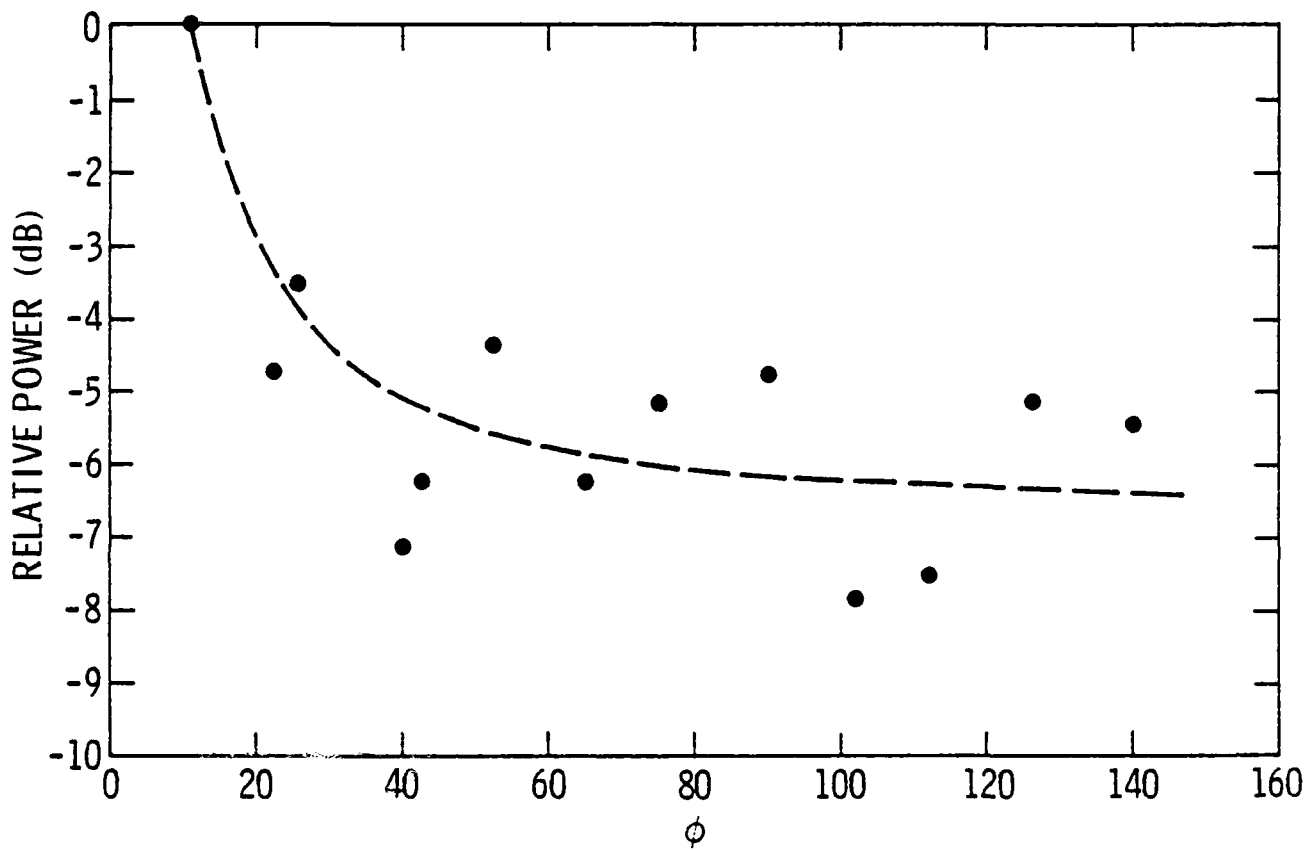


Fig. 8 Relative power received from EDM 4 (Fig. 5) as a function of ϕ .

which was mentioned already in Part A of this Task. The quantity K_I in Eq.(12) is the well-known stress intensity factor (here taken to be in mode I, which means with the applied stress σ normal to the flow). Variations in K_I (usually referred to as ΔK_I , the stress intensity range) due to applied stress variations, $\Delta\sigma$, induce fatigue crack growth. As will be seen also, the reduced stress intensity factor k_I depends mainly on the geometry of the flaw. Since EDM notches have a finite width, we will thus have to consider at least three quantities to determine K_I : a , the crack depth; $2c$, the crack length; and ρ , the crack root radius (see Fig. 5). For the present EDM notches $c = a$ (semicircular EDMs). As was shown by Budiansky and Rice⁹, k_I is directly related to the ultrasonic scattering from flaws. In order to compare scattering from EDMs with true fatigue cracks ($\rho \times 0$) it is thus necessary to evaluate k_I as completely as possible.

(a) Linear Elastic Analysis

As was discussed by Wilhelm¹¹ for a crack with tip radius ρ , the stress at the tip is governed by the stress intensity factor. Assume a cut perpendicular to the EDM notch, and let us approximate this cut by an ellipse with major axis a and radius ρ at the vertex of this ellipse, this stress intensity factor is given by

$$K_t = \frac{\sigma_m}{\sigma} = \left[1 + 2\sqrt{\frac{a}{\rho}} \right] \quad (13)$$

Then a proportionality has to exist between K_I and σ_m where σ_m is the maximum stress near the crack tip due to the presence of the flaw. This relation is of the form¹¹

$$K_I = \text{Const } \sigma_m \sqrt{\rho} \quad (14)$$

Using Eq.(13), Eq.(14) becomes

$$K_I = \text{const } \sigma \left[1 + 2\sqrt{\frac{a}{\rho}} \right] \sqrt{\rho} \quad (15)$$

In the limit $\rho = 0$

$$K_I = 2 \text{ const } \sigma \sqrt{\rho} \quad (16)$$



In order to determine the proportionality control, we compare Eq.(16) with the elasto-plastic analysis of a crack.

(b) Elasto-Plastic Analysis

The stress intensity factor (in mode I) for put-through cracks has been calculated by Irwin¹² using elasto-plastic analysis to be

$$K_I = 1.1 \sigma \sqrt{\frac{\pi a}{Q}} \quad (17)$$

where Q is given by

$$Q = \phi^2 - 0.212 \left(\frac{\sigma}{\sigma_y} \right)^2 \quad (18)$$

(ϕ the elliptical integral, $\phi = \int_0^{\pi/2} [\sin^2 \theta + (\frac{a}{c})^2 \cos^2 \theta]^{\frac{1}{2}} d\theta$, and σ_y = yield stress).

Comparing Eqs.(16) and (17) we obtain

$$\text{Const} = 0.55 \sqrt{\frac{\pi}{Q}} \quad (19)$$

Inserting this value into Eqs.(15) and (12) yields

$$k_I = 0.55 \sqrt{\frac{\pi}{Q}} \left[1 + 2 \sqrt{\frac{a}{\rho}} \right] \sqrt{\rho} \quad (20)$$

As previously mentioned k_I thus is mainly determined by the geometry of the crack (except for a stress correction in Q , as seen from Eq.(18)). Comparison of Eqs.(4a) and (20) shows that for $\rho = 0$, the two relations for k_I agree, if $Q \approx 3$ which is a reasonable value for semicircular cracks. This Eq.(20) is plotted in Fig. 9 for the EDMs 1-3 geometries. The $\rho = 0$ value corresponds roughly to that of a sharp fatigue crack. The parameter σ/σ_y was varied between 0 and 1, showing that the effects of any externally applied load on k_I (for that geometry) is not larger than about 5% and that the effect of on k_I is not more than about 16% (including a "true" fatigue crack). Thus we expect that the scattering coefficients for EDMs 1-3 should show very little differences. From the above calculations, we should be able to estimate the scattering coefficient for a true fatigue crack thus giving

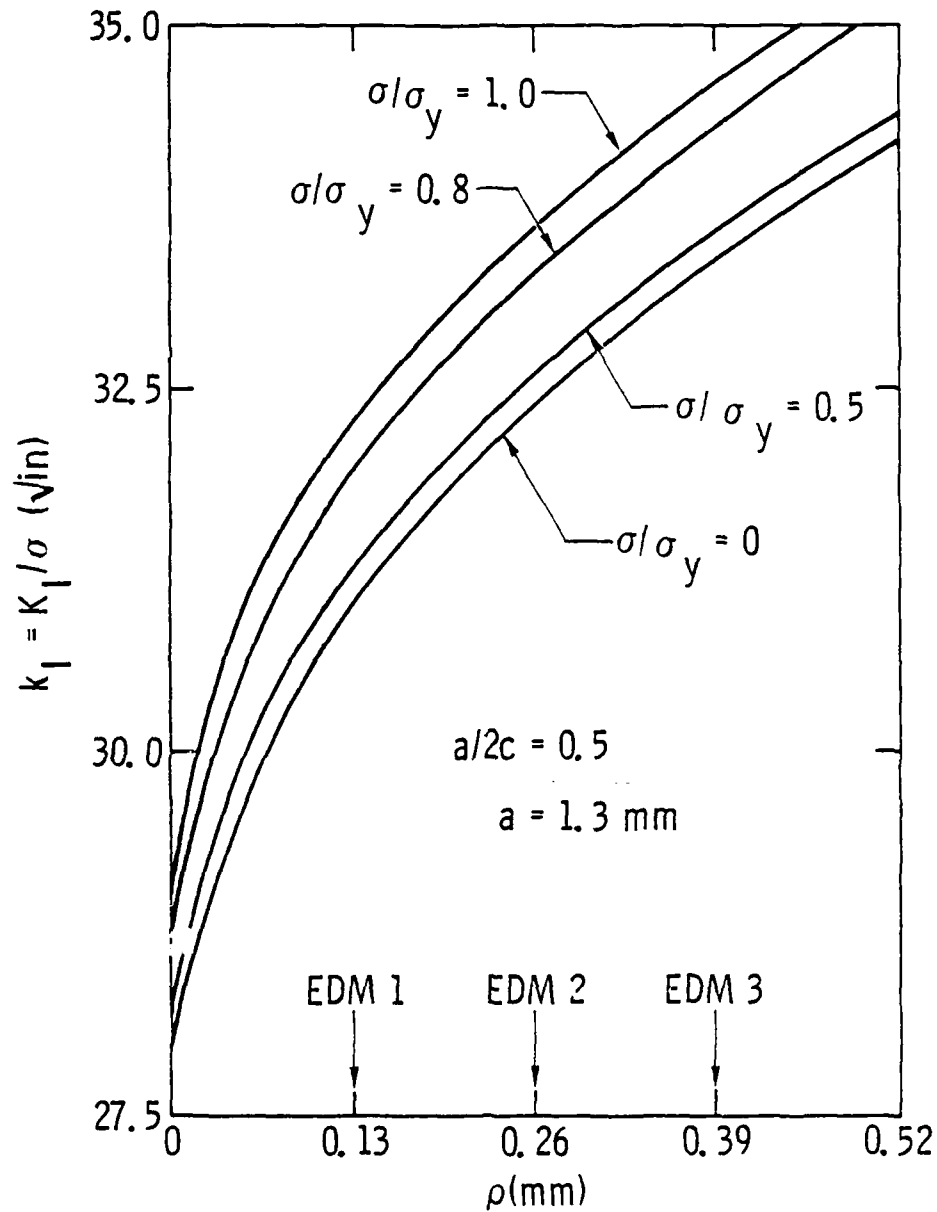


Fig. 9 k_I as a function of semicircular surface flaw root radius ρ (see Fig. 5) with normalized stress σ/σ_y (σ_y = yield stress) as a parameter.



Rockwell International

Science Center
SC595.32SA

estimation on effects due to closure or rough fracture surfaces on the scattering. To separate the latter effects from each other, an external applied stress can be applied which will eliminate the crack closure stress. Thus, we should get a good idea on the calibrations by various fracture mechanics properties on the scattering coefficient and thus on the reliability of k_I measurements using surface waves.

REFERENCES

1. T.M. Wagh and G.S. Kino, 1976 Ultrasonic Symp. Proc. pp 125-128 (1976).
2. G.S. Kino, Project I, Unit IV, Task I, pp. 159-175, Interdisciplinary Program for Quantitative Flaw Definition, Rockwell International, June 30, 1977.
3. G.S. Kino, Ginzton Lab. Report No. 2742, Sept. 1977.
4. B.A. Auld and G. Elston, Project. I, Unit V, Task 2, pp 267-270, Interdisciplinary program for Quantitative Flaw Definition, Rockwell International, June 30, 1977.
5. F.W. Smith, A.F. Emery and A.S. Kobayashi, "Stress Intensity Factors for Semicircular Cracks, Part 2 - Semi-infinite Solid," J. Appl. Mech. 34, pp 953-959 (1967).
6. J.L. Swedlow, "The Surface Crack: Physical Problems and Computational Solutions," ASME (1972).
7. F.W. Smith and D.R. Sorensen, "The Semi-Elliptical Surface Crack - A Solution by the Alternating Method," Int. J. Fracture 12 pp 47-57 (1976).
8. C.M. Segedin, "Note on a Penny-Shaped Crack Under Stress," Proc. of the Cambridge Phil. Soc., Vol. 47, pp 396-400 (1951).
9. B. Budiansky and J.R. Rice, "On the Estimation of a Crack Fracture Parameter by Long Wavelength Scattering," Preprint of a Report for ARPA Materials Research Council, July, 1977.
10. J.P. Gyskenyesi and A. Mendelson, "Stress Analysis and Stress-Intensity Factors for Finite Geometry Solids Containing Rectangular Surface Cracks," J. Appl. Mech. 44, pp 443-448 (1977).
11. D.P. Wilhem, "Fracture Mechanics Guidelines for Aircraft Structural Applications," Technical Report AFFDL-TR-69-111, Feb. 1970.
12. G.R. Irwin, "Crack-Extensions Force for a Put-Through Crack in a Plate," J. Appl. Mech. 29, pp. 651-654 (1962).



MEASUREMENTS OF THE ANGULAR AND FREQUENCY DEPENDENCE
OF ACOUSTIC SURFACE WAVE SCATTERING FROM SURFACE CRACKS⁺

B.R. TITTMANN, Groupe de Physique des Solides, Université Paris VII,
and Science Center Rockwell International

and

M. DE BILLY, F. COHEN-TENOUDJI, A. JUNGMAN, G. QUENTIN
Groupe de Physique des Solides de l'Ecole Normale Supérieure*,
University Paris VII.

Summary

The objective of this work is the experimental definition of the interaction of acoustic surface waves with cracks to form the basis of defect characterization techniques and to test and guide theoretical developments. We report here preliminary results obtained at low frequencies (2 - 10 MHz) on samples of glass and steel with notches as defects and at high frequencies (100 MHz) on ceramic samples with cracks (produced with the indentation technique).

The first phase of the work saw the construction of three measurement systems based on different approaches to surface wave detection (transmission) :

- (a) the use of interdigital transducers on piezoelectric delay lines for work in the 100 MHz frequency range;
- (b) the use of narrow band contact wedge transducers for work in the 2 - 25 MHz frequency range and
- (c) the use of broad-band waterbath transducers (2 - 10 MHz) to allow Fourier Analysis with an on-line computer.

⁺ This work was carried out at the "Groupe de Physique des Solides de l'Ecole Normale Supérieure", during B.R. Tittmann's stay as "Professor Associé" at the University of Paris VII, as the beginning of a cooperative research program with the Science Center of Rockwell International. This preliminary work has not been supported by any contract from DARPA-AFML.

* Laboratoire associé au C.N.R.S.

The most important result of the measurements during the second phase of the work is the observation of a series of sharp nulls in the angular dependence of the backward scattered surface wave amplitude. The position and spacing of the nulls scale with the size of the cracks in a simple way and suggest a possible approach to the length estimation of surface cracks.

Introduction

Surface cracks are an increasingly important source of fracture in structural materials and have recently been given considerable attention from the point of view of characterization towards a more effective failure prediction (1-6). The cracks are typically generated during finishing operations such as grinding and machining and consist of arrays of semi-elliptical cracks (4). The previous methods of characterization with dye penetrant techniques and statistical methods have recently been augmented by acoustic surface wave techniques (6). Here we present preliminary results on studies intended to aid in the identification of individual cracks which could subject components to anomalously severe surface damage.

Experimental technique

Three measurement systems have been constructed based on different approaches to surface wave detection. The first of these uses an interdigital transducer on a piezoelectric delay line which is inclined at an angle to the sample surface so as to couple the surface wave from the delay line through a coupling medium onto the sample (7). Two such delay lines have been incorporated into a goniometer which was constructed to allow a precision adjustment of the angle which the delay lines make with the sample surface and to permit the rotation of the sample and the delay lines on an individual basis for measurements of the angular dependence of the scattered waves in pitch-catch or pulse-echo. The electronic apparatus supporting this system is a Matec Model 9000 with the Model 960 (10 MHz - 300 MHz) Plug-In, and a low-noise wide band amplifier.

The second system uses narrow-band contact wedge transducers as transmission and receiving elements, which are commercial units at nominally 2.2, 5 and 10 MHz. The transducers and sample are mounted in a fixture which allows the precision rotation of the transducer around an axis



through the surface flaw while maintaining good coupling between transducer and sample. The supporting electronics is an Arenberg pulser plus receiver.

The third system uses a commercial broad-band waterbath transducer which sends bulk waves at the critical angle at a partially submerged sample with the surface flaw at the center of rotation of the sample. This system is at present limited to pulse-echo experiments only but has the advantage of allowing Fourier analysis of the received pulse with an on-line computer to provide quasi-continuous frequency dependence information over the range of frequency : 2 - 10 MHz. The electronic system here is a Velonex pulser as transmitter and low noise wide band amplifiers as receiver.

The samples used in the experiments were notches or grooves in steel and crown glass plates for the low frequency measurements and artificial cracks put into commercial hot-pressed silicon nitride (NC 132) by the indentation technique (8), for the high frequency measurements. Before the experiments on the simulated defects (described in more detail with the results) calibration runs were performed where possible with round defects as scattering centers to show that the apparatus would not introduce a background angular dependence. In all cases the measurements were performed with the defect in the far-field of the transducers.

Results

The experimental results are summarized in Figs. 1 - 4, where representative results for the low frequency narrow-band measurements are given in Figs. 1 and 2, the high frequency work on ceramics is summarized in Fig. 3 and feasibility tests for broad-band experiments are demonstrated in the photos of Fig. 4.

Fig. 1 shows a plot of the relative power (dB) as a function of the back scatter angle (degrees) in a pulse-echo experiment at 2.2 MHz ($\lambda_{\text{Rayleigh}} = 1.35 \text{ mm}$) with a half-penny shaped slot (radius $a = 1.0 \text{ mm}$, width $c = 0.45 \text{ mm}$) notched into a commercial steel plate. The curve shows a strong fall-off of scattered power with angle in a way symmetric with respect to the normal to the long dimension of the slot. This fall-off with angle has been typical of all our measurements without regard to defect size or frequency although the rate of fall-off appears very

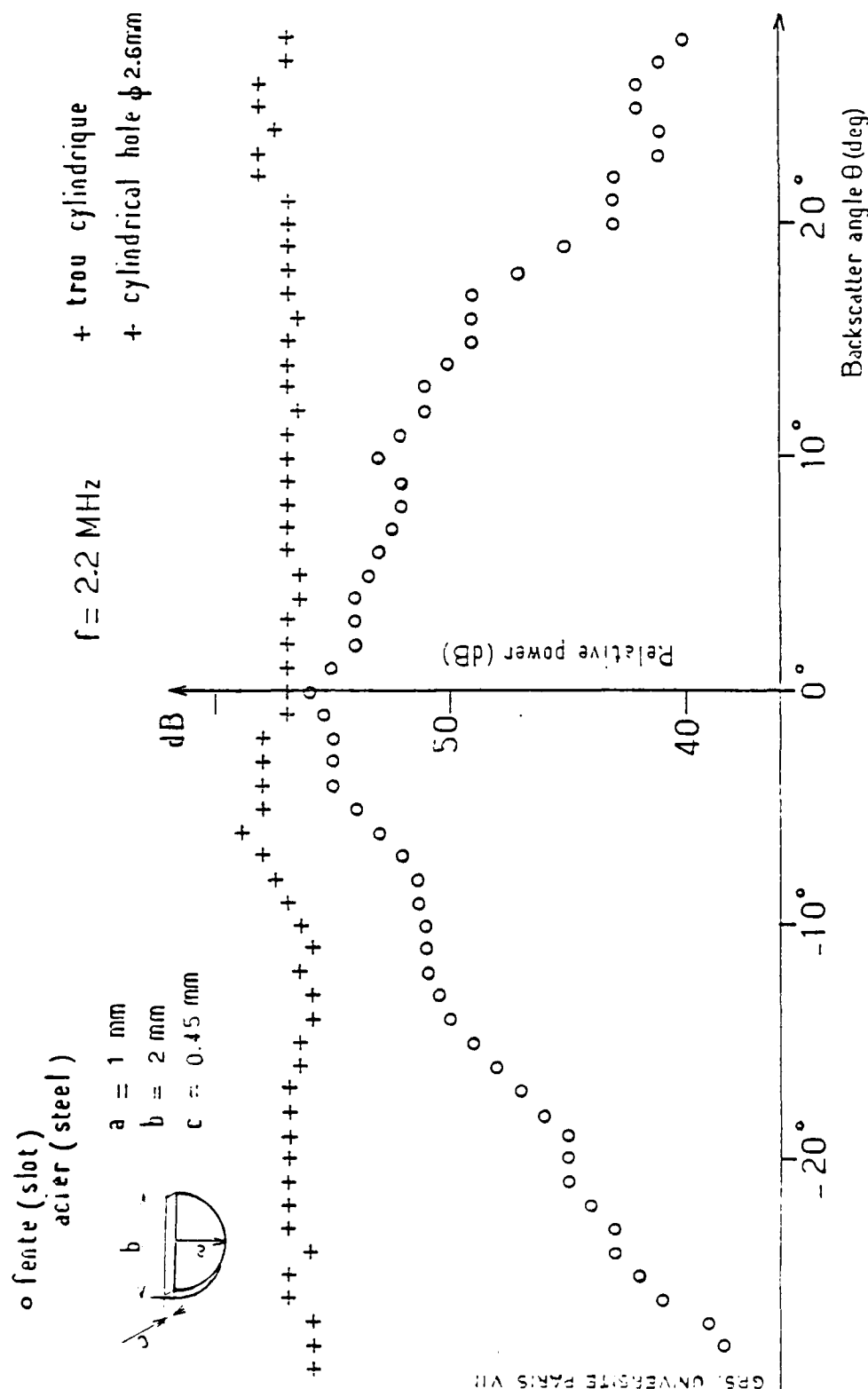


Fig. 1 Angular dependence of backscattered power at 2.2 MHz for a half-penny shaped slot (radius = 1 mm) and for a cylindrical hole (radius = 1.3 mm) in steel. $\theta = 0$ corresponds to the direction normal to the slot plane.



sensitive to these and other parameters. Also shown in Fig. 1 is the result of a calibration run with a cylindrical hole (2.6 mm in diameter) which gave a rather flat response over a range of angles of at least $\pm 70^\circ$, indicating negligible interference from the apparatus. Fig. 2 is a similar result at 2.2 MHz ($\lambda_{\text{Rayleigh}} = 1.42 \text{ mm}$) for an elliptically shaped slot in a crown glass plate for which the slot length b was very long ($b = 2.4 \text{ cm}$) compared to its depth a ($a = 1.4 \text{ mm}$) and its width c ($c = 0.5 \text{ mm}$). For this case the slot length probably exceeds the width of the surface wave beam so that contributions from the ends of the slot are probably negligible. This no doubt explains the dramatic fall-off with angle (25 dB from peak at $\theta = 10^\circ$) without any indication of structure.

Quite in contrast to these measurements are those obtained on the indentation cracks in ceramic at 100 MHz ($\lambda_{\text{Rayleigh}} = 50 \mu\text{m}$). As seen in Fig. 3 the curves obtained for two half-penny shaped cracks display considerable structure with well-defined peaks and nulls, whose spacings scale roughly as the crack radius ($a_1/a_2 = 80 \mu\text{m}/120 \mu\text{m} = 0.67$). This result is not surprising since for this case the wavelength $\lambda_{\text{Rayleigh}}$ is considerably smaller than the crack radius so that the surface wave sees primarily the crack geometry near the surface. Under this condition the scattering object is thought to behave like two slightly separated scattering centers producing an interference of the scattered radiation and therefore a structure in the angular dependence for backscattered waves. If this simple analysis is borne out by further experiments, this result could lead to a simple yet powerful technique for estimating the size of a surface flaw.

Finally in Fig. 4 are displayed photos of oscilloscope traces obtained with the broad-band system for a cylindrical hole as defect in a steel plate. The top photo shows the time domain signal with a well-defined wide-band surface wave pulse while the bottom photo shows the amplitude of the frequency spectrum as obtained on a H.P. 5553B-3552B Spectrum analyzer. The Fourier analysis is also routinely performed on a H.P. 9821A calculator. The photos are intended to simply demonstrate the feasibility of carrying out measurements with this technique.

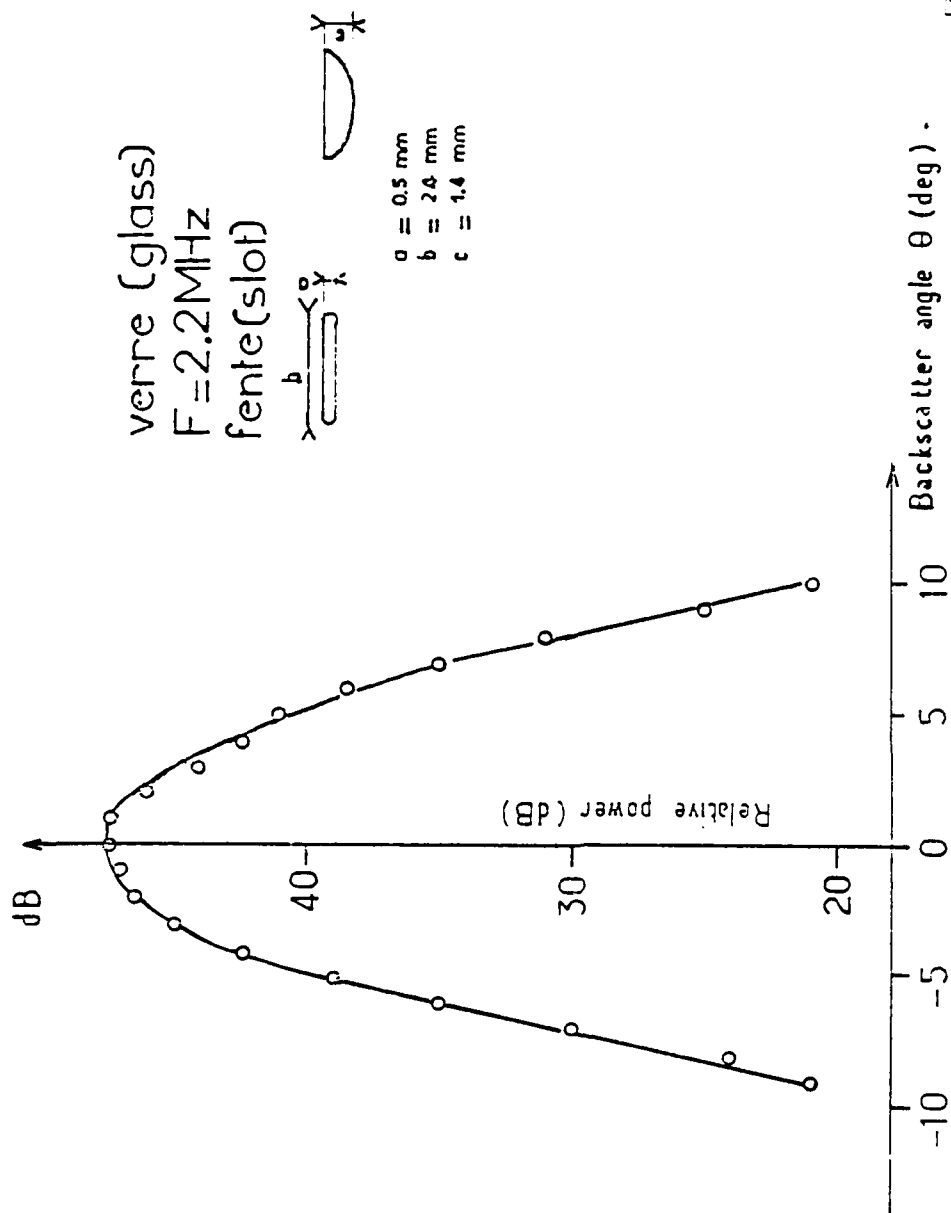


Fig. 2 Angular dependence of backscattered power at 2.2 MHz for an elliptical slot (length = 2.4 mm, depth = 1.4 mm) in glass. $\theta = 0$ corresponds to the direction normal to the slot plane.

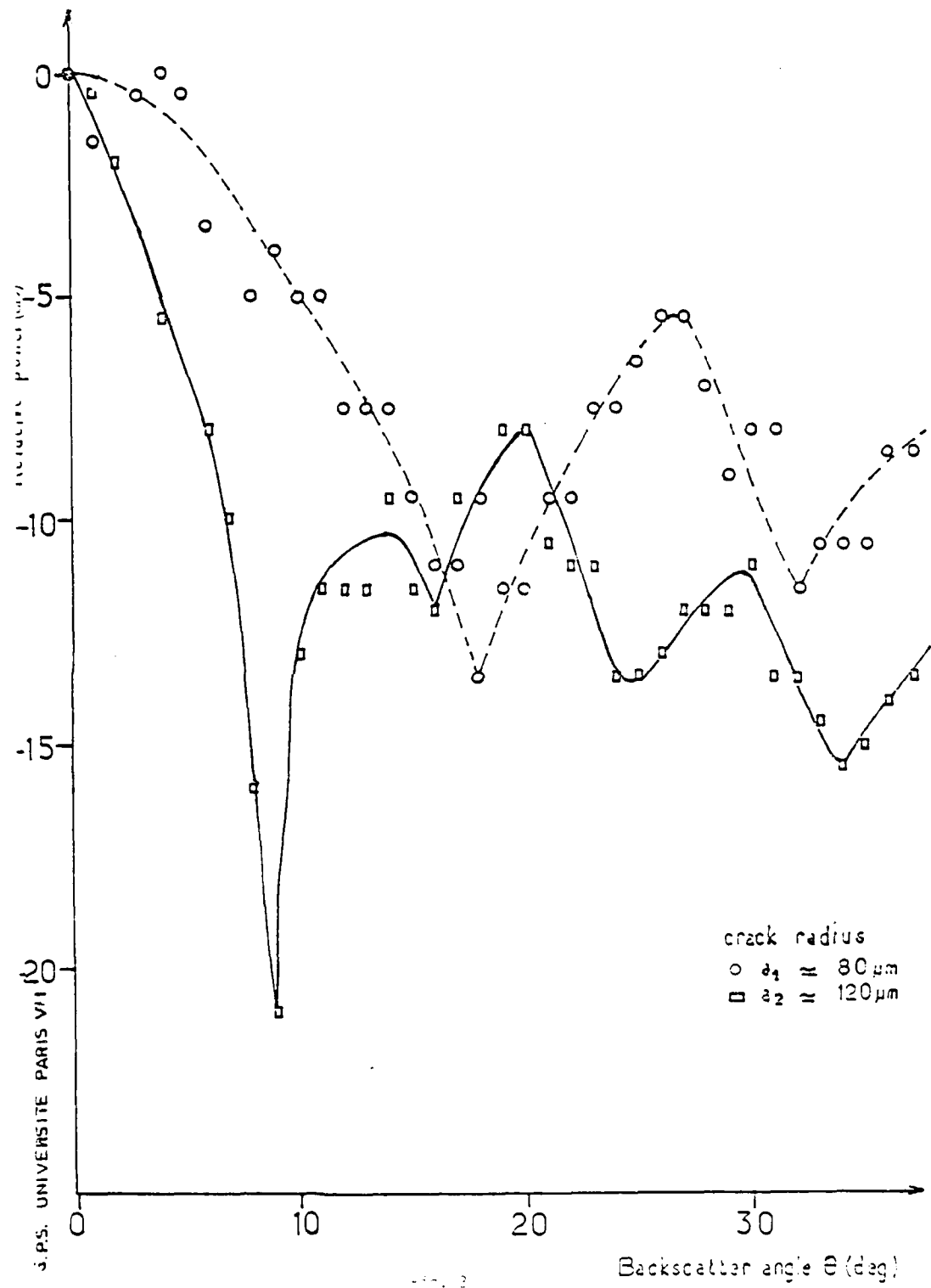
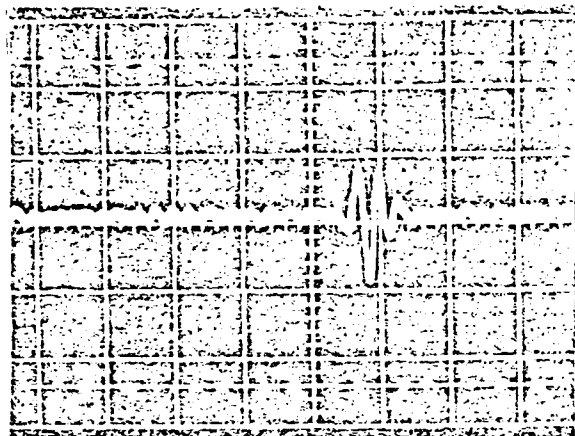
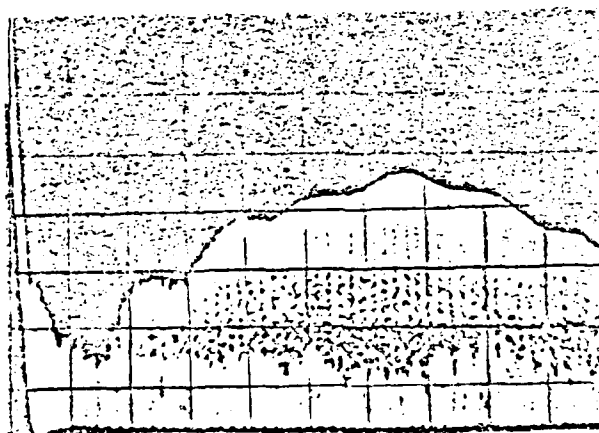


Fig. 3 Angular dependence of backscattered power at 100 MHz for two different cracks (radii $a_1 = 80 \mu\text{m}$) made into commercial ceramics by the indentation technique. $\theta = 0$ corresponds to the direction normal to the slot plane. The data have been normalized at $\theta = 0$.



Time Domain Signal

($x = 0.5 \mu\text{sec/div}$, $y = 0.1 \text{ V/div}$)



Frequency Domain Signal

($x = 1 \text{ MHz/div}$, $y = 10 \text{ dB/div}$)

Fig. 4 Photographs of oscilloscope traces for the time-domain signal (top) and the corresponding frequency domain signal (bottom) for backscattering from a cylindrical hole (radius 1.3 mm) in steel. The experiment was carried out with a commercial broadband transducer immersed in a waterbath and inclined to the partially submerged sample surface at the critical angle.



Conclusion

The work described in this report comprises our initial effort towards the goal of characterizing surface flaws by angular and frequency dependence studies of surface wave scattering. The preliminary results indicate considerable promise for a simple approach to the problem of estimating the long dimension of surface cracks in the regime $\lambda_{\text{Rayleigh}} < \text{crack radius}$. The measurements described here have been made on polished samples; nevertheless the influence of rather small values of the surface roughness has been noticed and will be studied in a similar manner as that which our laboratory has used previously for bulk wave scattering by rough surfaces (9).

References

1. A.G. Evans and R.L. Jones, Jnl. Amer. Ceram. Soc., in press.
2. J.J. Mecholsky, S.W. Freiman, R.W. Rice, J. Mater. Sci., 11, 1310, 1976.
3. R.W. Rice, Ceramics for High Performances Applications (ed. J.J. Burke, A.E. Gorum, and R.N. Katz), Brook Hill, March 1974, p. 282.
4. J.J. Mecholsky, S.W. Freiman and R.W. Rice, Jnl. Amer. Ceram. Soc., 60, 116, 1977.
5. A.G. Evans, G.S. Kino, B.T. Khuri-Yakub and B.R. Tittmann, Materials Evaluation, April 1977, p. 85.
6. B.T. Khuri-Yakub, A.G. Evans, and B.R. Tittmann, J. of Applied Physics, in press.
7. B.T. Khuri-Yakub and G.S. Kino, Appl. Phys. Lett., in press.
8. J.J. Petrovic and M.G. Mendiratta, Jnl. Amer. Ceram. Soc., 59, 163, 1976.
9. M. de Billy, F. Cohen-Tenoudji, A. Jungman and G. Quentin : The possibility of assigning a signature to rough surfaces using ultrasonic backscattering diagrams. I.E.E.E. Trans. on Sonics and Ultrasonics, S.U. 23, 356-363 (1976).

Acknowledgements

The authors are very grateful to O. Buck and A.E. Evans for supplying us with the defect samples, P. Khuri-Yakub for the design, construction and demonstration of the 100 MHz surface wave transducers, to H. Nadler for the design of the 100 MHz goniometer, and to J. Doucet for the construction of the low frequency goniometers.

PROJECT II, UNIT A, TASK 2

OPTIMIZATION OF EMATS FOR SURFACE FLAW DETECTION

R. B. Thompson, C. F. Vasile, C. M. Fortunko
 Rockwell International Science Center
 Thousand Oaks, California 91360

Introduction

The objective of this task is to develop practical formulae which can be used in the design of EMAT systems for the characterization of surface flaws. These will be based, to as great an extent as possible, upon the theoretical expressions developed in this program for the radiation pattern of EMATs and for the scattering of energy by surface flaws. They will then be used to design transducer aperture functions (length, width, frequency, possible apodization) and multiple transducer configurations that will (a) provide an output most directly related to the critical flaw parameters and (b) provide the lowest probability of missing a poorly oriented flaw.

Approach

Work has just begun on this task, so this report will be quite short. The first step is the evaluation of the deviation of the transducer radiation pattern. This is rather complex to evaluate in the near field, but relatively simple in the far field. For example, consider the transducer shown in Fig. 1. For this configuration, a normal force is applied to the surface of the material along the serpentine path of the meander coil. The resulting far field radiation along the surface is given by the product of three factors, the circularly symmetric radiation from a point source, and factors individually describing the directionability effects of the aperture and length of the transducer. It can be readily shown that

$$\text{Far Field Amplitude} \propto \left[\frac{\sin[\pi N_1 \sin\theta]}{\pi N_1 \sin\theta} \right] \times \frac{\sin\left(\pi \left[N_2 \cos\theta + \frac{\sin^2 N_2 \pi}{2} \right]\right)}{\cos\left[\left(\frac{\pi}{2}\right) \cos\theta\right]} \quad (1)$$

AD-A132 082

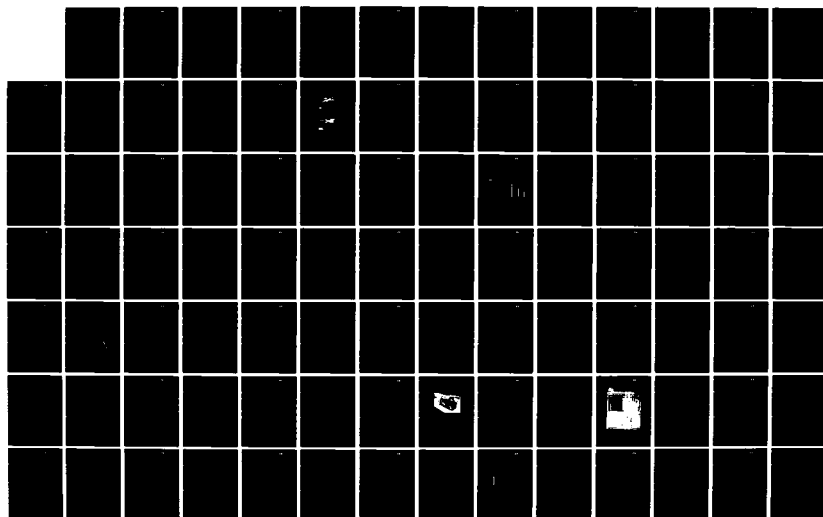
INTERDISCIPLINARY PROGRAM FOR QUANTITATIVE FLAW
DEFINITION(U) ROCKWELL INTERNATIONAL THOUSAND OAKS CA
SCIENCE CENTER 1978 SC595.325A F33615-74-C-5180

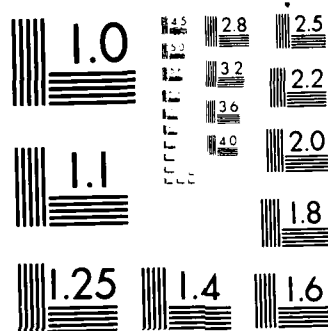
3/4

UNCLASSIFIED

F7G 14/2

NL





MICROCOPY RESOLUTION TEST CHART
 NATIONAL BUREAU OF STANDARDS-1963-A

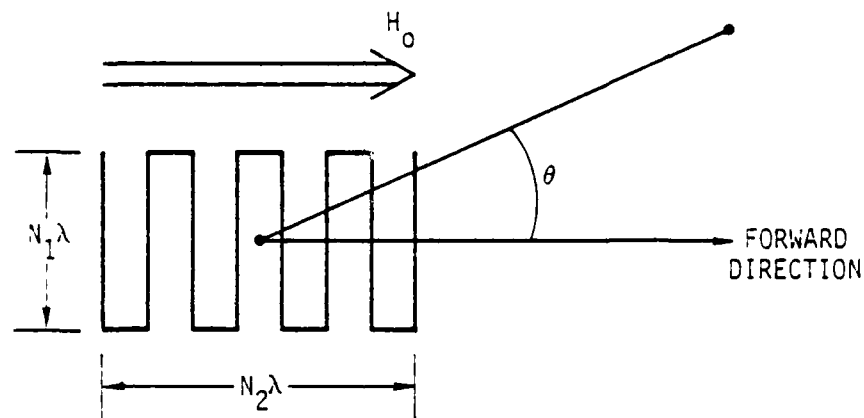


Fig. 1 Top view of meander coil of width $N_1\lambda$ and length $N_2\lambda$.

where $N_1\lambda$ is the transducer width and $N_2\lambda$ is its length. Although apparently complex, some simple conclusions can be drawn from these expressions. For example, considering the aperture function alone, the first null occurs when

$$\begin{aligned}\theta_A &= \sin^{-1} 1/N_1 \\ &\approx 1/N_1 \text{ when } N_1 \gg 1\end{aligned}\tag{2}$$

Likewise, considering the second term describing the end fire radiation from an array, the first null occurs when

$$\begin{aligned}\theta_E &= \cos^{-1}(1 - 1/N_2) \\ &\approx (2/N_2)^{1/2} \text{ when } N_2 \gg 1\end{aligned}\tag{3}$$

These two functions are plotted as a function of N_1 and N_2 in Fig. 2. It can be seen that the first null of the aperture function occurs at smaller angles than that of the end fire function for an equivalent length.

These results can be used to optimize transducers for various purposes. For example, the transfer impedance of a pair of transducers varies as $N_1N_2^2$. If this is to be held constant to produce a given sensitivity in a particular application, trade-offs can be made between exciting a collimated beam ($N_1 \gg N_2$ $N_1N_2^2$ constant) which can be directed in a well-controlled direction or a beam with a wider angular spread ($N_2 \gg N_1$ $N_1N_2^2$ constant) which will be less sensitive to the orientation of a flaw. It must be also noted that this latter result is achieved with a decrease in bandwidth and have poorer spatial resolution.

In future work, these results will be extended to include the case of nonnormal as well as normal forces, radiation of angle beams into the material as well as surface waves, and interactions with flaws so that ultrasonically optimum transducer systems can be designed.

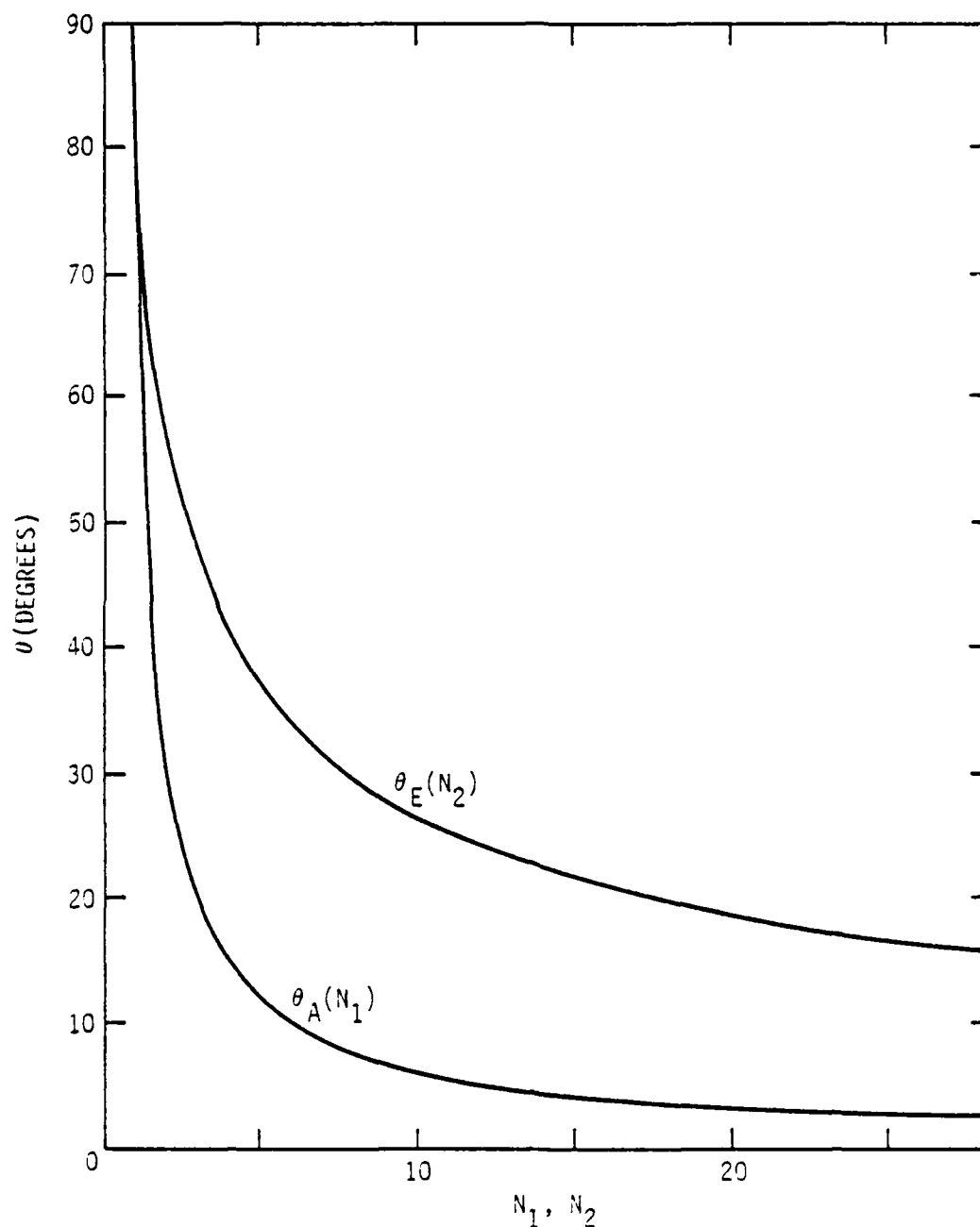


Fig. 2 Variation of first null of radiation pattern associated with transducer width θ_A and length θ_E . The total pattern is the product of the functions as given in Eq. (1).



PROJECT II, UNIT B, TASK 1
QUANTITATIVE MEASUREMENT OF CRACK PARAMETERS
USING MICROWAVE EDDY-CURRENT TECHNIQUES

A. J. Bahr
SRI International
Menlo Park, California 94025

Introduction

The objective of this task is to develop and evaluate a waveguide crack model that can be used to predict the scattering of microwave energy from a cracked metal surface. Another objective is to evaluate the potential of microwave techniques for predicting the dimensions of inclusions and surface cracks in ceramics. This report summarizes the progress that has been made on this task for the period November 14 through December 31, 1977.

Waveguide Crack Model

The work during this reporting period has concentrated on the development of a waveguide crack model. Our initial efforts have been directed toward developing a first-order theory. To this end, we have made the following simplifying assumptions:

- (1) The crack is assumed to take the form of a rectangular slot having length a , width b , and depth d as shown in Fig. 1. The opening of this slot is assumed to be situated in an infinite metallic plane located at $z = 0$.
- (2) The electric-field distribution in the mouth of the slot is assumed to be entirely y directed, and to vary sinusoidally in the x direction. This assumption implies that $a \gg b$ and $d > b$.
- (3) The size of the slot in terms of the electromagnetic wavelength is assumed to be such that the slot is below resonance and the fields within the slot are evanescent.

Our first objective is to determine how the energy scattered by the slot varies as a function of slot dimensions. We can calculate the relative power scattered by the electrically small slot by using an equivalent circuit

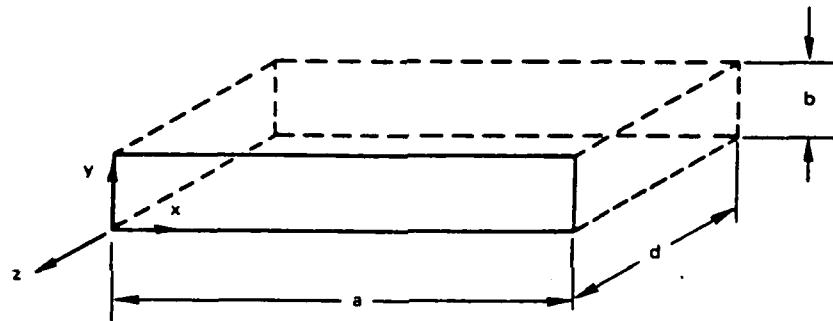


FIGURE 1 A RECTANGULAR-SLOT CRACK MODEL

wherein the crack cavity is represented by an admittance loading the slot antenna. Below slot resonance this crack admittance is an inductive susceptance if the losses in the crack are negligible.

The equivalent circuit for the crack scatterer is shown in Fig. 2. The crack admittance is jB_c , and $(G_r + jB_r)$ is the radiation admittance of the slot antenna. The current I can be related to the magnetic field at the entrance to the crack.

When the slot is small, the scattered power, P_s , is closely approximated by the power dissipated in the radiation conductance.¹ Hence,

$$P_s = \frac{1}{2} R_e(V_r I_r^*) \quad (1)$$

where V_r and I_r are the voltage and current across and through the radiation conductance, respectively. Simple circuit analysis shows that

$$P_s = \frac{1}{2} |I|^2 \frac{G_r}{G_r^2 + (B_r + B_c)^2} \quad (2)$$

The radiation admittance for a slot antenna has been derived by Rhodes,^{2,3} where it is assumed that

$$E_y(x, y, 0) = \frac{V_0}{b} \sin |k(\frac{a}{2} - |x - \frac{a}{2}|)| \quad (3)$$

Here, V_0 is an amplitude factor and k is the wave number. The resulting formulas are sufficiently complex so that numerical results must be obtained with a computer.

A specific example of the variation of the radiation admittance for a slot as a function of ka is shown in Fig. 3. The parameters of the slot are given in the figure. The quantity η_0 is the free space wave impedance, which is equal to 120π . It has been found that the radiation conductance is not sensitive to the width parameter, b/λ . However, the radiation susceptance is sensitive to this parameter. Fortunately, it appears that the radiation susceptance is more than an order of magnitude smaller than the cavity susceptance.

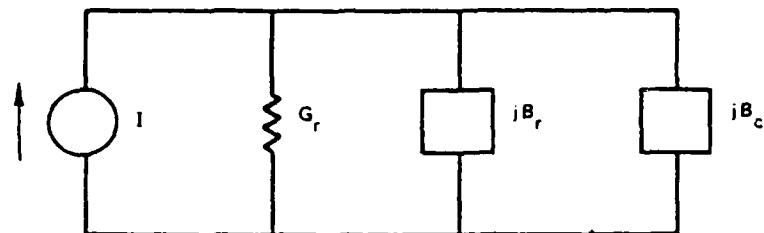
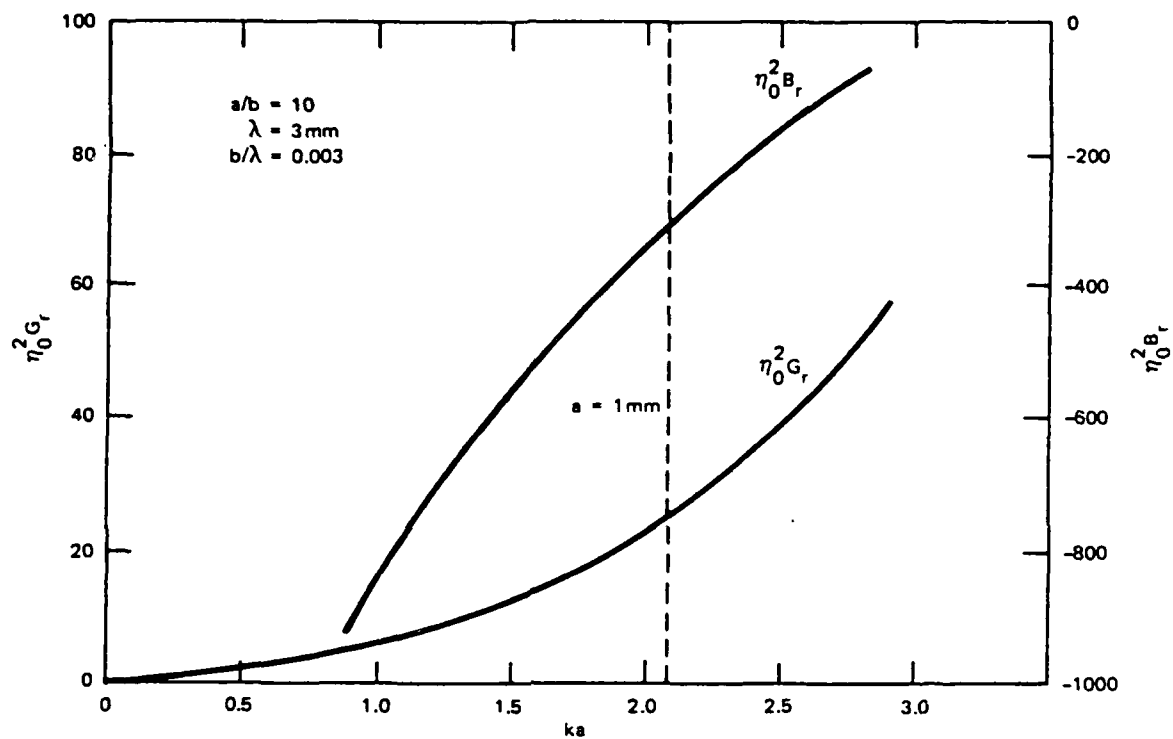


FIGURE 2 EQUIVALENT CIRCUIT FOR A CRACK SCATTERER

FIGURE 3 RADIATION ADMITTANCE OF A SLOT AS A FUNCTION OF ka



In order to evaluate Eq. (2), it is necessary to derive an expression for B_c . Cockrell⁴ gives the following expression for the cavity susceptance:

$$B_c = \frac{1}{V_0^2 \sin^2 \frac{ka}{2}} \operatorname{Im} \left\{ \int_0^a \int_0^b (\vec{E}_i \times \vec{H}_i^*) \cdot \hat{a}_z \, dx dy \right\} \quad (4)$$

where \vec{E}_i , \vec{H}_i are the electric and magnetic fields inside the cavity, respectively, and \hat{a}_z is a unit vector pointing along the positive z axis. The interior electric field can be expressed as a sum of TE waveguide modes, viz.,

$$E_{yi} = \sum_{n=1}^{\infty} \sum_{m=0}^{\infty} Q_{nm} \sin \left(\frac{n\pi x}{a} \right) \cos \left(\frac{m\pi y}{b} \right) \sinh [\Gamma_{nm} (z + d)] \quad (5)$$

where

$$\Gamma_{nm}^2 = \left(\frac{n\pi}{a} \right)^2 + \left(\frac{m\pi}{b} \right)^2 - k^2 \quad (6)$$

The coefficients Q_{nm} are determined by equating Eq. (5) and Eq. (6) at $z = 0$. We find that only $m = 0$ modes are excited and that

$$Q_{n0} = \frac{4V_0}{b} \cos \left(\frac{ka}{2} \right) \frac{(-1)^{\frac{n-1}{2}} ka}{[(n\pi)^2 - (ka)^2] \sinh [\sqrt{(n\pi)^2 - (ka)^2} d/a]} \quad (7)$$

for n odd, and zero for n even.

From Maxwell's equations, we find that the interior magnetic field is given by

$$H_{xi} = -j \frac{1}{\eta_0 k} \frac{\partial}{\partial z} E_{yi} \quad (8)$$

Substituting into Eq. (4) and evaluating, we find that

$$B_c = - \frac{8a}{b} \frac{ka}{\eta_0 \tan^2 \left(\frac{ka}{2} \right)} \sum_{n \text{ odd}} \frac{1}{(\Gamma_{n0} a)^3 \tanh (\Gamma_{n0} d)} \quad (9)$$

As an example, we have calculated $P_s/(\frac{1}{2}|I|^2)$ as a function of d/a assuming $a/b = 10$, $a = 1$ mm, and $\lambda = 3$ mm. The series in Eq. (9) was truncated to the two leading terms. The result is shown in Fig. 4. Generally, the variation of scattered power with crack depth is nonlinear. However, for crack depths in the range $0.1 < d/a < .5$, the variation is approximately linear. The theory is not strictly applicable for $d/a < .1$, but, of course, the scattered power must go to zero when $d/a = 0$. The curve flattens out for large crack depths because, for the chosen parameter values, the evanescent field decays to a small value before the bottom of the crack is reached. Our theory appears to be in qualitative agreement with the experimental results obtained by Hruby and Feinstein.⁵

Future Plans

During the next period we plan to carry out a more extensive parametric study of the theory developed so far. In addition, experiments designed to test the theory will be conducted. Finally, consideration will be given to determining how a measurement and calibration could be carried out to make the measurement of crack depth (and other crack parameters) truly quantitative.

Later in the program we plan to consider how the theory can be modified to accommodate interior crack shapes other than rectangular (e.g., a penny-shaped crack). Also, other theoretical formulations such as the one based on the Lorentz reciprocity relations⁶ will be studied. Such an approach is attractive because it involves quantities that are easily measurable at the ports of the microwave inspection system.



SC595.32SA

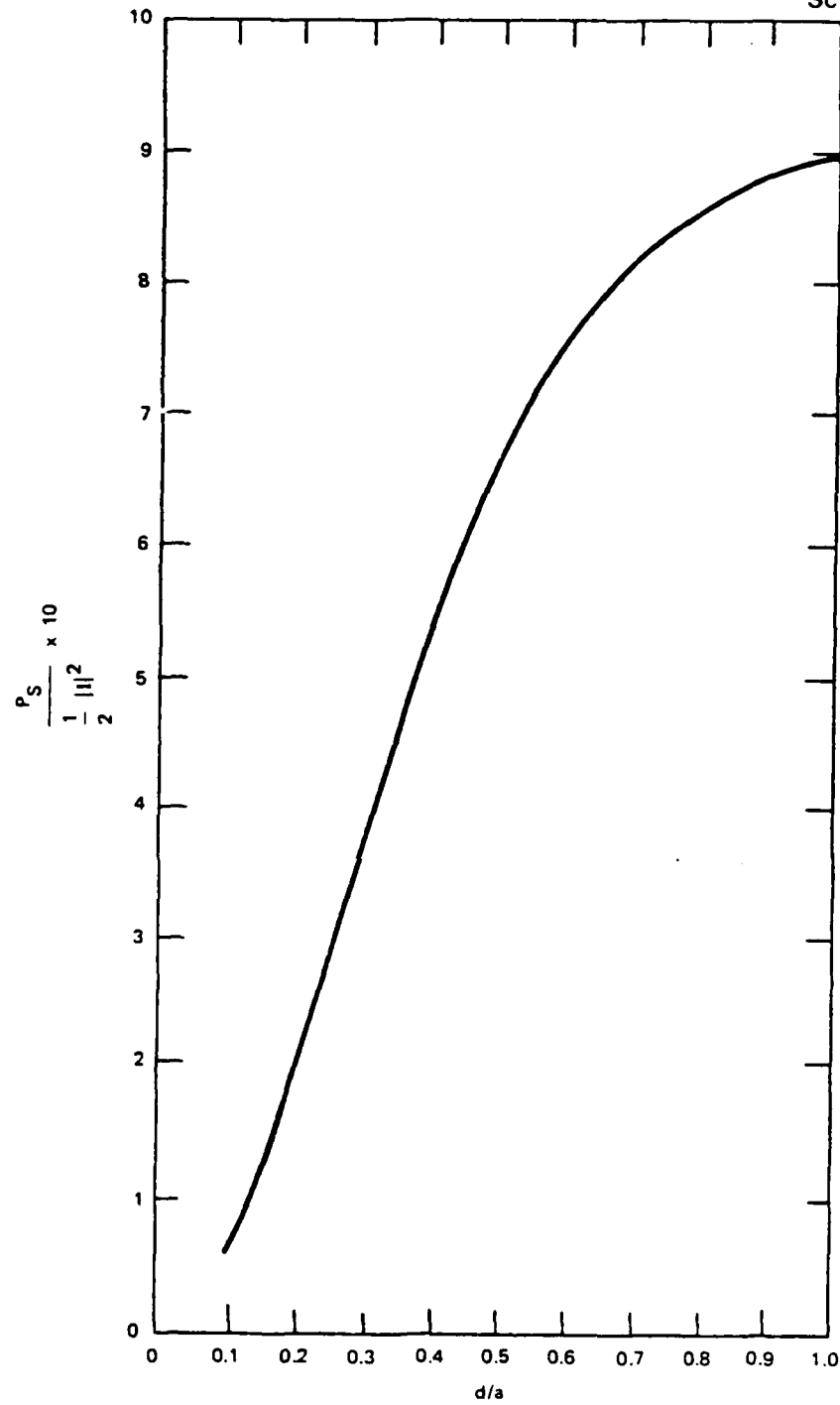


FIGURE 4 VARIATION OF SCATTERED POWER WITH DEPTH
FOR A RECTANGULAR CRACK

References

1. R. F. Harrington, "Electromagnetic Scattering by Antennas," IEEE Trans. Antennas and Propagation, Vol. AP-11, pp. 595-596, September 1963
2. D. R. Rhodes, "On a Fundamental Principle in the Theory of Planar Antennas," Proc. IEEE, Vol. 52, pp. 1013-1021, September 1964
3. D. R. Rhodes, "On the Stored Energy of Planar Apertures," IEEE Trans. Antennas and Propagation, Vol. AP-14, pp. 676-683, November 1966
4. C. R. Cockrell, "The Input Admittance of the Rectangular Cavity-Backed Slot Antenna," IEEE Trans. Antennas and Propagation, Vol. AP-24, pp. 288-294, May 1976
5. R. J. Hruby and L. Feinstein, "A Novel Nondestructive, Noncontacting Method of Measuring the Depth of Thin Slits and Cracks in Metals," The Review of Scientific Instruments, Vol. 41, pp. 679-683, May 1970
6. B. A. Auld, private communication, December 1977



PROJECT II, UNIT B, TASK 2

FERROMAGNETIC RESONANCE PROBES FOR THE DETECTION OF
SURFACE FLAWS IN METALS

B.A. Auld, G. Elston, D.K. Winslow
Stanford University

C. Fortunko
Rockwell International Science Center
Thousand Oaks, California 91360

Introduction

It is the objective of this task to produce a demonstration model of a microwave eddy current probe using a high sensitivity ferromagnetic resonator to use it in the quantitative determination of flaw parameters.

Background

This study is concerned with a new technique for the detection of surface flaws in metals - ferromagnetic resonance probing. Although the name suggests that this method would be applicable only to magnetic metals, it is in fact, a variant of conventional eddy current testing and is therefore applicable to both non-magnetic and magnetic materials.

In ordinary eddy current testing a small search coil, having in some cases a ferrite core for field concentration, is placed near the metal test specimen and scanned over its surface. This coil is driven with an RF current, typically at frequencies below one megahertz, which causes induced eddy currents to flow in the metal. It is the disturbance of these eddy currents by the presence of a flaw and the observation of the resulting change in impedance of the coil that constitutes the basic detection mechanism. In some cases the coil is tuned to resonance with a capacitor in order to enhance the change of input impedance caused by the presence of the flaw. Because of the relatively low operating frequency the penetration of the eddy currents into the metal is of the order of a fraction of a millimeter, and buried flaws lying close to the surface can therefore be detected.

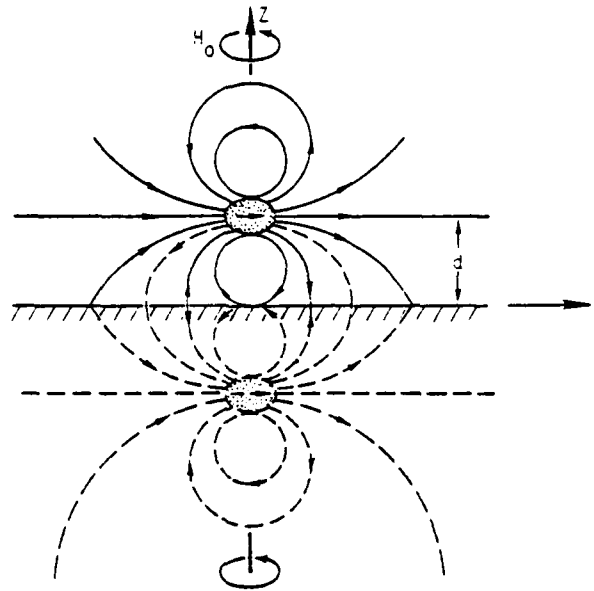
Ferromagnetic resonance flaw detection, by contrast, uses a small ferromagnetic crystal as the probe. When such a crystal is placed in a dc magnetic field and excited by an RF field, it becomes a miniature resonator

(typically 0.2 to 0.3mm in diameter) in which the resonance consists of a precession of the crystal magnetization about the dc magnetic field. This processing magnetic dipole moments generated eddy currents on a metal surface placed in proximity to the crystal resonator, and the presence of these eddy currents causes a shift of the resonant frequency. The frequency shift is, in turn, further modified by the presence of a surface flaw. Consequently, a ferromagnetic resonance probe is analogous to a conventional resonant eddy current test coil, but with the advantages of being much more compact, and having much higher Q. Both of these features lead to higher detection sensitivity. There are, however, important differences between ferromagnetic resonance flaw detection and the traditional eddy current approach. Because the ferromagnetic resonator has a rotating magnetic dipole moment it produces a quite different pattern of eddy currents than the fixed dipole moment of a conventional test coil. Also, since the resonator's dipole moment rotates about the dc bias field, the eddy current pattern depends upon the orientation of the bias field. Figures 1 and 2 show the variation of the eddy current distribution with time for two geometries. In Fig. 1 the dc magnetic field is normal to the surface and the current pattern rotates 360° each RF cycle. When the field is parallel to the surface a circular eddy current pattern exists when the RF magnetization is normal to the surface (Fig. 2). This is similar to the distribution produced by a pancake coil eddy current probe. One quarter cycle later the distribution shown in Fig. 1 occurs, and the current loops continue to shift to the right as a function of time.

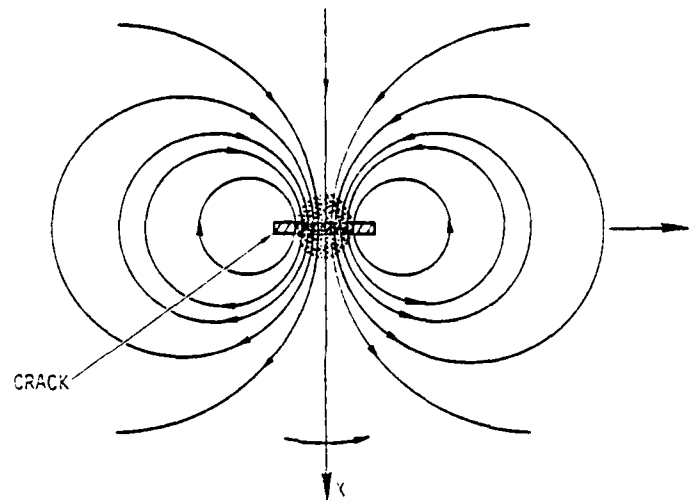
Another point of difference with a conventional probe is that the operating frequency is much higher. The resonant frequency of a ferromagnetic resonator is determined by the dc magnetic field and has a minimum value below which the dc magnetic field is insufficient to saturate the magnetic crystal. For a sphere of pure yttrium iron garnet (YIG) this minimum frequency is 1630 MHz. Using gallium-doped YIG or disk-shaped samples this can be reduced, but at a sacrifice of Q. In any case, it is not possible to obtain a high Q resonance at frequencies much below 1000 MHz. The significance of this is that the skin depth in a metal test specimen is less than 2.5 μ m and the perturbation due to a surface flaw is caused by the surface currents flowing down into the flaw, rather than by the disruption of volume eddy currents typical of conventional low frequency eddy current testing.



MAGNETIC FIELD NORMAL TO CONDUCTOR



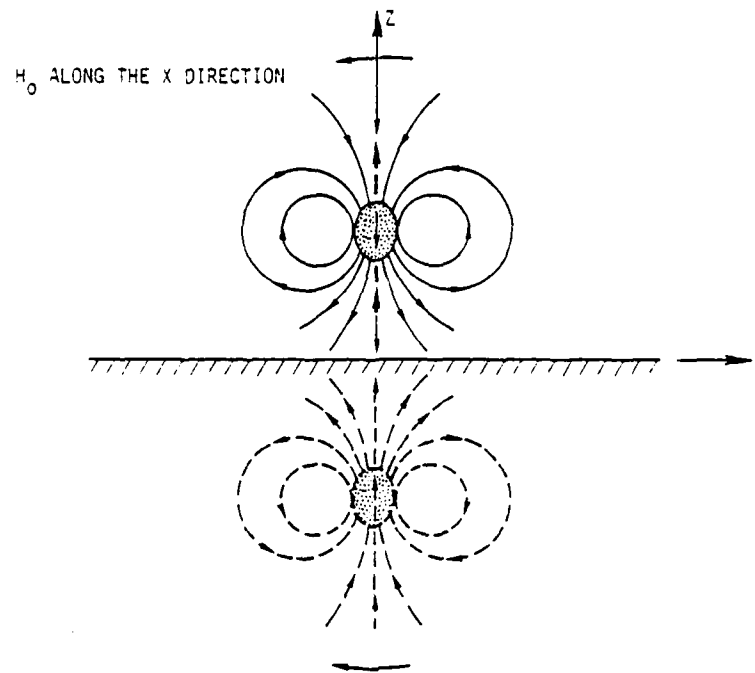
a) Magnetic field distribution around resonator and its image.



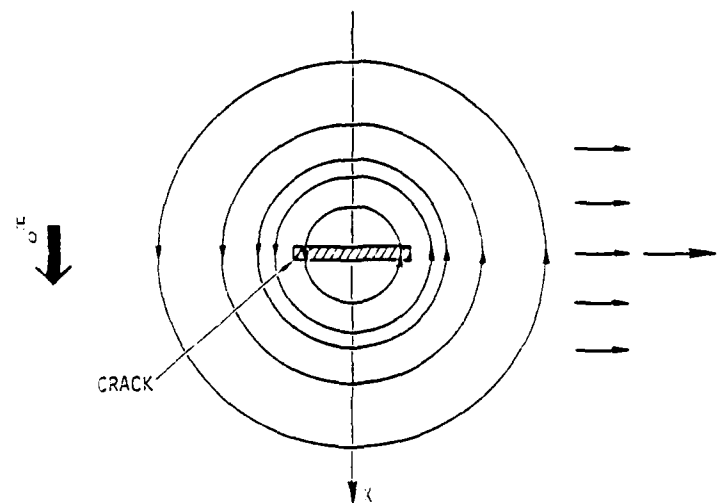
b) Rotating eddy current distribution on conducting wall.

Fig. 1 RF magnetic field and eddy current distributions when magnetizing field is parallel to conducting surface.

DC MAGNETIC FIELD PARALLEL TO CONDUCTOR



a) Magnetic field distribution around resonator and its image.



b) Linearly traveling eddy current distribution.

Fig. 2 RF magnetic field and eddy current distributions when magnetizing field is normal to conducting surface.

SC73-129



The current state-of-the-art in eddy current testing lacks adequate procedures for interpreting test data in terms of the size, shape and orientation of a flaw and is in this respect, much less highly developed than ultrasonic testing. This is in spite of the fact that there exists an electromagnetic scattering theorem that is completely analogous to an acoustic scattering theorem that encompasses a variety of^{1,2} analytical techniques currently used in ultrasonics. This electromagnetic theorem, generalized to include ferromagnetic resonance, and its application to eddy current detection of surface flaws is being studied under the support of the NSF Thrust Program on Nondestructive Testing at Stanford. A less general form of the theorem was, in fact, used in References 3 and 4 to analyze eddy current detection of spheroidal flaws of dimensions much smaller than the skin depth. This is not really a practical case since, even at frequencies below 1 MHz, it would require the flaw to be smaller than $10\mu\text{m}$ in dimension. For ferromagnetic resonance testing, one requires a method of analysis applicable to flaws that are much larger than a skin depth. The theory being developed under the NSF program is a refined and more rigorous version of the Slater perturbation theory used in Reference 2. It expresses the detection signal in terms of the perturbed and unperturbed fields integrated over the surface opening of a surface crack or, alternatively, as an integral of certain combinations of fields within the crack. To evaluate these integrals one may either treat the crack as a very small waveguide that is far below cutoff or use solutions of the type presented in Reference 5.

Probe Construction and Performance

Figure 3 shows a hand held probe that has been built in the form of a block approximately $1\text{''} \times 1\text{''} \times 0.25\text{''}$ in size, containing small samarium cobalt magnets and a 15 mil diameter pure YIG sphere mounted with its center less than one diameter from the $1\text{''} \times 1\text{''}$ surface that contacts the test specimen. The contact area was chosen to be this large so as to avoid tilting and variations of lift-off as the probe is moved over the sample of a flat sample. It could be made smaller than $0.25\text{''} \times 0.25\text{''}$ if other provisions were made for mechanical stability. This is a passive probe, in which the YIG resonator act as a filter tuned to 3600 MHz with a 3 dB bandwidth of 3 MHz.

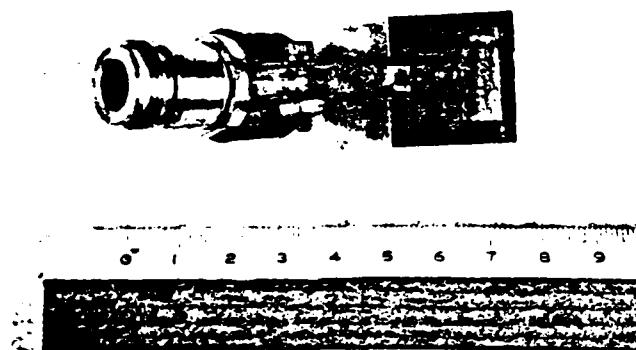
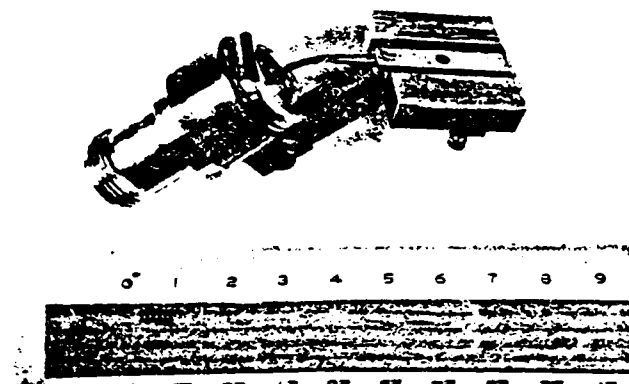


Fig. 3 A passive hand held YIG resonator probe with permanent magnet biasing.



Greater frequency sensitivity would be produced by an active probe. One could place a negative resistance element in parallel with the YIG resonator to narrow the bandwidth or one could use the resonator as a circuit element in a YIG-controlled transistor oscillator. These approaches narrow the bandwidth and hence increase the sensitivity of the technique. An oscillator has been constructed and tested using a gallium doped YIG sphere ($4 M_s = 800$) and is being modified for use as a flaw detecting probe. The bandwidth of 0.2 MHz obtained thus far, as compared to 3 MHz for the passive probe, illustrates the advantages of this approach.

To test the passive probe we fabricated a series of test slots in an aluminum plate. These slots extended completely across the 2" lateral length of the plate and were fabricated in a variety of slot depths and opening widths. Other test slots were fabricated by clamping pieces of shim stock between polished blocks of aluminum. As a check, machined and clamped slots of the same dimensions were compared and found to be in reasonable agreement. Measure frequency shifts in MHz are plotted in terms of slot opening width and depth in Fig. 4, and Fig. 5. Also shown are contours of constant cross-sectional slot area A (or slot volume per unit length).

It will be recalled that the data in Reference 2, taken with a rather large (100 mil x 10 mil) YIG disc resonator, showed the frequency shift to be proportional to A and this was explained on the basis of an approximate perturbation theory. The theory being developed under NSF support shows that the dependence on crack size is more complicated than this and, in fact, the data shown in Figs. 3 and 4, indicate that the frequency shift for a small (15 mil) YIG sphere resonator does not correlate with A at all. In fact, the frequency shift is practically independent of depth until it becomes comparable to or less than the width. This is to be expected if the slot is regarded as an electromagnetic waveguide below cutoff, since the fields excited into the surface penetrate only a finite distance into the depth and would not interact with the bottom of a slot lying below the penetration depth. In the present geometry, however, the slots are 2" long and eddy currents perpendicular to the slot length will support a TEM mode that penetrates to the bottom of the slot. Hence, interpretation of the data of Figs. 4 and 5 in terms of the theory is, at present, not clear.

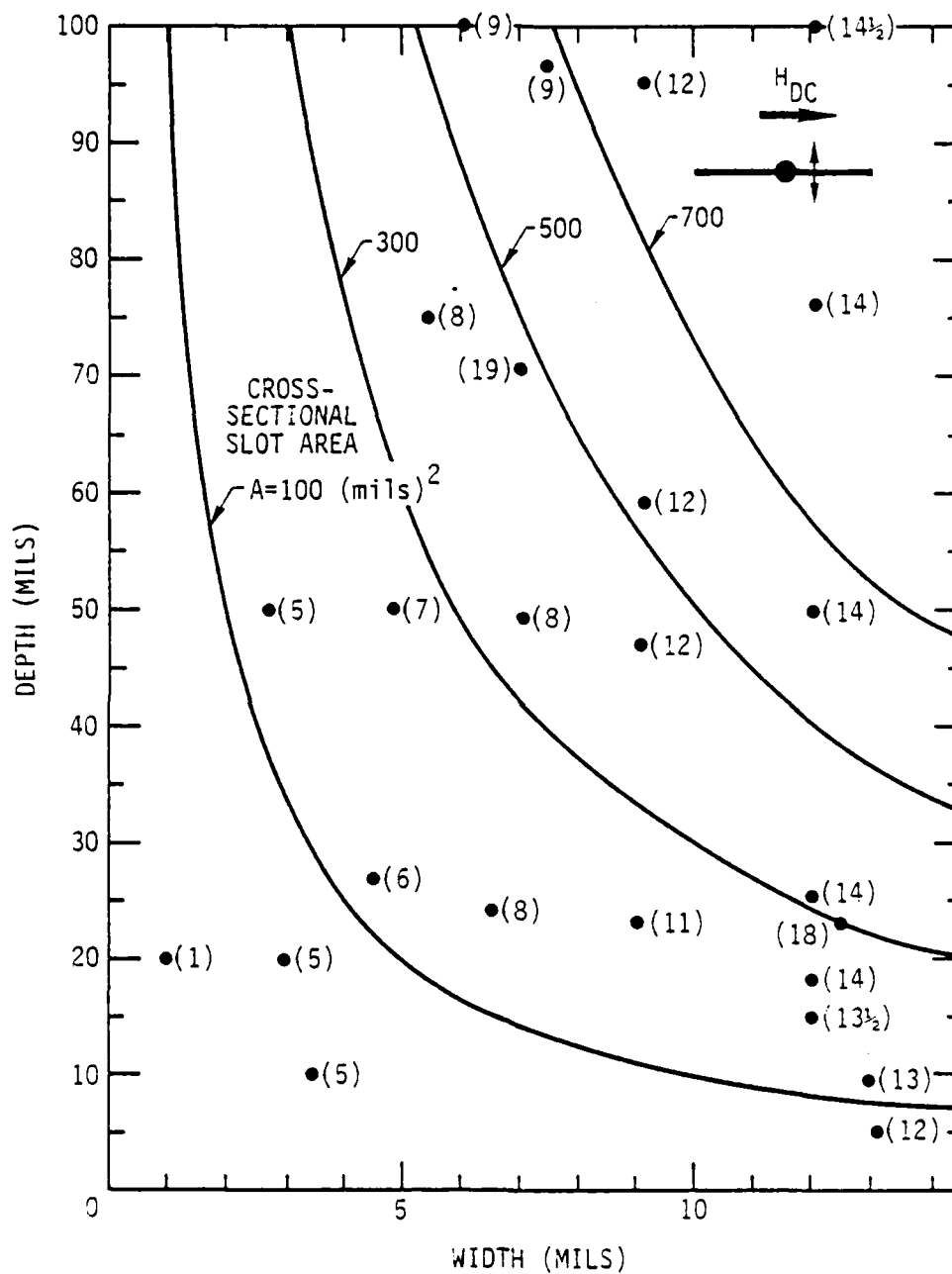


Fig. 4 Measured frequency shifts (in MHz) as a function of slot surface width and depth. Parallel magnetizing field case.

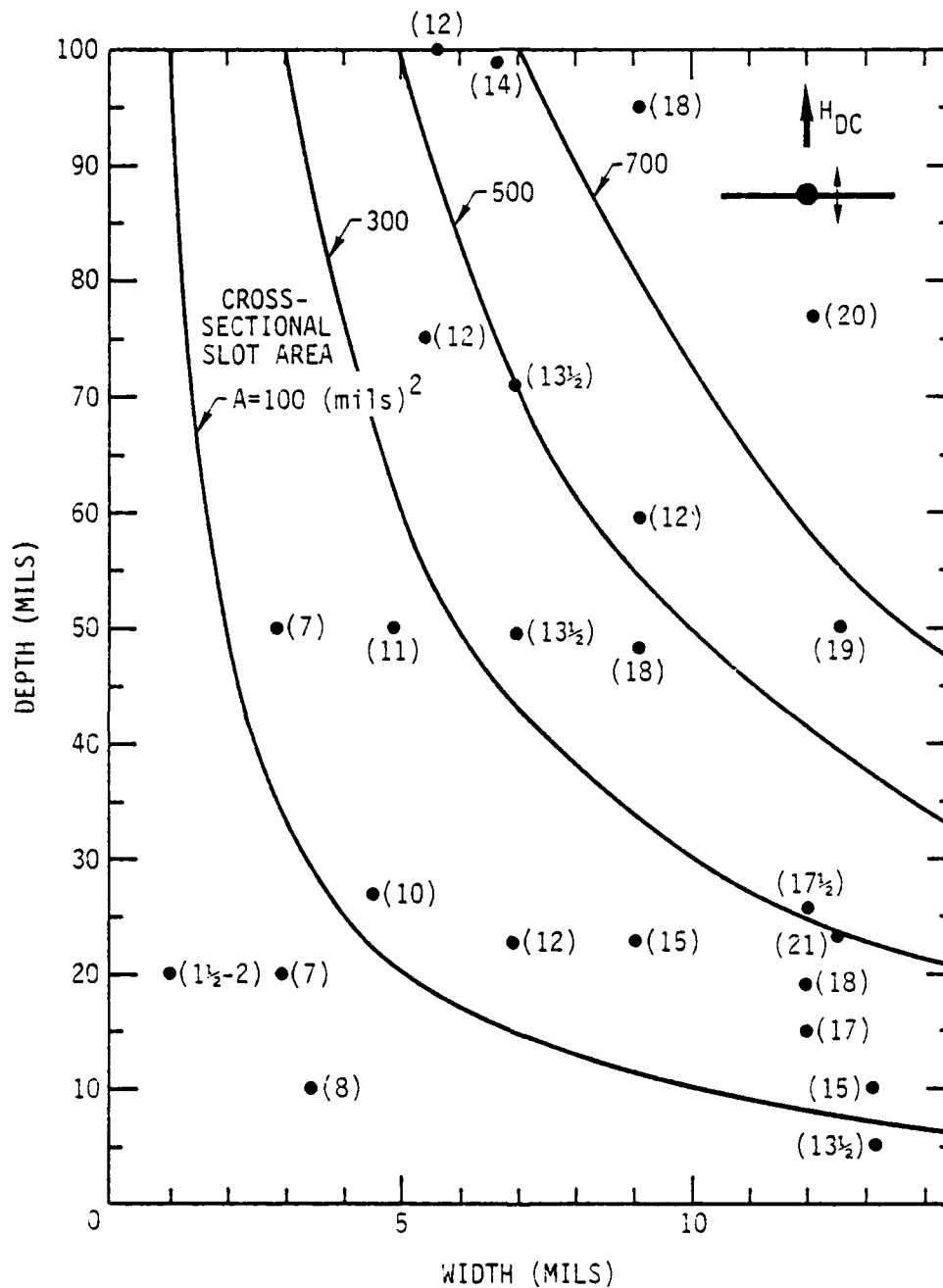


Fig. 5 Measured frequency shifts (in MHz) as a function of slot surface width and depth. Normal magnetizing field case.



An explanation may possibly be provided by the small size of the probe. The fields produced have many high spatial harmonics which may not effectively couple to the TEM mode. The results do indicate, however, that a slot 10 mils deep by 5 mils wide is very easily detectable. These slots are 2" long but experiments performed with the probe placed near the end of the slot shows that the frequency shift is unaffected if the probe is more than 50 mils from the end. This gives an indication of the lateral extent of the probe field, so that the probe is effectively sampling a section of the slot that is approximately 50 mils long. Additional data on the length dependence of the frequency shift was obtained by measurements on through slots in a deposited chrome-gold ($\sim 2000\text{\AA}$) film on glass. A 200 mils long x 1 mil wide slot gave a frequency shift of 15 MHz and a 100 mils long x 1 mil wide slot gave a frequency shift of 12 MHz. This indicates a sampling length of not more than 100 mils. Efforts are being made to fabricate EDM slots and fatigue cracks with a surface length of the order of tens of mils. A closed fatigue crack with a surface length of about $\frac{1}{2}$ " has been detected in stainless steel without use of any sophisticated electronics.

References

1. G.S. Kino, Rockwell Special Report Third Year Effort, Contract No. F33615-74-C-5180, p. 159-175, June 30, 1977.
2. B.A. Auld and G. Elston, *ibid*, pp. 267-270.
3. M.L. Burrows, "A Theory of Eddy Current Flaw Detection," (University Microfilms, An Arbor, Mich. 1964).
4. C.V. Dodd, W.E. Deeds and J.W. Luguire, "Integral Solutions to Some Eddy Current Problems," *Int. J. Nondestructive Testing* 1, pp. 29-90 (1969).
5. A.H. Kahn, R. Spal and A. Feldman, "Eddy current Looses Due to a Surface Crack in Conducting Material," *J. Appl. Phys.* 48, pp. 4454-4459 (1977).



PROJECT III, UNIT A, TASK 1

ULTRASONIC MEASUREMENT OF ADHESIVE BOND STRENGTH

G.A. Alers and R.K. Elsley
Rockwell International Science Center
Thousand Oaks, California 91360

Introduction

The general objective of this program is to develop a nondestructive method which would enable the strength of adhesion in a completed adhesive bond to be predicted. Since ultrasonic waves easily penetrate the layered structures involved and since acoustic pulses reflected from the layer of adhesive are easily detected, it is anticipated that ultrasonic techniques should hold the maximum possibility for providing the needed strength information. Furthermore, the ultrasonic test methods employed are readily transferred to production facilities where speed of inspection is paramount.

For the particular phase of the program reported here, the emphasis has been placed on a careful study of the Fourier transform of the ultrasonic signal reflected from the bonded sandwich. In this representation, the frequencies at which standing waves occur in the adherends and in the adhesive layer can be so accurately measured that small shifts due to abnormal conditions at the adhesive-adhered interface should be detectable. Unfortunately, the problem of establishing this correlation first requires the development of two important procedures. First, controlled mechanical tests must be performed which can be interpreted in terms of a mechanism of failure and which can make possible the establishment of a model to explain any correlations that are observed. Second, the unwieldy but rigorous theory that is available to predict the standing wave frequencies of a particular bond must be simplified so that unusual frequency shifts can be recognized and quantified. Both of these basic problems were addressed seriously during the past six months and procedures for accumulating useful strength data and the corresponding, detailed ultrasonic data have now been established. Unfortunately, the application of these procedures to real adhesive bonds had just begun and only a small amount of preliminary correlations are presented in this report.

In the more broad sense, the current emphasis placed on seeking correlations with strength in the Fourier transform representation of the ultrasonic data is only a first step in the development of signal processing techniques for predicting bond strength. Other representations and other characteristic features in the signals will be systematically considered as reliable data is developed. For example, the frequency dependence of the effective attenuation in the adhesive should be extracted from the signals because it is the physical parameter that determines the frequency at which splitting of the standing waves in the adherends can be observed and this splitting is known to be correlated with some types of interfacial weakness. No matter what the best signal feature may turn out to be, it is important to establish a reliable method of measuring bond strength and a way of collecting detailed ultrasonic waveforms before any correlations can be attempted. The present report describes the establishment of these two important foundations and starts the process of correlating mechanical strength with a few of the most obvious signal features.

In the report following, careful control was exercised over each step in the experimental program and a useful amount of high quality mechanical and ultrasonic data has now been accumulated on a well defined set of specimens. Mathematical modeling efforts have enabled corrections for bond line thickness variations to be taken into account in a rigorous manner. Unfortunately, the simple correlations between ultrasonic parameters and the strength which looked promising in the past do not appear to be surviving the detailed scrutiny provided by the current data set. However, more physically meaningful methods of treating the ultrasonic data as well as microscopic examination of the fracture surfaces to elucidate the failure mechanisms have yet to be considered and will form the backbone of the program in the immediate future. Subsequent to these studies based upon Fourier transform analysis, the data will be re-examined with other types of signal features being tested for correlations.

Strength Measurements

The term "strength of an adhesive bond" is often used glibly and must be more carefully defined for the purposes of this program. Two separate measures of strength are required to define the mechanical response of an



adhesive system since bonded joints can be made to fail under either pure shearing stresses or pure peeling stresses. One would hope that fracture mechanics models of the response of a given kind of defect to these two loading modes would provide relationships whereby the failure stress could be predicted from a measurement of the characteristics of the defect. Unfortunately, the fracture mechanics of heterogeneous media such as found in adhesive bonded structures is not well developed and only rather crude estimates can be made. A semi-empirical analysis of a simple peel test¹ can yield a numerical value for the work of extending a crack a unit distance - an equivalent fracture surface energy parameter. This number can be inserted into a Griffith type energy balance equation² that predicts the critical size of an interfacial disbond between layers of considerable disparity in their elastic properties (rubber to steel) subjected to a shearing stress. The legitimacy of this procedure has not been established but we will use it here because no other analysis exists.

The test specimens were made from a pair of 1" wide by 6" long strips of aluminum (alloy 6061) bonded together using Chemlok 304 adhesive because it does not contain a scrim cloth nor does it evolve any gasses to produce porosity during cure. The aluminum strips were chosen to be 1/8" thick to insure their rigidity during the peel tests and to approximate well the "thick adhered" condition for shear tests. Furthermore, this thickness results in closely spaced resonant frequencies when the ultrasonic data is analyzed, thereby yielding more special frequencies at which to deduce properties of the adhesive layer. All specimens were prepared with the identical adhesive but different surface preparations on the aluminum to obtain specimens which would fail by a weakness of adhesion rather than by cohesive failure. All specimens had 5 mil copper wires inserted at three locations along the 6" dimensions to maintain a constant bond line thickness during the curing process.

Peel tests were performed in an Instron machine using especially designed grip fixtures to insure that the force applied to the ends of the aluminum strips did not introduce any torques. A schematic diagram of this peel test system is shown in Fig. 1 which defines the physical dimensions and forces used in the formulae to deduce the crack extension force parameter, G . It has been shown¹ that the crack extension force is defined by

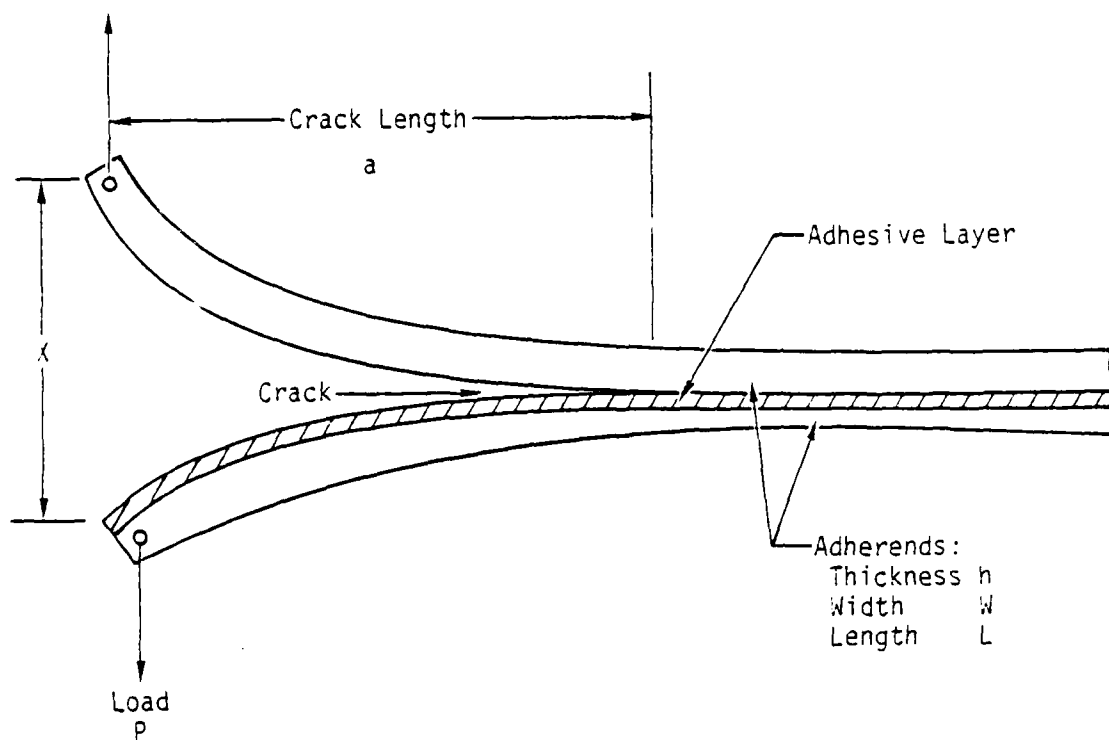


Fig. 1 Schematic diagram of a peel test configuration that measures the force necessary to cause the crack to extend. An interfacial failure mode is shown in this example.



$$G = \frac{P^2}{2w} \frac{dC}{da} \quad (1)$$

where C is the compliance of the specimen given by

$$C = \frac{\Delta x}{\Delta P} \quad (2)$$

If there were no adhesive, the compliance could be calculated from the theory of elasticity to be

$$C = \frac{24 a^3}{Ewh^3}$$

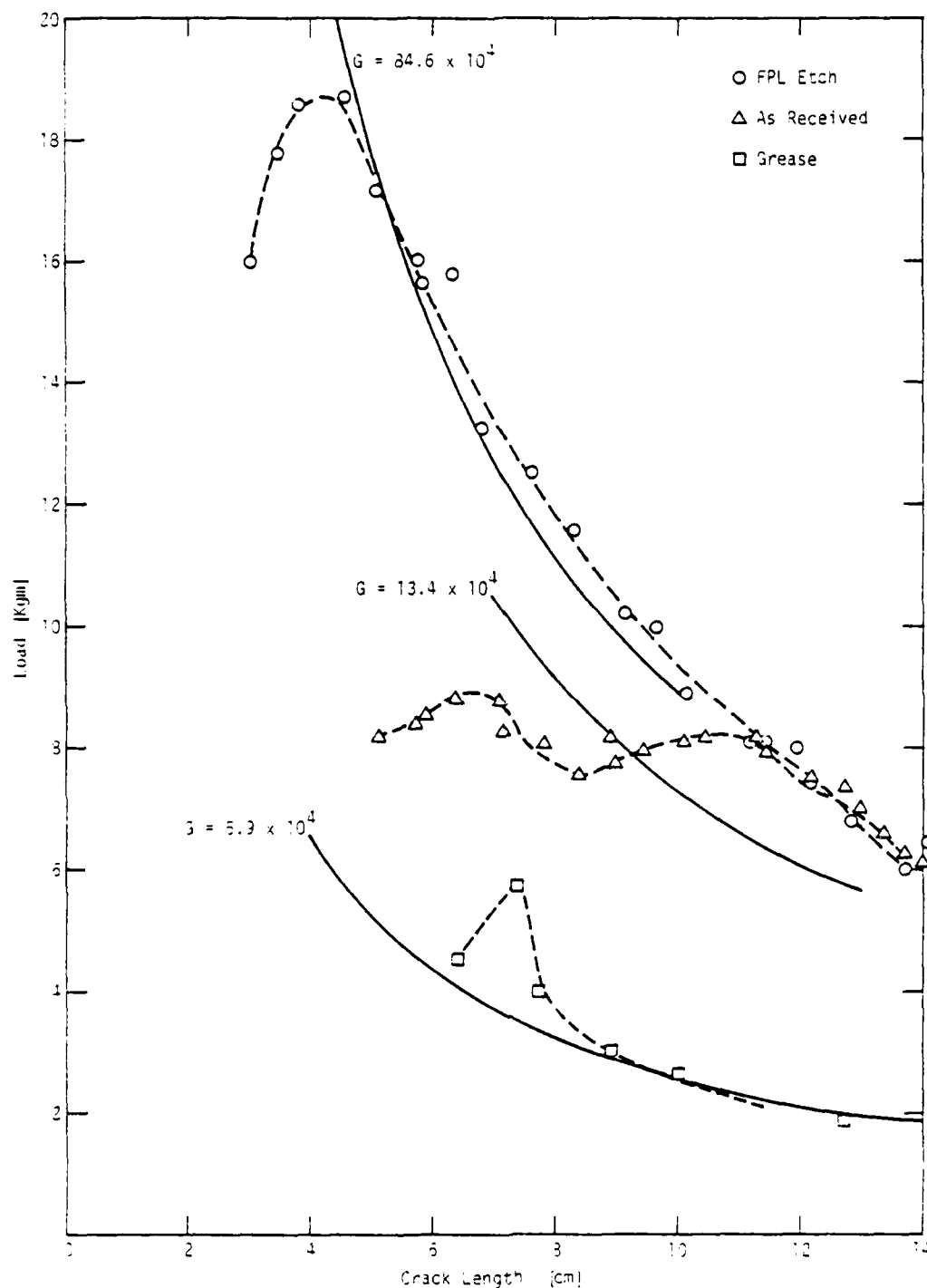
where E is the Young's modulus of the adhered material. For our purposes, we will define the effective compliance of our sandwich structure to be

$$C = k a^3 \quad (4)$$

where k is an empirical constant determined by measuring the change in crack opening displacement, Δx , corresponding to a change in load, ΔP , at a fixed value for the crack length. (This compliance measurement was made in practice by reducing the load slightly at each of a series of crack lengths and measuring the corresponding change in displacement and then plotting the compliance value deduced from Eq.(2) as a function of a^3 to define the parameter k in Eq.(4)). Inserting Eq.(4) into Eq.(1) yields

$$G = \frac{P^2 k}{6w} a^2 \quad (4)$$

which predicts that a plot of P vs a should be a hyperbola for a constant G value. Figure 2 shows this result for experimental data obtained on three test specimens with three different modifications of the aluminum surface prior to bonding. Obviously, the surface treatment has a profound influence on the peel strength and the crack extension force observed. It is the objective of this program to expose a correlation between the G value and some measurable ultrasonic parameter.



SC595-105

Fig. 2 Load, P , vs crack length, a , values for three peel specimens with different surface preparations. The crack extension force G has the units of dynes per cm or ergs per cm^2 . If its value is constant for all crack lengths, experimental data should fall on the hyperbolae defined by the solid lines.



Compression shear tests were performed by putting a pair of 6" long slots on opposite sides of the 1" wide x 6" long adhesively bonded peel test specimens and then cutting one half inch wide pieces to make twelve 1" x $\frac{1}{2}$ " specimens. Two strips with identical surface preparations were assembled so that a total of 24 nominally identical compression shear specimens were available to establish the statistical spread in strength values. Figure 3 shows the failure probability deduced from the compression shear test data on a set of specimens using three different kinds of surface treatments. Unlike the peel strength data, the samples with their interfaces degraded by grease showed a higher resistance to shear failure than the samples which were prepared using the as received condition of the aluminum surfaces. Again, it is the objective of this program to expose a correlation between the shear strength and some measurable ultrasonic parameter.

Ultrasonic Measurements

Since the mechanical tests described above generate strength data on a point-by-point basis over the entire length of each six inch long specimen, the ultrasonic measurements must also provide detailed information at each point. This is obviously a large amount of data that can only be handled by the mass storage capabilities of a digital computer. An entire RF waveform showing all the reflections from the aluminum adhered surfaces and the thin adhesive layer was digitized and stored along with the location of the ultrasonic probe and the specimen name in the computer memory. Twelve waveforms taken at $\frac{1}{2}$ inch intervals along the length of each six inch long specimen comprised the complete set of ultrasonic data. Subsequent to collecting and storing these data, the waveforms were recalled and Fourier analyzed to produce the graphs of reflected amplitude vs frequency shown in Figs. 4 and 5. In addition, the computer was programmed to locate and print out the frequencies at which the minima in reflectivity occurred. These minima frequencies are listed in the table on the left side of each figure.

Theoretical Analysis

The acoustic reflectivity of a multilayered medium has been treated in considerable detail in the textbook by Brekhovshikh³ who comments: "It is not sensible to write out the expressions for a large number of layers

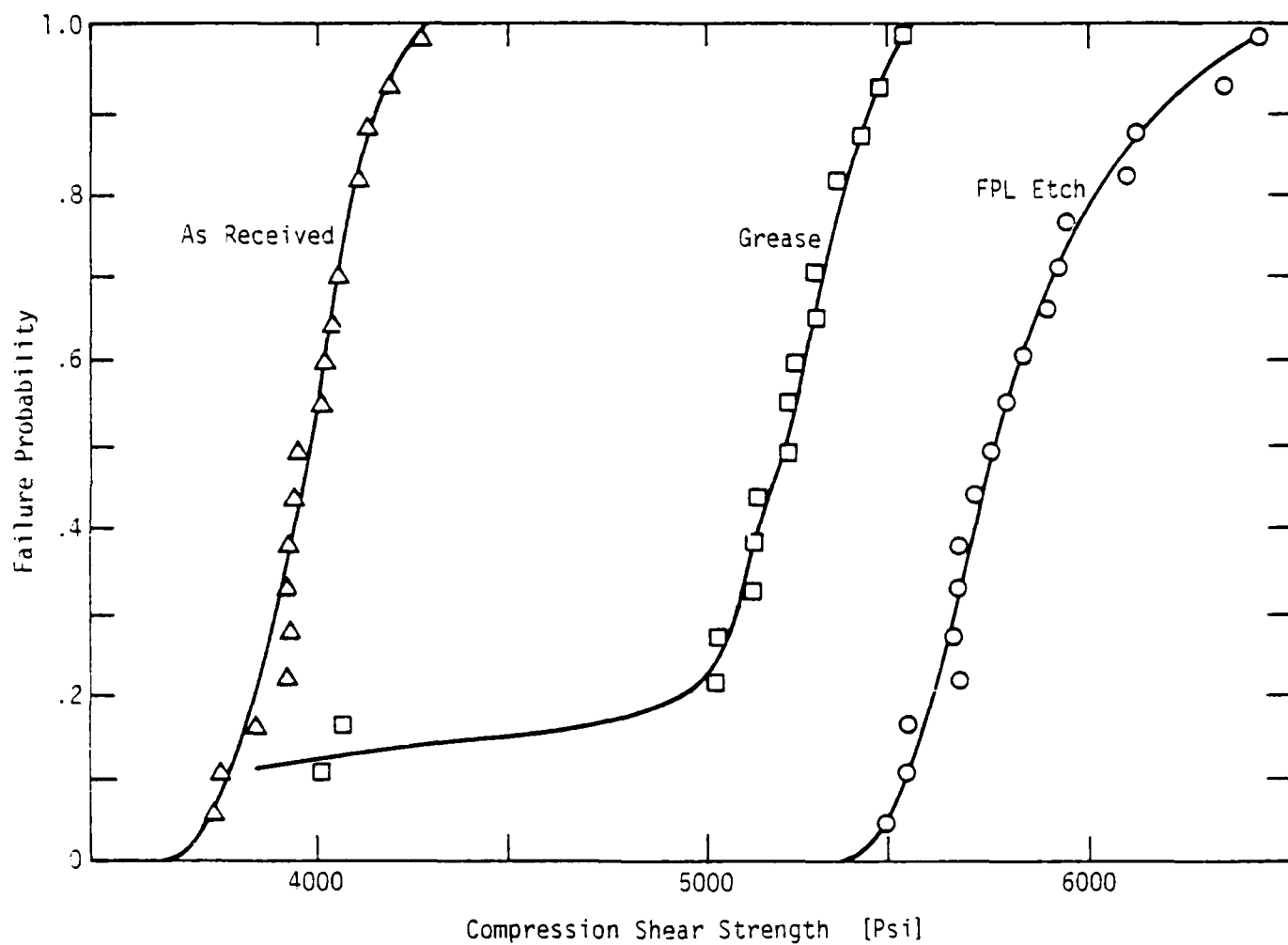


Fig. 3 Distribution in compression shear strengths observed in specimens prepared with three different techniques for degrading the adhesive to aluminum interface. All samples showed clearly interfacial failures.

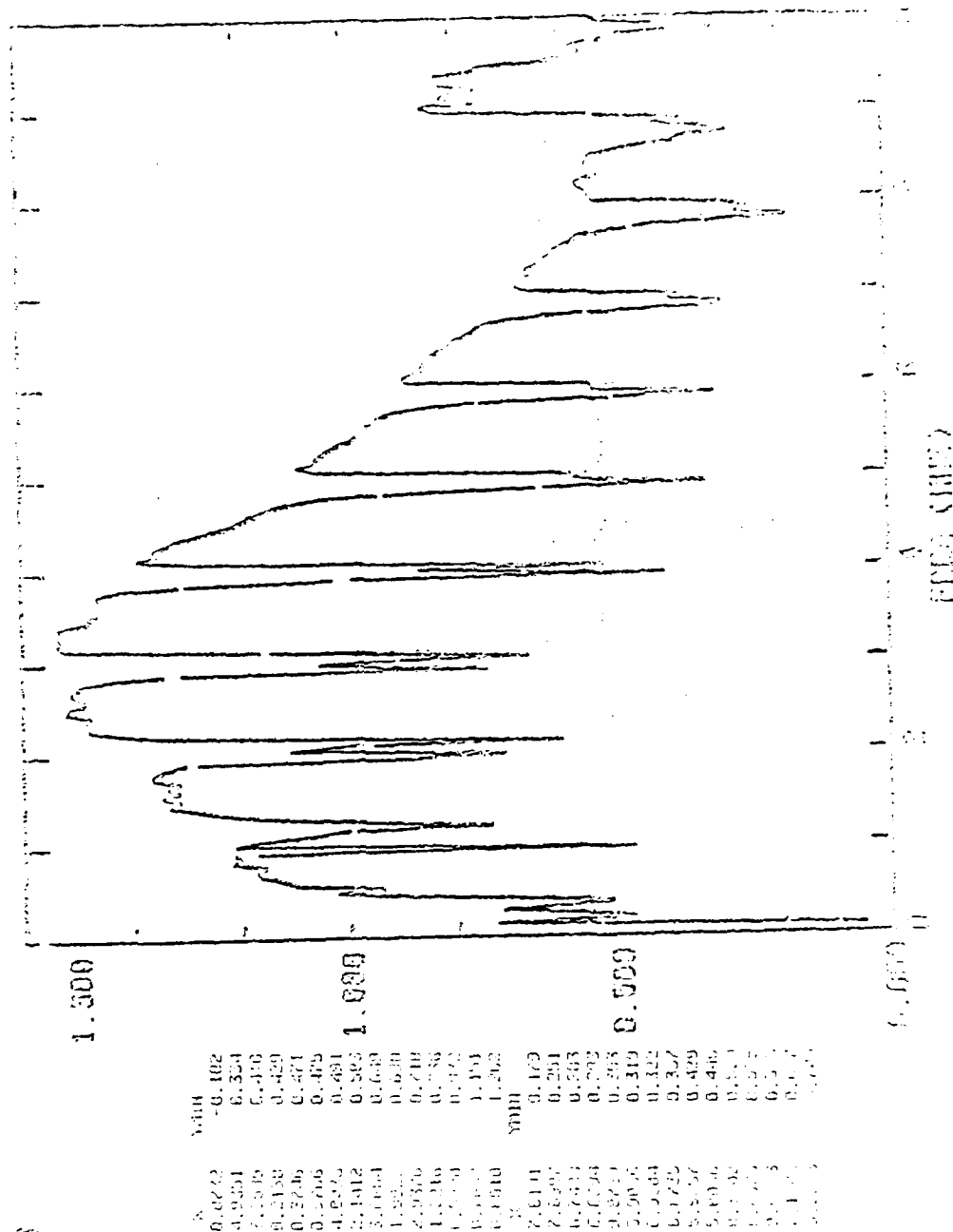


Fig. 4 Fourier transform of the ultrasonic signal reflected from a sample whose compression shear strength had a low value of 4.03 ksi.

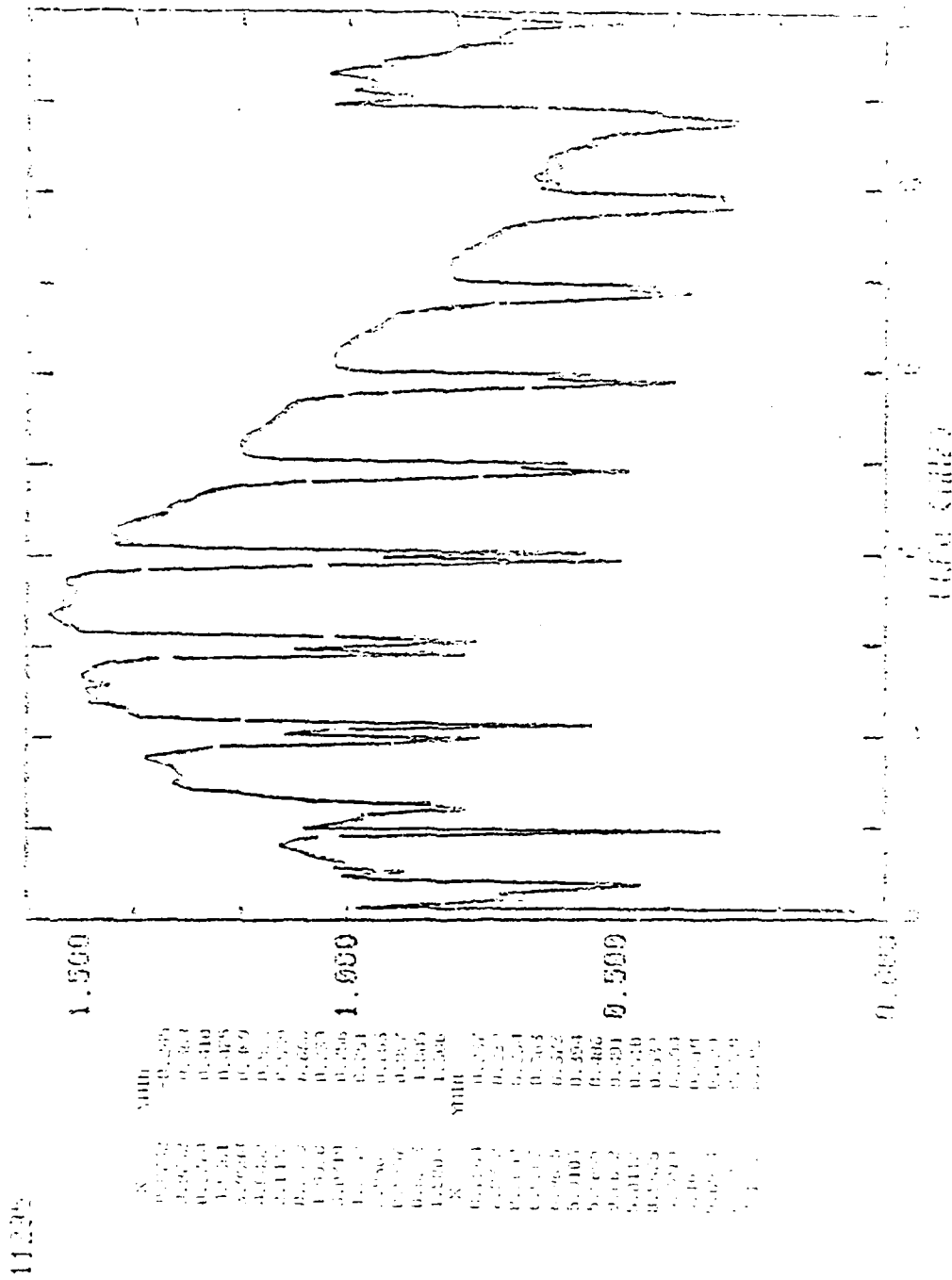


Fig. 5 Fourier transform of the ultrasonic signal reflected from a sample whose compression shear strength had a high value of 6.10 ksi.



(greater than three) because the expressions have an extremely unwieldy and unclear form." However, for the case appropriate to our experiments (identical layers symmetrically disposed about the adhesive layer) a considerable simplification occurs. Sparing the reader views of impressively long algebraic expressions, the final result for the reflection coefficient takes the form

$$R = \frac{EF}{4A^2 + F^2} - 2i \frac{EA}{4A^2 + F^2} \quad (5)$$

where E, F and A are quadratic functions of two important frequency dependent variables

$$\delta = \tan \frac{2\pi t}{\lambda_a} \quad (6)$$

and
$$\epsilon = \tan \frac{2\pi d}{\lambda_m} \quad (7)$$

with various coefficients involving ratios of the acoustic impedances of the layers. In these equations, the thickness of the adhesive is t and that of the adhered is d while λ_a and λ_m are the acoustic wavelength in the adhesive and the metal adhered respectively. Obviously, the reflectivity reaches a minimum whenever $E = 0$ which occurs for values of δ and ϵ that satisfy the equation

$$\left(\frac{Z_3}{Z_1} - \frac{Z_1}{Z_3}\right)\delta + 2\left(\frac{Z_2}{Z_1} - \frac{Z_1}{Z_2}\right)t + \left(\frac{Z_1 Z_3}{Z_2^2} - \frac{Z_2^2}{Z_1 Z_3}\right)\delta \epsilon^2 = 0 \quad (8)$$

where the subscripts 1, 2 and 3 refer to the water bath, the adhered and the adhesive respectively and Z is the acoustic impedance. Equation 8 is quadratic in ϵ so two solutions exist and describe the splitting of the standing wave resonances of the adhered. The standing wave resonance in the adhesive is described by solutions of Eq.(8) for which δ is only approximately equal to zero since the solutions occur at the frequency for which values of δ and ϵ cooperate together to satisfy Eq.(8).

Equation 8 is very useful because it predicts the frequencies at which prominent features occur in the frequency spectra shown in Figs. 4 and 5. In particular, the lowest frequency of resonance (the dumb-bell mode) can be easily calculated, and the amount of the splitting is simply the difference between two adjacent roots of the equation. This simplicity of calculation will enable us to use one feature of the spectrum to calculate such an illusive quantity as the local bond line thickness (t) so that other features can then be reliably predicted for comparison with the observations.

Strength - Ultrasonic Parameter Correlations

Previous studies have indicated that the frequency of the dumb-bell mode or the splitting of the lowest split resonance could be correlated with the shear strength of the bond. Also, the highest frequency at which splitting is observed in the total spectrum was found to be a very easy predictor of the strength for interfaces degraded by a layer of grease. The new data obtained in this phase of the program provides an excellent opportunity to verify or reject these earlier observations.

An examination of the total spectrum for each specimen whose strength measurements are displayed in Fig. 3 showed that choosing the frequency above which splitting is not longer observed required a very unreliable and subjective judgement. Hence, it is not very accurate. Furthermore, the samples prepared with a grease layer of contamination were not seriously degraded in shear strength so the effect on the splitting should not be very large. The best method for displaying any correlation between the highest frequency for splitting and the strength is to prepare the histogram shown in Fig. 6. It can be seen from this data presentation that most of the weak, grease degraded bonds showed a lower value for the highest split resonance frequency than most of the strong samples prepared with the FPL etch. The weakest samples (prepared with as-received surfaces) displayed only slightly lower frequencies for split resonances and were very similar to the grease degraded samples. Quite obviously samples with much more dramatically reduced strengths must be prepared and tested and a more accurate measure of the disappearance of splitting will have to be developed.

Turning to the more quantitative spectral parameters of the value of the frequency of the dumb-bell mode or the splitting in the lowest frequency

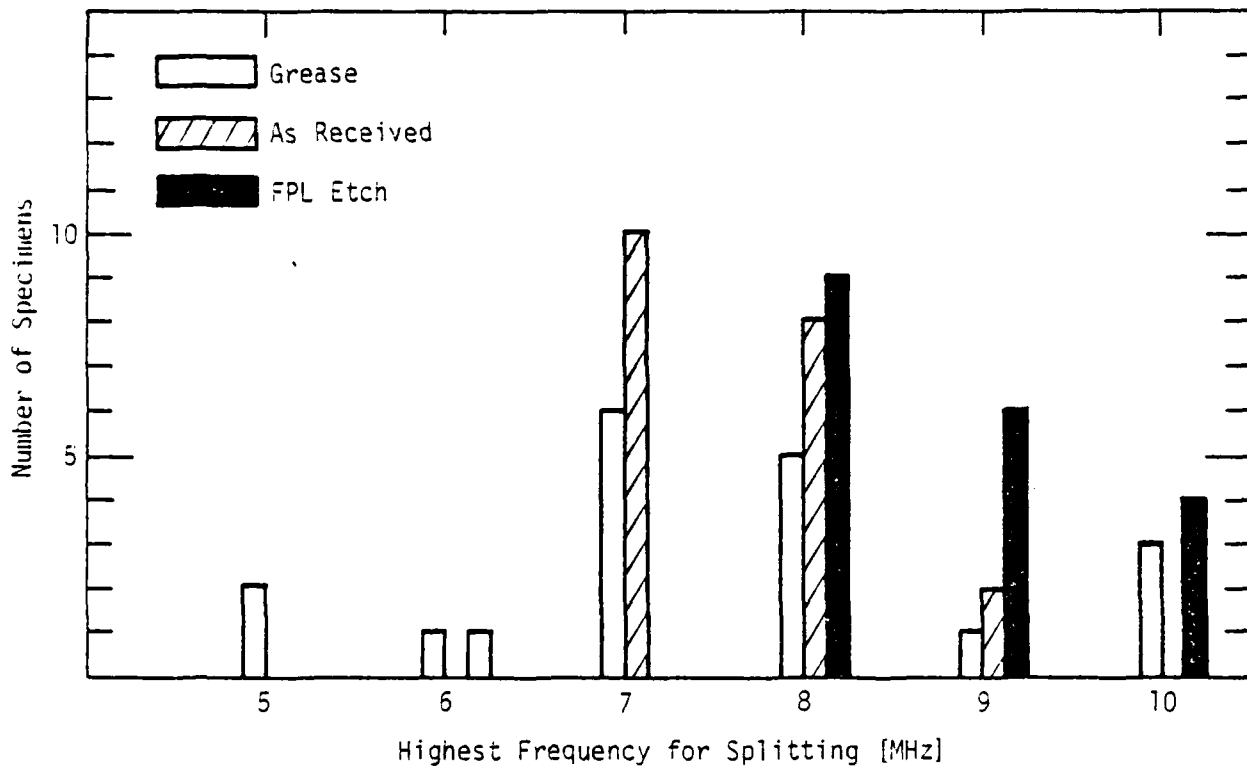


Fig. 6 Histogram showing the number of specimens whose frequency spectra showed a particular value for the highest frequency at which splitting could be observed.



resonance, it was found that no correlation with the dumb-bell resonance could be made because the thickness of the bond line dominates this resonant frequency. Using this mode to define the effective bond line thickness and then using that value to correct the observed splitting of the lowest split resonance proved to be a very effective way of reducing the scatter in the data. Unfortunately, no correlation with strength could be seen in the corrected data. This disappointing results may be caused by not having specimens with dramatically different strength values or the fact that the lowest split resonance is not sensitive enough to interface variations.

In order to look for correlations using the properties of the higher frequency resonance, a special technique was used to overcome the effects caused by bond line thickness variations. All the data were examined to find individual samples whose dumb-bell mode resonant frequencies were nearly identical. Using this smaller set of samples, strength differences can be correlated with ultrasonic parameters for a constant value of the dumb-bell resonance which in turn implies a constant bond line thickness. Figure 7 shows how the degree of splitting at each higher frequency resonance varies with the frequency of that resonance. The data points at each frequency correspond to specimens with different compression shear strengths, so it can be concluded that the amount of splitting does not show an obvious, systematic variation with strength. The solid line is a theoretical curve calculated from the solutions of Eq.(8) using the dumb-bell mode resonant frequency to define the only adjustable parameter in the expression (the bond line thickness). Agreement between theory and experiment appears to be within the experimental scatter of the data at frequencies below about 4 MHz. This implies that at these low frequencies, the condition of the interface between the metal and the adhesive has little influence on the standing wave resonances.

Using the crack extension force values deduced from the peel tests shown in Fig. 2, and the values of the loads at failure in the compression shear tests shown in Fig. 3, it is possible to deduce a value of the length of a critical disbond at the interface between the adhesive and the metal using a Griffith type formula due to Gent.² The results of this calculation predict that a flaw 10 mils in diameter could be responsible for the failure of the grease degraded bonds, a 40 mil diameter flaw for the as-received aluminum



SC595.32SA

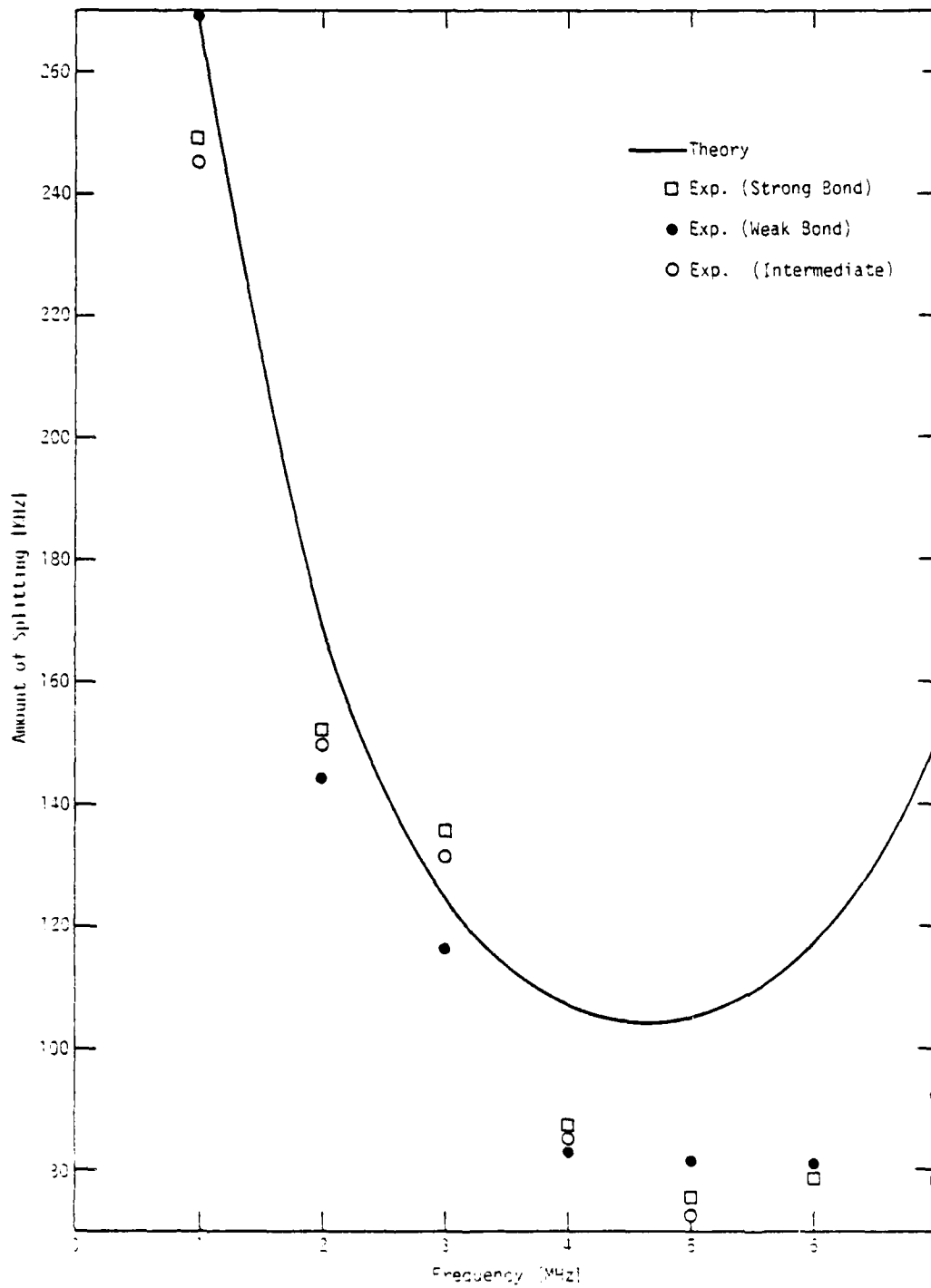


Fig. 7 Variation in the degree of resonant frequency splitting as a function of frequency for three samples having differing compressive shear strengths but nearly identical bond line thicknesses.

bonds and a 110 mil defect for the FPL etched samples. All of these defects should be observable under an optical microscope and a search for them will be carried out in the near future. However, it must be remembered that the fracture mechanics arguments are not very rigorous so the sizes listed above should be taken only as order of magnitude estimates.

Conclusions

1. The fracture mechanics of adhesive bonds containing localized defects has been reviewed and used to define mechanical tests which measure the basic parameters from which the strength of bonds subjected to both peel and shear can be predicted.
2. Methods of preparing and testing adhesively bonded sandwich structures under peel and shear forces have been established.
3. Computer programs to rapidly scan ultrasonic transducers over adhesively bonded specimens and to record detailed RF waveforms at many locations along the specimens have been prepared.
4. The mathematical description of the interaction of ultrasonic waves with the layered media used in these tests has been reduced to a simple formula which predicts the location and splitting of the resonant frequencies observed in the Fourier transform of the reflected ultrasonic signals.
5. Verification of the previous observation that the bond strength could be correlated with the frequency at which the resonances in the ultrasonic reflectivity are no longer split was not very satisfying the measurement of the last split resonance is not only a subjective judgement but is also inaccurate and because the specimens tested to date have too narrow a range of strengths.
6. Verification of the previous observations that the value of the dumb-bell mode resonance or the magnitude of the splitting of the low frequency resonances could be correlated with strength was not successful because the range in strengths of the specimens tested to date was too small.
7. Now that the procedures for measuring bond strength and for collecting detailed ultrasonic waveforms have been developed and tested, many more specimens can be tested over a wider range of



strengths. New ultrasonic parameters for correlating with strength will be searched for using both new data and the old data stored in the computer. In particular, parameters that depend upon attenuation effects at the higher frequencies will be investigated and some new measurements of the physical properties of the adhesive at very low frequency will be carried out.

References

1. G.P. Anderson, S.J. Bennett and K.L. DeVries, "Analysis and Testing of Adhesive Bond," published by Academic Press, New York, 1977.
2. A.N. Gent, Rubber Chemistry Technology Journal, Vol. 47, p. 202 (1974)
3. L.M. Brekhovshikh, "Waves in Layered Media," Vol. 6, Applied Mathematics and Mechanics Monographs, Academic Press, New York, 1960.

PROJECT III, UNIT A, TASK 2

ULTRASONIC ELLIPSOMETER APPLIED TO
ADHESIVE BOND INSPECTION

C. Vasile, R. B. Thompson, and G. A. Alers
Rockwell International Science Center
Thousand Oaks, California 91360

Introduction

A fundamental problem in the measurement of adhesive bond strength is the determination of the strength of adhesion of the bond between the polymeric adhesive material and the metal sheets which are being joined. This is made difficult by the thinness of the layer of material affected by the bonding process. The most conservative estimate would place its dimensions at one interatomic distance. However, in fact, it is probably considerably greater because the microscopic surface is rough and the oxide layer porous so that the polymers and metal oxide are probably mechanically entwined over distances of several hundred atomic diameters. In any event, it is necessary to develop an inspection technique which is sensitive to the physical properties of very thin layers of material.

A similar problem occurs in the measurement of the properties of very thin transparent layers of contaminants on metal surfaces, and a solution has been found in the optical ellipsometer, Figure 1. When an elliptically polarized light beam is reflected from the surface, its ellipticity changes because the complex reflection coefficient for the component polarized in the plane of the surface is different from that for the component polarized in the plane of incidence. Furthermore, this ellipticity shift is influenced by thin layers of materials on the surface of the conductor and this effect can be used to measure the thickness and optical properties of those layers. Since the two components of the optical beam have otherwise identical propagation properties, the technique is a relative measurement with very high sensitivity. In particular, layers as thin as one atomic layer, or $5 \times 10^{-4} \lambda$, can be detected and studied.

It has been suggested that the elastic wave analog of this device might prove useful in the measurement of adhesive bond strength. Thus, for a

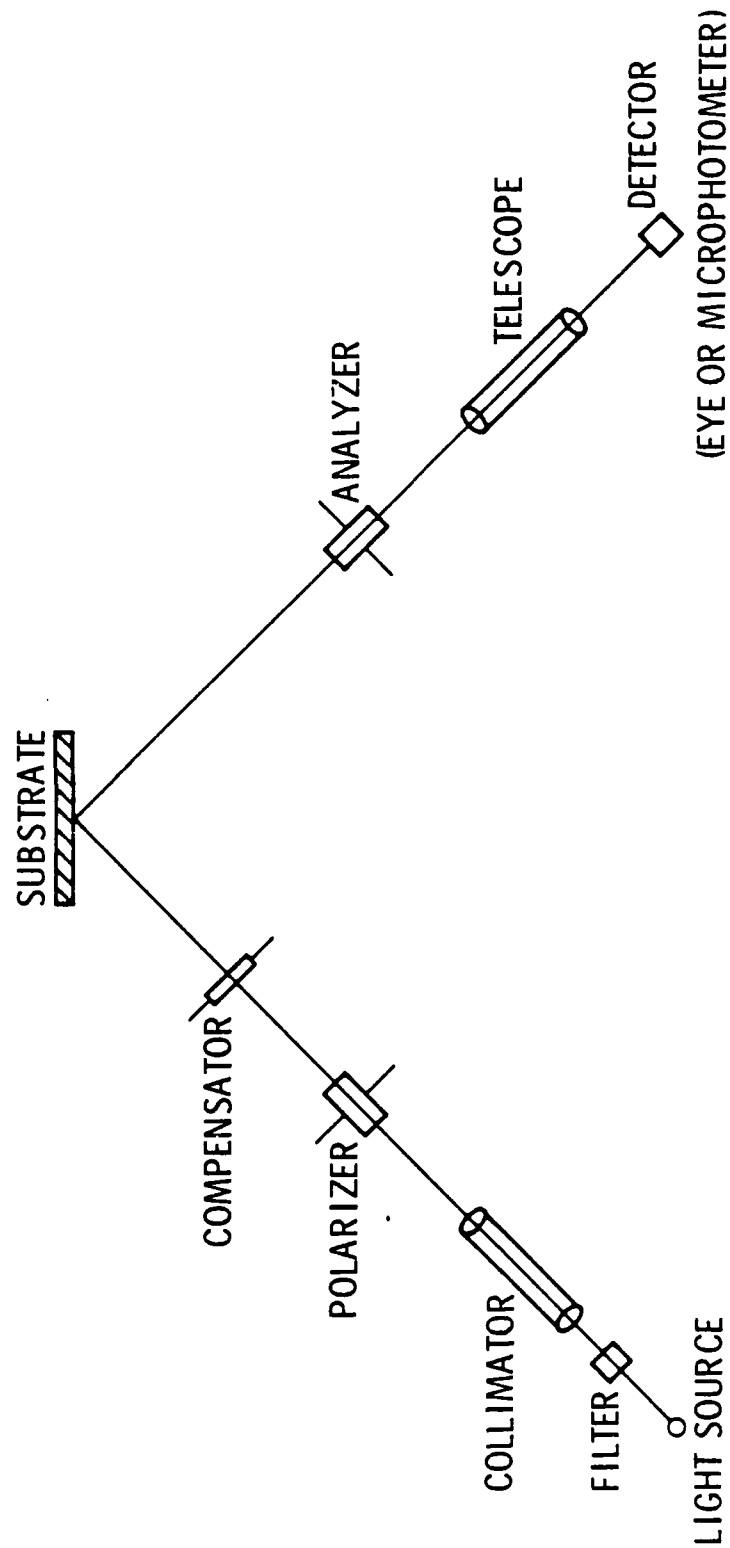


Fig. 1 Optical ellipsometer.

1 MHz device, the ultrasonic shear wavelength is on the order $3 \times 10^3 \mu\text{m}$. A sensitivity comparable to that of the optical device would imply that layers as small as $1.5 \mu\text{m}$ could be studied. Of course, this is a very speculative number since many parameters enter into determining the sensitivity which may not scale simply. Nevertheless, experimental investigation is strongly warranted.

The construction of an ultrasonic ellipsometer is made possible by newly developed electromagnetic transducer (EMAT) technology. These can independently excite both SH and SV shear waves, as opposed to usual piezoelectric immersion or wedge transducers which only excite the SV waves. Figure 2 illustrates one possible way that this could be realized using the periodic permanent magnet EMAT. Current driven through the axial coil excites the SM wave, while current driven through the circumferential coil excites the SV wave. A pair of such transducers, combined with electronic elements to control the phase and amplitude of the currents delivered to the two transmitter coils and detected in the two receiver coils, constitutes an ultrasonic ellipsometer as shown in Figure 3.

A prototype of such a device was constructed as part of the Rockwell International IR&D program. Two problems were found. First, due to the recovery time problems, it was impossible to inspect thin sheets such as those typically used in adhesive bonding. Second, a strong electrical coupling between the two coils was observed to arise through the permanent magnet core. Since the coils are orthogonal, this coupling was not anticipated. However, currents in one coil can cause the magnetization to precess and reradiate into the orthogonal coil. This coupling was sufficiently severe to make it impossible to separately control the two polarizations and achieve the null condition in the output of the receivers that makes the optical ellipsometer so sensitive to thin layers on the reflecting surface.

Current Approach

Two changes in the originally proposed device have been made to accommodate these problems. To avoid the recovery time limitations, it has been decided to excite plate modes rather than quasi-plane waves. In this way, the waves can propagate along the sample and be detected after sufficient



SC595.32SA

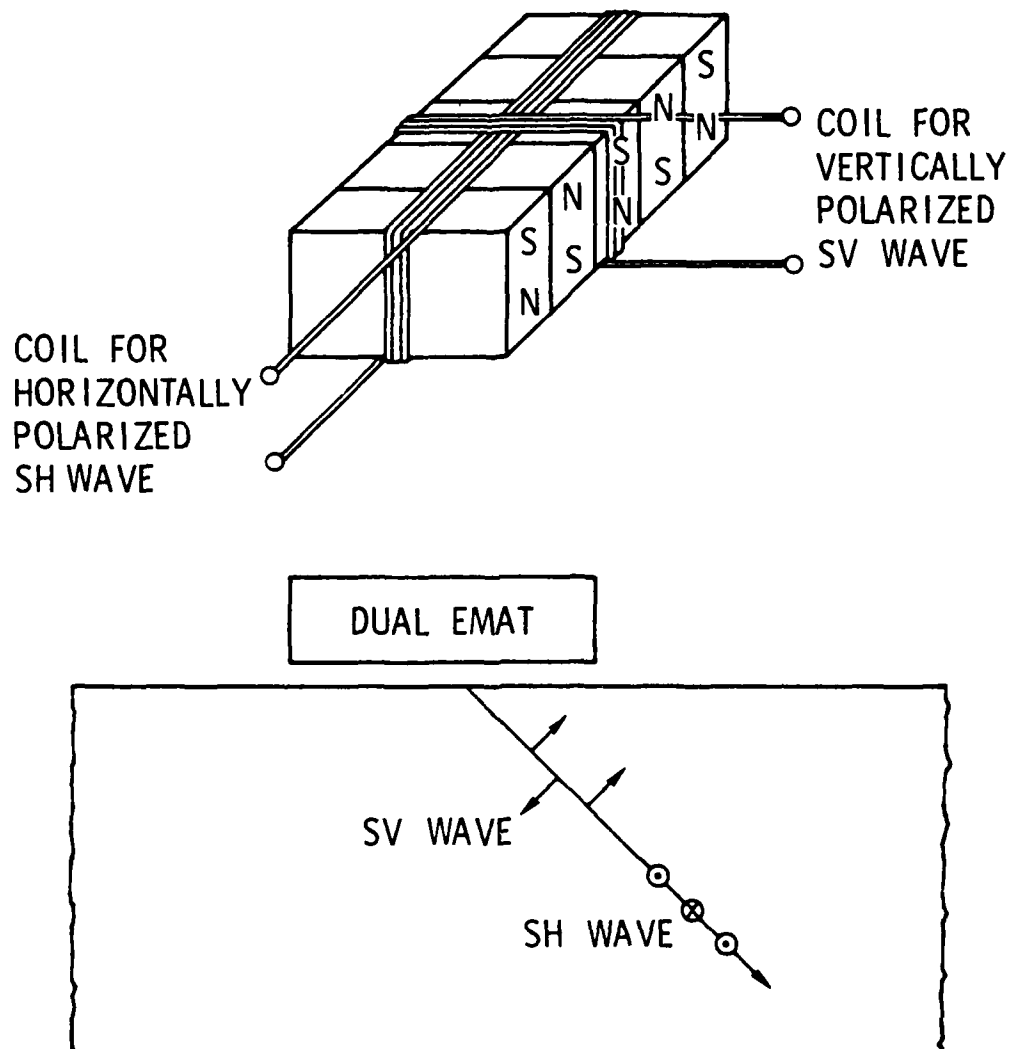


Fig. 2 Periodic magnetic EMATs can excite shear waves of arbitrary elliptical polarization.

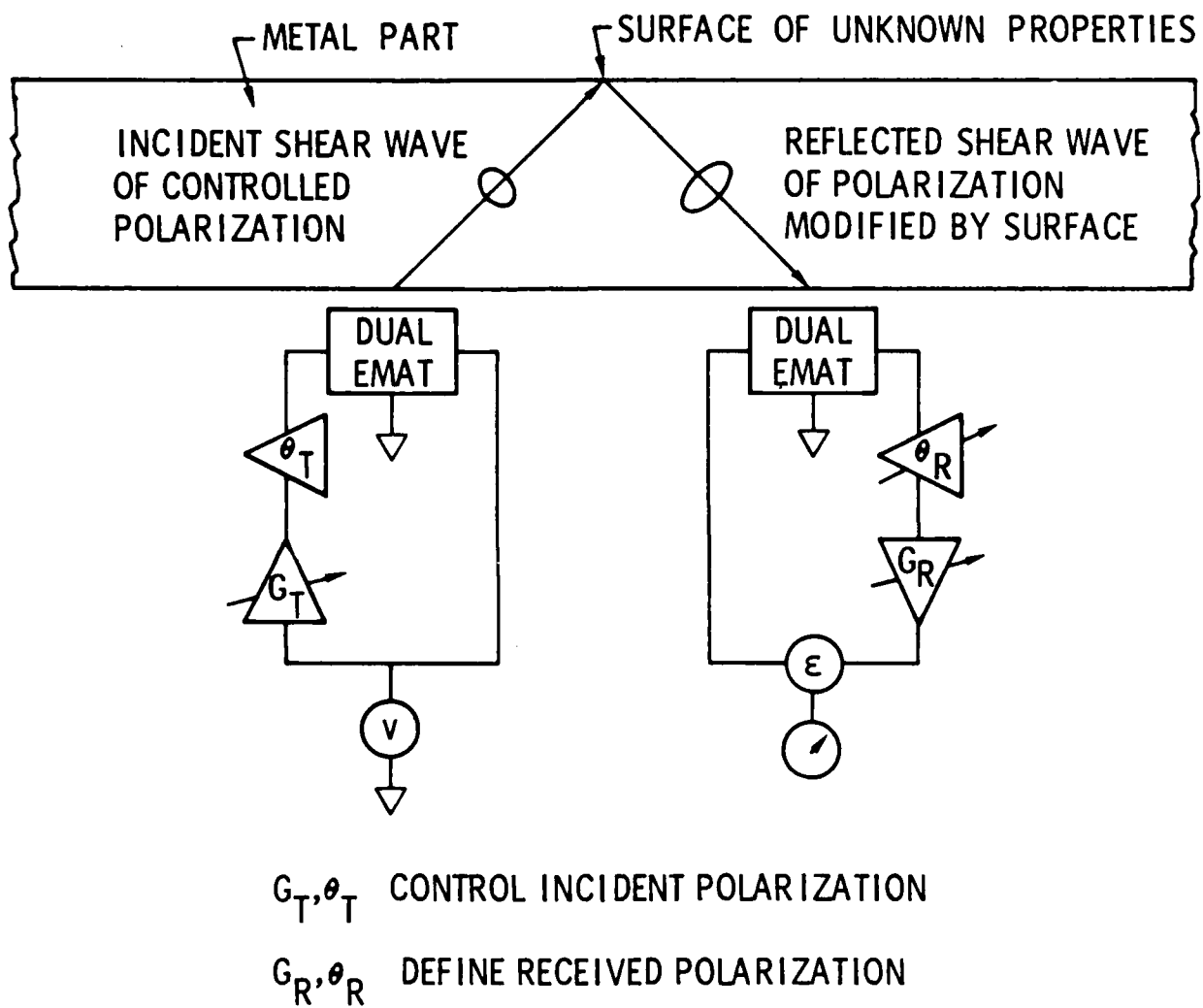


Fig. 3 Elastic wave ellipsometer.



delay that the receiver has recovered. In order for this to work satisfactorily, it is necessary that waves of two polarizations be excited that are degenerate in velocity except for perturbations produced by the adhesive. Otherwise, it would be difficult to separate changes in the polarization produced by the adhesive from changes in polarization produced by changes in propagation distance. This is in general impossible, but one special point exists where two plate modes do exhibit degeneracy. As shown in Figure 4, the SH_1 mode and the S_0 mode dispersion curves are tangential at one point. Here each can be decomposed into plane shear wave components, each bouncing at 45° between the two faces of the plate. The SH_1 mode is made up of horizontally polarized shear waves and the S_0 mode is made up of vertically polarized shear waves. The principles of the plate wave device are then completely analogous to the plane wave case. The device described below has been designed accordingly with a period of 0.25 in. to operate on a 0.125 in. thick plate. In order to overcome the problem of electrical coupling between the coils, we have designed two separate transducer pairs, each pair being specific to either the SV or the SH polarizations. Each of these transducer pairs will be placed on an aluminum plate which is bonded with a thin adhesive layer to a similar plate and the amplitude of the waves reaching the receivers will be accurately measured and compared as in an optical ellipsometer. The acoustic aperture of each transducer has been made small (2λ) so that when they are placed side by side, the radiation patterns will overlap and, therefore, interact with the same region of the adhesive bond. Meander coil windings have been incorporated to minimize electrical cross-talk by confining the induced eddy current to the transducer region. These transducer sets are presently being fabricated and will be tested during the next period.

Before the transducers can be used side by side for quantitative measurements of the amplitude of SV and SH waves that exist after interaction with an adhesive bond, the individual characteristics of each transmitter-receiver pair must be well established on specimens with well defined acoustic responses. A special adhesively bonded specimen will be prepared with a large area of both bonded and unbonded material so that each transducer can be tested on both bonded and unbonded plates. Two 1-ft by approximately 3-ft

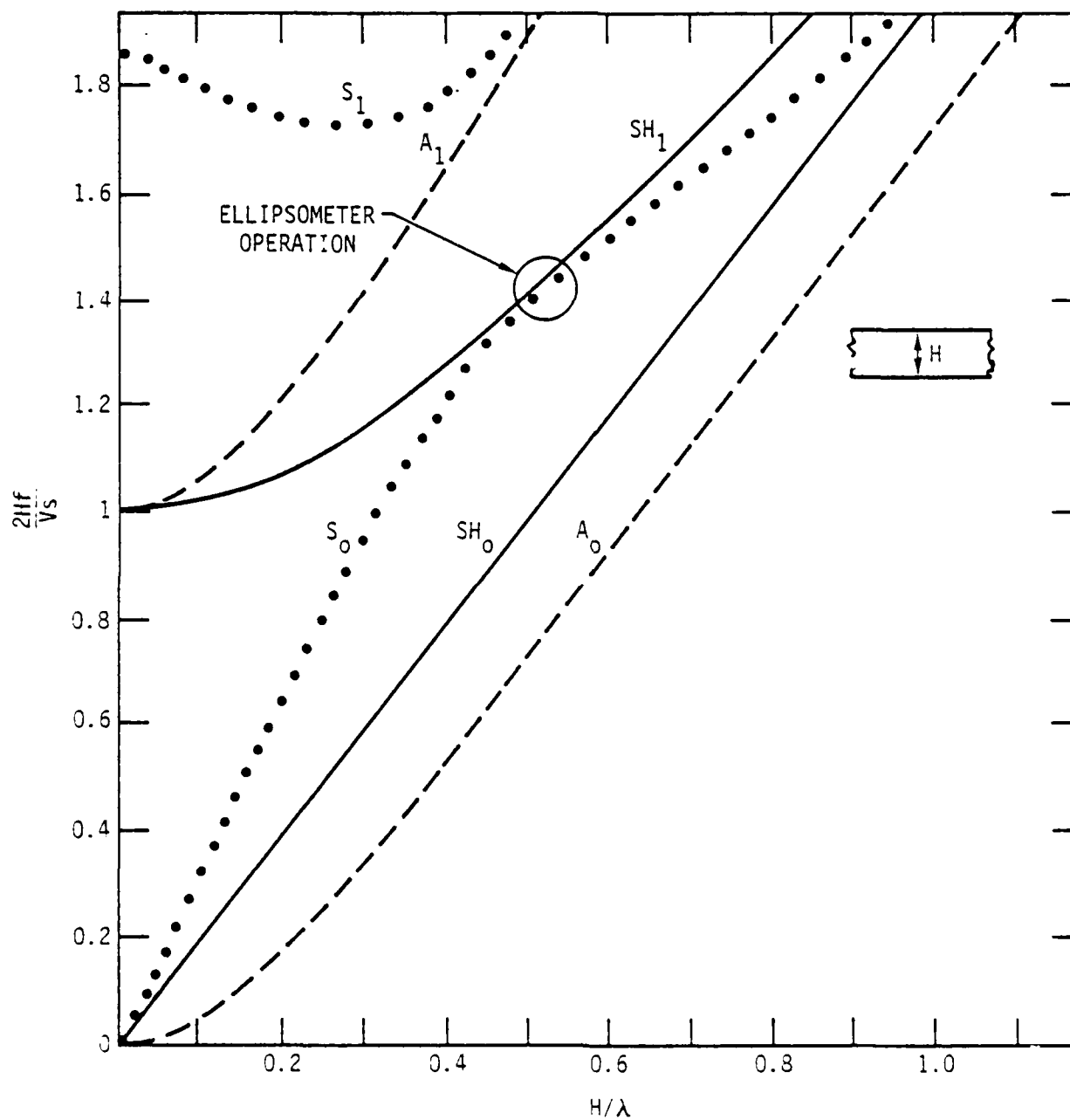


Fig. 4 Dispersion of plate waves showing point of ellipsometer operation.



long aluminum sheets of 1/8-in. thickness will be adhesively bonded together over the central 1-ft x 1-ft region using the same adhesive (Chemlok 304) and surface preparation techniques that are being used in the other parts of this program. This will provide space enough for an EMAT transmitter-receiver pair to operate in a pitch-catch mode over a completely unbonded and a completely bonded interface condition. After the characteristics of each pair are established, the pairs will be operated side by side to determine if optical ellipsometer operation can be achieved.

PROJECT III, UNIT A, TASK 3

COHESIVE BOND STRENGTH PREDICTION

Paul L. Flynn
S. Paul Henslee
General Dynamics
Fort Worth Division

Introduction

A special project was conducted to resolve the inadequacies of the attenuation data on bonded FM-400 specimens obtained in mid 1977. The poor data on FM-400 was attributed to interfering effects caused by filler, scrim and small voids. To solve these problems, a study was undertaken to characterize the separate contributions to sound velocity, attenuation and density made by the resin, filler and scrim in adhesives.

The effect of cure temperature on acoustic parameters was investigated on three film adhesives, FM-73, FM-400, and RB-398. FM-73 is an unfilled 250°F (121°C) cure epoxy, while FM-400 and RB-398 are aluminum filled 350°F (177°C) epoxies. Acoustic properties were measured on the filled and unfilled adhesives without scrim cloth.

The effect of moisture content on acoustic properties was investigated on the same adhesives by comparing the responses of dry and moisture saturated specimens. The effect of the scrim cloth was measured by comparing the response of FM-400 with and without scrim. The scattering properties of the scrim by itself in water was also measured. Variation in filler content occurred naturally in the FM-400 cure temperature variation specimens, so additional data was taken and correlated with filler density.

Attenuation spectra (attenuation coefficient as a function of frequency) proved to be the most consistent indicator of cure state, moisture content and filler density. Higher cure temperature caused lower attenuation spectra to higher values.



Background

The 1976 project to predict cohesive bond strength produced good correlations between NDE parameters and bond strength. Bond strength variation was produced by mixing Chemlok 304, a two-part paste epoxy, in different ratios. As the strength of the adhesive increased its sound velocity increased and its attenuation decreased. The 1977 project extended this same treatment to a commercially important aerospace adhesive, FM-400. FM-400 contains a large portion of aluminum powder filler and a heavy knit nylon scrim cloth in a matrix of 350⁰F (177⁰C) cure epoxy. Bond strength variation was produced by curing the laminates at different temperatures. As the adhesive cured, it became stronger and its sound velocity increased, but scatter in the attenuation data precluded any meaningful correlation. The scatter in attenuation data was attributed to small voids caught in the pattern of the scrim fabric.

As a result of the interference caused by the scrim in FM-400, it was decided to characterize the contribution of each different component in an adhesive and compare their effects with the effects of conditions known to reduce cohesive bond strength. The components in an adhesive include: (1) the polymeric resin, (2) the filler, (3) the scrim cloth, each of which have an important contribution to the strength of the adhesive. The resin is certainly the most important part of the system. It must wet the bonding surfaces and the surfaces of the scrim and filler and then cure to a strong, stable polymer. The filler acts as a reinforcement to the resin and thus adds stiffness and high temperature strength. The integrity of the resin-filler interface is important because of the opportunity for adhesional failure. Filler content will affect the adhesive's strength and will also contribute to acoustic properties of the adhesive. The scrim can also trap gas to form small voids and can filter filled adhesive to produce resin rich areas. The scrim can also affect bond strength and durability.

External parameters can also effect the strength of a bonded joint. Inadequate cure temperature can produce adhesive with limited high temperature strength. In-service high temperature exposure can degrade most polymer adhesives. Moisture content leads to both cohesive and adhesional degradation.

While it is not inconceivable to correlate each degrading influence with a NDE parameter, it would be quite difficult to separate the effects of each variable and then sum their strength degrading potentials. For these reasons, I have chosen to investigate each variable separately and to quantitatively identify the effect of each of the acoustic properties of several adhesives. When each individual contribution is understood, it may then be possible to predict cohesive strength under the unavoidable influence of several combined variables.

Comparison of Data Analysis Systems

All previous ultrasonic spectroscopy for this program has been done on the PDP-11/45 system with an analytical Fourier transform program. This program differs from standard FFT programs in that the frequency range and resolution is not strictly governed by the sampling conditions. The analytical transform extrapolates between each sampled point in the time domain to give a piece-wise linear or parabolic continuous function. The program then simply calculates a numerical approximation to a continuous Fourier integral. Frequency domain points can be calculated at any frequency by simply using that frequency in the Fourier kernel. However, the ability to calculate any frequency point is no guarantee of the significance of the answer.

Because the PDP-11/45 is currently occupied by other programs and because data analysis is easier to compare among groups that use the same transform, a versatile fast Fourier transform package for the HP-2100 computer system was programmed. The system uses a 256 by 256-point oscilloscope scanner and a A to D converter to provide time base ultrasonic data to the computer. At the present time, all of the FFT calculations are programmed in Fortran, so a 512-point transform takes a few minutes to run. The system contains several options directed through a conditional GO TO statement which allows forward and reverse FFT, Hanning window, plotting, power, storing data, digital filtering, division and multiplication of complex arrays and suppression or amplification of specified portions of arrays. Although slow, the system has provided accurate data analysis with data significance assured by the sampling theory built into the standard FFT.



Unlike the analytic transform, the FFT system provides the magnitude of each array plotted so that quantitative measurement of signal strength in the time or frequency bases is easily handled. This feature is useful when one spectrum is divided by another to give a normalized spectrum when measuring attenuation as a function of frequency.

It would be very desirable to implement a FFT system such as this on the PDP-11 or to upgrade the HP-2100 system to operate on the same level. Run time could be shortened considerably by programming the FFT calculation subroutine in Assembly language or by installing a fast Fortran board for the 2100. If the memory of the 2100 could be expanded or augmented with a reliable mass memory, the number of points in the FFT could be increased to provide higher resolution spectra. A transient pulse recorded could also be used to digitize the signal to provide data input format not limited to the resolution and range of an oscilloscope scanner.

Materials and Procedures

Materials

This study used three aerospace adhesives of current industry-wide interest: FM-73, FM-400, and RB-398. The characteristics and role each of these adhesives played in this program are listed separately below.

FM-73U

FM-73U is an unfilled, unscrimmed, 250°F (121°C) cure epoxy film. It could be accurately called a neat resin. It was used to study the behavior of a curing epoxy resin. Samples were cured at 174, 197, 200, 205, 224, 245, and 260°F.

FM-73M

This adhesive has the same resin as FM-73U, but contains a matte dacron scrim. It sees wider commercial use than FM-73U because it is easier to handle. This adhesive was used in the unfilled adhesive moisture content study in the dry, 1.5%, and 3.0% H₂O states.

RB-398

RB-398 is a 350°F cure adhesive that contains a moderated amount of aluminum powder filler and is supported by a heavy knit nylon scrim. The filled resin was removed from the scrim and used to study the curing behavior of a moderately filled adhesive. Specimens were cured at 270, 324, and 350°F. Moisture conditioned specimens of RB-398 which included the scrim cloth were interrogated in the dry and moisture saturated states.

FM-400

FM-400 is a 350°F cure adhesive that is heavily filled with aluminum powder and is supported on a heavy knit nylon scrim. Again, the filled resin was removed from the scrim and used to study the cure behavior of the adhesive. Specimens were cured at 274, 310, and 350°F. FM-400 specimens with scrim were used to study the effect of moisture content on attenuation. The scrim cloth was also extracted and interrogated to provide a means of comparing scrimmed and unscrimmed adhesive samples.

Specimen Preparation

The adhesive specimens for the cure temperature studies were cured in a metallographic mounting press. A small amount of resin was placed in the steel cylinder and heated to the desired temperature with a thermostatically controlled heater. The surface of the cylinder was sprayed with a mold release agent to prevent sticking. The cylinder was pressurized with the hydraulic jack to a pressure of 100 psi. All specimens were cured for one hour. The cylinder was then allowed to cool and the inner plunger was pressed out. This process yielded uniform thickness resin castings with little porosity. The 1½ in. diameter cylinder provided convenient sized specimens for ultrasonic analysis.

All of the specimens produced by this technique were very uniform, except the unscrimmed FM-400 castings made for the cure temperature study. These specimens showed a distinct light area around one side of the clip. Upon further investigation it was discovered that the light and dark areas were caused by non-uniform filler concentration. As the resin was heated, it became very fluid and was extruded around the plunger. This occurred only on the side of the die with the largest gap between the plunger and cylinder.



This resin leakage left one side of the chip with a greater amount of resin than the other. The resin-rich side of the chip was dark and the filler-rich side was light.

The specimens interrogated in the moisture effects study were procured from a stock of FM-73M and FM-400 specimens soaked and dried to study mechanical behavior of adhesives under the AFML project, "Fatigue Behavior of Adhesively Bonded Joints." The RB-398 specimens were borrowed from an IR&D project with similar objectives. All specimens were made by laminating three layers of scrimmed adhesive film and curing under recommended conditions in a mold release coated aluminum foil bag. This process yielded large specimens approximately 0.035 in. thick that were cut into 1 in. square chips for ultrasonic study.

The scrim cloth material was extracted from uncured FM-400 film by dissolving the uncured resin in acetone. This removed both the resin and filler when done in an ultrasonic cleaner. The scrim cloth was then mounted on a wire frame to prevent curling.

Data Acquisition and Analysis

The ultrasonic response of the adhesive specimens was measured by illuminating them with normal incidence, compressional pulses under water immersion. A broad band 15 MHz transducer was used initially, but it was eventually replaced with a 25 MHz transducer. The received signals were set through a time delay circuit to an oscilloscope display scanner. From here, voltage levels were sent to an A to D converter and into the HP-2100 for processing. This system allowed up to 256 timebase amplitudes to be extracted over 8 μ sec. By varying the time scale on the oscilloscope, data could be sampled over longer periods of time. Also the number of digitized points could be set from within the computer to allow input of only the desired information.

One of the basic acoustic properties that was determined in this characterization was the variation in attenuation with frequency. This was done by comparing the FFT spectra of signals returned from the top and back surface of a layer of cured adhesive. The top surface reflection was used as a reference spectra because it contained the frequency response characteristics of the measurement system. The back surface reflection

contained the measurement system characteristics plus the effects of traversing the adhesive layer. The adhesive specimens were made thick enough so that each signal could be sampled separately in the time domain. The measurement system response was eliminated by dividing the back surface spectrum by the top surface spectrum. This operation was done in complex terms so that no generality was lost in normalization. The power spectrum of this array then represented the intensity lost by the pulse traveling through the layer and interacting with each surface. This quantity was then plotted in logarithmic terms against frequency.

The attenuation component of the signal loss can be separated from the surface reflection part by the equation:

$$\frac{A}{A_0} = \frac{4Z_{AD} Z_{H_2O}}{(Z_{AD} + Z_{H_2O})^2} e^{-2\alpha_{AD}T} \quad (1)$$

where A = amplitude from bottom surface
 A_0 = amplitude from top surface
 Z_{AD}, Z_{H_2O} = acoustic impedances of adhesive and H_2O
 α_{AD} = attenuation of adhesive
 T = thickness of adhesive

Thus,

$$\frac{\ln \frac{A}{A_0} - \ln \frac{4Z_{AD}Z_{H_2O}}{(Z_{AD} + Z_{H_2O})^2}}{-2T} = \alpha_{AD} \quad (2)$$

The output-input of the computer was in the \log_{10} of power ratio, so it was necessary to multiply by $(2.303/2.0)$ to get $\ln(A/A_0)$. The impedance term compensated for energy lost at the interfaces by a uniform vertical shift of the logarithmic data. The thickness term in the denominator controlled the slope of the final data.

The thickness of the adhesive chips was measured with a micrometer and the impedance was measured by comparing the top surface reflection to the



reflection from an aluminum block. The impedance values were also checked against measured density and velocity of sound values.

The resulting data set included velocity of sound, density, impedance and attenuation as a function of frequency over the bandwidth of the transducer.

Results

Cure Studies

FM-73U

The first series of specimens tested to measure the effect of cure temperature on damping behavior was FM-73U cured between 197 and 260°F. The response of this material, as seen in Fig. 1, was first considered peculiar because attenuation systematically increased with cure temperature. The extreme temperatures of the cure series were repeated with new specimens cured from 174 to 260°F. The 174°F cure was very soft and tacky when removed from the press. The ultrasonic testing results agreed well with the first series at 260 and 200°F, as seen in Fig. 2. The 174°F cure specimen showed distinctly different behavior above 15 MHz. The general curing behavior of FM-73U can be described in two steps. Upon initial crosslinking, the attenuation is reduced, especially above 15 MHz. Then as the resin continues to cure, the attenuation continues to increase in a systematic manner.

The sound velocity and impedance both increased dramatically between 174 and 200°F, but afterwards the increase was slight.

RB-398

The attenuation behavior of unscrapped RB-398 was very systematic upon going from the soft 270°F specimen to full cure at 350°F, see Fig. 3. If this same behavior is exhibited in bonded specimens, it would be possible to separate undercured specimens on a reliable basis. Overall, the attenuation of this filled adhesive was much less than FM-73U.

The velocity of sound increased only a few percent on curing from 270 to 350°F and the impedance was hardly affected. The constancy of sound

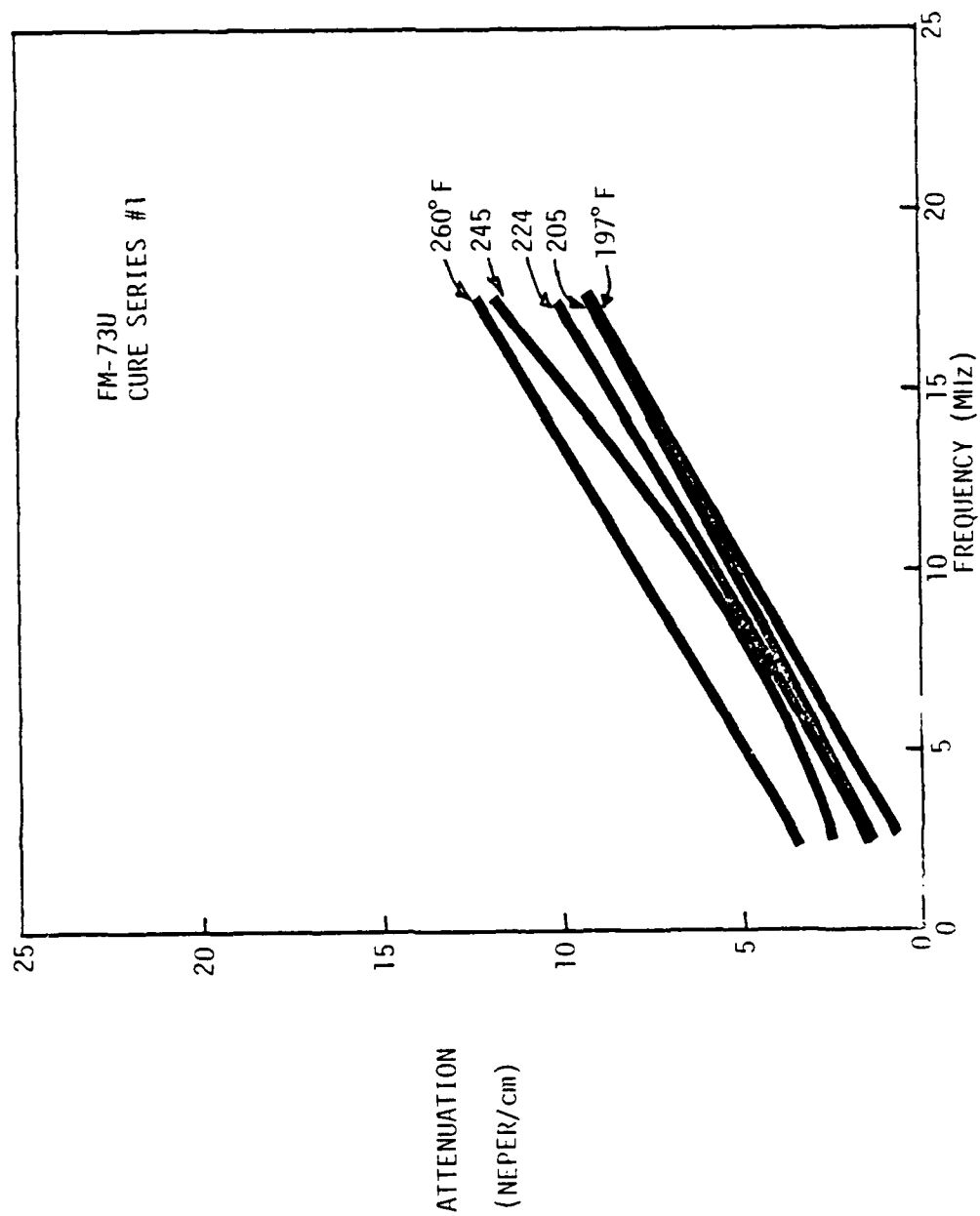


Figure 1. Attenuation Spectra on FM-73U Resin Cured Between 197 and 260° F

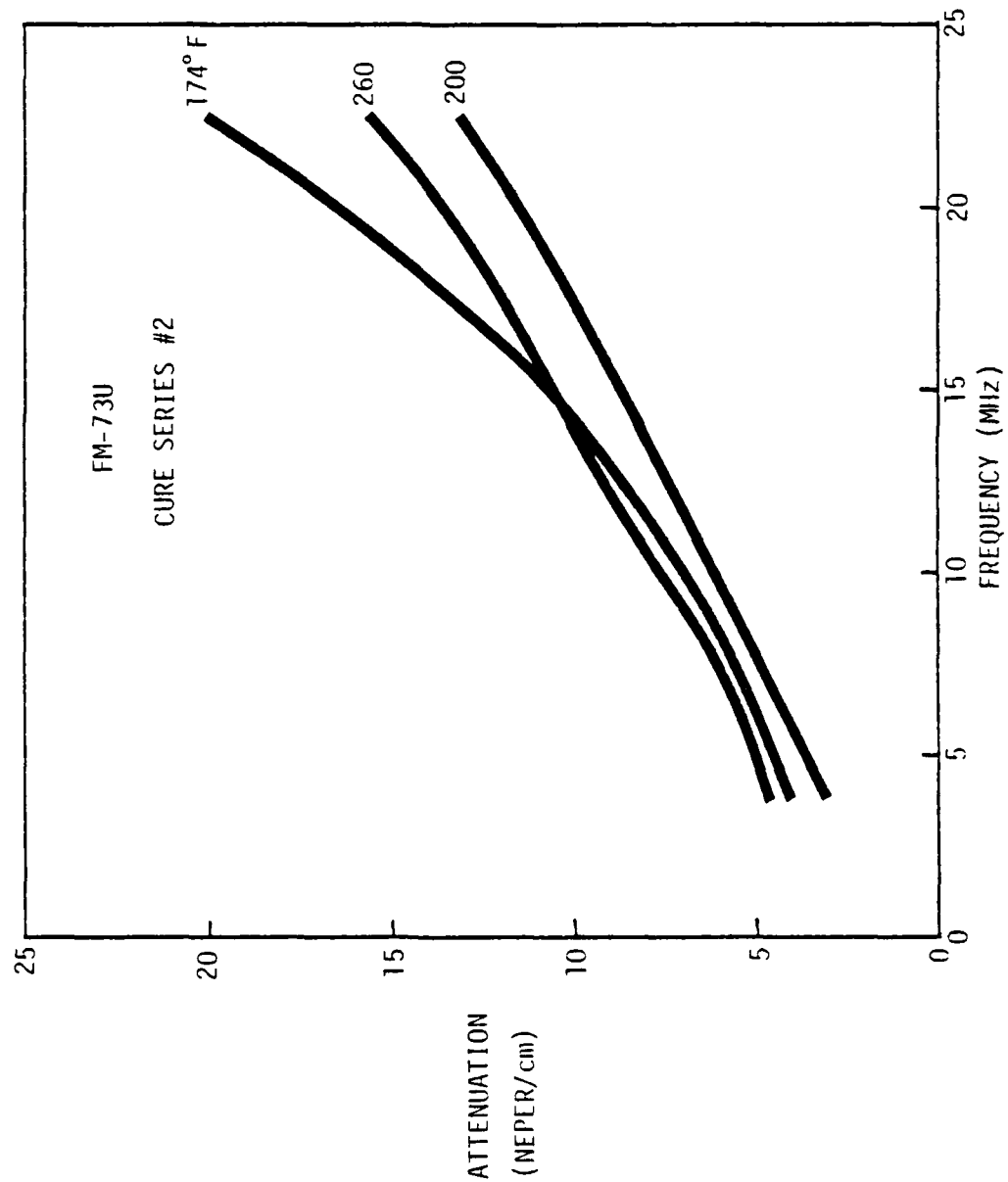


Figure 2. Attenuation Spectra on FM-73U Resin Showing the Behavior of Uncured, 174° F with Respect to the more Complete Cures at 200 and 260° F.

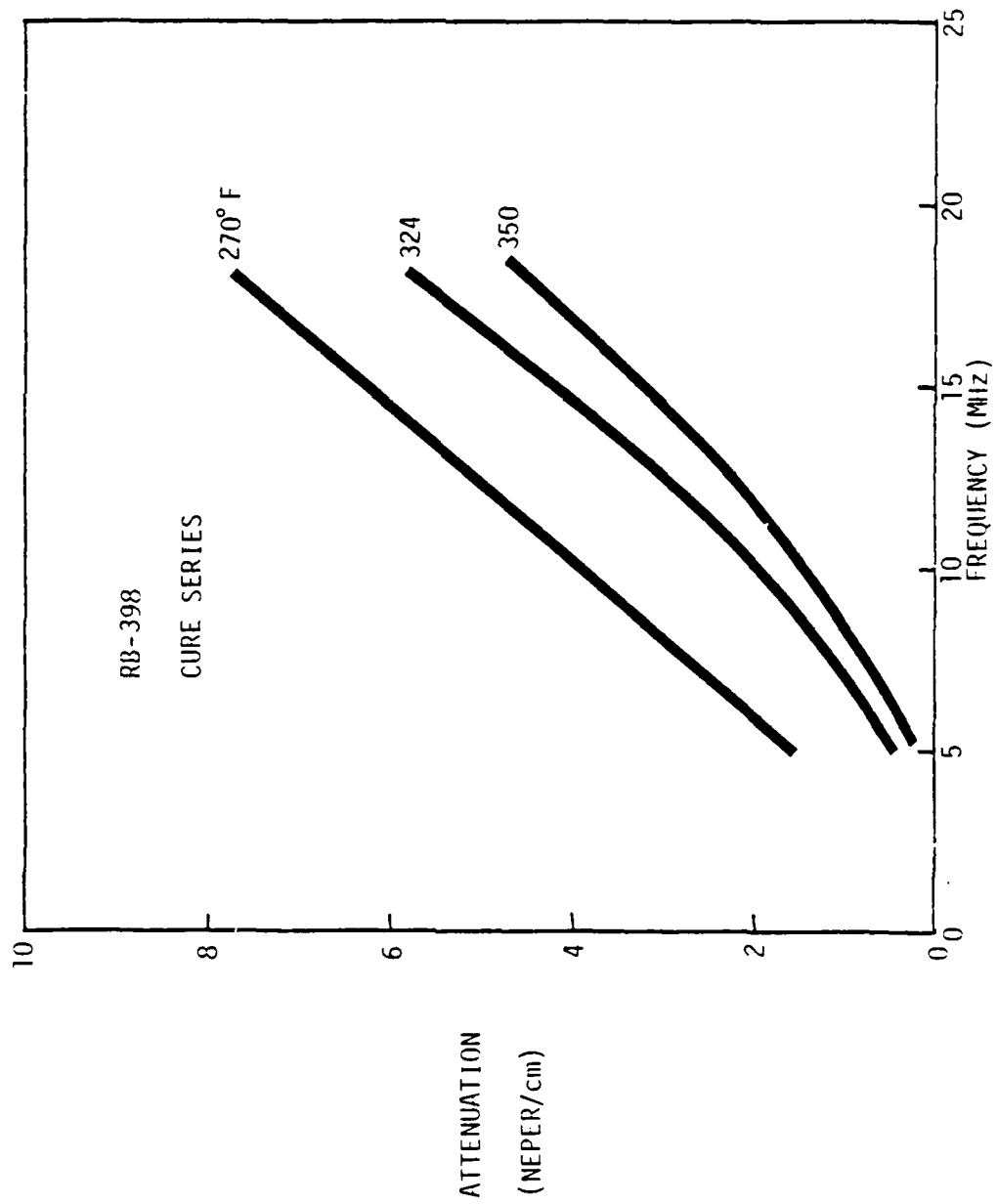


Figure 3. Attenuation Spectra on RB-398 Filled Resin Showing Systematically Lower Attenuation with Increased Cure Temperature.



velocity and impedance would make it easy to extract attenuation values from bondline data with unknown thickness.

FM-400

The cure temperature study on unscrimed FM-400 showed no clear trend with cure temperature, as seen in Figs. 4 and 5. The only clear separation occurred between the light and dark areas caused by filler concentration. The light, high filler areas, Fig. 4, showed lower attenuations than the dark, low filler areas shown in Fig. 5.

The filler content of each area is shown in Figs. 6 and 6b at 166X. The light area shows filler particles packed closely together while the dark area has a filler content of about 50% which is representative of the original material. For comparison purposes, the filler content of RB-398 is shown in Fig. 6c, along with photomicrographs of the previously investigated Chemlok 304 in Fig. 7. RB-398 has a finer aluminum powder filler than FM-400 and the quantity is considerably less. The Chemlok samples also contain a small amount of filler. Both components of Chemlok 304 must contain equal amounts of filler because there appears to be no filler concentration variation with the different mixture ratios.

Moisture Content Studies

FM-73M

The presence of moisture in FM-73M adhesive increased the attenuation at all frequencies. The dry specimen showed a linear increase in attenuation with frequency from 5 to 17 MHz. The 1.5 and 3.0% moisture levels exhibited higher attenuation at low frequencies and an increasing greater departure from the dry data at higher frequencies, see Fig. 8. Moisture content had little effect on sound velocity and impedance values.

FM-400 and RB-398

Moisture content has similar effects on the filled adhesives RB-398 and FM-400, each with scrim. The attenuation-frequency response for these materials is seen in Fig. 9. The FM-400 specimens were conditioned at 150°F in 100% RH which produced a moisture uptake of 4.0%. RB-398 was

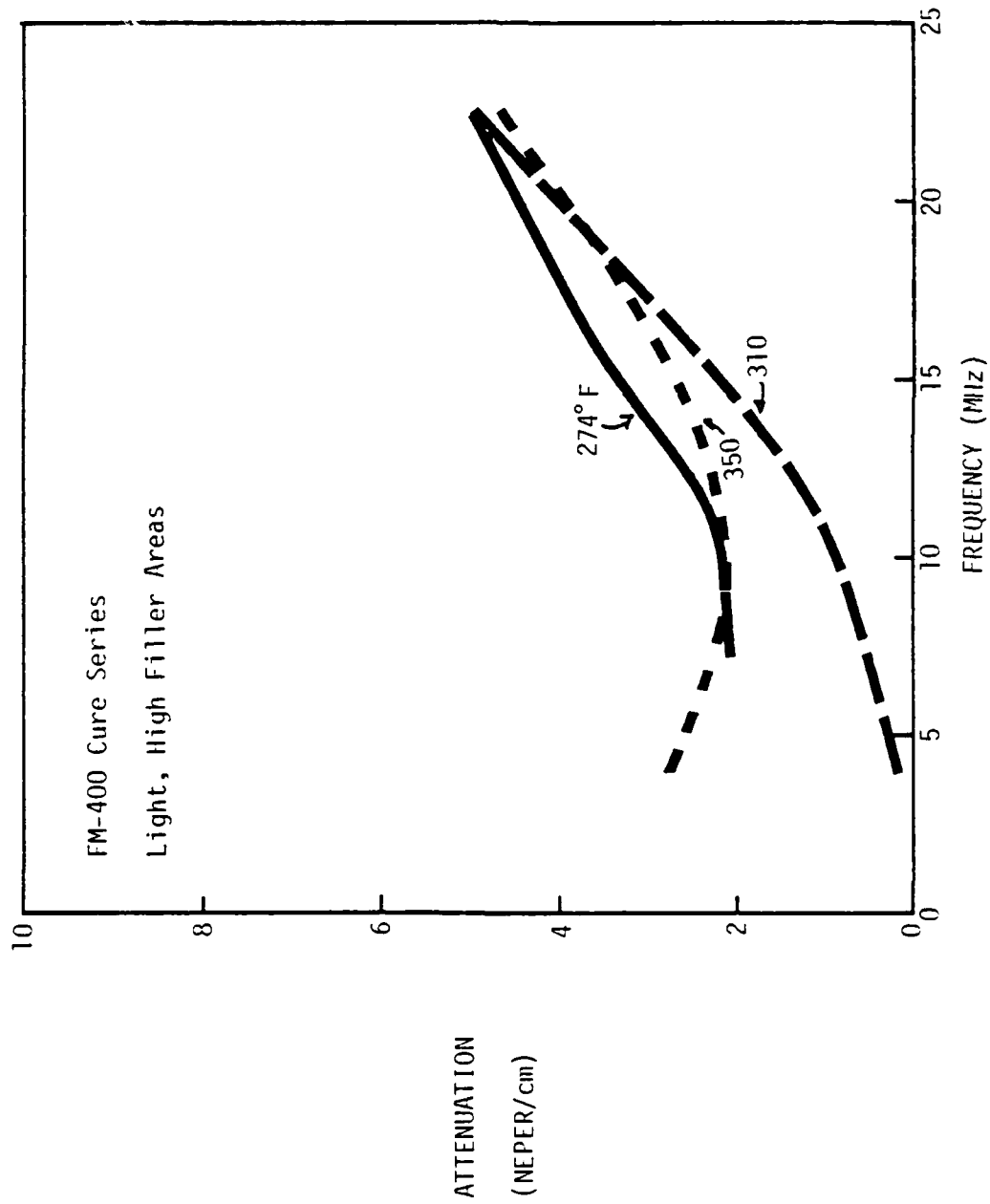


Figure 4. Attenuation Spectrum on FM-400 Filled Resin with a High Concentration of Aluminum Powder Filler.

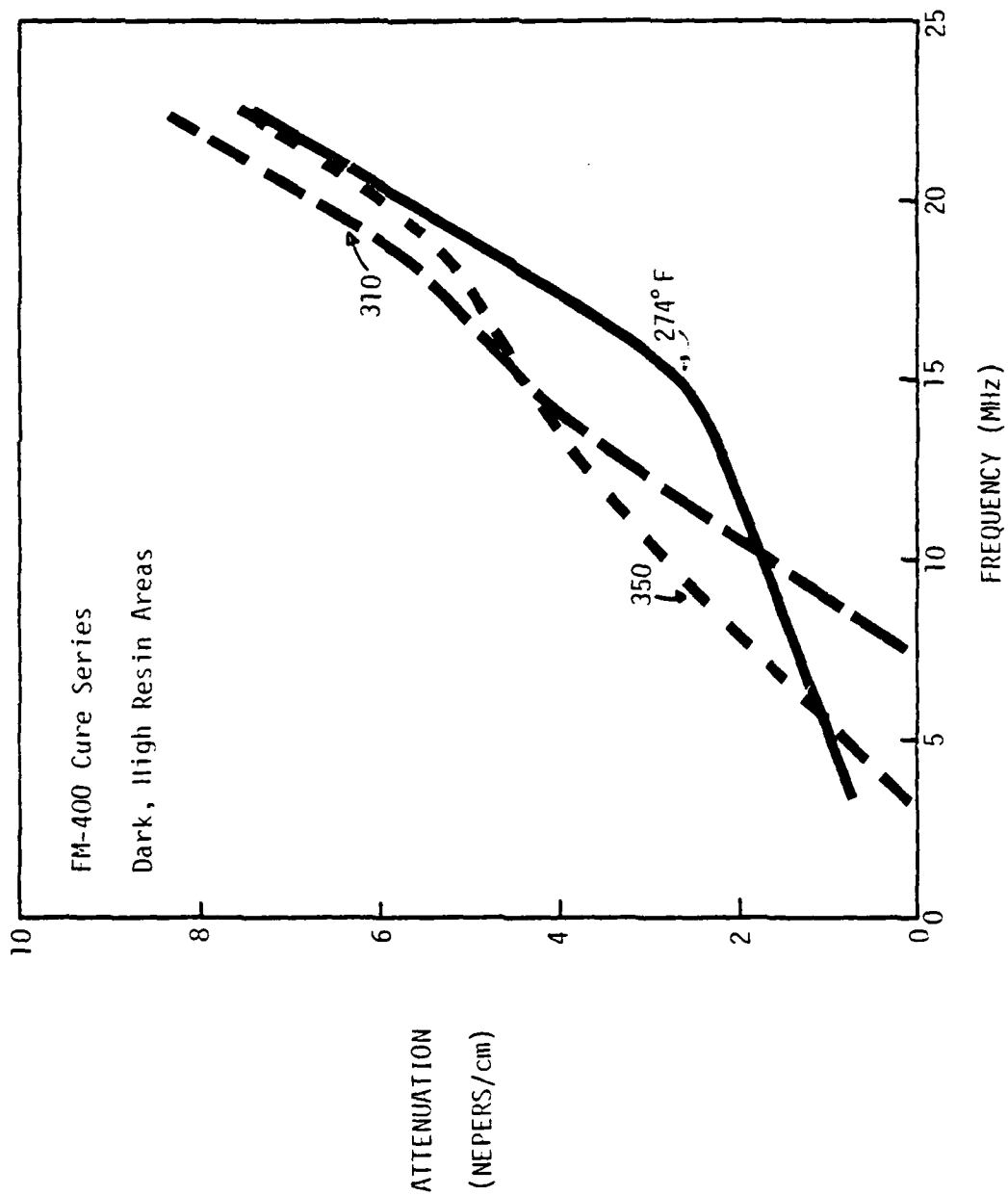


Figure 5. Attenuation Spectrum on FM-400 Filled Resin with a Normal Concentration of Aluminum Powder Filler.

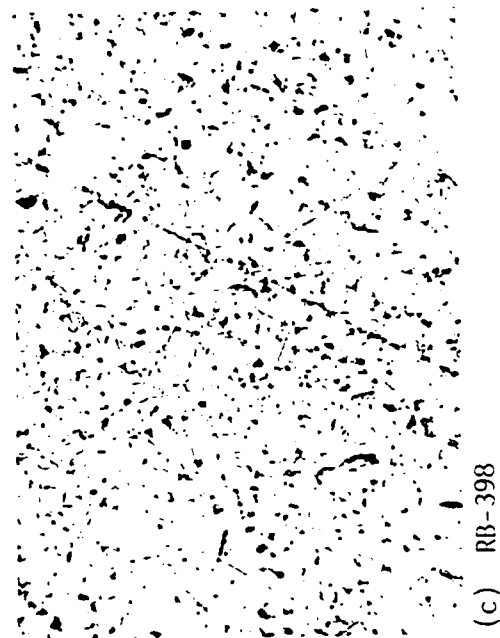
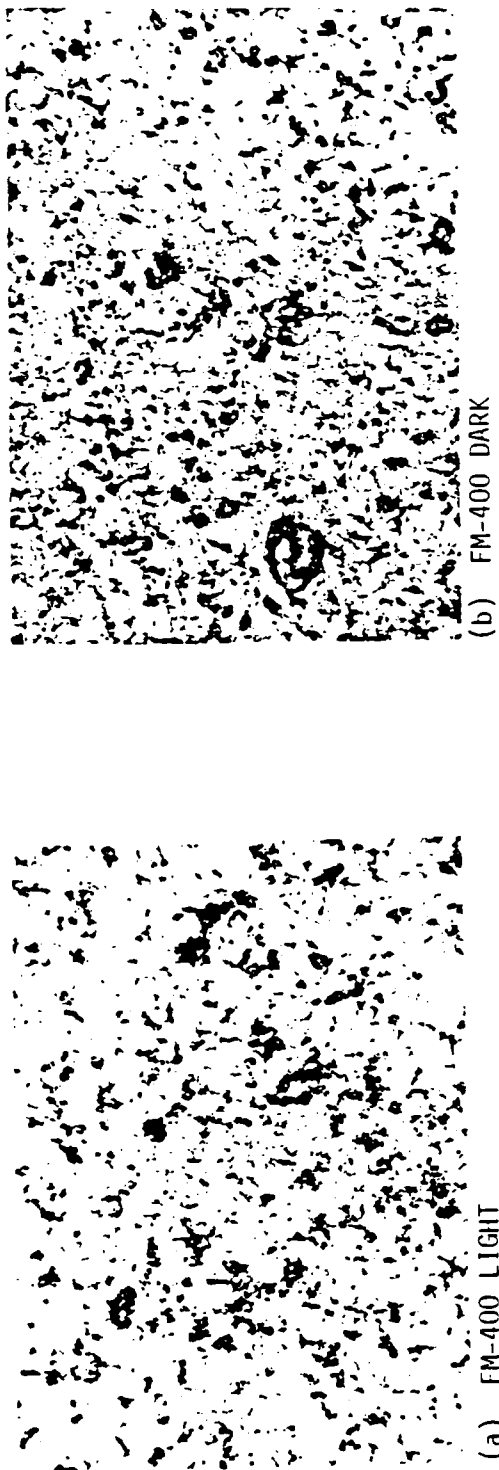


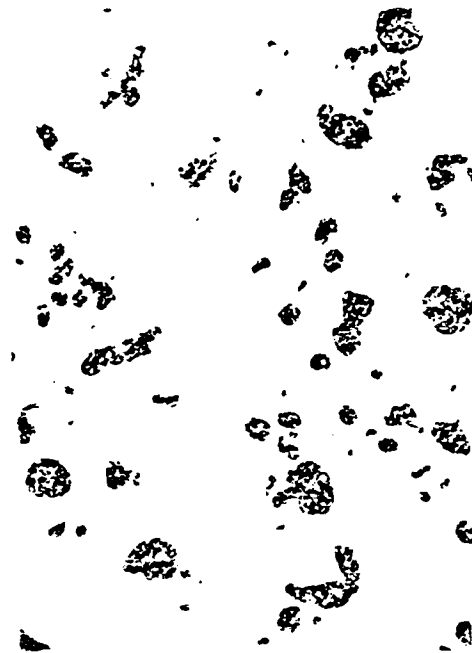
Figure 6. Photomicrographs of (a) FM-400 High Filler Area, (b) FM-400 Normal Filler, (c) RB-398. All at 166X with Phase Contrast.



Rockwell International

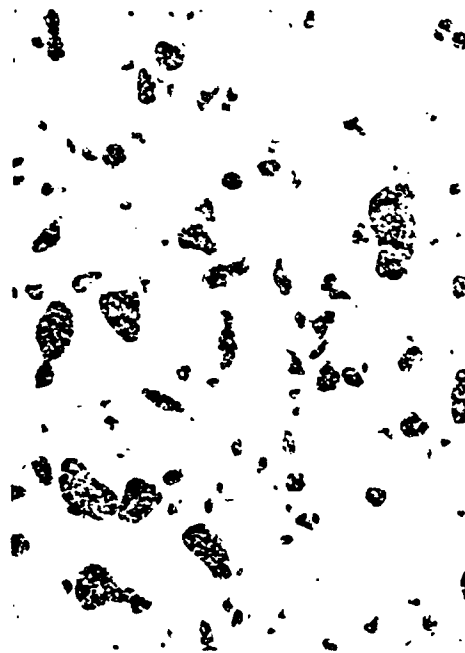
Science Center

SC595.32SA



(a) SOFT 2:3

(b) STRONG 1:1



(c) HARD 3:1

Figure 7. Photomicrographs of Chemlok 304 Adhesive Used in 1976 Experiment. (Numbers Beneath each Photo Indicate Proportions of each Constituent. 100X Polarized Light.)

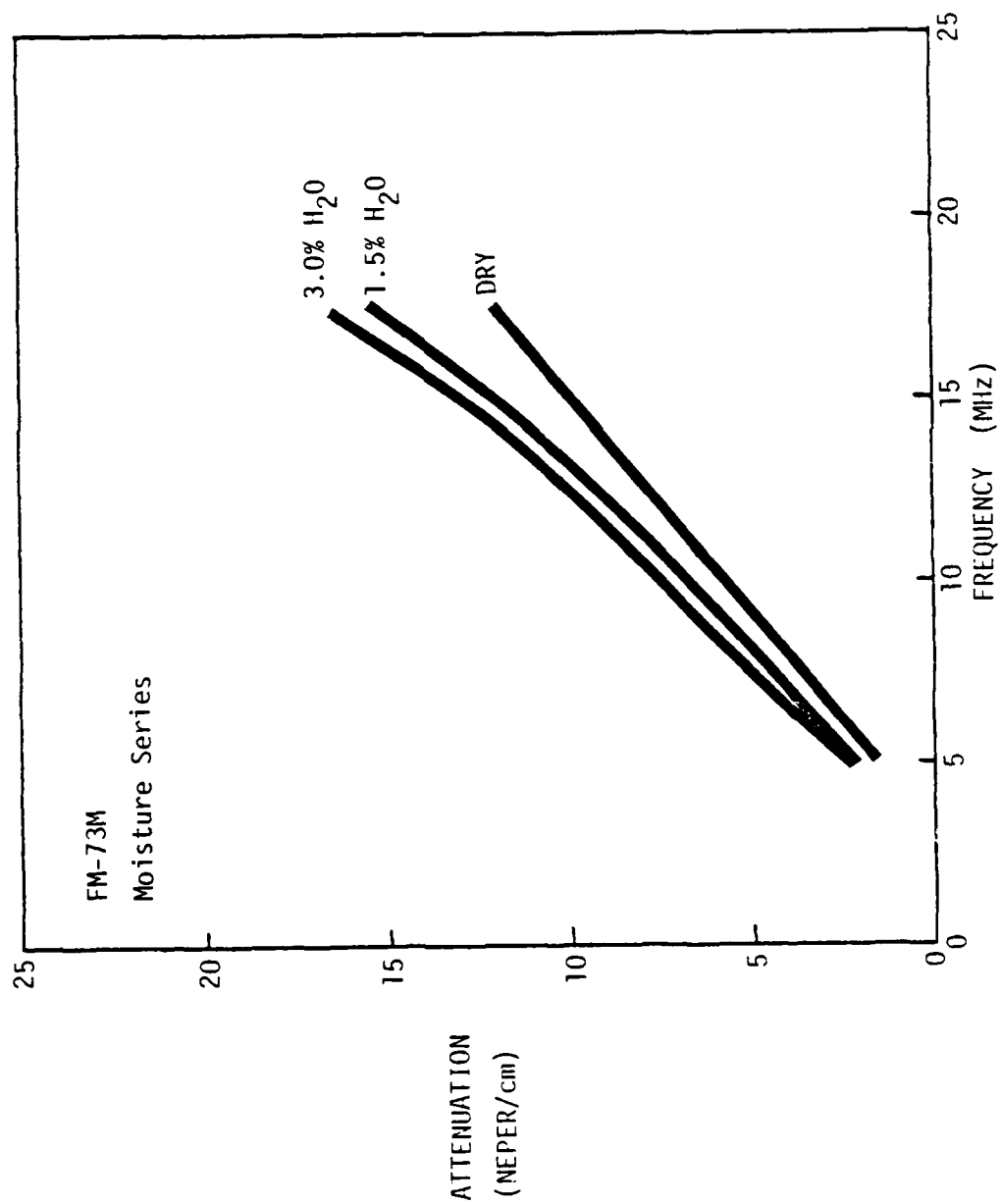


Figure 8. Attenuation Spectra of FM-73M at Different Moisture Levels.

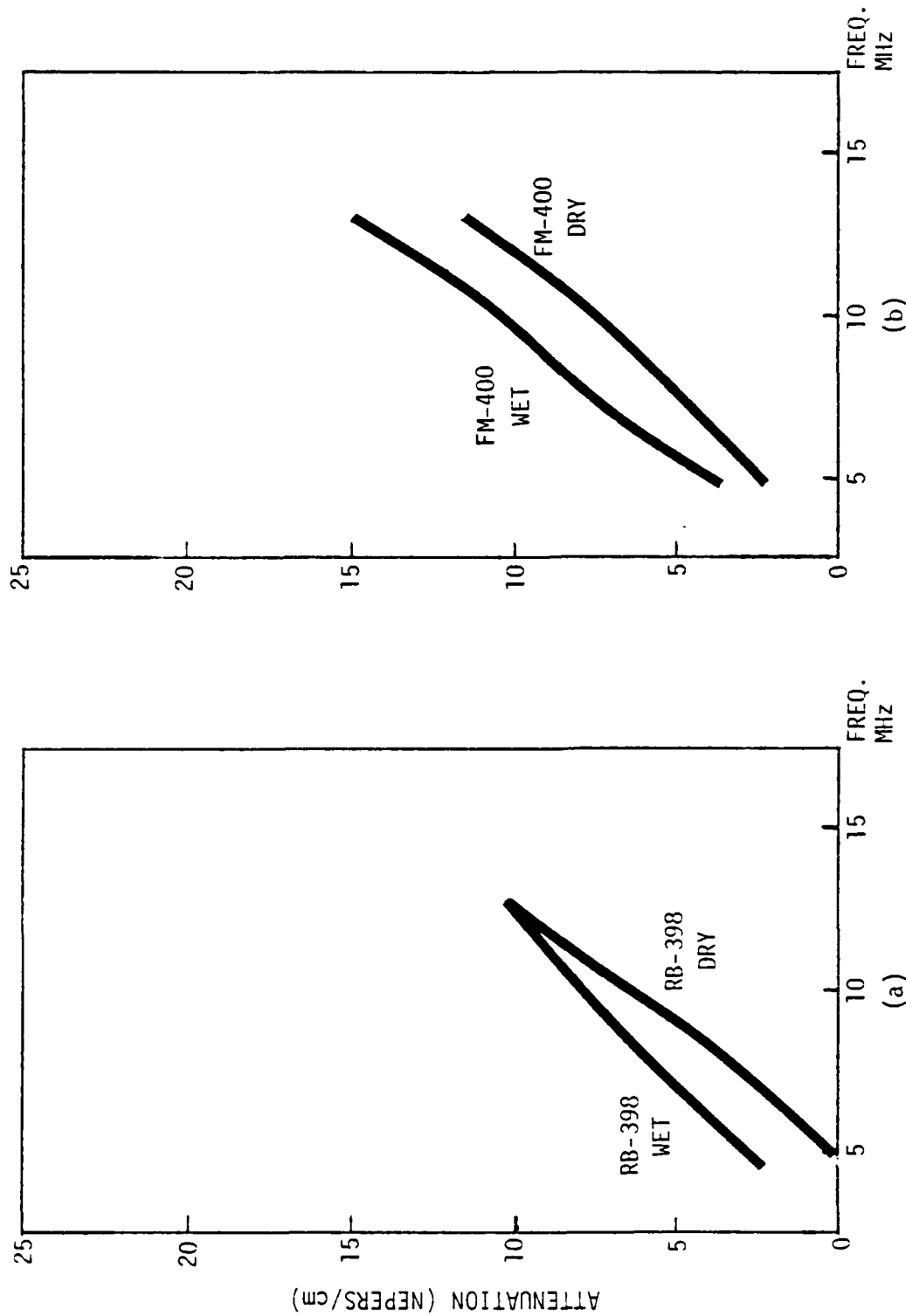


Figure 9. Attenuation Spectra on (a) RB-398 and (b) FM-400 Adhesives in Dry and Moisture Saturated Conditions

conditioned at room temperature in water to give 3.0% H₂O. The attenuation increase in FM-400 was uniform over the entire frequency range while the RB-398 data appeared to converge at higher frequencies. The limited bandwidth on these specimens was caused by the degradation of the 15 MHz transducer. It was replaced by a broadband 25 MHz transducer.

Sevin Cloth Study

The effect of scrim fabric on the attenuation spectrum of FM-400 is seen in Fig. 10. The scrim fabric was assigned a thickness of 0.008 in. in the attenuation calculation. The scrim cloth showed a much higher attenuation coefficient than the unscrimmed FM-400 resin. The scrimmed FM-400 fell closer to the scrim material, indicating that the attenuation of the scrimmed material is dominated by the fabric.

Discussion

Detection of Individual Variables

When taken one at a time, each of the variables caused a rational, systematic variation in attenuation, sound velocity and impedance. The cure temperature series on FM-73U, an unfilled 250°F cure epoxy, showed high attenuation in the uncured state which was lowered dramatically on initial curing. With further curing, the attenuation gradually increased. The uncured attenuation spectrum was parabolic, while the more highly cured spectra were linear and parallel. This may be an important feature in the detection of uncured resin and indicates that important information may be obtained at higher frequencies. The parallel progression of attenuation spectra for specimens cured above 200°F may indicate a curing mechanism different from the initial cure or may be caused by inaccurate impedance compensation.

The attenuation spectra of the cure temperature series on RB-398, a moderately filled 350°F cure epoxy, shows a consistent progression to lower attenuation with increased cure temperature. The highly filled 350°F cure epoxy, FM-400, showed more sensitivity to filler content than to cure temperature. There may be a critical filler content, after which the behavior of the material is more strongly governed by the filler content than

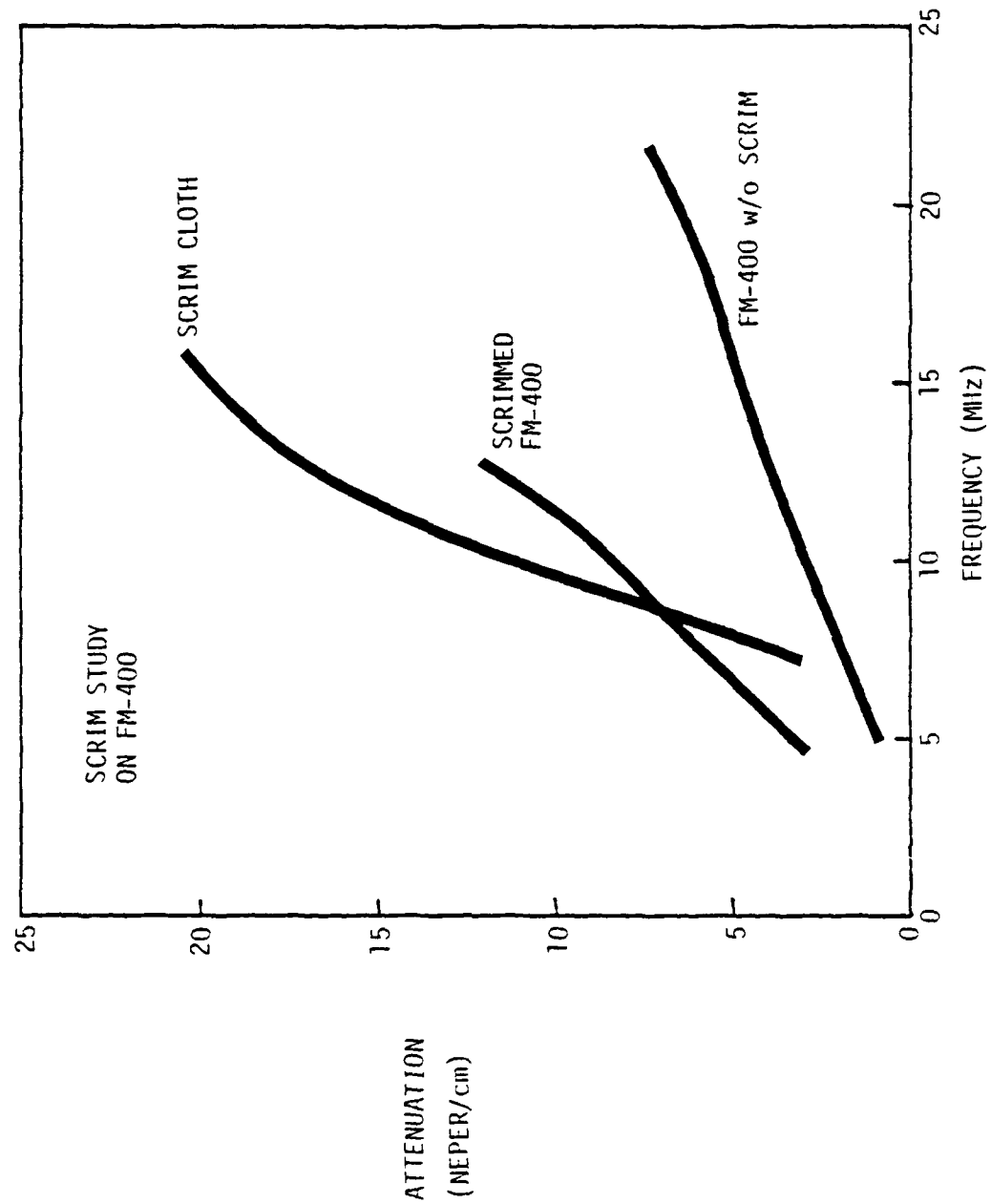


Figure 10. Attenuation Spectra for FM-400 Filled Resin, Scrapped FM-400 and FM-400 Scrim Fabric in H_2O .

by the resin properties. The filler particles are about 2×10^{-3} cm in diameter while 20 MHz radiation gives a wavelength of about 20×10^{-3} cm. It may be necessary to use higher frequency excitation to allow interrogation of the resin layers between filler particles. However, one would be limited by attenuation in both the aluminum adherend and in the adhesive.

If one could be sure of the cure and composition of the adhesive, the detection of moisture could be done by observing an increase in attenuation. This effect was seen for both filled and unfilled adhesives. This effect may be caused by changes in the bulk properties of the resin or by the formation of microcracks. This phenomenon has been seen by other workers and deserves further investigations due to the great impact moisture content can have on the mechanical properties of polymers.

At this time, the nondestructive characterization of an adhesive subjected to more than one variable is not possible. The result of combined variables was graphically demonstrated in the poor correlation exhibited in the 1977 study on FM-400. If the strength of the adhesive is determined by cure temperature and other variations also occur in filler content or microporosity, the important variable may be hidden. It will only be possible to separate the different effects when the contribution of each variable is understood over the entire frequency range. Then it may be possible to extract information about different variables from different frequency ranges.

If each of the variables can be characterized, it may be possible to limit each to a usable range. It may be possible to use NDE to predict cohesive strength properties of an adhesive when the constituents are controlled to prevent large interfering effects. For example, it may be possible to predict the cohesive strength of RB-398 on a matte scrim, while a heavier knit scrim would cause too much interference. Similarly, it may be possible to successfully interrogate FM-400 if the filler content were lowered. In this manner, it may make sense to manufacture an adhesive particularly suited for NDE. This would be particularly true when the only excuse for not using adhesively bonded structure is the lack of an adequate strength NDE system.



Recommendations

From this special project on acoustic characterization of adhesives, the following recommendations can be made:

- (1) Continue the acoustic characterization work until cure, filler, scrim, and moisture effects are known on sound velocity, attenuation, density and impedance.
- (2) Use the complete characterization data to find the most sensitive frequency range of each parameter to characterize each variable.
- (3) Design an aerospace adhesive with good mechanical properties, that has a resin, filler level and scrim fabric amenable to NDE analysis for cohesive strength prediction.
- (4) After the optimum balance between mechanical and NDE properties is determined for an adhesive, use it in a laminated structure to prove the concept. This structure should eventually include multilayered and curved panels representative of advanced aircraft construction.

Future Plans

Now that the ultrasonic properties of the bulk adhesives in many states of cure and moisture content are known, it is possible to predict the response of an adhesively bonded sandwich to ultrasonic interrogation. Using these new data, a statistical correlation of shear strength with the acoustical parameters will be attempted. Aluminum, single lap shear specimens bonded with the RB-398 (form 1B) adhesive system will be fabricated with etched and unetched aluminum surfaces to generate two distinct categories of bond types. Ultrasonic spectroscopy and Fokker bond test parameters will be cataloged on various specimens in an attempt to correlate with compression shear strength measurements on the bond.

PROJECT III, UNIT B, TASK 1

MOISTURE DISTRIBUTION ANALYSES IN COMPOSITES

D. H. Kaelble and P. J. Dynes
Rockwell International Science Center
Thousand Oaks, California 91360

Introduction

The objective in this years program is to develop the instrumental and analytic capability to measure moisture content, evolution rate and concentration profiles in advanced composite materials.

Accomplishments during this period include:

1. Development and successful testing of a test cell for composite bar specimens.
2. Design of a test cell for analysis of moisture effusion from through holes in composite plates.
3. Progress on mathematical conversion of computer programs adapted to minicomputer or microprocessor capability, and
4. Early extension of inverse diffusion theory to treat moisture absorption/desorption kinetics of composites with microstructure damage.

Accomplishments

A moisture evolution analyzer (DuPont Model 902H) has been modified to permit direct sampling of moisture evolution from limited length segments of bar specimens used for serviceability and fatigue life testing of advanced composites. Figure 1 shows the effusion rate \bar{J} versus test time t at zero relative humidity and 50°C for a moisture saturated NARMCO T300 graphite/5208 epoxy composite bar specimen. The short time limit of measurement is determined by the maximum rate capability $\bar{J} = 170 \mu\text{gm/min}$ of H₂O evolution for the DuPont analyzer cell. The decrease in effusion rate shown in the experimental curve of Fig. 1 is now analyzed to isolate moisture content by the integral area beneath the curve. Analysis of the curve shape provides direct information on composite microstructure degradation and the moisture concentration profile (for Fickian diffusion).

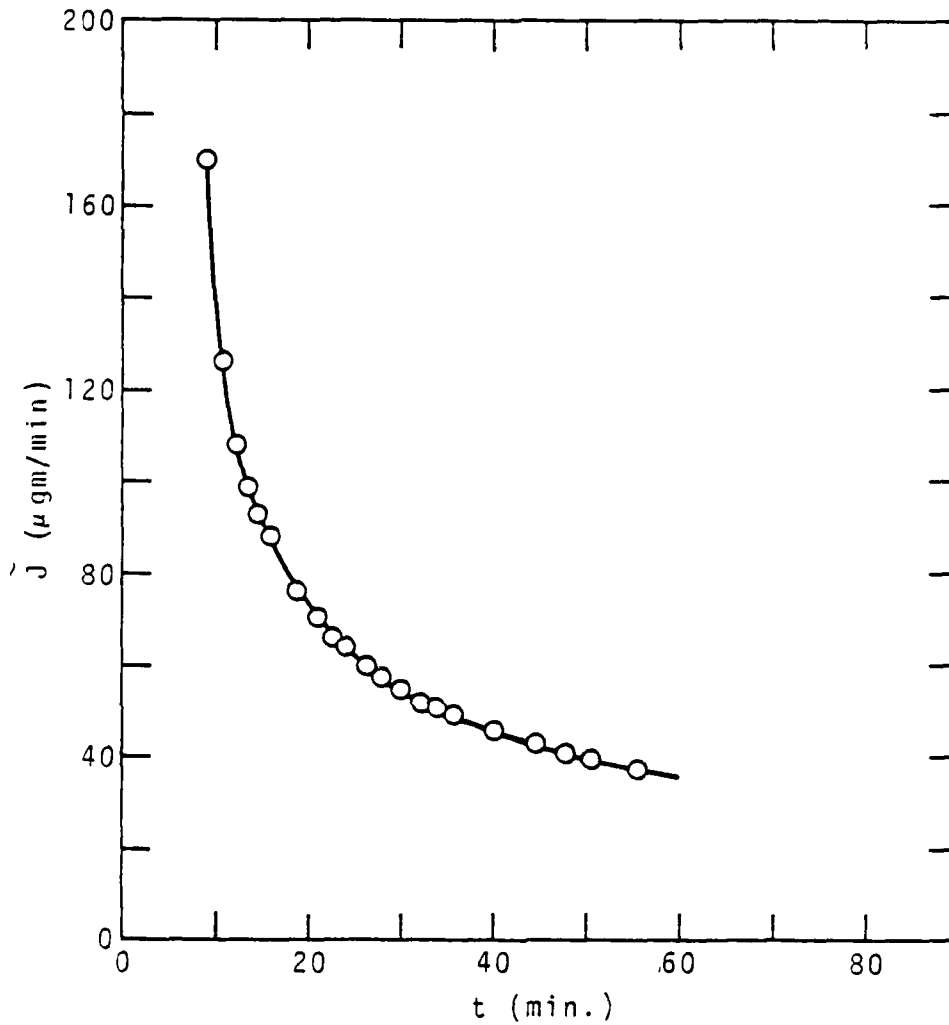


FIG.1 MOISTURE EVOLUTION ANALYSIS OF 3.81 cm LENGTH OF COMPOSITE BAR (WIDTH = 3.81 cm, THICKNESS = 0.215 cm) AT 50°C USING SLEEVE TYPE SAMPLING CELL (SEE UPPER RIGHT FIG. 2). COMPOSITE IS WATER SATURATED (1.51% BY WEIGHT H_2O) T300 GRAPHITE/5208 EPOXY UNIAXIAL REINFORCEMENT WITH PLYS PARALLEL TO THICKNESS.

The schematics of Fig. 2 illustrate four sampling cell designs under development for moisture distribution analysis. The upper two designs are specifically adapted for laboratory measurement and are now developed and in use. The lower two designs are specifically adapted for field measurements of surfaces (lower left) and through thickness holes (lower right) on large composite plate areas.

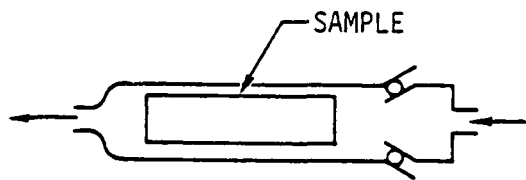
The present inverse Fickian model for calculation of moisture concentration profiles⁽¹⁾ has now been extensively tested with ideal moisture effusion data and the sensitivity of the model to data inputs such as time scale of measurement t , and diffusion coefficient D has been evaluated. The existing inverse Fickian model is shown to generate an accurate moisture concentration profile when provided with adequate data inputs with regard to both time t and D . Incomplete time data and inaccurate diffusion coefficient data are shown to skew these moisture profile computations. Current studies of computational sensitivities to improper t and D data are now guiding the improved and systematic design of moisture diffusion experiments.

Our earlier studies (see ref. 1) have shown that graphite-epoxy composite laminates often deviate from regular Fickian diffusion response. It has also been shown that these deviations reveal primary information on microstructure and strength degradation induced by the hydrothermal exposure. This same result has recently been reported by other workers^(2,3). Dr. J. Richardson, Science Center, now considers it feasible to extend his Fickian inverse diffusion equations⁽¹⁾ for moisture concentration profiles to treat systems with microstructure degradation. This extension of the present analysis will retain classical assumptions concerning spatial invariance of water diffusivity and solubility in the continuum phase but will add a coupled, two-phase diffusion model. The first (high diffusivity) phase will describe a one-dimensional capillary structure of microcracks in which water is physically held by capillary forces. The second phase will describe the longer time response in moisture effusion from the bulk composite intervening the microcracks. This extended moisture effusion analysis model will be utilized to more clearly interpret the microscopic character of structure degradation.

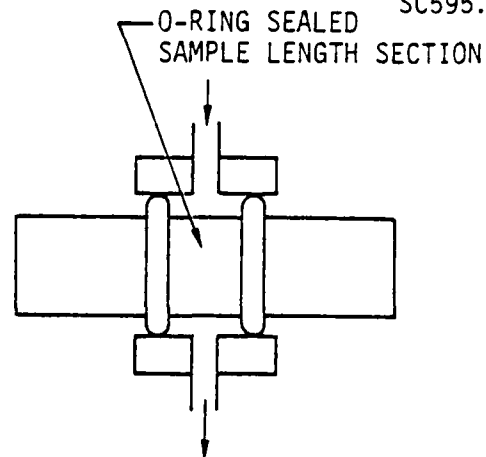


Rockwell International

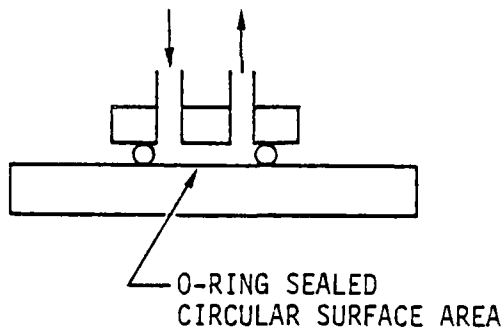
Science Center
SC595.32SA



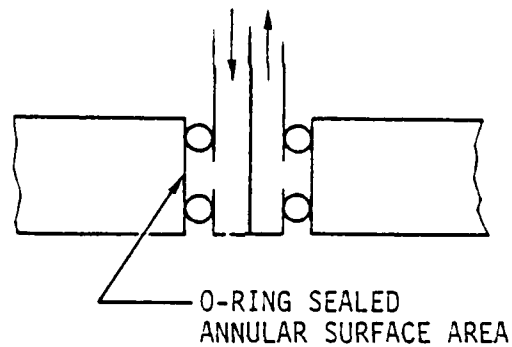
FULL ENCLOSURE
SAMPLE CHAMBER



SLEEVE TYPE FOR
BAR SPECIMENS

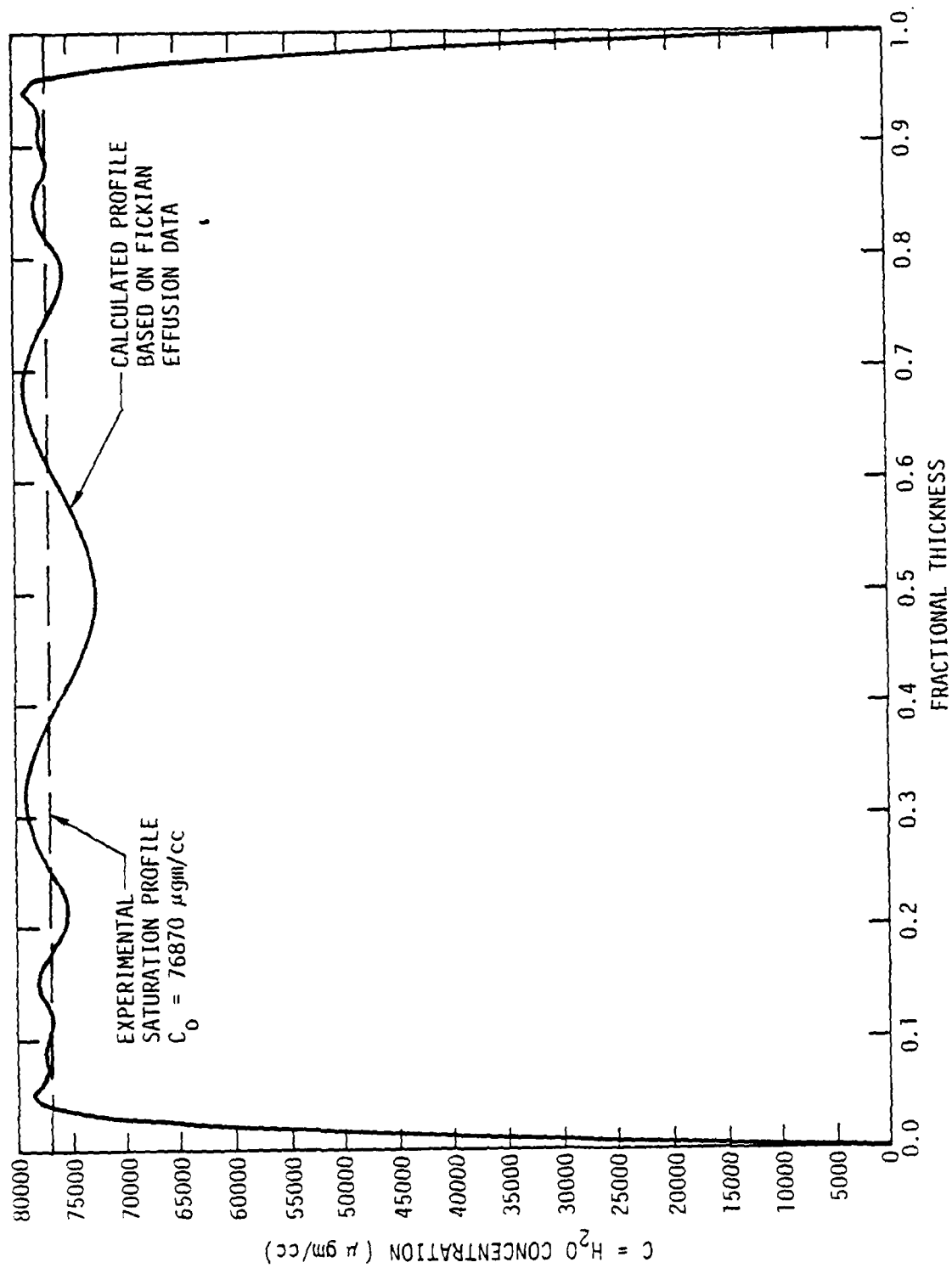


FACE PLATE FOR
SINGLE SURFACE
PLATE SPECIMENS



INSERT PROBE FOR INTERIOR
HOLES ON PLATE SPECIMENS

FIG. 2 MODIFIED SURFACE SAMPLING CELL DESIGNS FOR LABORATORY
(UPPER VIEWS) AND IN-SERVICE (LOWER VIEWS) APPLICATIONS



SC595.32SA

FIG. 3 COMPUTATIONAL ESTIMATION OF MOISTURE CONCENTRATION PROFILE IN
NARMCO 5208 EPOXY SATURATED WITH WATER USING CORRECT
 $D = 4.52 \cdot 10^{-6} \text{ cm}^2/\text{min.}$



A photographic view of the modified moisture evolution analyzer (MEA) with a composite bar specimen enclosed by the sleeve type sampling cell is shown in Fig. 4. Note that the MEA unit is highly portable and amenable to usage in the field. The early phase of the implementation of "on-board" microprocessor capability is now under study. The first phase of this effort is the conversion of existing computer programs for moisture distribution analysis to operate on existing minicomputers to which the MEA unit will be directly linked.

References

1. D. H. Kaelble and P. J. Dynes, "Methods for Detecting Moisture Degradation" in Interdisciplinary Program for Quantitative Flaw Detection Special Report Third Year Effort covering July 1, 1976 - June 30, 1977.
2. E. L. McKague, J. E. Halkais and J. D. Reynolds, "Moisture in Composites: The Effect of Supersonic Service on Diffusion," J. Comp. Matls., 9, 2 (1975).
3. J. M. Angl and A. E. Berger, "Moisture Effect on Carbon Fiber Composites," National SAMPE Tech Conf. Series, 8, Society for Advancement of Material and Process Engineering (1976) pp. 383-427.

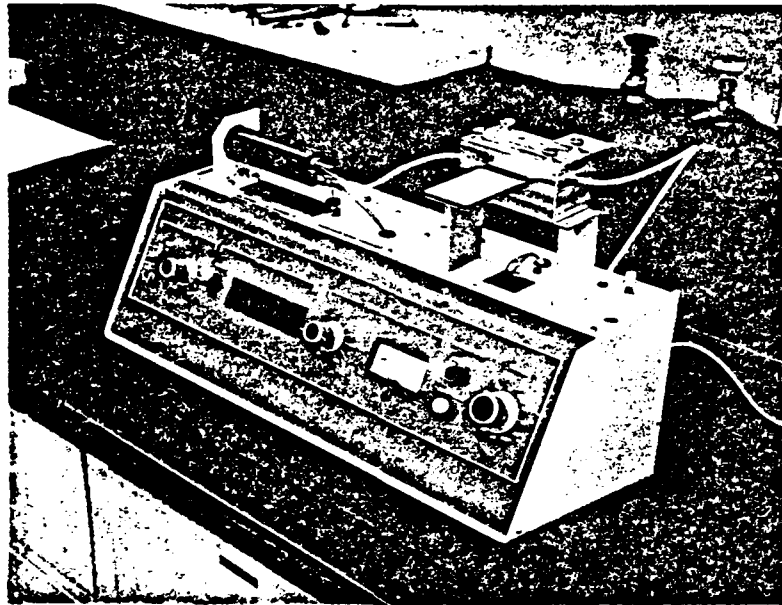


FIG. 4 MODIFIED MOISTURE EVOLUTION ANALYSER FITTED WITH BAR SAMPLING CHAMBER (UPPER RIGHT) AND MEASURING A COMPOSITE SERVICE LIFE SPECIMEN (SEE FIG. 1 DATA).



Rockwell International

Science Center

SC595.32SA

PROJECT III, UNIT B, TASK 2
ACOUSTIC EMISSION SIGNATURE ANALYSIS IN COMPOSITES

L.J. Graham
Rockwell International Science Center
Thousand Oaks, California 91360

Introduction

In previous studies of the characteristics of acoustic emissions generated in graphite-epoxy composites, empirical observations were made relating the frequency content and the amplitude distributions of the emission signals to singular points on the loading curve of a specimen and to the composite's moisture content.^{1,2} Up to now, these relationships have been difficult to study systematically because of limitations in efficiently handling the large amount of data contained in the emission signals. Under a separate program (Science Center IR&D) an acoustic emission characterization system has been designed and built which abstracts pertinent information from each emission signal as it occurs during a test and stores this information in compact digital form for later data processing.³ There have been some problems in the final checkout and calibration of this system which has delayed the planned specimen testing program under this task. However, three preliminary tests have been run and enough data obtained using the new characterization system to at least conceptually demonstrate its potential power to categorize emission types and follow the time evolution of those types during a test.

The first objective of this task is to relate the various emission types which are defined by signature analysis to specific failure mechanisms which can occur during a specimen test. Identification of these failure mechanisms will be based on the choice of specimen, inferences from the loading history, visual observations during the tests, and extensive post-test microscopic examination of the specimens. The ultimate objective of this two-year program is to demonstrate failure prediction from the acoustic emission signatures in at least one case where specimen failure proceeds by well-defined, sequential mechanistic steps. The feasibility of failure prediction for several practical specimen configurations having less well-defined failure paths will also be reported.

Acoustic Emission Characterization System

Since success of the task objectives depends so much upon the use of the unique instrumentation that is being put into operation, a brief description of its features will be given here. A photograph of the instrumentation is shown in Fig. 1.

Signals from one or two transducers are processed in real time to determine the initiation of an acoustic emission burst. This is based on an operator preset pulse amplitude threshold and a minimum quiet time between AE bursts. Once the beginning of a burst is detected, several measurements of certain characteristics of the bursts are made in parallel circuitry. When the end of the burst is detected, these measurements are converted to a compact digital format and stored in a buffer memory. The specified measurements total 32 bytes of data per event with instantaneous storage rates of up to 150 microseconds per event and at average rates of 1000 events per second. As the buffer memory becomes filled, the data for 104 events are transferred to a single track of a floppy disk without interrupt. Two floppy disk drives are used so that when one diskette is filled (8008 events), the second is ready to accept more data while the diskette is replaced in the first one.

Real-time distribution analysis of up to four parameters simultaneously by a microprocessor controlled graphics terminal is planned, but for now post-test processing of the data is done using a Nova minicomputer. Modifications to pattern recognition software which was used last year in the analysis of acoustic emission signals² is underway to accommodate the new data format and to include some extended capabilities.

The twenty-three pieces of information recorded for each acoustic emission event are listed in Table I. Representative data from one of the composite specimen bend tests are shown in Table II. Also shown as the last four parameters in Table I are front panel settings which usually remain constant throughout a test and are not automatically recorded. They can be changed at any point in a test and this change can be kept track of by changing the run number at that time. Post-test analysis of the emission data can then use the run number as a sorting parameter to investigate the effects of the four settings. In Table II, the last two columns (columns 24 and 25) are additional data files which are created when the acoustic emission data

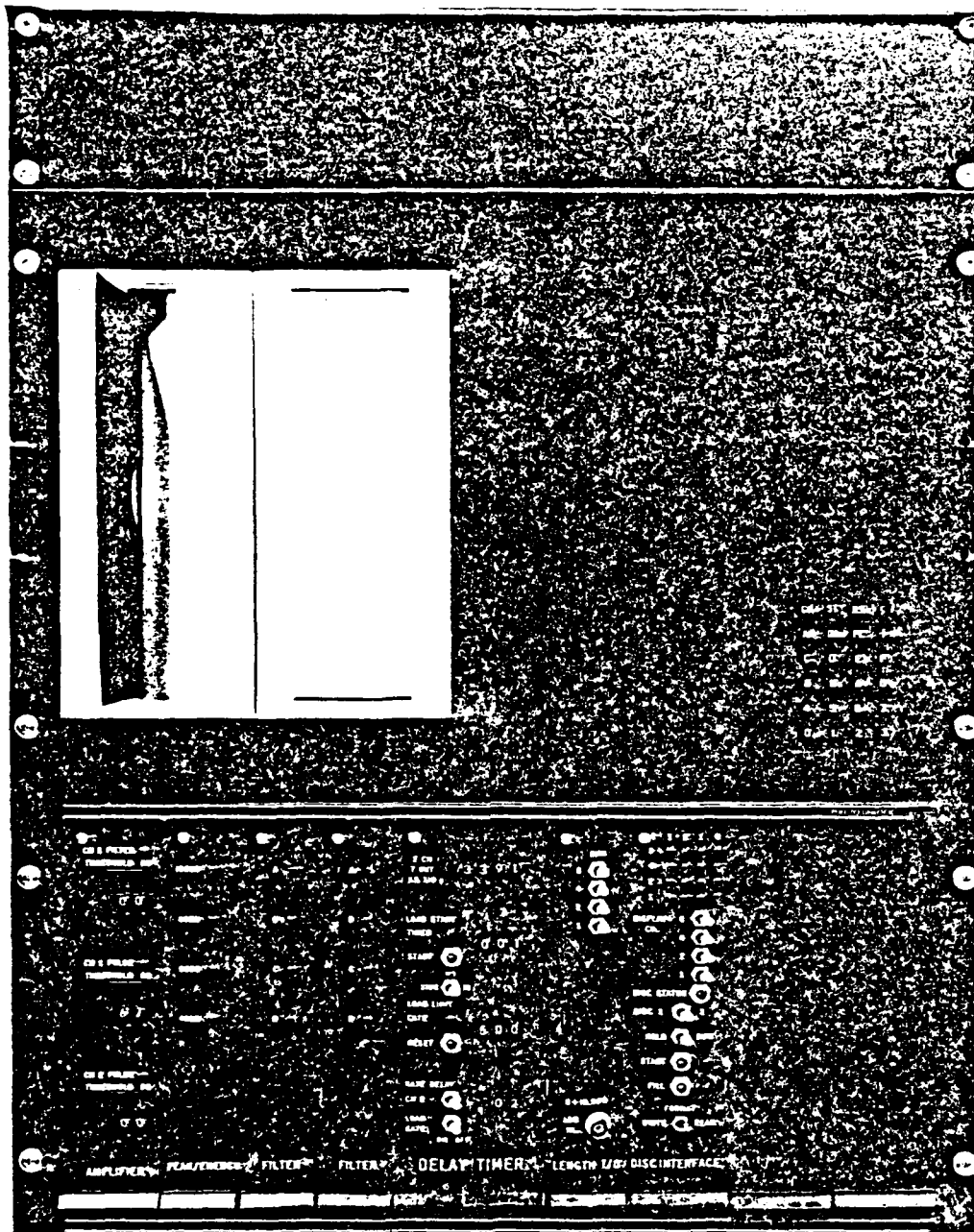


Figure 1. Acoustic emission characterization system.

Table I. Data record summary.

Measurement	Scale	0 DB REF	Range
1. Run Number	Hexadecimal		0 to 15
2. Event Number	BCD Counts		0 to 8007
3. Event Time	BCD Seconds		0 to 9999.999
4. Analog Volts	BCD Volts		0 to 19.99
5. Peak Amplitude	BCD DB	1 μ V	0 to 99
6. Energy Counts	BCD 200 μ V. μ s/count		0 to 1,999,999
7. Ring Down Count	BCD DB	1 count	0 to 118
8. Event Duration	BCD DB	1 μ s	0 to 118
9. Event Rise Time	BCD DB	1 μ s	0 to 118
10. Filter Amplifier Overflow	1 bit Flag		0 or 1
11. 31.6 kHz Peak	BCD DB	10 μ V*	0 to 79
12. 56.2 kHz Peak	BCD DB	10 μ V*	0 to 79
13. 100 kHz Peak	BCD DB	10 μ V*	0 to 79
14. 177.8 kHz Peak	BCD DB	10 μ V*	0 to 79
15. 316 kHz Peak	BCD DB	10 μ V*	0 to 79
16. 562 kHz Peak	BCD DB	10 μ V*	0 to 79
17. 1 MHz Peak	BCD DB	10 μ V*	0 to 79
18. 1.778 MHz Peak	BCD DB	10 μ V*	0 to 79
19. Biangulation Delay Time	BCD μ s		0 to <u>99</u> ,999
20. Load Gate Delay Time	BCD ms		0 to 99,999
21. Filter Amplifier Gain	BCD DB	Unity	0 to 79
22. Channel 1 Discriminator Gain	BCD DB	10 mV	0 to 79
23. Channel 2 Discriminator Gain	BCD DB	10 mV	0 to 79
2nd Channel Time Out	Decimal μ s		10 to 99,990
Load Start	Decimal ms		0 to 99,900
Load Limit	Decimal ms		0 to 99,900
Rate Delay	Decimal ms		0.1 to 9.9

*Varies with filter amplifier gain.



Table II. Representative data table.

Run Number	Event Number	Event Time Sec	Analog Volts	Peak Amplitude DB	Energy Counts 200V, us/count	Ring Down Count DB	Event Duration DB	Event Rise Time DB	Filter Andl Overflow DB	31.6 KHz Peak DB	50.2 KHz Peak DB	100 KHz Peak DB	177.6 KHz Peak DB	216 KHz Peak DB	352 KHz Peak DB	1 MHz Peak DB	1.776 KHz Peak DB	Strangulation Delay Time us	Load Gate Delay Time us	Filter Amplifier Gain DB	Channel 1 Disc Gain DB	Channel 2 Disc Gain DB	Emission Type	Emission Sub-type
4	23540	241.050	7.87	39	142	9	27	15	0	0	0	0	0	19	21	16	14	0	0	10	43	10	0	0
4	23541	241.704	7.89	33	117	0	10	23	0	0	0	0	0	13	18	17	9	0	0	10	43	10	0	0
4	23542	241.735	7.86	41	195	10	37	23	0	0	0	0	0	16	23	18	10	0	0	10	43	10	0	0
4	23543	241.736	7.83	67	2503	34	57	31	0	0	0	0	0	41	49	24	22	0	0	10	43	10	0	0
4	23544	241.755	7.89	92	61439	49	74	27	1	0	0	0	0	64	63	50	40	0	0	10	43	10	0	0
4	23545	241.846	7.90	59	1892	31	55	39	0	0	0	0	0	29	29	20	16	0	0	10	43	10	0	0
4	23546	241.850	7.83	40	111	9	22	21	0	0	0	0	0	12	18	17	10	0	0	10	43	10	0	0
4	23547	241.831	7.89	34	117	0	0	0	0	0	0	0	0	12	18	13	12	0	0	10	43	10	0	0
4	23548	241.632	7.87	70	10341	42	63	27	0	0	0	0	0	57	59	41	40	0	0	10	43	10	0	0
4	23549	241.919	7.88	54	757	29	54	26	0	0	0	0	0	32	34	28	20	0	0	10	43	10	0	0
4	23550	242.037	7.87	57	1862	34	59	31	0	0	0	0	0	34	30	24	21	0	0	10	43	10	0	0
4	23551	242.127	7.86	46	135	12	27	27	0	0	0	0	0	10	17	14	23	0	0	10	43	10	0	0
4	23552	242.148	7.90	51	302	24	39	27	0	0	0	0	0	23	30	20	19	0	0	10	43	10	0	0
4	23553	242.162	7.91	75	8750	41	56	25	0	0	0	0	0	44	45	34	30	0	0	10	43	10	0	0
4	23554	242.165	7.91	33	117	0	0	41	0	0	0	0	0	12	16	13	11	0	0	10	43	10	0	0
4	23555	241.169	7.86	43	134	6	32	25	0	0	0	0	0	14	19	13	13	0	0	10	43	10	0	0
4	23556	241.171	7.90	35	120	0	0	0	0	0	0	0	0	14	13	13	17	0	0	10	43	10	0	0
4	23557	242.531	7.88	50	802	30	50	29	0	0	0	0	0	29	33	27	40	0	0	10	43	10	0	0
4	23558	241.344	7.90	39	171	0	24	11	0	0	0	0	0	10	17	20	11	0	0	10	43	10	0	0
4	23559	242.336	7.90	46	162	16	37	7	0	0	0	0	0	8	17	21	16	0	0	10	43	10	0	0
4	23560	240.338	7.87	71	5430	27	56	31	0	0	0	0	0	42	43	43	43	0	0	10	43	10	0	0
4	23561	241.359	7.87	33	119	0	6	45	0	0	0	0	0	14	13	11	9	0	0	10	43	10	0	0
4	23562	241.431	7.86	70	3740	37	53	23	0	0	0	0	0	23	40	40	47	0	0	10	43	10	0	0
4	23563	241.502	7.91	70	13670	47	63	33	0	0	0	0	0	17	42	56	54	0	0	10	43	10	0	0
4	23564	241.525	7.89	36	132	0	30	15	0	0	0	0	0	16	17	13	12	0	0	10	43	10	0	0
4	23565	241.605	7.91	52	535	27	40	29	0	0	0	0	0	26	34	25	36	0	0	10	43	10	0	0
4	23566	241.716	7.91	70	837	42	60	29	0	0	0	0	0	41	43	40	42	0	0	10	43	10	0	0
4	23567	241.818	7.91	36	142	0	0	0	0	0	0	0	0	13	10	12	13	0	0	10	43	10	0	0
4	23568	242.641	7.90	25	117	6	19	37	0	0	0	0	0	5	15	20	12	0	0	10	43	10	0	0
4	23569	242.050	7.89	36	145	0	10	23	0	0	0	0	0	7	12	20	12	0	0	10	43	10	0	0
4	23570	241.106	7.91	44	172	18	31	15	0	0	0	0	0	7	21	17	11	0	0	10	43	10	0	0

are transferred from the floppy disks to the minicomputer. These are used to keep track of emission event types and sub-types during the post-test pattern recognition analysis and facilitates identification of the time evolution of these types.

A complete definition of the parameters listed in Table I and a description of their use in various test modes are given in Reference 3. The most unique feature of the Acoustic Emission Characterization System is the ability to collect frequency spectral information from each emission event. A bank of 8 parallel filters with their center frequencies sets at quarter decade intervals and constant relative bandwidth (constant Q) are used to separate the various frequency components in each event. Each filter output is monitored with a peak detector having an 80 dB dynamic range. A filter bank amplifier preset by the operator places this range anywhere within the dynamic range of the main amplifier chain.

An example of the frequency spectral information which is obtained is shown in Fig. 2. This figure was constructed by recording the acoustic emissions from a composite specimen test on a modified videotape recorder,⁴ searching the tape for two emissions of different spectral types, and then playing them back repetitively into a swept frequency spectrum analyzer (Hewlett Packard Model 141S/8553B/8552A) and into the Acoustic Emission Characterization System. The same was done for a 1 millisecond portion of the recorded signal immediately preceding the emission bursts to establish the electronic noise level amplitude as detected by both instruments. In both Figs. 2(a) and 2(b), the emission event amplitudes and background noise amplitudes as detected at the filter output are superimposed on the Polaroid photographs of the spectrum analyzer display. The difference between the two emission types can be clearly seen by either spectral representation which illustrates that the new system can categorize emissions by their frequency content.

Progress to Date

Specimen design is a particularly important consideration in this test program because of the number of different failure processes that can occur in the graphite-epoxy materials and their different relative occurrence in the various laminate lay-ups and loading configurations. Another

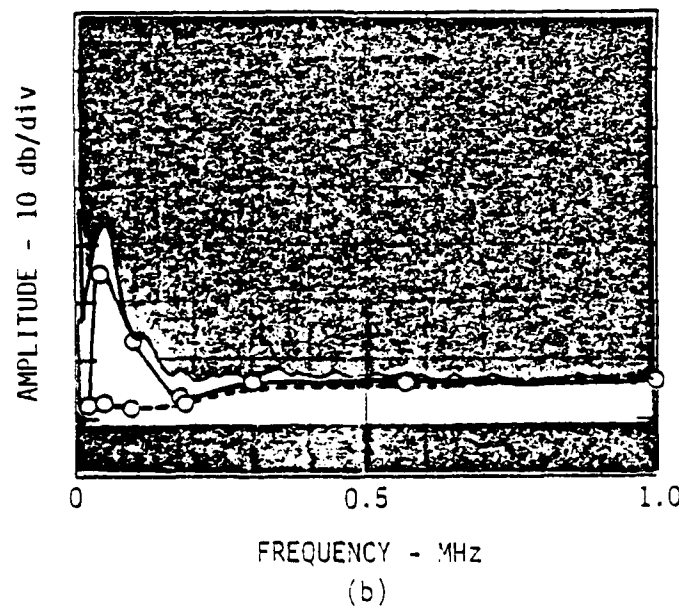
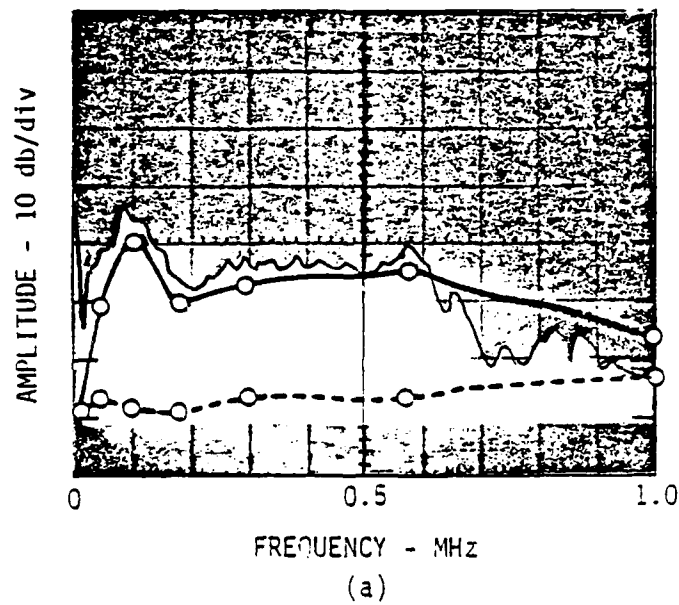


Figure 2. Comparison of spectral analysis results.

consideration in specimen design for acoustic emission testing is that extraneous noises from the loading machine and from the load application points are reduced to an absolute minimum so as not to confuse the analysis of the flaw generated emissions. With these two considerations in mind, two general specimen configurations were decided upon, bend and compression specimens. Several bend specimen geometries will be used to enhance one or another failure process.

Because of the complex failure paths that can occur in composites, a simplified model of the failure process in a structural element was adopted for the purpose of designing the specimen tests. It was assumed that the failure initiation step involves one of three mechanisms; matrix crazing due to a tensile stress normal to the fiber direction, delamination due either to compression buckling of a ply at a flawed region between plies or to interlaminar shear stresses, and fiber buckling at defects on the compression surface. All of these mechanisms are affected by moisture and at least the first two are also believed to produce characteristic acoustic emission signals, based on previous work. Initial tests will therefore concentrate on these mechanisms with and without the affects of moisture. Twenty-five bend specimens have been prepared from a unidirectional composite plate designated SC4 previously⁵ (Hercules 3501-5 Epoxy/Type AS graphite fiber), and, as mentioned before, three of these specimens have been tested, primarily for the purpose of checking out the operation of the new instrumentation. Enough of this material is available for compression specimens and further bend specimens as found necessary. The feasibility of making specimens from the epoxy material without the graphite fibers has been determined and plans for doing this are underway.

After the initial step in the failure process, several mechanisms can occur depending upon the load transfer process from the weaker structural links in the composite to successively stronger ones. These mechanisms are trans-fiber fracture of the matrix, fiber-matrix interface debonding, fiber fracture, and fiber pull-out. Identification of unique acoustic emission signatures for each of these mechanisms will be attempted using cross-ply laminate specimens and epoxy specimens containing single fibers. Plans for obtaining these specimens have been initiated.



Related Programs

Two acoustic emission programs in which AFML also has an interest have been running in parallel with this subject task. Highlights in the progress of these programs are presented in the following paragraphs.

Advanced Composite Serviceability Program. - This program will determine the consequences of manufacturing flaws, damage from flight-induced loads, and other degradational effects encountered by the B-1 aircraft vertical stabilizer, generic of primary structure defect and damage types. It is being carried out for AFML by the Los Angeles Division (LAD) and Science Center (SC), Rockwell International and the Illinois Institute of Technology Research Institute (IITRI). As a result of a feasibility study made in June 1977 by SC personnel, the decision was made to install acoustic emission (AE) instrumentation on the multi-specimen fatigue tests at IITRI. General instrumentation requirements were defined from the results of the feasibility study and equipment was purchased by IITRI which would permit monitoring of up to five specimens simultaneously for an indication of flaw growth during the fatigue testing. This was intended to provide a continuous qualitative record of the relative activity in the specimens to complement the information from other more quantitative but periodic NDE inspections.

The basic problem in monitoring the flaw generated AE during these tests was one of discriminating these signals from the other noise signals in the test environment. Based on the results of the feasibility study, five special transducers and frequency filters were constructed to use with the purchased instrumentation which would eliminate most of the extraneous noise by frequency selectivity. One other source of noise which has the same frequency content as the flaw generated emissions is caused by fretting of the specimen at the loading grips. The initial study indicated that these burst type noises were generally of lower amplitude than the AE seen in laboratory specimen tests and so could be discriminated on that basis. Electrical noise spikes picked up by radiation and through the power connections, primarily caused by nearby electrical relays, were less frequent but also troublesome, but could be eliminated by line isolation or extra shielding.

In January 1978, the AE monitoring instrumentation was assembled and a three-specimen fatigue test monitored. Some changes which had been made in

the mechanical loading fixture which provided better acoustic coupling between the extraneous noise sources and the AE transducers were found to not present a serious problem. However, grip noise, particularly for one of the specimens, was extremely bad during the initial portion of the test. It was also found to vary with time during temperature transients in the environmental chamber in which the specimens were tested. This required operator attention during these periods to adjust the instrumentation settings to obtain reasonable background noise detection levels.

About three hours into the test, one specimen became very noisy and after another half-hour it failed in the gripped region and the test was halted. Because of the other problems with grip noise, this failure was not predicted from the AE record, but post-test analysis indicated that with more experience and confidence in the AE monitoring system it could easily have been predicted.

Based on this experience, a tentative operating procedure was written for use by IITRI personnel on further tests. Specific recommendations were also made for ameliorating the grip noise problem and grip failures. The operating procedure will be updated periodically during the specimen testing program as experience is gained in using the AE monitoring system.

TTCP-PAG3(a) Action Group on Acoustic Emission. - This action group of the Technical Cooperation Program has as members representatives from eight military R&D laboratories in the U.S. and U.K. (Australia, Canada, and England) and from the Science Center. Its charter is to establish methods for quantitative AE data transferability between various laboratories where different types of instrumentation may be in use and between laboratory and field tests, and to study the basic AE characteristics and source mechanisms for selected materials.

A common problem when comparing AE data obtained at two different laboratories is that the AE signals which are analyzed to obtain those data depend strongly upon the characteristics of the instrumentation used to detect and process them. They also depend to some extent upon the test specimen geometry and transducer placement on it. As a result, quantitative agreement between two sets of data is rare and sometimes even qualitative agreement is not obvious. In an attempt to obviate this problem, the members of the Action



Group selected a "standard" broadband noise source (helium gas jet) which could be injected at a localized point on a specimen. This would establish a "system response" in the defined frequency range of 0.2 to 1.0 MHz which could be used to normalize subsequent AE data.

At a meeting in November 1977, the success of this normalization method was affirmed when substantial agreement was found in the normalized amplitude and frequency spectral content of AE signals from two sets of specimens tested in the various laboratories although quite different results were observed before normalization. A report of these results was prepared for submission to the TTCP Committee and plans for journal publication of the results were formulated.

Work is currently underway to confirm and extend these results. Each of the nine laboratories is testing a specimen of their own design and sending duplicate specimens to one other laboratory for comparative testing. Reportable data will include other AE parameters such as event count, emission count, amplitude distributions, and energy as well as the frequency spectra to provide a data base for finding a method for also normalizing these parameters through the system spectral response. These results will be evaluated at a meeting in May 1978 at which time a limited number of specimen and material combinations will be selected for a concentrated effort at data normalization and materials characterization by the entire group.

Acknowledgements

The efforts of R. Govan in specimen fabrication and testing and Dr. R.K. Elsley and G. Lindberg in computer software development are gratefully acknowledged.

References

1. L.J. Graham, "Microstructure Effects on Acoustic Emission Signal Characteristics," in Interdisciplinary Program for Quantitative Flaw Definition, Special Report Second Year Effort, AFML Contract No. F33615-74-C-5180, Science Center, Rockwell International, p. 297-320, July 1976.
2. L.J. Graham, "Microstructure Effects on Acoustic Emission Signal Characteristics," in Interdisciplinary Program for Quantitative Flaw Definition, Special Report Third Year Effort, AFML Contract No. F33615-74-C-5180, Science Center, Rockwell International, p. 364-378, July 1977.
3. R.L. Randall and L.J. Graham, "Acoustic Emission Characterization System," to appear in Proc. Instrument Soc. of America Meeting, Albuquerque, NM, May 1978.
4. L.J. Graham and G.A. Alers, "Acoustic Emission in the Frequency Domain," Monitoring Structural Integrity by Acoustic Emission, ASTM STP 571, Amer. Soc. for Testing and Materials, p. 11-39, 1975.
5. D.H. Kaelble and P.J. Dynes, "Methods for Detecting Moisture Degradation in Graphite-Epoxy Composites," in Interdisciplinary Program for Quantitative Flaw Definition, Special Report Second Year Effort, AFML Contract No. F33615-74-C-5180, Science Center, Rockwell International, p. 269-296, July 1976.



PROJECT III, UNIT C, TASK 1

DEFECT FRACTURE PROBABILITIES

A. G. Evans
Rockwell International Science Center

Introduction

Fracture from surface cracks in ceramics is reasonably well-comprehended in terms of established fracture mechanics solutions that take account of the crack depth, aspect ratio and orientation. However, fracture from volume defects, such as voids and inclusions, has not been thoroughly investigated. The pertinent theory and experiments will be conducted in this task. Initially, fracture from spherical and cylindrical voids has been analyzed, and correlated with available data for polycrystalline Al_2O_3 . The analysis will subsequently be extended to include ellipsoidal voids and inclusions, as well as defects of irregular shape. A comprehensive analytic basis for interpretation of the fracture results on disc samples will then have been established.

The analysis for spherical voids combines fracture mechanics solutions for radial cracks emanating from voids with functions for the size and spatial distribution of void surface cracks. This approach allows the stress dependence of the fracture probability to be derived as functions of the void radius and the flaw distribution parameters. The void size dependence of the fracture probability is found to be a strong function of the shape parameter, m , of the flaw distribution; specifically, for small values of m , voids of appreciable size have little effect on the fracture probability, while for large m values, fracture is strongly influenced by the presence of voids.

Analysis of Fracture From Spherical Voids

Fracture from cavities is most realistically treated by examining the extension of flaws at (or near) the cavity surface^{1,2,3}. The flaws are

considered to extend when the stress intensity due to the combined stress field of the cavity and the flaw, attain the critical value for local crack extension. The flaw responsible for fracture in polycrystalline ceramics may either pre-exist or may develop due to subcritical extension of grain boundary cusps. In either case, a distribution of flaws should exist, prior to final fracture, in the vicinity of the cavity surface. The analysis of fracture from cavities is thus a statistical problem, involving the extension of crack distributions in localized stress fields.

1. Stress Intensity Factor Solutions. The first three-dimensional problem of interest pertains to the equatorial annular crack emanating from a spherical cavity, normal to the applied stress (Fig. 1). The tensile stress normal to the crack plane σ_z is⁷

$$\sigma_z = \sigma_\infty \left[1 + \frac{(4-5\nu)}{2(7-5\nu)} \left(\frac{r}{r+x} \right)^3 + \frac{9}{2(7-5\nu)} \left(\frac{r}{r+x} \right)^5 \right] \quad (1)$$

where ν is Poisson's ratio. A lower bound for the stress intensity factor can be obtained by imposing this stress onto the surface of a penny crack (with $\sigma_z = 0$ for $x < 0$), by analyzing the function⁶;

$$K = 2 \left(\frac{a}{\pi} \right)^{\frac{1}{2}} \int_0^1 \frac{\sigma_z x dx}{(1-x^2)^{\frac{1}{2}}} \quad (2)$$

Substituting σ_z from Eq. (1) and integrating gives the result plotted in Fig. 1, obtained for $\nu = 0.2$. An approximate correction for the additional displacement due to the cavity surface (based on that obtained for a two-dimensional calculation), and the crack solution, are also shown.

Secondly, a solution is obtained for a partial circular crack on the surface of a spherical cavity (Fig. 2); a configuration that would be most typical of a void in a polycrystalline ceramic. For this purpose consider the crack shown in Fig. 2b. The maximum stress intensity factor location in the configuration coincides with the position of maximum surface traction, i.e., at 0 and 0'. A lower bound for the stress intensity factor at these locations (for $a/r \leq 0.3$) is^{6,8};



SC595.32SA

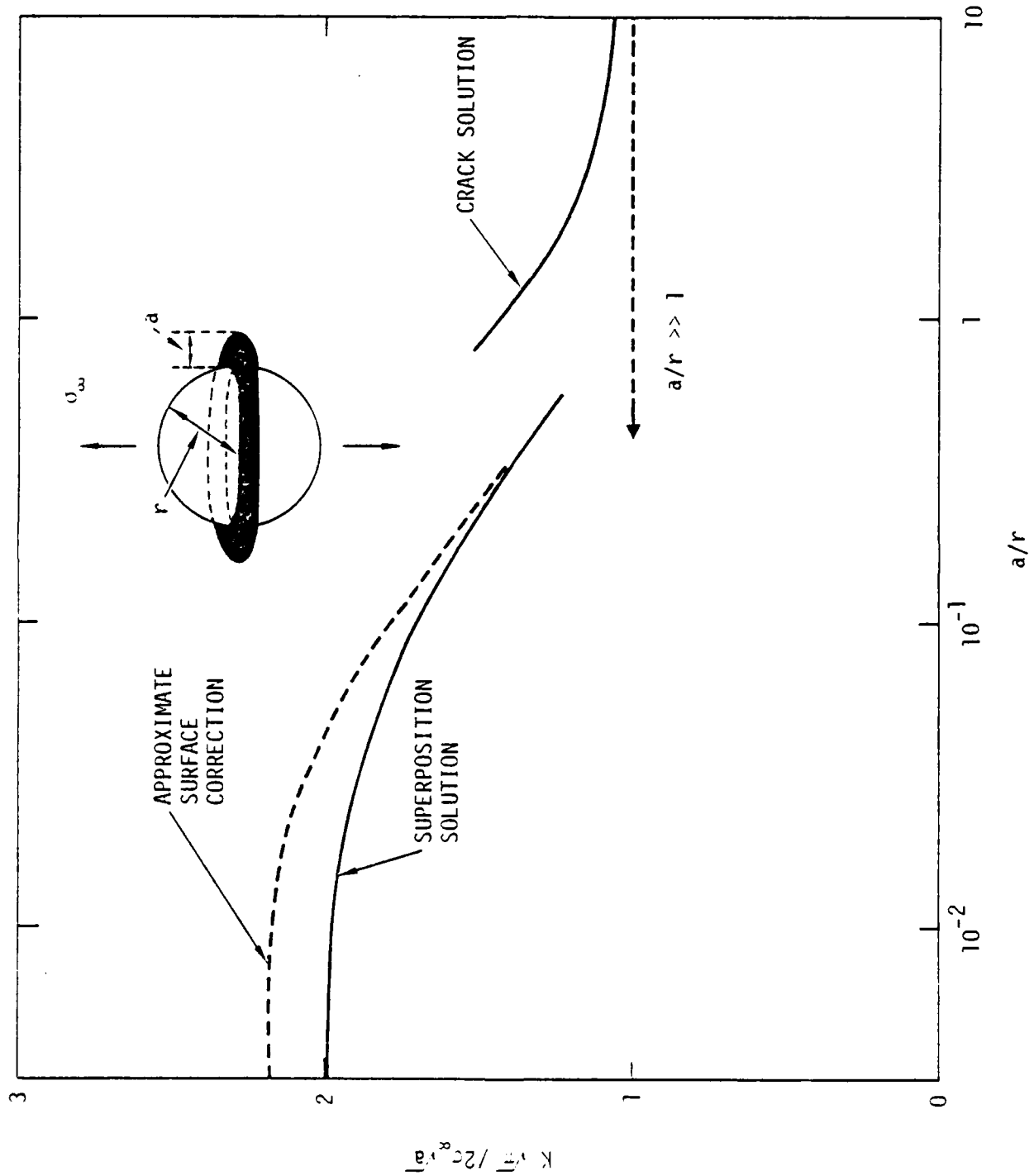


Fig. 1 Stress intensity solution for annular crack.

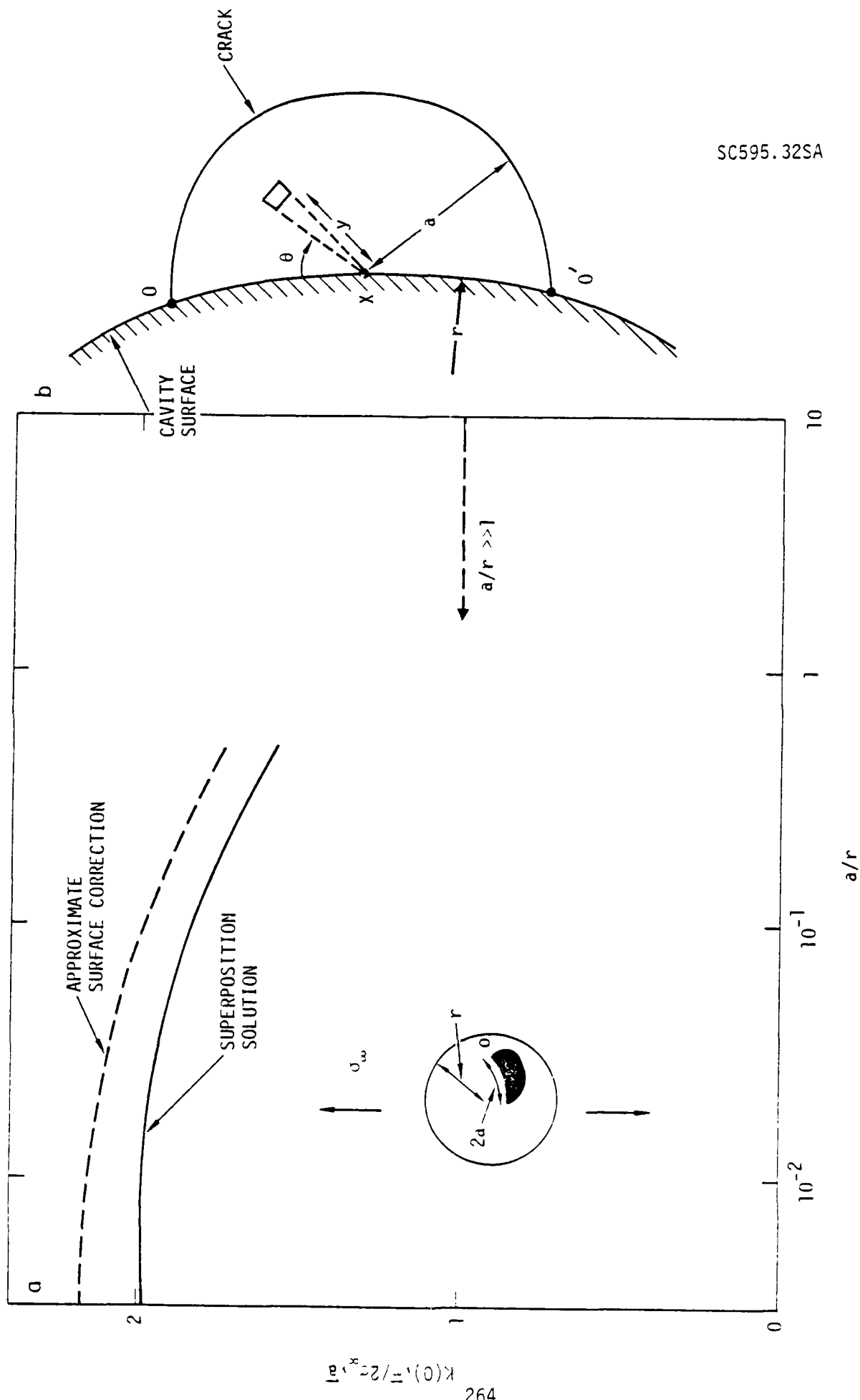


Fig. 2 Stress intensity factor solution for surface crack.



$$K = \frac{2}{(\pi a)^{3/2}} \int_0^\pi \int_0^a \frac{\sigma_y [1 - (y/a)^2]^{1/2} \sigma_z^0}{[1 - 2(y/a) \cos \Theta + (y/a)^2]} dy d\theta \quad (3)$$

where y is the radial distance from the crack center (Fig. 2b).

The pressure distribution σ_z^0 can be deduced from Eq. (1) as;

$$\sigma_z^0 = \sigma_\infty \left[1 + \frac{(4-5\nu)}{2(7-5\nu)} (1 + \xi a \sin \theta)^{-3} + \frac{9}{2(7-5\nu)} (1 + \xi a \sin \theta)^{-5} \right] \quad (4)$$

Substituting σ_z^0 into Eq. 3 and integrating yields the result plotted in Fig. 2a, obtained for $\nu = 0.2$. Again an appropriate surface correction is constructed, and plotted on the same figure. In this case, since the crack front of interest is always located at the cavity surface (Fig. 2b) the surface correction should not exhibit a marked dependence on a/r .

Inspection of Figs. 1 and 2 indicates that stress gradient effects are negligible for $a/r < 10^{-2}$. Further, it is apparent that the stress gradient has a relatively small effect on K for the semi-circular surface crack (Fig. 2a). This result pertains because the positions of maximum K occur at the cavity surface. However, since the K values for the fully-developed annular crack (Fig. 1) are lower (for given a/r) than for the surface crack, stable growth of the surface crack to either a full annular crack, or to an intermediate configuration, appears possible. The condition that pertains at instability is thus likely to more closely resemble that for the annular crack than for the surface crack (c.f. circular crack development in Hertzian fracture⁹). However, the incidence of stable crack growth prior to instability would complicate the statistical analysis of fracture from cavities, as emphasized in the following section.

2. Fracture Statistics. The probability of fracture $\Phi(S)$ when fracture occurs by the unstable extension of non-interacting surface cracks is, in general, related to the state of stress, S , by¹⁰;

$$-\ln [1 - \Phi(S)] = \int_A dA \int_0^S g(S) dS \quad (5)$$

where A is the stressed area and $g(S)dS$ is the number of flaws in unit area that extend unstably in the stress range S to $S + dS$. The function $g(S)$ can be deduced from experimental strength data^{10,11} and usually, several flaw populations exist over the entire strength range¹¹ ($0 \rightarrow \infty$); so that several functional forms are needed to fully-describe $g(S)$. However, for a restricted range of strength, the reduced Weibull function¹² is usually found to afford an adequate description;

$$\int_0^S g(S) dS = \left(\frac{S}{S_0} \right)^m \quad (6)$$

where m is a shape parameter and S_0 a scale parameter. This fracture probability relation can be used in conjunction with stress fields at cavity surfaces and K solutions to obtain expressions for cavity fracture. Some caution should be exercised, however, when the subcritical extension of surface cracks is involved (see Section 2), because this violates one of the postulates used to derive Eq. (5). For flaws located at the surface of a spherical cavity, the only stresses that exist (Fig. 3a) are the tangential stresses¹⁷,

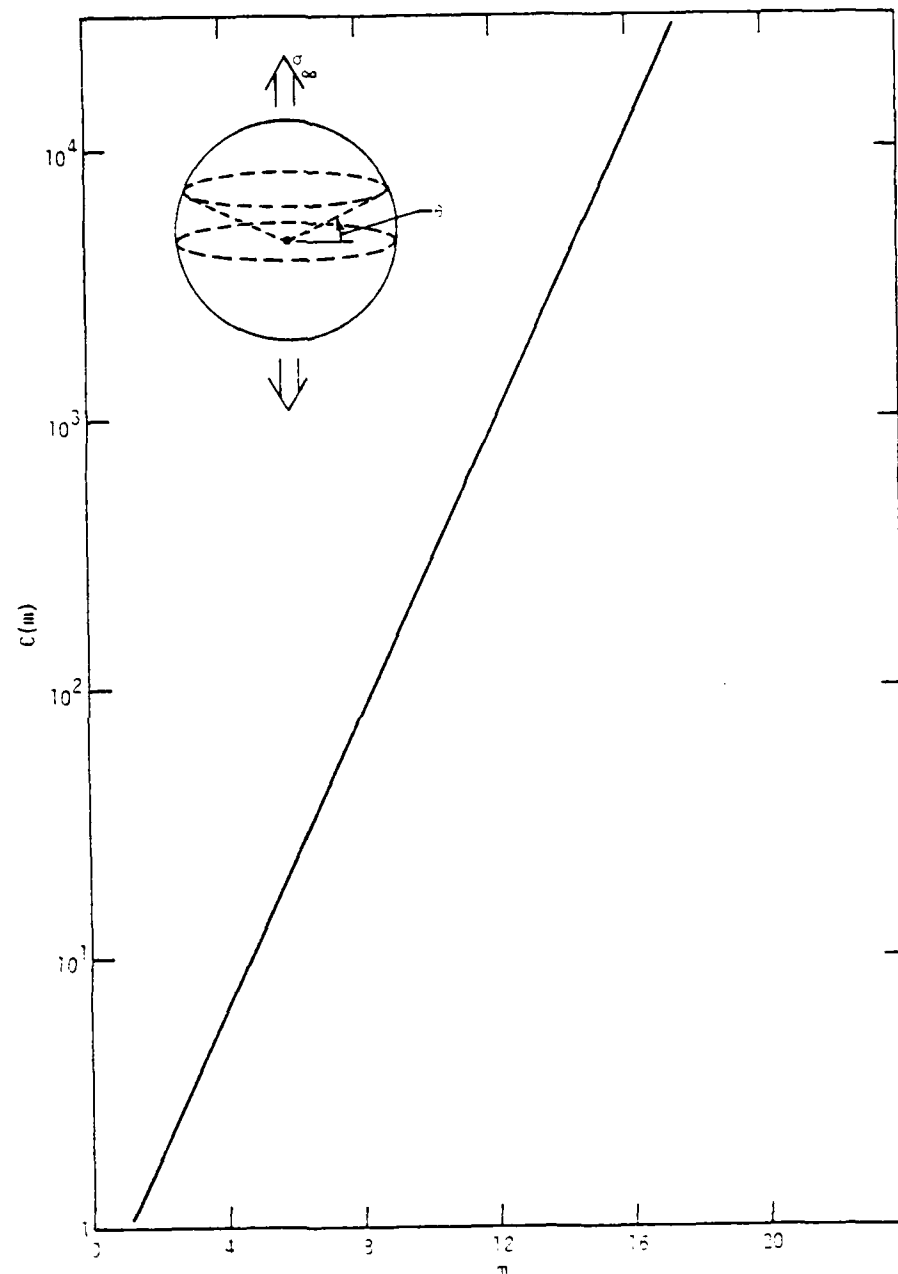
$$\begin{aligned} \sigma_{\theta} &= \frac{3\sigma_{\infty}}{2(7-5\nu)} \left[4-5\nu + 5 \cos 2\theta \right] \\ \sigma_{\alpha} &= \frac{3\sigma_{\infty}}{2(7-5\nu)} \left[5\nu \cos 2\theta - 1 \right] \end{aligned} \quad (7)$$

where θ is the angle defined in Fig. 3a.

The statistical problem is thus concerned with the analysis of biaxial fracture. The fracture criterion that has most successfully described multiaxial fracture¹⁴ (as well as angular dependencies of fracture¹⁸) in ceramics is that based on the co-planar strain energy release rate;

$$S_T^2 = \sigma_n^2 + \frac{4\tau_m^2}{(2-\nu)^2} \quad (8)$$

where S_T is the flaw extension stress in equi-triaxial tension, σ_n is the tensile stress normal to the flaw and τ_m is the maximum in-plane shear



SC78-159

Fig. 3a Strength integral for surface cracks.

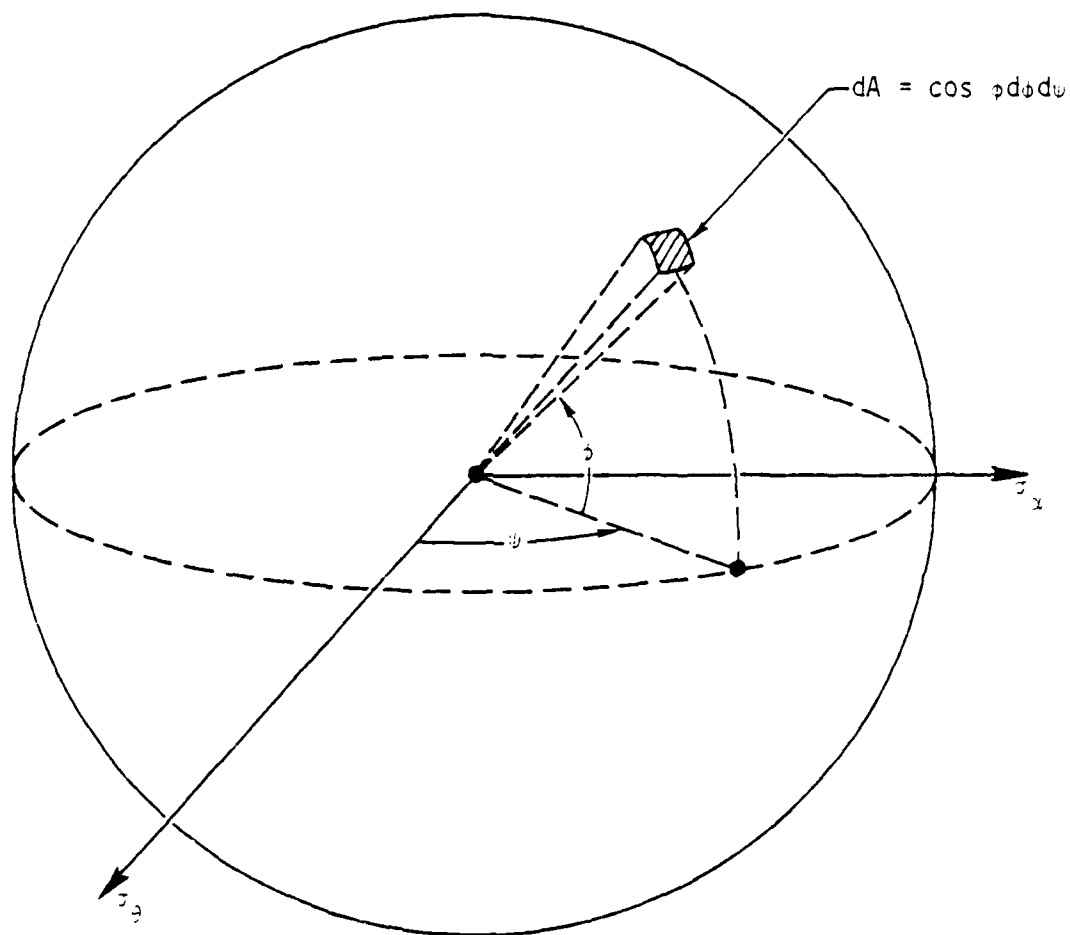


Fig. 3b Unit sphere used for fracture analysis.

AD-A132 082

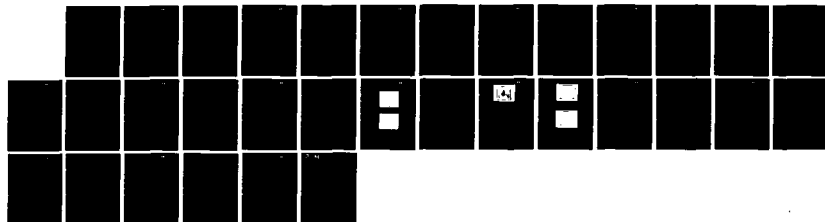
INTERDISCIPLINARY PROGRAM FOR QUANTITATIVE FLAW
DEFINITION(U) ROCKWELL INTERNATIONAL THOUSAND OAKS CA
SCIENCE CENTER 1978 SC595.325A F33615-74-C-5180

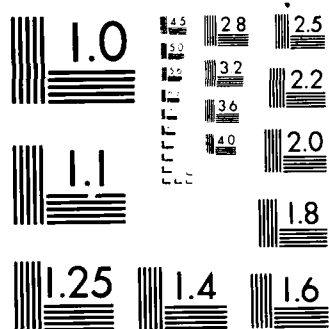
4/4

UNCLASSIFIED

F/G 14/2

NL





MICROCOPY RESOLUTION TEST CHART
NATIONAL BUREAU OF STANDARDS-1963-A



stress. For flaws located in the surface element dA of the spherical volume shown in Fig. 3b, the stresses σ_n and τ_m are related to the stresses σ_θ , σ_α and the angles ϕ and ψ defined in the figure by;

$$\begin{aligned}\sigma_n^2 &= \cos^4 \phi \left[\sigma_\alpha^2 \sin^4 \psi + \sigma_\theta^2 \cos^4 \psi + 2\sigma_\alpha \sigma_\theta \cos^2 \psi \sin^2 \psi \right] \\ \tau_m^2 &= \cos^2 \phi \left[\sigma_\alpha^2 \sin^2 \psi (1 - \cos^2 \psi \sin^2 \psi) + \sigma_\theta^2 \cos^2 \psi (1 - \cos^2 \psi \cos^2 \psi) \right. \\ &\quad \left. + 2\sigma_\alpha \sigma_\theta \cos^2 \phi \cos^2 \psi \sin^2 \psi \right]\end{aligned}\quad (9)$$

If the strength distribution in triaxial tension is now defined by a Weibull-type function (see Eq. 6);

$$g(S_T) = \left(\frac{S_T}{S_0} \right)^k \quad (10)$$

consideration of the eight equivalent areal elements $dA = \cos \phi d\phi d\psi$ (Fig. 3b) on a unit sphere allows the biaxial strength distribution function to be derived for a given θ^{14} ;

$$g(S_\infty)_\theta = \frac{2}{\pi} \int_0^{\pi/2} \int_0^{\pi/2} \left(\frac{S_T}{S_0} \right)^k \cos \phi d\phi d\psi d S_T \quad (11)$$

Then substituting Eq. (11) into Eq. (5) allows the probability of fracture from the cavity to be expressed as;

$$\begin{aligned}-\ln[1 - \Phi(S_\infty^C)] &= 8r^2 \int_0^{S_\infty} \left(\frac{S_\infty}{S_0} \right)^k dS_\infty \int_0^{0.35\pi} \cos \phi \cos \theta \\ &\quad \left(\frac{9 \cos^2 \phi}{4(7-5\nu)} \right) \left[\cos^2 \phi (4-5\nu + 5 \cos^2 \theta)^2 \cos^4 \psi + (5\nu \cos^2 \theta - 1)^2 \cos^2 \phi \sin^4 \psi \right. \\ &\quad + 2(4-5\nu + 5 \cos^2 \theta) (5\nu \cos^2 \theta - 1) \cos^2 \phi \cos^2 \psi \sin^2 \psi \\ &\quad + (4/(2-\nu))^2 [(5\nu \cos^2 \theta - 1)^2 \sin^2 \psi (1 - \cos^2 \phi \sin^2 \psi) \\ &\quad + (4-5\nu + 5 \cos^2 \theta)^2 \cos^2 \psi (1 - \cos^2 \phi \cos^2 \psi) + (4-5\nu + 5 \cos^2 \theta) \\ &\quad \left. (5\nu \cos^2 \theta - 1) \cos^2 \phi \cos^2 \psi \sin^2 \psi \right] \Bigg\}^{(k+1)/2} d\psi d\phi d\theta \\ &\equiv 8r^2 B(k, \nu) S_0^0 (S_\infty^C/S_0^0)^{k+1} / (k+1)\end{aligned}$$

(12)

The equivalent fracture probability for uniaxial tension¹⁴ is;

$$-\ln [1 - \Phi(S_{\infty}^u)] = A_g I_u(k, \nu) S_0^0 (S_{\infty}^u/S_0^0)^{k+1}/(k+1) \quad (13)$$

where A_g is the gauge surface area. Expressing Eq. (13) in the more conventional notation;

$$-\ln [1 - \Phi(S_{\infty}^u)] = A_g (S_{\infty}^u/S_0^0)^m \quad (14)$$

and substituting into Eq. (12) the fracture probability from the cavity becomes;

$$-\ln [1 - \Phi(S_{\infty}^c)] = 8r^2 C(m, \nu) (S_{\infty}^c/S_0^0)^m \quad (15)$$

where $C(m)$ is plotted in Fig. 3a for $\nu=0.2$.

Now, a stress gradient correction must be applied, using the appropriate K solution. The annular crack result is used for this purpose. The stress intensity factor is given, in general, by

$$K = \frac{2}{\sqrt{\pi}} \sigma_{\infty} \sqrt{a} F_2(a/r, \theta) \quad (16)$$

For $\theta = 0$, $F_2(a/r)$ can be expressed from Fig. 1, by interpolation between the crack solution and the superposition solution, as;

$$F_2(a/r) \Big|_{\theta=0} = 1 + \frac{0.36}{0.3 + (a/r)} \quad (17)$$

The effective flaw strength S^* is thus, for $\alpha < 0.6$,

$$\frac{S}{S^*} = 0.33 + 2 (0.11 - 0.18\alpha)^{1/2} \cosh(\gamma/3) \equiv D(\alpha) \quad (18)$$

where

$$\gamma = \cosh^{-1} [0.35 (1+\alpha)/(0.11 - 0.18\alpha)^{3/2}]$$



and for $\alpha > 0.6$

$$\frac{S}{S_*} = 0.33 + 2(0.18\alpha - 0.11)^{\frac{1}{2}} \sinh(\gamma'/3)$$

where

$$\gamma' = \sinh^{-1} [0.35(1+\alpha)/(0.18\alpha - 0.11)^{3/2}] \quad (19)$$

Assuming that a similar relation pertains for all θ in the tensile range, the fracture probability becomes;

$$-\ln [1 - \Phi(\hat{S}_\infty)] = 8r^2 \left(\frac{\hat{S}_\infty}{S_0} \right)^m C(m) D \left[\frac{1}{r} \left(\frac{K_c}{S_\infty} \right)^2 \right]^m \quad (20)$$

The fracture probabilities predicted by Eq. (20) are plotted in Fig. 4 as a function of the normalized strength \hat{S}_∞/S_0 for several relative void radii, r/r_0 , and a typical m of 4; r_0^2 and K_c^2/r_0^2 are chosen to be unity. The probabilities obtained from Eq. (15) are also plotted for comparison.

3. Fracture Studies. The applicability of the fracture relations derived in the preceding sections can only be adequately assessed if cavities with well-defined surface crack distributions are prepared and tested. Preliminary studies are reported for cylindrical holes. The holes are prepared by drilling, and should contain surface cracks with a size distribution similar to that produced by surface grinding. The pertinent crack size distribution function for the hole might thus be estimated from separate strength tests on samples with ground surfaces.

The strength results are tabulated in Table I. As anticipated, the presence of the holes reduced the strength. Inspection of the samples containing the holes indicated that the fracture, in all cases, initiated within the hole near the outer surface.

For the samples without cavities, the fracture probability in four point flexure, for fracture occurring within the inner span, can be derived directly from Eq. (5) as;

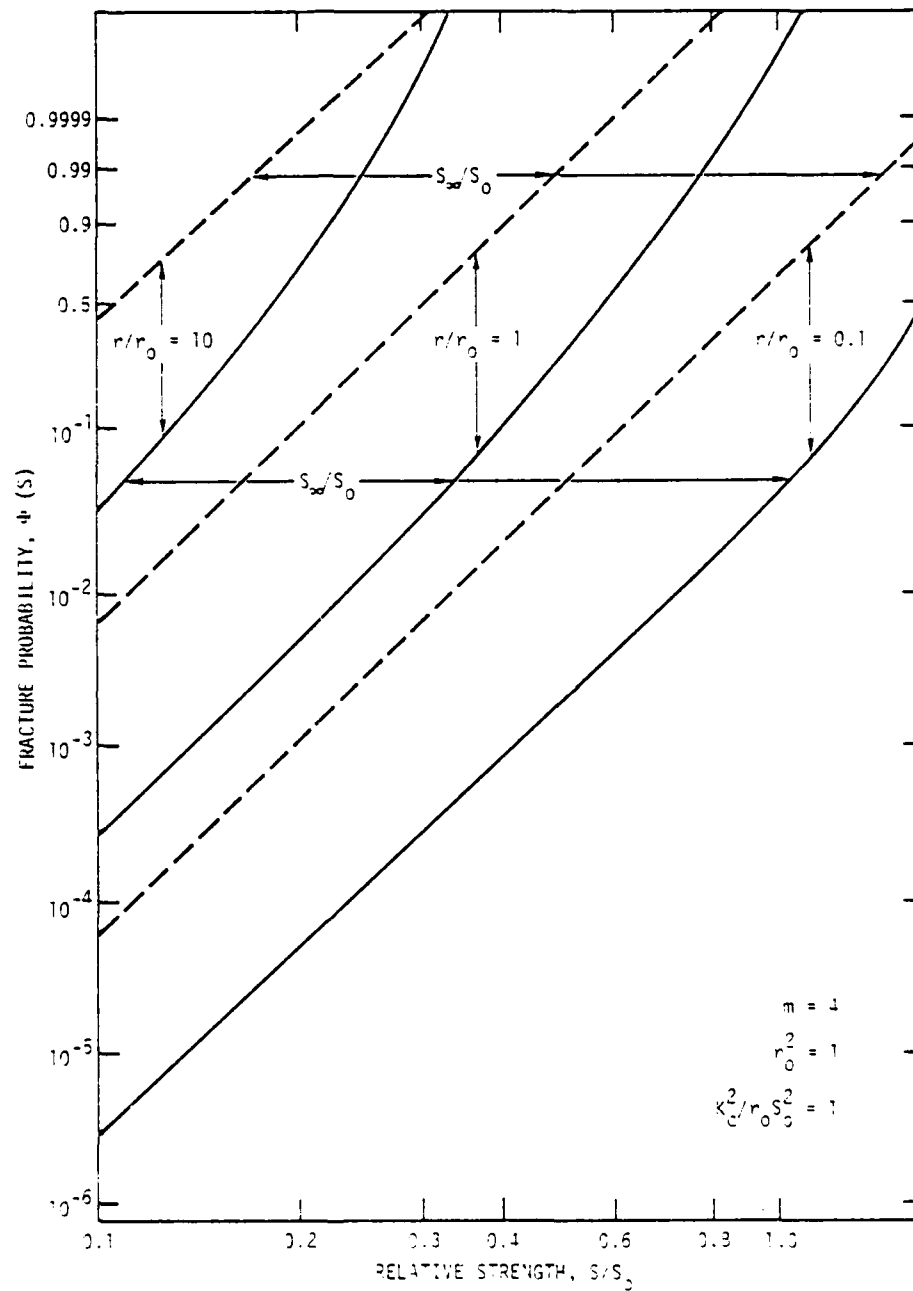


Fig. 4a The relations between fracture probability and strength.

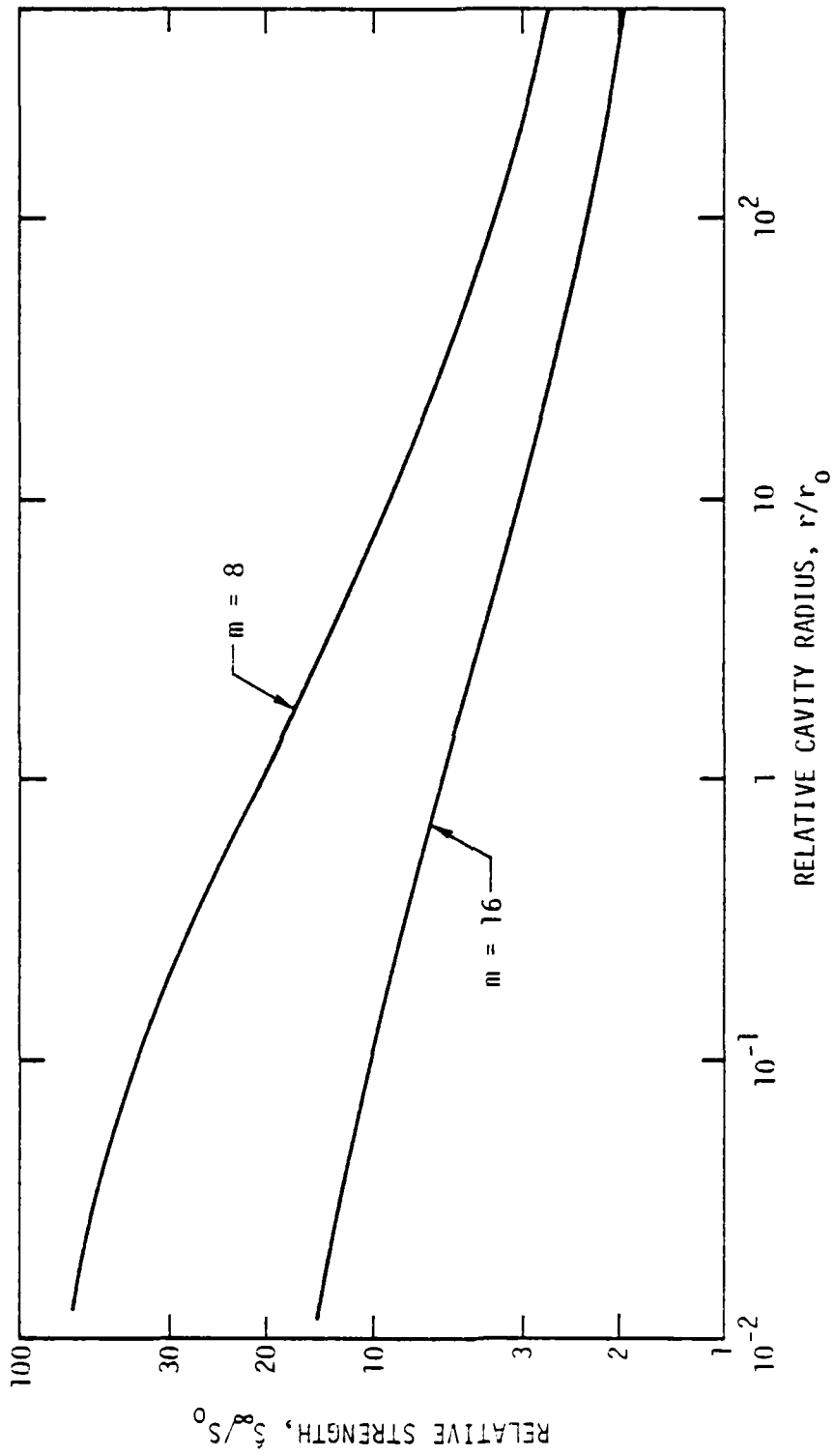


Fig. 4b The effect of void radius on the fracture strength at constant probability.

TABLE I

Sample Type	Fracture Probability ($\Phi=n/(N+1)$)	Fracture Strength (MPa)
As Machined Samples	0.125	258
	0.25	276
	0.375	286
	0.50	309
	0.625	325
	0.75	372
	0.875	380
Drilled Holes	0.125	137
	0.25	140
	0.375	150
	0.5	162
	0.625	224
	0.75	229
	0.875	234



$$\begin{aligned} -\ln \left[1 - \Phi(S_a) \right] &= \left(\frac{\hat{S}_a}{S_o} \right)^m \left[\ell b + 2\ell \int_0^{d/2} \left(1 - \frac{2z}{d} \right)^m dz \right] \\ &\equiv \left(\frac{\hat{S}_a}{S_o} \right)^m \ell [b + d/(m+1)] \end{aligned} \quad (21)$$

where ℓ is the inner span, b the sample width, d the sample depth, S_a the outer fiber stress at fracture and z the distance from the tensile surface; the first term in the parentheses relates to fracture from the tensile surface, and the second term allows for fracture from the side faces. For the samples containing the drilled cavities, the fracture probability (c.f.

Eq. 20) is

$$\begin{aligned} -\ln \left[1 - \Phi(S_H) \right] &= \left(\frac{\hat{S}_H}{S_o} \right)^m \left\{ \left(\ell b - \pi r^2 + \frac{\ell d}{(m+1)} \right) + 4r A(m) Z^m \int_0^{d/2} \left(1 - \frac{2z}{d} \right)^m dz \right\} \\ &\equiv \frac{\hat{S}_H}{S_o}^m \left\{ \left(\ell b - \pi r^2 + \frac{\ell d}{(m+1)} \right) + \frac{2r A(m) Z^m}{(m+1)} \right\} \end{aligned} \quad (22)$$

Equating Eq. (21) and (22) allows the strength ratio \hat{S}_H/\hat{S}_a to be predicted for equivalent fracture probabilities. The strengths of the samples with the drilled holes, predicted from the strengths of the samples without holes (using $K_C = 4 \text{ MPa}\sqrt{\text{m}}$) are plotted in Fig. 5. Comparison with the measured strengths indicates a relatively good correlation; with the predicted strengths being slightly larger than the measured strengths. The small disparity may arise because the cracks in the immediate vicinity of the corner between the hole and the surface experience a larger K than that anticipated by the present analytic solution.

4. Failure Prediction. The prediction of failure from isolated cavities in dense ceramics can directly utilize Eq. (20), when the cavities are nearly spherical in shape. (The derivation of fracture probabilities for ellipsoidal cavities and cavities of irregular shape will be conducted in a separate study²¹). The probability of service failure Φ_F , at a stress level σ_A , based on a nondestructive characterization of the cavity dimensions, if all cavities with an interpreted cavity radius r_i are accepted is²¹;

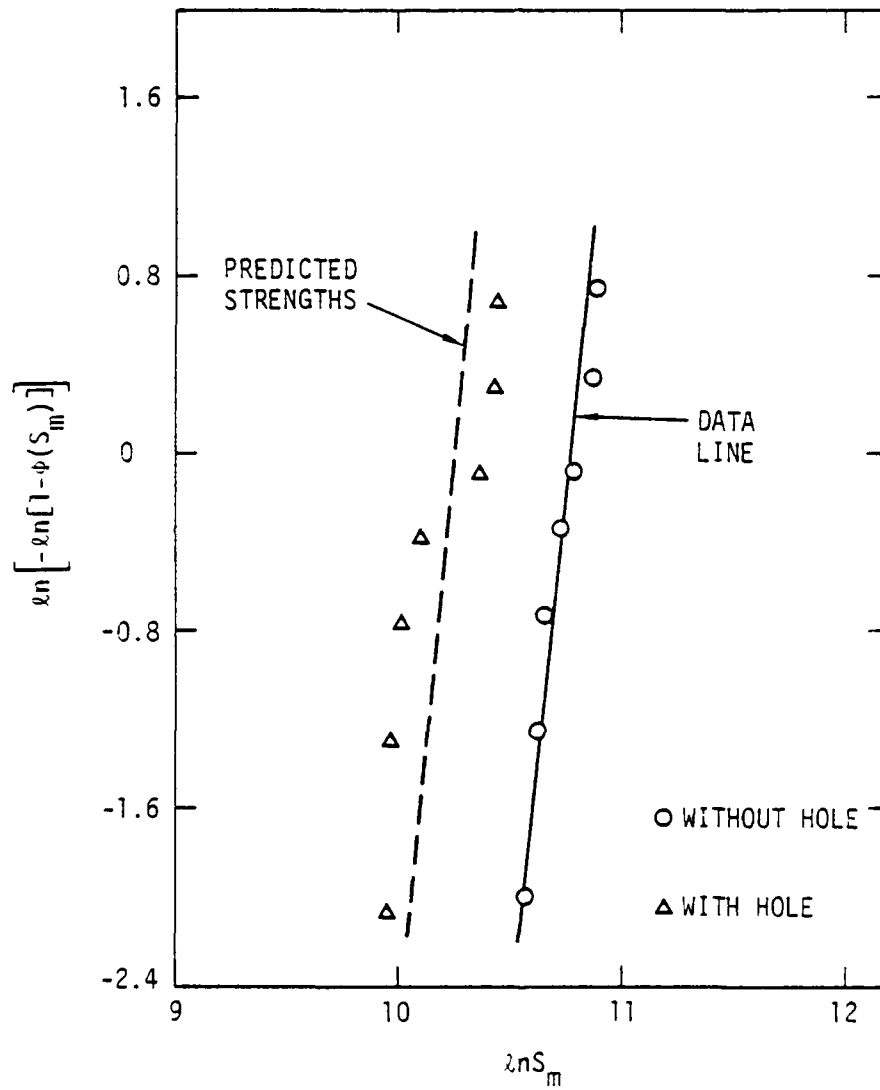


Fig. 5 A comparison of measured and predicted fracture strengths for fracture from cylindrical holes.



$$\Phi_F(\sigma_A, r_i^0) = \int_0^{\sigma_A} \int_0^{r_i^0} \int_0^{\infty} \phi(S_\infty) \phi(r_i|r) \phi(r) dr dr_i dS_\infty \quad (23)$$

where $\phi(S_\infty)dS$ is the derivative of Eq. (20), $\phi(r_i|r)dr_i$ is the probability that the nondestructively interpreted cavity radius r_i is in the range r_i to r_i+dr_i given that its actual radius is r . It is apparent, therefore, that some a priori knowledge of the cavity radius distribution in the material, $\phi(r)dr$, is needed to obtain the failure probability from the cavity failure function, in addition to a quantitative nondestructive method for characterizing (in a well-comprehended fashion) the cavity dimensions²².

References

1. See for example, R. W. Rice, Fracture Mechanics of Ceramics (Ed R. C. Bradt, D. P. H. Hasselman and F. F. Lange) Plenum, N.Y. 1974. p 323.
2. A. G. Evans and T. G. Langdon, Prog. Mater. Sci. 21 (1976) p. 195.
3. O. Vardar, I. Finnie, D. R. Biswas and R. M. Fulrath, Int. J. Frac 13 (1977) 215.
4. R. W. Davidge and G. Tappin, Proc. Brit. Ceram. Soc. 15 (1970) p. 47.
5. O. L. Bowie, Jnl. Matls and Physics 35, (1976) 60.
6. G. C. Sih, Handbook of Stress Intensity Factors (Lehigh Univ. Press) 1973).
7. S. Timoshenko and J. N. Goodier, Theory of Elasticity (McGraw-Hill) 1951.
8. A. G. Evans and E. A. Charles, Acta Met 25 (1977) 919.
9. B. R. Lawn and T. R. Wilshaw, Jnl. Mater. Sci 10 (1975) 1049.
10. J. R. Matthews, F. A. McClintock and W. A. Shack, Jnl. Amer. Ceram. Soc., 59 (1976) 304.
11. A. G. Evans and R. L. Jones, Jnl. Amer. Ceram. Soc., March/April 1978, in press.
12. W. Weibull, Jnl. Appl. Mech. 18 (1951) 193.
13. M. Adams and G. Sines, Jnl. Amer. Ceram. Soc. 59 (1976) 300.
14. A. G. Evans, Jnl. Amer. Ceram. Soc., in press.
15. A. F. Grandt, Intl. Jnl. Frac. 11 (1975) 283.
16. S. Batdorf and J. G. Crose, Jnl. Appl. Mech. (1974) 41.
17. J. N. Goodier, Trans ASME (Jnl. Apl. Mechs.) 55 (1933) 39.
18. J. J. Petrovic and M. G. Mendiratta, Jnl. Amer. Ceram. Soc. 60 (1977) 463.
19. A. G. Evans and E. A. Charles, Jnl. Amer. Ceram. Soc. 59 (1976) 371.
20. M. Isida, "Methods of Analysis and Solutions of Crack Problems" (Ed. G. C. Sih) Noordhoft 1973 p. 56.
21. J. M. Richardson and A. G. Evans, to be published.



PROJECT III, UNIT C, TASK 2

FAILURE PREDICTION ANALYSES

J. M. Richardson, A. G. Evans, N. Mann
Rockwell International Science Center

Introduction

The ability of nondestructive techniques for predicting failure can be quantified by means of false-accept, false-reject curves. The expressions relating the false-accept rate (or the failure probability) and the false-reject rate (or the rejection probability) have been derived in terms of the probability functions that describe the important material and test variables. Some insights concerning the appropriate probability functions has already been obtained from other studies (e.g., Task 2), but this aspect of the problem will receive greater emphasis following the acquisition of the first sets of inspection and fracture data.

Probabilistic Failure Prediction.

The defect inspection technique will provide information about the dimensions, orientation and character of the defect. The extent to which each of these might be defined by a specific inspection technique or might be important in terms of its effect on failure remains to be determined. The details of the probabilistic analysis thus await the generation of the relevant information. However, it is certain a priori that a knowledge of at least one dimension (e.g., maximum dimension) of the defect will be required to predict failure. The probabilistic approach to failure prediction has thus been derived at a preliminary level, for a specific defect type (e.g., a void), on the premise that the inspection technique provides an estimate of only its maximum dimension.

The estimate b_i of the actual maximum defect dimension, b_a , will depend on the defect orientation and shape so that, in general, the probability that the estimated maximum defect size will be in the range b_i

to db_i will be characterized by a function $\phi(b_i|b_a) db_i$. The detailed form of the function will depend on the model for the estimate (e.g., Born, Rayleigh) the number of independent measurements and the intrinsic range of defect shapes and orientations. The functional forms for $\phi(b_i|b_a)$ are presently being evaluated using the Rayleigh model, a random void orientation and a normal distribution of void shapes. The corresponding fracture probability for ellipsoidal voids as a function of the maximum dimension, b_a , is characterized by a function $\phi(S|b_a)dS$; which reflects the probability that the fracture of an ellipsoidal void with a maximum dimension b_a will occur at an applied stress level between S and $S + dS$. The functional forms of $\phi(S|b_a)$ are being derived by an extension of the spherical void analysis presented in Task 2. Once these two probabilities have been established, the fracture probability can be related to the estimate of the defect size, b_i , by

$$\phi(S, b_i) dS db_i = \int_0^{\infty} \phi(S|b_a) \phi(b_i|b_a) \phi(b_a) db_a db_i dS \quad (1)$$

where $\phi(S, b_i)$ is the probability that fracture will occur in the stress range S to $S + dS$ if the defect size estimate is in the range b_i to $b_i + db_i$; $\phi(b_a) db_a$ represents the size and spatial distribution of voids, a function that must be supplied by a priori metallographic studies.

The false-accept, false-reject curve for this problem can now be derived if the service stress distribution in the component is known, e.g., by finite element analysis. For a tensile stress σ_A in the region of the defect, satisfactory service performance requires that the strength level S should exceed σ_A . Hence the probability that service performance will be satisfactory (Fig. 1) is;

$$\phi_o db_i = \int_{\sigma_A}^{\infty} \phi(S_i b_i) db_i dS \quad (2)$$

The equivalent probability that service performance will be unsatisfactory (Fig. 1) is;

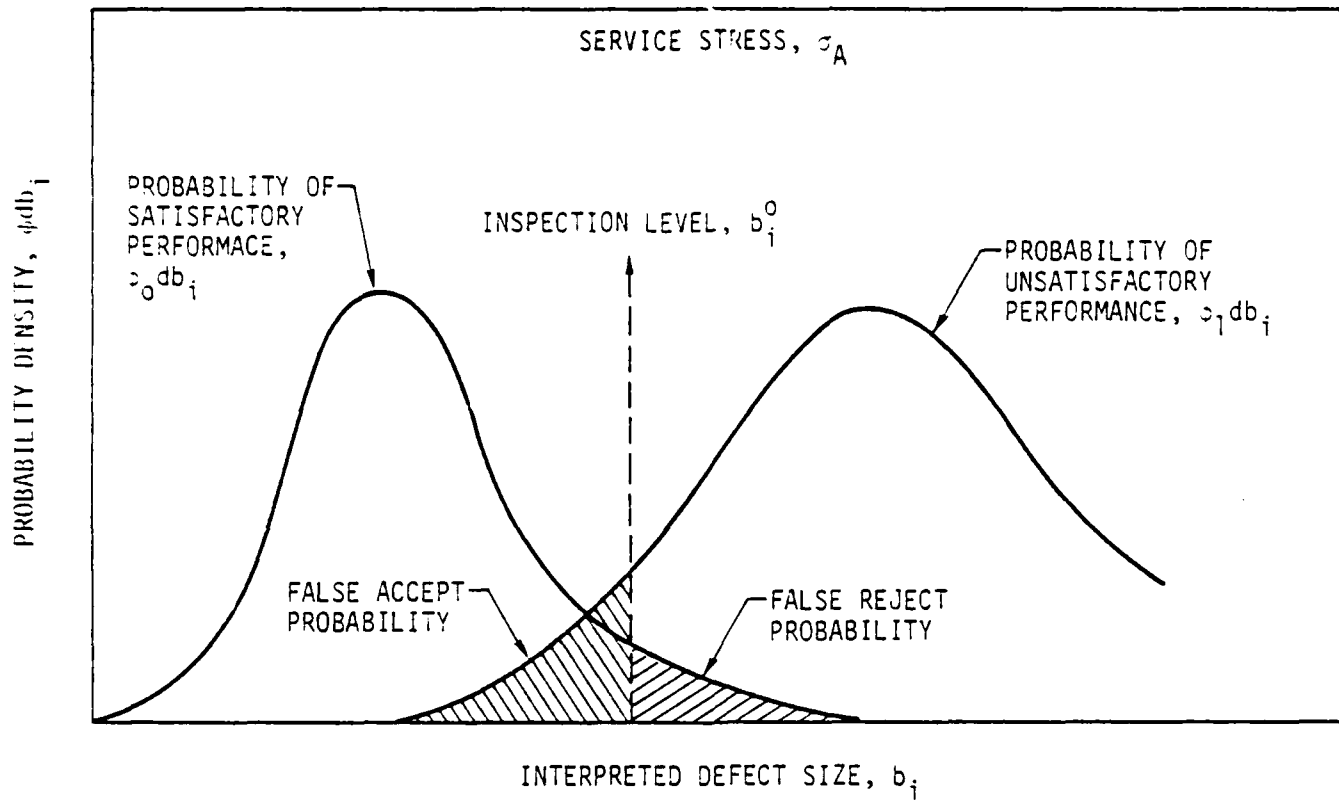


Fig. 1 False-accept and false reject probabilities plotted as a function of the maximum allowed inspection size, b_i^0 .

$$\phi_1 db_i = \int_0^{\sigma_A} \phi(S, b_i) db_i dS \quad (3)$$

The false-accept σ_A and false-reject σ_R probabilities can now be obtained by superimposing on Fig. 1 the chosen inspection level b_i^0 ; defined as the largest value of the estimated maximum dimension of the void that will be permitted to exist for acceptance of the component. These probabilities, given by

$$\begin{aligned} \Phi_A(\sigma_A, b_i^0) &= \int_0^{b_i^0} \phi_1 db_i \\ \Phi_R(\sigma_A, b_i^0) &= \int_{b_i^0}^{\infty} \phi_0 db_i \end{aligned} \quad (4)$$

are plotted schematically in Fig. 2 for two inspection techniques. It is evident from both Eq. (4) and Fig. 2 that Φ_A and Φ_R are interrelated through b_i^0 , for a specific inspection procedure and material system; once one of the quantities b_i^0 , Φ_A or Φ_R has been specified for the system, the other two must also be specified, by definition. The false-accept, false-reject curve (Fig. 2b) is thus a characteristic of the inspection process for the material system. This important concept means that different inspection systems can be quantitatively compared, with regard to their failure prediction capabilities, for material systems of practical interest. For example, reference to Fig. 2b indicates that system B is much superior to system A in that a specific failure (or false-reject) probability coincides with a much lower rejection (or false-reject) probability - especially at the lower failure probability extreme that pertains for most structural components.

The ultimate intent of the Project is to construct false-accept, false-reject curves of the type depicted in Fig. 2b for each inspection procedure (or combination of procedures) for the two or three structural ceramics proposed for study.

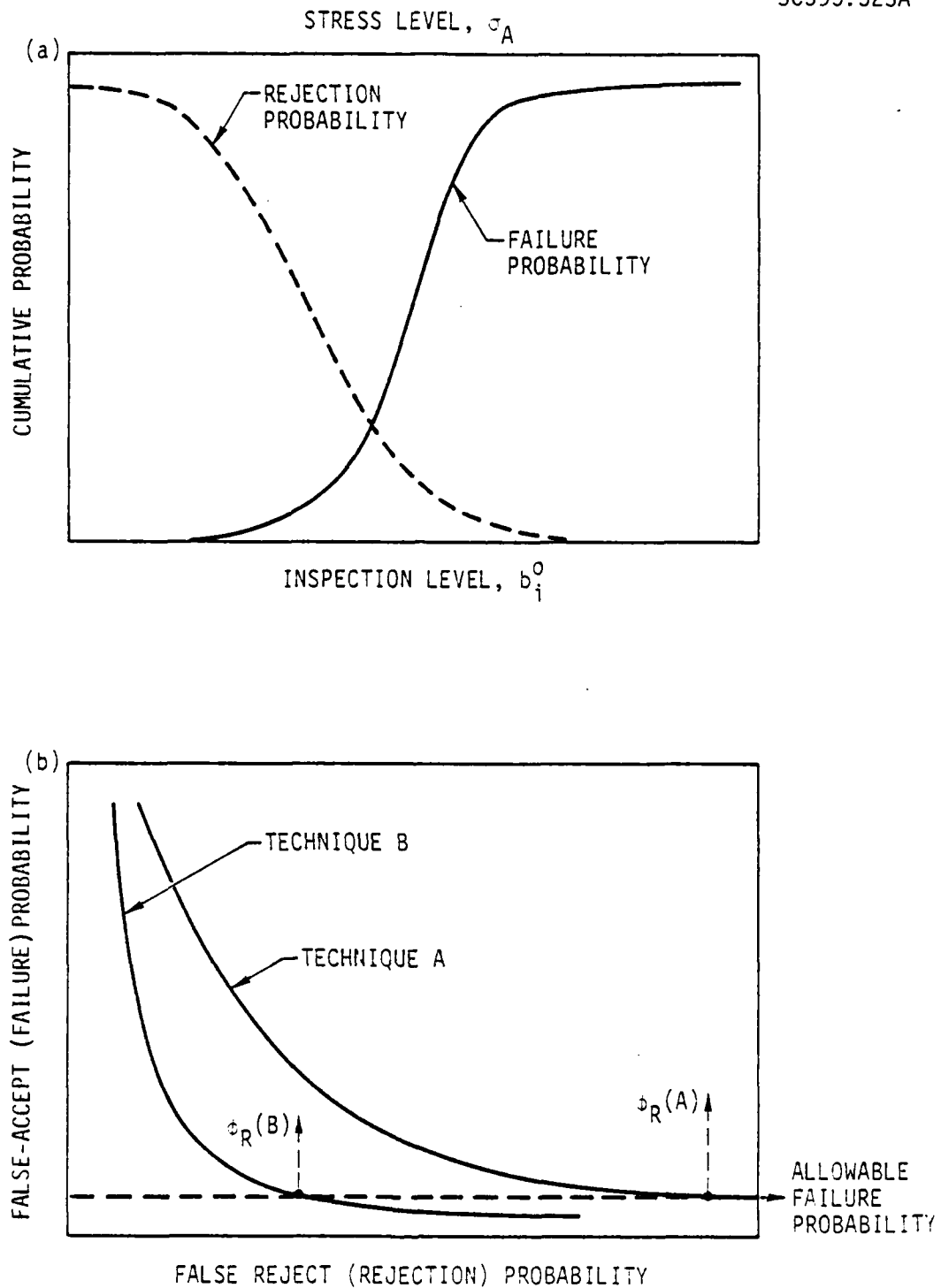


Fig. 2 Unified plots of the false-accept, false-reject rate.

PROJECT III, UNIT C, TASK 3

HIGH FREQUENCY ULTRASONIC DEFECT
CHARACTERIZATION IN CERAMICSG. S. Kino and B. T. Khuri-Yakub
Stanford UniversityIntroduction

A high frequency (200 MHz - 500 MHz) A-scan system has been constructed to detect different types of inclusions (C, SiC, Fe, WC, BN, Si), with sizes varying from 25 μm to 500 μm . A Fourier Transform routine has been used to analyze the back scattered signals from these defects, in order to characterize them in the frequency domain. We describe in this report, a new method for making contact to the ceramic, which does not require a contacting layer. We describe our first results with an electronically scanned B imaging system, operating with 2 ns pulses, which we have developed to decrease the search time for flaws. We also discuss a computer simulated inverse filter routine to be used to analyze defect signatures.

New Contacting Method.

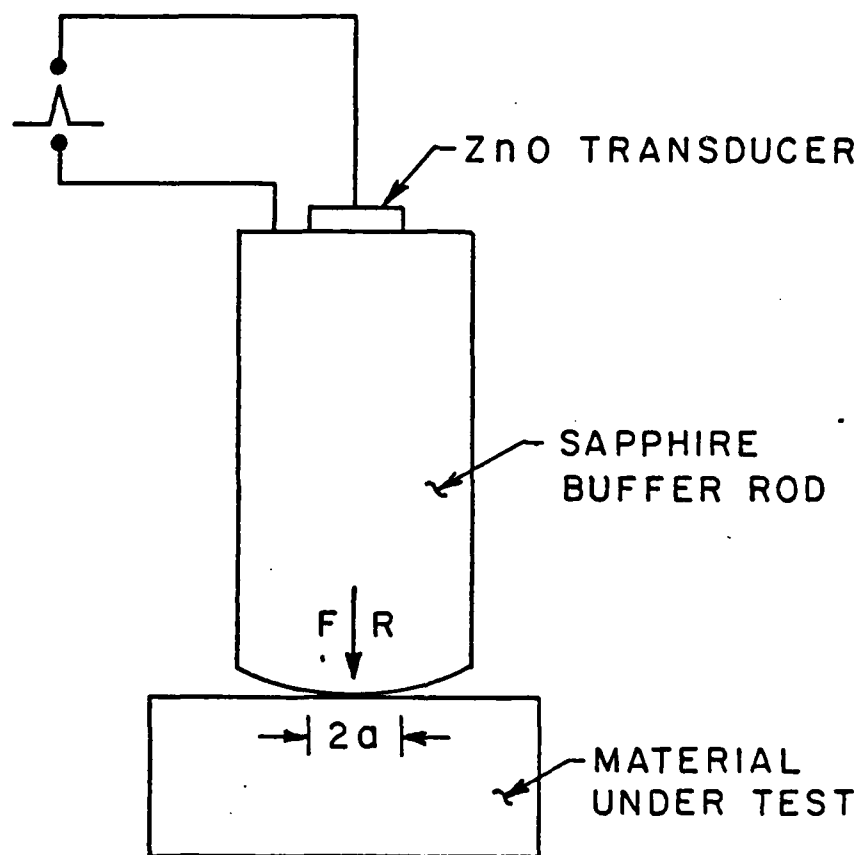
Previously, we have been using a 25 μm gold foil as a contacting agent between the ceramic and the sapphire buffer rod. Obviously it would be preferable to eliminate the need for the foil contacting layer. So we have overcome this requirement by rounding off the lower end of the sapphire rod as shown in Fig. 1. The sapphire buffer rod is ground to a radius of curvature R of the order of 20 mm. By applying a force F to make contact, we obtain a flat contact region of a radius a. The relations between F, R, and a are given by the Hertzian contact formula:

$$FDR = a^3$$

where

$$D = \frac{3}{4} \frac{1 - \nu^2}{E} + \frac{1 - \nu'^2}{E'}$$

and ν, ν' are Poisson's ratio for the sapphire and the ceramic, respectively, and E, E' are the Young's modulus of elasticity of the sapphire and the ceramic, respectively.



$$R = 20 \text{ cm}$$

$$2a = .1 \text{ cm}$$

$$F = 172 \text{ N} \quad \cong 39 \text{ Lbs.}$$

Fig. 1 A schematic of the transducer system.

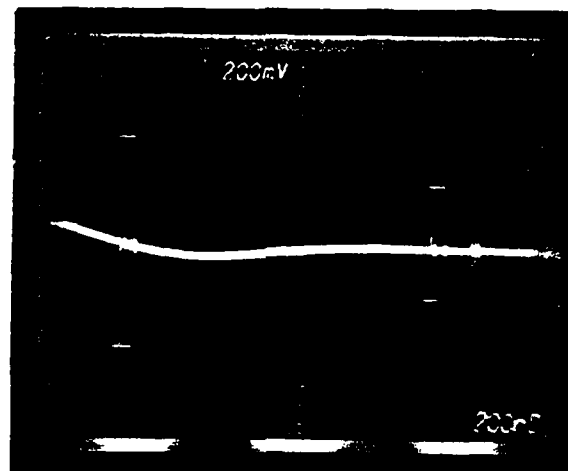
Typically, for a contact area with a diameter $2a = 1$ mm, and a radius of curvature of 20 mm, a force of 172 N is necessary to make good contact between the sapphire and the ceramic, as shown in Fig. 2. It is observed from this result that more of the acoustic energy is coupled into the ceramic relative to that obtained using gold foil. Furthermore, much less force is required to make contact and alignment of the transducer and workpiece is far less critical than with the previous arrangement.

B-Scan System.

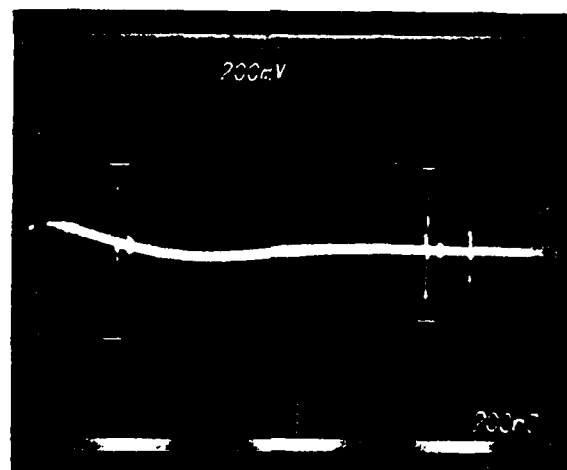
A problem with any A-scan system is the length of time it takes to mechanically scan a whole sample and find the location of flaws within it. One way to speed up the process is to use an array of transducers and electronically switch from one to the other. We have constructed such a device, which is a long piece of sapphire with an array of ZnO transducers laid down on it, as shown in Fig. 3. One transducer at a time is excited with a narrow pulse, which is emitted as a beam of approximately 1 mm in diameter. So the return echoes pertain to flaws in this region. We then excite the next transducer and examine a similar region displaying the return signals (from 16 transducers) simultaneously on an oscilloscope. A device of this type had never been built before for operation in the frequency range from 100 - 500 MHz. The design problem is difficult because great care is needed to acoustically isolate the transducers, and to electronically isolate the channels, in order to decrease the cross-talk between elements. Additional problems occur in obtaining good sensitivity, in the design of high frequency switches and in eliminating spurious responses. We have developed suitable circuits for such a system. It uses a 2 cm long sapphire rod with 16 transducers on it, each transducer has a diameter of $750\text{ }\mu\text{m}$ and the separation between transducers was $250\text{ }\mu\text{m}$. We used $8\text{ }\mu\text{m}$ of r-f sputtered ZnO as the transducer material (which corresponds to a resonant frequency of about 300 MHz). A photo of the system is shown in Fig. 3. A typical output of the B-scan system is shown in Fig. 4. The echoes from the end of the sapphire rod are displayed on 16 channels. Figure 5 shows the result of a test on a disk of ceramic 5 mm in diameter which intercepts five acoustic beams. The ceramic



SC595.32SA

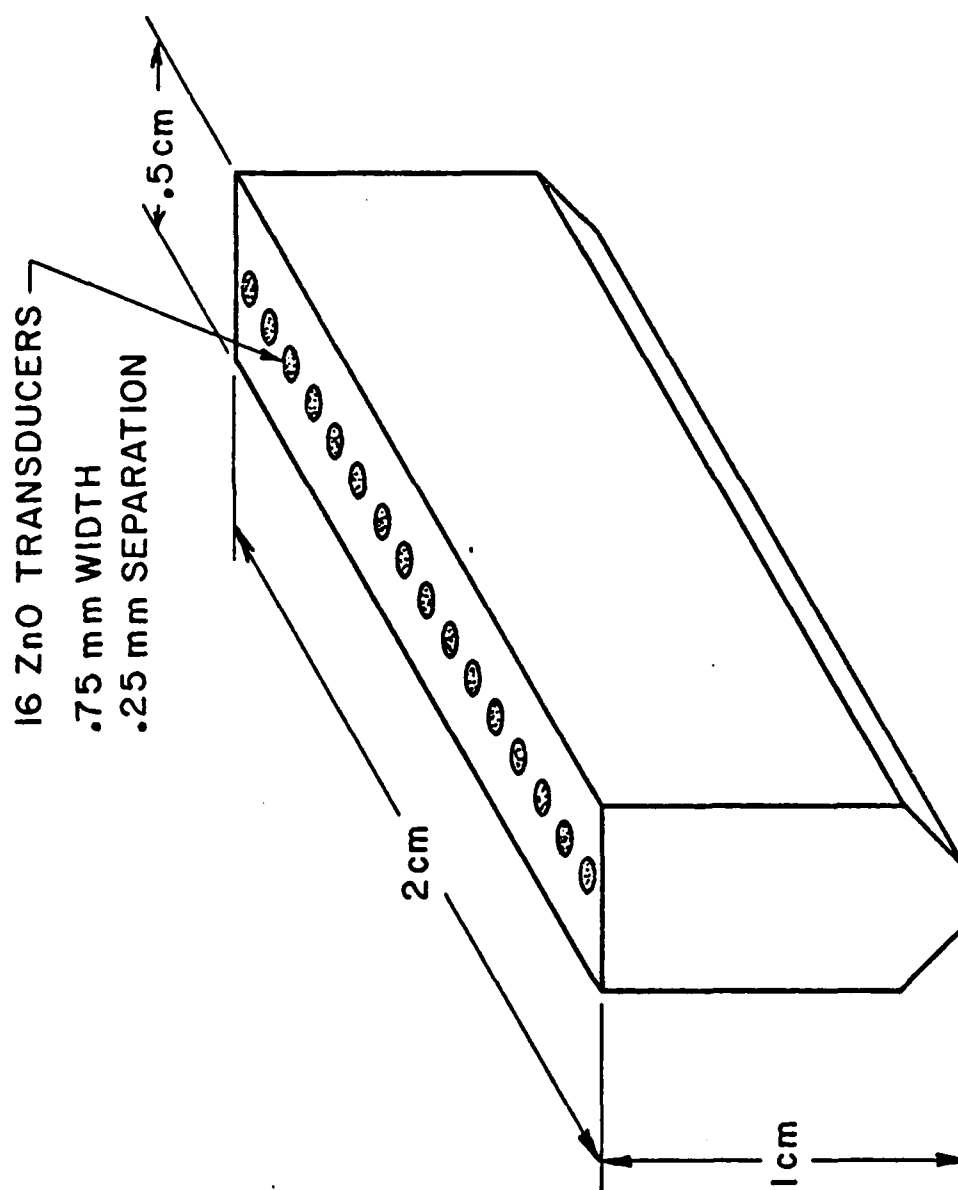


CONTACT WITH Au FOIL



CONTACT WITHOUT Au FOIL

Fig. 2 A comparison of the interface transmission for the gold foil and Hertzian contact schemes.



ZnO ON SAPPHIRE TRANSDUCER ARRAY

Fig. 3 A schematic of the B-scan system.



Rockwell International
Science Center

SC595.32SA

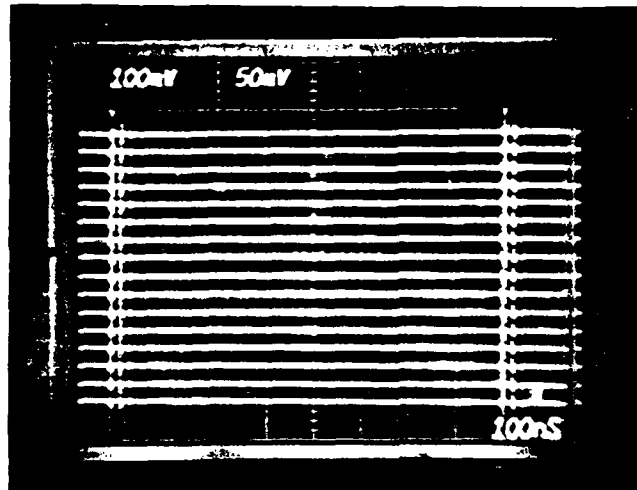


Fig. 4 The outputs from the 16 channel B-scan system.

SC595.32SA

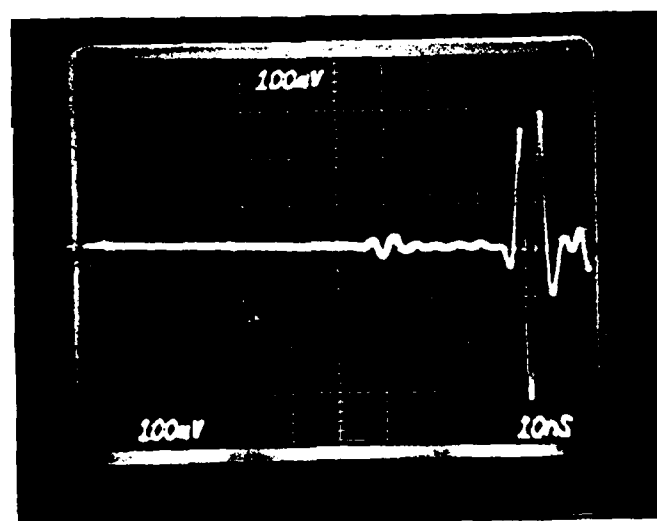
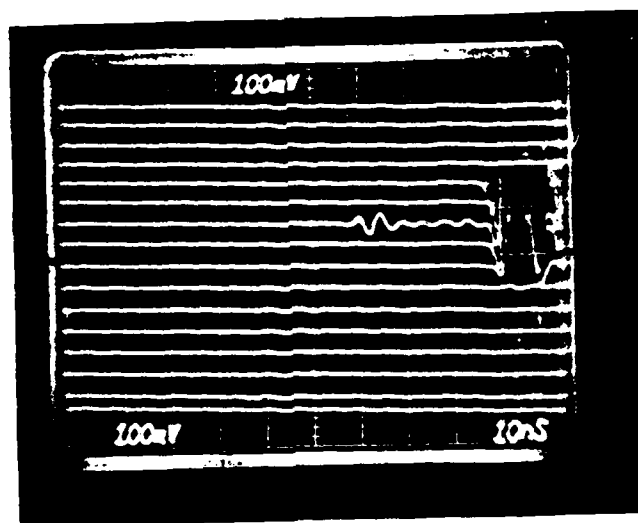


Fig. 5 The effect of a hemispherical void on the signal from the B-scan system.



has built into it a defect, in the form of a hemispherical surface void of radius $200\text{ }\mu\text{m}$. The reflection from the void can clearly be seen on the beam. We have thus proven feasibility of an electronically scanned imaging system for use at these frequencies.

This system has the additional capability of displaying the scan from only one transducer that corresponds to the one which intercepts the defect. This is convenient in order to carry out either a Fourier transform analysis or inverse filtering analysis as discussed in the following section. So the device has capability equal to that of our earlier single transducer system.

Inverse Filtering.

We had also developed a FFT routine to analyze the frequency spectrum of the defects. We are presently working on this technique on isolated WC inclusions in Si_3N_4 . Using this technique, we compare the measured scattering power spectrum of a defect to theory and use this result to identify the type and size of the defect. Another approach to this problem is to compare the time domain scattering spectrum to theory. In order to do this we have to remove the effect of the transducer response by inverse filtering the time domain signals.

Inverse filtering is a well known process that has been used extensively in the field of communication as an equalizer or telephone transmission channels. Lately, it has been suggested for use in NDE to improve the depth resolution and give better characterization of back scattered signals from flaws. The idea here is to separate the specular reflection from the other modes excited in a defect whenever the transducer response is too long (relatively narrow bandwidth) and the echoes are overlapping. In other words, we can make direct comparison to the theoretical time domain response of a defect. Such a process is being implemented presently on a digital computer, and we expect to have results on processing of real signals in our next progress report.

PROJECT III, UNIT C, TASK 4

MICROFOCUS X-RAY AND IMAGE ENHANCEMENT
OF RADIOGRAPHIC DATAJ. J. Schuldies
Air ResearchIntroduction

The objective of this work will be to obtain a quantitative measure of the capabilities of microfocus X-ray and image enhancement of radiographic data for defect characterization in structural ceramics. Included in this evaluation will be an estimate obtained from the radiographic data, of the size of specific isolated defects.

Technical Approach

Radiographic evaluations of the ceramic test specimens will be made using a 100 kv Magnaflux microfocus X-ray system. This unit is capable of achieving a focal spot size of approximately 0.05 mm with a Gaussian intensity distribution. This results in a suppression of radiation outside of the primary beam, improving radiographic details and permitting geometric enlargements with a minimum loss in image quality.

Exposures will be obtained at varying incident angles to the test specimen major surface to determine the effects of X-ray beam perpendicularity on defect size estimations in a parallel surface configuration. Radiographic enlargements or selected specimens will also be obtained to define the limitations and advantages of this technique on image quality and, therefore, defect detection sensitivity.

Additionally, radiographic data will be reconstructed using a Spatial Data Systems image enhancement unit. Digital image processing will be explored to define the degree of defect detection improvement which may be achieved in ceramics. Various modes of image enhancement will be employed to identify optimum processing of gray-scale data to achieve maximum resolution of single defects. This approach will, therefore, establish defect detection sensitivity levels for a single defect of a given type.



Progress

Several test specimens of hot pressed silicon nitride (NC-132) have been received for the initial evaluation. These specimens contain tungsten carbide, silicon carbide and silicon inclusions of 25, 50, 100 and 200 micron size.

Fixturing is being procured to accurately position the test specimens in the center of the incident X-ray beam. A 0.5 milliwatt gas laser has been received to facilitate specimen positioning at the exact center of the beam regardless of specimen orientation.

PROJECT III, UNIT C, TASK 5

CONVENTIONAL ULTRASONIC INSPECTION
METHODS APPLIED TO CERAMICS

G. A. Alers and R. K. Elsley
Rockwell International Science Center
Thousand Oaks, California 91360

Introduction

The availability of a set of ceramic test specimens that contain various known defect types makes possible a detailed intercomparison of various NDE techniques. In other parts of this project, microfocus X-ray methods and specialized ultra-high frequency ultrasonic methods are being used to inspect and classify the defects intentionally placed inside the test specimens. This project is intended to determine the capabilities and limitations that are characteristic of what might be called "conventional" ultrasonic inspection methods which use a commercial transducer immersed in a water bath and a mechanical scan over the part. Such an inspection system is considered to include a computer to control the scanning process as well as perform rapid signal analysis of any echoes returned from defects in the part. Because of the limitations imposed by commercially available transducers and analog to digital conversion instruments, a "conventional" ultrasonic inspection is considered to have an upper frequency limit of approximately 25 MHz or possibly 50 MHz if the rapid digital signal processing capabilities are sacrificed.

The Inspection System

The "conventional" ultrasonic inspection system operating at the Science Center consists of a small water tank into which the sample can be placed and a mechanical scanning device that allows the transducer to be moved along three orthogonal axes as well as rotated to insure that the ultrasonic beam will enter the sample along its surface normal. Motion in the plane of the sample surface (the X and Y coordinates) is achieved through stepping motors which are computer controlled. By maintaining a record of the number



of step instructions that have been sent to these motors, the computer is able to keep track of the position of the transducer and hence locate the position of any ultrasonic indication relative to the sample edges. A Biomation Model 8100, fast A to D converter digitizes the RF ultrasonic signal provided by a Panametrics 5052 PR Pulser/Receiver, the transducer and the specimen. Special programs have been prepared to average together a large number of repetitions of the ultrasonic signal in order to achieve a high degree of accuracy in the digital description of the waveform that is ultimately stored in the computer memory for signal processing. Additional programs are available to Fourier transform the time domain waveforms or subsections thereof using various window functions as well as to generate maps which display the physical location and amplitude of echo signals returned from the specimen.

Results

Since the ceramic specimens have become available only recently, the data to be reported here consists of preliminary information gathered to define the optimum choice of transducers and sensitivity settings. Two high frequency, broad band transducers were already available when the specimens arrived so both were used to collect whatever data was possible.

The first transducer and the one most likely to give the greatest resolving power and sensitivity to small defects was a 1/2-inch diameter, 15 MHz Panametrics unit with a focal length of 1-1/2-inches in water. Qualitative studies using this transducer indicated that it could be made to focus its ultrasonic output on the defect region in the middle of the specimen as well as on the back surface of the specimen. However, the signals observed did not behave in the correct quantitative manner and it was concluded that refraction of the convergent sound beam at the water to ceramic interface caused most of the longitudinal sound wave energy to be sent nearly parallel to the specimen surface and a large amount of mode conversion into shear waves to occur. The remedy for this situation is to obtain a special transducer with a very specifically designed focal length.

The second transducer was a 1/2-inch diameter, 15 MHz broad band unit which was not focused. This transducer has the disadvantage that it cannot locate a reflecting point with much accuracy and its sensitivity

suffers because the ultrasonic energy is distributed over a large (nominally 1/2-inch diameter) area. However, its output approximates a plane wave and hence it is well suited for quantitative comparisons between scattering theory and experiment. Figure 1(a) shows the time domain echo pattern observed from sample No. 132 using this nonfocused transducer. Figure 1(b) shows the region of the time domain between the front surface echo and the first reflection from the back surface on a greatly expanded scale. The reflection from the "defect" in the center of the specimen is now clearly visible. As a first exercise in signal analysis, the "defect" echo was separated from the other signals by a Hanning window function and Fourier transformed. The resultant frequency spectrum was then normalized by the transducer response function determined from the Fourier transform of the reflection from the front surface. The resultant frequency domain representation of the "defect" scattering function is shown in Fig. 2. Features at the low and high frequency ends of this function should not be taken too seriously because they arise from the extreme ends of the frequency spectra of the input functions but the peak near 12 MHz is probably real. Theoretical predictions by many authors describing the scattering of longitudinal waves by spherical inclusions in various solids predict that there is a small maximum in the frequency dependence of the scattering cross section when ka lies between 1 and 2 (where k is the wave number of the incident wave and a is the radius of the scattering sphere). Applying this rule-of-thumb to the present case, it can be concluded that the diameter of the inclusion in this ceramic sample lies between 130 and 260 microns. Data supplied with this sample stated that the intentional defect is a silicon sphere with a diameter of 200 microns, in agreement with the mathematical estimate.

Conclusions

1. "Conventional" ultrasonic inspection techniques which use commercially available instrumentation and transducers in a water bath environment are capable of detecting the larger defects in the ceramic samples provided.

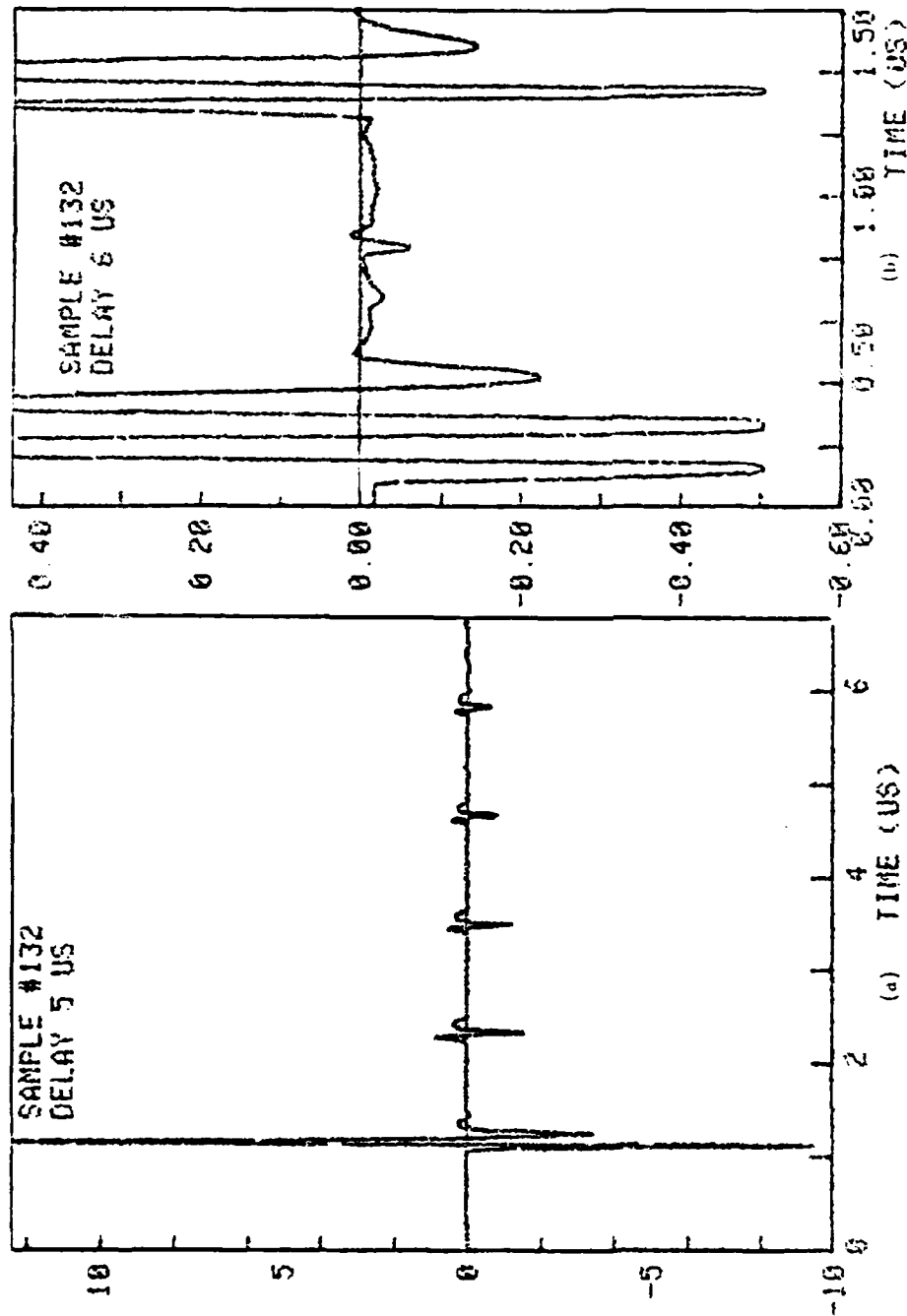


Fig. 1 Computer printouts of the echo pattern observed on a ceramic sample 0.609 cm thick with a defect at its center. (a) Low gain, long time display of echoes, (b) high gain, short time display showing the defect echo.

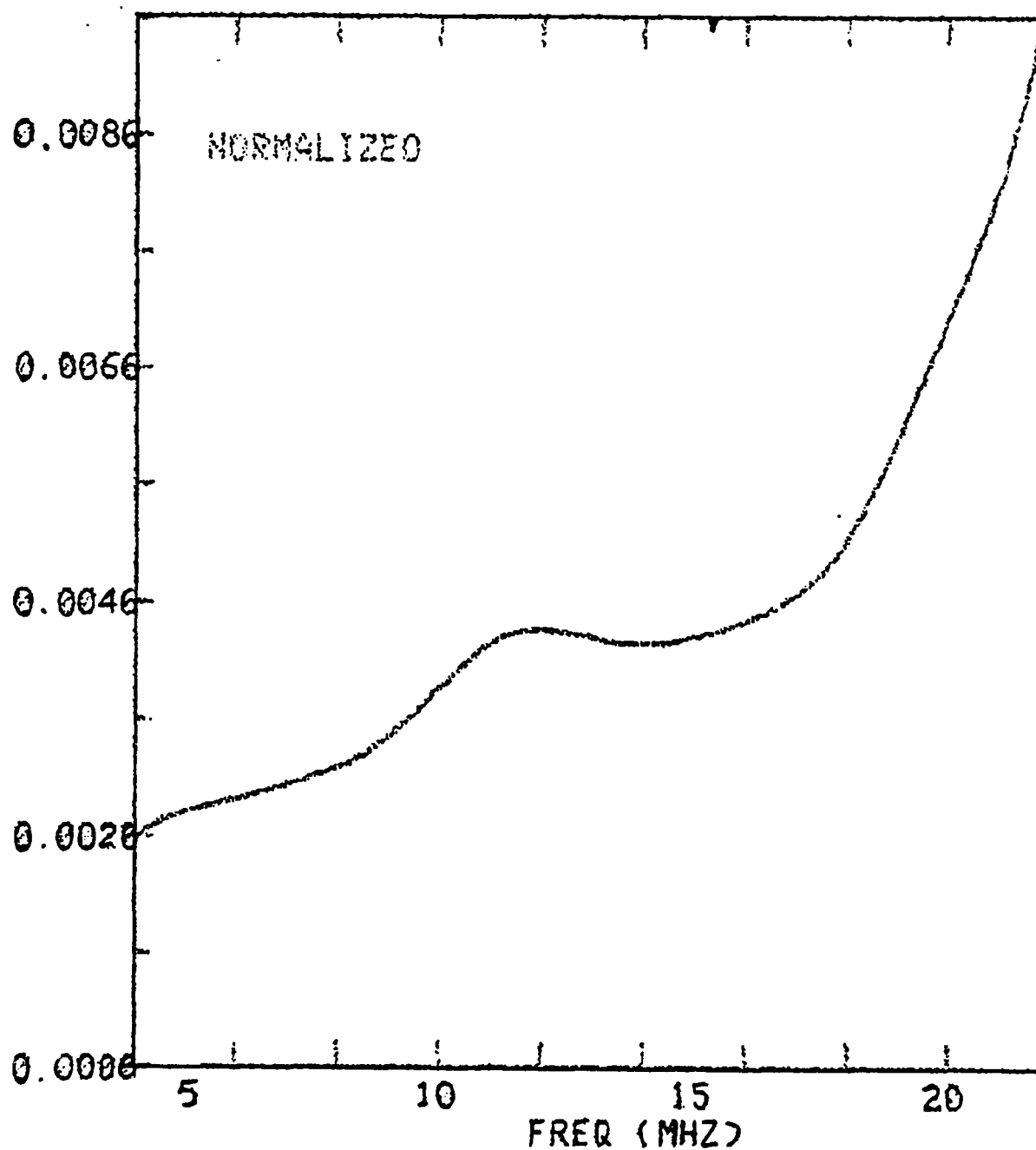


Fig. 2 Fourier transform of the defect echo signal after correction for the frequency response of the transducer.



Rockwell International

Science Center
SC595.32SA

2. Signal analysis techniques involving on-line digital processing of the RF ultrasonic signals appears able to correctly estimate the dimensions of the inclusions.

3. The use of focused transducers to enhance the resolving power and increase the signal-to-noise ratios of the system requires a very careful choice of transducer because of the large refraction of the sound waves at the water to ceramic interface.

END

FILMED

9-83

DTIC